The Wien Effect in Electric and Magnetic Coulomb systems - from Electrolytes to Spin Ice

Vojtech Kaiser

THE WIEN EFFECT IN ELECTRIC AND MAGNETIC COULOMB SYSTEMS

FROM ELECTROLYTES TO SPIN ICE

suive la page de titre utilisé à TU Dresden

THE WIEN EFFECT IN ELECTRIC AND MAGNETIC COULOMB SYSTEMS

FROM ELECTROLYTES TO SPIN ICE

THÈSE / DISSERTATION

en vue d'obtenir le grade de

DOCTEUR DE L'UNIVERSITÉ DE LYON, DÉLIVRÉ PAR L'ÉCOLE NORMALE SUPÉRIEURE DE LYON

zur Erlangung des akademischen Grades
DOCTOR RERUM NATURALIUM (DR. RER. NAT.)

présentée à / *vorgelegt*
l'École Normale Supérieure de Lyon
et / *und*
der Fakultät Mathematik und Naturwissenschaften
der Technischen Universität Dresden
par / *von*

MGR. VOJTĚCH KAISER

née / *geboren am* 25. November 1987
à / *in* Ústí nad Labem (République tchèque / *Tschechische Republik*)

LYON / DRESDEN — 2014

Laboratoire de Physique de l'École Normale Supérieure de Lyon
L'Ècole Doctorale de Physique et d'Astrophysique
Max-Planck-Institut für Physik komplexer Systeme

Abstract

A Coulomb gas comprises charged particles that interact via the long-range Coulomb interaction. The ubiquity of such systems in nature is hardly surprising as the electromagnetic force is one of the four fundamental forces of nature and the Coulomb interaction is its manifestation in a quasistatic limit. Examples include simple and complex electrolytes, colloidal solutions, but also emergent quasiparticles in solid state materials. Coulomb gases possess a richness of phenomena due to the long-range nature of the interactions.

An unexpected yet compelling example of a Coulomb gas was found in spin ice (Castelnovo et al., 2008). Spin ice is a highly frustrated Ising ferromagnet with a largely degenerate manifold of states in which the spins follow rules originally proposed for describing the proton disorder in water ice (Harris et al., 1997). Magnetic monopoles appear when these constraints are violated. The monopoles obtain a magnetic charge due to an intricate interplay between the ice rules and the dipolar interactions of the spins. In effect, a spin can be seen as a magnetic dipole that fractionalizes into two deconfined magnetic charges.

This thesis is devoted to the study of non-equilibrium behaviour of Coulomb gases and spin ice. At the centre of this study lies the second Wien effect which is a linear increase in conductivity if an electric field is applied to a weak electrolyte (Wien, 1931). The conductivity increases due to additional mobile charges whose dissociation from Coulombically bound pairs is enhanced by the field. In the grand canonical ensemble, this enhanced dissociation results in a remarkable increase of the total charge density.

The increase in conductivity has experimental implications for a large variety of materials which can be modelled as Coulomb gases. The second Wien effect is a non-equilibrium process beyond linear response. The seminal theory of Onsager (1934) gives a detailed analysis of the effect. We use numerical simulations to confirm its validity in a lattice Coulomb gas but mainly to study its extensions. The nature of the extensions requires us to also study the equilibrium of Coulomb gases and the transport in them.

Our lattice simulations are a minimal but tunable and extensible model for the Wien effect (Kaiser et al., 2013). The results allow us to uncover the role of the ionic atmosphere which counteracts the second Wien effect. We further use the simulations to characterize the field

dependent mobility of the Coulomb gas which influences the observed increase in conductivity. As the Wien effect is robust and highly universal, we show how it can serve as a diagnostic tool for the field dependence of mobility. The simulations also provide us with an access to the charge correlations which describe the microscopic process behind the Wien effect.

Afterwards we take a closer look at the emergent gas of monopoles in spin ice – the magnetolyte. This is a very alluring task because the magnetic behaviour of spin ice reflects the properties of the Coulomb gas contained within. It has been previously demonstrated that the specific heat of spin ice can be derived from Debye–Hückel theory for screening in electrolytes (Castelnovo et al., 2011). The second Wien effect was proposed to measure the charge of the magnetic monopoles using μ-SR (Bramwell et al., 2009).

We describe the full non-equilibrium dynamics of the magnetolyte including both the second Wien effect and the response of the network of spins that underpins the emergence of the magnetic monopoles and prevents any permanent magnetic currents in particular. The absence of permanent currents would eventually hinder the second Wien effect. However, periodic driving permits stabilizing a density of magnetic monopoles which lies above the equilibrium value. We show that the corresponding non-linear susceptibility of spin ice increases with the amplitude of driving while following the same function that Onsager used to predict the increase in charge density with electric field in electrolytes. This result holds over a broad range of frequencies. We present a simple kinetic model to describe the low and high frequency crossovers to this behaviour. Throughout, we use a straightforward extension of the lattice Coulomb gas simulations to refine our predictions.

It is a highly unusual result to find an analytic theory for the non-equilibrium behaviour of a highly frustrated system beyond linear response. We discuss the experimental conditions necessary for measuring the proposed signatures of the second Wien effect in spin ice and conclude that they are within the current experimental capabilities.

Résumé

Les gaz de Coulomb sont composés de particules chargées couplées entre elles par interaction coulombienne à longue portée. L'ubiquité de tels systèmes n'est pas surprenante, puisque l'interaction coulombienne est une conséquence de l'électromagnétisme, l'une des quatre forces fondamentales connues dans l'Univers. De part la nature de ces interactions, la physique du gaz de Coulomb est très riche, comme par exemple dans des électrolytes plus ou moins complexes, dans des suspensions de colloïdes, mais aussi à travers l'émergence de quasi-particules en matière condensée.

C'est justement dans des composés de glace de spin que le concept de gaz de Coulomb a pris une dimension inattendue, avec la découverte de monopôles magnétiques (Castelnovo et al., 2008). Dans la glace de spin, le couplage ferromagnétique entre spins Ising rend le système fortement frustré. Son état fondamental est extensivement dégénéré, et respecte localement la même contrainte que les protons dans la glace (eau sous forme solide) (Harris et al., 1997). Chaque spin est un dipôle magnétique et peut donc être vu comme la juxtaposition de deux charges magnétiques. Lorsque la contrainte des états fondamentaux est brisée, les excitations qui en résultent prennent la forme de monopôles magnétiques déconfinés.

Dans cette thèse nous nous intéressons au comportement hors d'équilibre des gaz de Coulomb et de la glace de spin. Au centre de cette étude se trouve le deuxième effet de Wien, qui est une croissance linéaire de la conductivité en fonction du champ électrique appliqué à un électrolyte faible (Wien, 1931). Ce phénomène est une conséquence directe de l'interaction coulombienne qui pousse les charges à se lier par paires ; le champ électrique va alors aider à dissocier ces paires et créer des charges mobiles qui amplifient la conductivité. Dans l'ensemble grand canonique, cette dissociation donne lieu à une augmentation remarquable de la densité totale de charges.

L'augmentation de la conductivité a des implications expérimentales pour un grand nombre de matériaux qui peuvent être modélisés par un gaz de Coulomb. Le deuxième effet de Wien est un processus hors-équilibre non-linéaire, remarquablement décrit par la théorie de Onsager Onsager (1934). Nous utilisons des simulations numériques pour confirmer sa validité dans un gaz de Coulomb sur réseau, mais surtout pour étudier ses extensions. La nature de ces extensions nous pousse à

étudier aussi le comportement des gaz de Coulomb à l'équilibre et ses propriétés intrinsèques de transport.

Nos simulations sur réseau constituent un modèle minimal mais ajustable et extensible pour l'effet de Wien (Kaiser et al., 2013), qui permettent de découvrir le rôle de l'environnement ionique qui agit contre le deuxième effet de Wien, ainsi que de caractériser la mobilité du système et sa dépendance en fonction du champ externe. Comme la mobilité est directement liée à la conductivité et que l'effet Wien est robuste et universel, nous montrons comment ce dernier peut servir comme un outil de diagnostic de la dépendance de la mobilité en fonction du champ. Les simulations nous ont aussi donné accès aux corrélations de charges qui décrivent le processus microscopique à la base de l'effet Wien.

Dans un second temps, nous regardons plus précisément le gaz émergent de monopôles dans la glace de spin, aussi appelé "magnétolyte" (Castelnovo et al., 2008), capable de décrire de manière remarquable les propriétés magnétiques de glace de spin. Castelnovo et al. (2011) ont précédemment montré comment la chaleur spécifique de ces cristaux pouvait être calculée grâce à la théorie d'écrantage de Debye-Hückel, tandis que le deuxième effet de Wien a été proposée pour mesurer la charge de ces monopôles magnétiques (Bramwell et al., 2009).

Nous décrivons la dynamique complète hors-équilibre de cette magnétolyte en incluant à la fois le deuxième effet de Wien et la réponse du réseau de spins qui est à la base de l'émergence des monopôles magnétiques. Ce réseau de spin sous-jacent empêche l'apparition de courants magnétiques permanent, ce qui entrave le deuxième effet de Wien. Cependant, un champ magnétique extérieur périodique permet de stabiliser une densité de monopôles magnétiques à une valeur supérieure que celle à l'équilibre. Nous montrons que la susceptibilité non-linéaire correspondante croît avec l'amplitude de ce forçage périodique, et qu'elle suit la même fonction utilisée par Onsager pour décrire la croissance de la densité de charges avec le champ électrique dans un électrolyte. Ce résultat est valable dans une large gamme de fréquences. Nous présentons un modèle cinétique simple pour décrire des limites de ce comportement aux basses et hautes fréquences. Tout au long, nous utilisons une simple extension des simulations de gaz de Coulomb sur réseau pour préciser nos prédictions.

Il est très rare de trouver une théorie analytique du comportement hors-équilibre d'un système hautement frustré au-delà de la réponse linéaire. C'est pourquoi pour finir, nous discutons les conditions expérimentales nécessaires pour mesurer les signatures du deuxième effet de Wien dans des composés de glace de spin, qui s'avèrent être a priori accessibles dans l'état actuel de la recherche dans ce domaine.

Zusammenfassung

Ein Coulombgas besteht aus geladenen Teilchen, die über langreichweitige coulombsche Wechselwirkungen verfügen. Dass solche Systems allgegenwärtig sind, ist nicht überraschend, da der Elektromagnetismus zu den vier Fundamentalkräften gehört, und die Coulombkraft dessen quasistatischen Grenzfall darstellt. Beispiele sind unter anderem einfache und komplexe Elektrolyte, kolloidale Suspensionen oder Anregungen in Form von Quasiteilchen in Festkörpern. Coulombgase weisen aufgrund ihrer langreichweitigen Wechselwirkung eine reichhaltige Phänomenenologie auf.

Ein unerwartetes aber überzeugendes Beispiel eines Coulombgases wurde in Spineis gefunden (Castelnovo et al., 2008). Bei Spineis handelt es sich um einen frustrierten Ising-Ferromagneten mit einem hochentarteten Grundzustand: eine Konfiguration ist ein Grundzustand, wenn alle magnetischen Momente (Spins) die „Eisregeln" befolgen, die ursprünglich für die erlaubten Protonenkonfigurationen in gewöhnlichem Wassereis formuliert wurden (Pauling, 1935; Harris et al., 1997). Magenetische Monopole entstehen, wenn die Eisregeln verletzt werden; deren magnetische Ladung entsteht aus dem komplexen Wechselspiel solcher Regelverletzungen mit den Dipolwechselwirkungen der Spins. Ein Dipol fraktioniert so in zwei magnetische Ladungen, die sich dann als unabhängige Monopole bewegen können.

Diese Doktorarbeit befasst sich mit Coulombgasen jenseits des thermischen Gleichgewichts; insbesondere untersucht sie den zweiten Wieneffekt. Dieser besteht aus dem linearen Zusammenhang zwischen dem Anstieg der Leitfähigkeit schwacher Elektrolyte in elektrischen Feldern und der Feldstärke des angelegten Feldes (Wien, 1931). Die Leitfähigkeit steigt durch die Erzeugung zusätzlicher mobiler Ladungsträger, deren Dissoziationsrate aus coulombsch gebundenen Ladungspaaren durch das Feld vergrößert wird. Im großkanonischen Ensemble führt diese erhöhte Dissoziationsrate zu einem bemerkenswerten Anstieg der gesamten Ladungsträgerdichte. Der Leitfähigkeitsanstieg kann für viele Materialien, die als Coulombgase modelliert werden können, experimentell nachgewiesen werden.

Der zweite Wieneffekt ist ein Nichtgleichgewichtsprozess jenseits der linearen Antwort (linear response). Die bahnbrechende Theorie von Onsager (Onsager, 1934) beschreibt diesen Effekt im Detail. Wir verwenden numerische Simulationen, um die Gültigkeit und Reich-

weite der Theorie in einem Gitter-Coulombgas zu beschreiben, aber insbesondere, um deren Erweiterungen zu untersuchen. Letzteres führt uns auch dazu, uns mit den Gleichgewichtseigenschaften des Coulombgases zu befassen.

Unsere Gittersimulationen stellen ein minimales aber gleichzeitig anpass- und erweiterbares Modell des Wieneffekts dar (Kaiser et al., 2013). Unsere Ergebnisse erlauben es, die Rolle der ionischen Atmosphäre, deren Anwesenheit den zweiten Wieneffekt abschwächt, zu untersuchen. Des Weiteren verwenden wir die Simulationen, um die feldabhängige Mobilität des Coulombgases zu charakterisieren, welche die beobachtete Zunahme der Leitfähigkeit beeinflusst. Da der Wieneffekt sehr robust und zudem universell ist, können wir zeigen, dass er auch verwendet werden kann, um die Feldabhängigkeit der Mobilität zu charakterisieren. Die Simulationen bieten zudem Einblick in die Ladungsträgerkorrelationen, die mit den mikroskopischen Prozessen verknüpft sind, die hinter dem Wieneffekt stehen.

Danach wenden wir uns dem emergenten Gas von magnetischen Monopolen im Spineis zu – einem Magnetolyt (Castelnovo et al., 2008). Dies ist eine besonders reizvolle Aufgabe, da das magnetische Verhalten des Spineises die Eigenschaften des Coulombgases, aus dem es besteht, widerspiegelt. Die spezifische Wärme von Spineis kann aus der Debye-Hückel-Theorie der Abschirmung in Elektrolyten abgeleitet werden (Castelnovo et al., 2011). Außerdem wurde vorgeschlagen, den zweiten Wieneffekt zu verwenden, um die Ladung magnetischer Monopole mittels Myonen-Spin-Spektroskopie (μ-SR) zu messen (Bramwell et al., 2009; Giblin et al., 2011).

Wir liefern eine vollständige Beschreibung der Nichtgleichgewichtsdynamik des Magnetolyten; diese beinhaltet sowohl den zweiten Wieneffekt als auch die Antwort des Spinsystems, aus dem die Monopole hervorgehen, und das insbesondere magnetische Gleichströme verbietet. Deren Abwesenheit wirkt letztendlich dem zweiten Wieneffekt entgegen. Dennoch kann durch Verwendung eines periodischen Magnetfelds eine über das Gleichgewichtsniveau erhöhte Dichte magnetischer Monopole erzeugt werden. Wir können zeigen, dass die zugehörige nichtlineare Suszeptibilität mit der Anregungsamplitude wächst und dabei dieselbe Form annimmt, die Onsager für den Anstieg der Ladungsdichte in Elektrolyten vorhergesagt hat. Diese Ergebnisse gelten für einen breiten Frequenzbereich. Wir präsentieren ein einfaches kinetisches Modell, das die Hoch- und Niedrig-Frequenzgrenzfälle des onsagerschen Verhaltens reproduziert. Wir verwenden durchgehend einfache Erweiterungen der Simulationen eines Gitter-Coulombgases, um unsere Analyse fortzuentwickeln.

Die Herleitung einer analytischen Beschreibung des Nichtgleichgewichtsverhalten eines frustrierten Magneten jenseits des „lin-

ear response" ist äußerst selten. Wir erörtern die experimentellen Bedingungen für den Nachweis des zweiten Wieneffekts in Spineis und schließen, dass dieser mit gegenwärtigen technischen Möglichkeiten beobachtbar ist.

ACKNOWLEDGEMENTS

First and foremost, I would like to express my gratitude to my doctoral advisors Peter Holdsworth and Roderich Moessner. Over the course of the past three years, they have provided invaluable scientific support without which this thesis would not have materialized. Whenever I had a question or a problem they rapidly responded with helpful answers and suggestions. I am also grateful that they have helped me navigate all the complexity that arises from doing a cotutelle doctorate.

Peter's insights and optimism have been a driving force throughout my thesis. I have especially valued them in moments where finding a correct solution required exploring new directions and perseverance. Peter's condensed matter courses together with an internship with him while he was visiting Dresden in 2010 were decisive for my choice of the topic of my PhD. Later interactions with Peter only confirmed this decision. His advice also helped me greatly during my teaching experience in Lyon.

Roderich's ability to distill a complex problem into a simple model has been both immensely helpful and inspiring. His insistence on seeing the broader picture while being precise in details allowed me to improve my results on many occasions. His scientific and organisational skills as the head of the Condensed Matter department are crucial for making Max Planck Institute for the Physics of Complex Systems a fascinating and stimulating place where one can discuss many aspects of modern physics and regularly attend world-class scientific events.

It is a pleasure to thank Steven Bramwell for his inspiring comments on my work from both theoretical and experimental perspectives, for showing me how interesting physical chemistry can be and welcoming me during my stay in London. He also provided me with many useful references to the chemical literature.

I am grateful to Ludovic Jaubert for providing the very first code I started my simulations with and for taking time to provide me with an introduction to spin ice and algorithms, as well as, for answering many related questions. I would like to thank Laura Bovo and Jonathan Bloxsom for elucidating many aspects of experiments on spin ice. Arnab Sen has provided many insightful comments on pinch points. I also thank Michael Faulkner for discussions on Coulomb gases.

I am grateful to my family and my friends for heartening support and many joyful shared moments. Most importantly, I would like to express my deepest gratitude to Annemarie for her continuing love and support and for her patience during the time of writing this thesis.

CONTENTS

List of Figures

List of Tables

List of Symbols

In this thesis, we use the SI units (*Le Système international d'unités*). Where possible, we follow the *International Union of Pure and Applied Chemistry* (IUPAC) nomenclature for chemical terms. If no unit is given the quantity is dimensionless.

Symbol	Quantity	Unit, other remarks
a	diamond lattice bond length	m ($\simeq 4.3$ Å in spin ice)
$\mathfrak{a}$	activity	
a_c	cubic lattice constant	m ($\simeq 10$ Å in spin ice)
A	magnetic vector potential	T.m
$\mathscr{A}$	Helmholtz free energy	J
α	Ewald sum parameter	
b	Wien effect parameter	$\mu_0 Q_\mathrm{m}^3 B/(8\pi(k_\mathrm{B}T)^2)$ or $Q_\mathrm{e}^3 E/(8\pi\epsilon(k_\mathrm{B}T)^2)$
β	inverse temperature	K^{-1}
$\mathbf{B}$, B	magnetic field	T
D	diffusion constant	m^2/s
$\mathscr{D}$	demagnetization factor	
$\mathbf{E}$, E	electric field	V/m
ϵ	permittivity	F/m, $\epsilon = \epsilon_0 \epsilon_\mathrm{r}$
ϵ_0	permittivity of vacuum / electric constant	8.8854×10^{-12} F/m
ϵ_r	relative permittivity / dielectric constant	
g	pair correlation function	
γ	activity coefficient	
$\mathbf{H}$, H	magnetic field	A/m
$\mathscr{I}$	ionic strength	m^{-3}
$\mathscr{I}_n$	numeric ionic strength	
$\mathbf{j}_\mathrm{m}$	electric current density	$\mathrm{A/m}^{-2}$
$\mathbf{j}_\mathrm{m}$	magnetic current density	A/(m.s)
k_B	Boltzmann constant	1.381×10^{-23} J/K
k_A	association rate constant	
k_D	dissociation rate constant	

Symbol	Quantity	Unit, other remarks
K_A	association equilibrium constant	
K_D	dissociation equilibrium constant	
$\mathscr{K}_A$	association concentration quotient	
$\mathscr{K}_D$	dissociation concentration quotient	
$\varkappa$	mobility	s/kg
$\varkappa_e$	electric mobility	C.s/kg = A.s^2/kg, $\varkappa_e = Q_e \varkappa$
$\varkappa_m$	magnetic mobility	A.m.s/kg, $\varkappa_m = Q_m \varkappa$
ℓ_B	magnetic field length	m
ℓ_D	Debye length	m
ℓ_E	electric field length	m
ℓ_H	magnetic field length	m
ℓ_T	Bjerrum length	m
$\mathbf{M}$, M	magnetization	A/m
m	magnetization relative to equilibrium value	
μ	magnetic moment	A.m^2 ($\mu \sim 9.87\ \mu_B$ in spin ice)
μ_0	permeability of vacuum / magnetic constant	$4\pi \times 10^{-7}$ N/A^{-2}
μ_r	relative permeability	
μ_B	Bohr magneton	9.274×10^{-24} A.m^2
n	number charge density	
n_f	free charge number density	
n_b	bound charge number density	
ν	chemical potential	J (often ν/k_B in K is given)
ν_0	bare charge chemical potential	J
N	total number of charges	
$N_\pm$	total number of positive/negative charges	
N_S	total number of spins	
N_T	total number of tetrahedra	
Ψ	electrostatic potential	V
q	relative charge density increase	
Q_e	electric charge	C
Q_m	magnetic charge	A.m
ρ	volumic density	m^{-3}
ρ_{Q_e}	volumic electric charge density	C.m^{-3}

Symbol	Quantity	Unit, other remarks
ρ_{Qm}	volumic magnetic charge density	A.m^{-2}
$\mathscr{R}$	proposal probability of MC step	
S	entropy	J/K
$\mathbf{S}$	probability current density	
$\mathscr{S}$	acceptance probability of MC step	
T	temperature	K
τ_{c}	chemical lag	s
τ_{L}	Langevin time lag	s
τ_{S}	magnetization time lag	s
$\mathscr{T}$	period of driving	s, or MC steps
U_{C}	Coulomb potential	J
$\tilde{V}$	volume per lattice site	m^3
$\tilde{V}_{\text{T}}$	volume per diamond lattice site	m^3
$\tilde{V}_{\text{S}}$	volume per rare-earth ion (spin)	m^3
$\mathbf{W}$, W	configuration vector	m
$\mathfrak{z}$	valence of an ion	

The rate constants and equilibrium constants are dimensionless because they relate to number densities. This introduces factors of characteristic volume per lattice site in general $\tilde{V}$ or per diamond lattice site $\tilde{V}_{\text{T}}$ to certain formulas, but simplifies applying theoretical calculations to simulation results on a lattice.

1

INTRODUCTION

In science, the recent discoveries and developments are often called the frontier. The word evokes uncharted territories where the struggle with the unknown should happen. There is however another meaning to this word – the area along an existing boundary – and often the frontier of physics lies where it meets another science. The boundary between physics and chemistry is one of the most fruitful places of collaboration. Physical chemistry (Moore, 1999), solid state physics (Ashcroft and Mermin, 1976), polymer science (Gennes, 1979), and even modern cuisine (This, 2002; Barham et al., 2010) have all benefited from this exchange of ideas.

This thesis lies on the crossroads of two fields lying along the physico-chemical frontier – condensed matter physics and electrochemistry. From an outside point of view the two sciences are completely disparate. The theory of both has nevertheless followed a very similar trajectory.

Electrolytes were first considered to consist of the solute and solvent in unmodified form, the solute being dissolved only by the action of an electric field. Later, it has been established that the solute dissociates into separate charged ions without any applied field. A crucial step was the realization that ions in an electrolyte obey the same laws as molecules in a gas. Finally, it was discovered that each ion is surrounded by a complex environment of other ions and solvent molecules. Therefore, a gas model of an electrolyte has to include a non-ideal behaviour. The deviations are described by rewriting the ideal gas law in terms of effective quantities such as activity and fugacity that replace concentration and pressure respectively (Moore, 1999).

Similarly, solid materials and especially crystals were initially seen as more or less regular structures of their constituents. The discovery of the electron and the advent of quantum mechanics brought a new model. A gas of electrons, or phonons and other quasiparticles was found to capture the electronic, acustic and other properties of solids. Again, further developments have shown that this gas deviates from ideality and properties of the quasiparticles arise from their interactions with surroundings. The interactions are often described by keeping the formulas in the ideal form while assigning an effective mass and other effective properties to the quasiparticles (Ashcroft and Mermin, 1976).

A special non-ideal gas, the *Coulomb gas*, is the unifying topic of this thesis. The Coulomb gas comprises charged particles of two or more species interacting with a Coulomb law which is proportional to $1/r$ in three dimensions[1]. Each sign of the charge is represented by at least one species and the sum of all charges is zero, i.e. the system is globally electroneutral.

Electrolytes were the first known example of Coulomb gases, possessing the electrostatic Coulomb interaction. These now encompass a large number of systems from biochemistry to fast ion conductors (Levin, 2002). There are also numerous examples of quantum Coulomb gases, e. g. electrons and holes in semiconductors. However, not only the fundamental electromagnetic force leads to the Coulomb potential but it can also be an emergent phenomenon. Many examples are formed by quasiparticles studied by condensed matter physics. In two dimensions, vortices in 2d XY model (Kosterlitz and Thouless, 1973; Villain, 1975; José et al., 1977) and in superfluids (Minnhagen, 1987) form a Coulomb gas. However, the two dimensional Coulomb interaction diverges at infinite seperation which makes it quantitatively different from the non-confining three dimensional one.

At this point, the *spin ice* as the other main actor of this thesis comes into play. Spin ice is a highly frustrated magnet (Harris et al., 1997). The competing interactions in its pyrochlore lattice of spins cannot be all satisfied at once leading to a high degeneracy of states. The extensive degeneracy of the states allows large fluctuations even at low temperatures that in turn give rise to unique quasiparticles – *magnetic monopoles*[2].

Magnetic monopoles in spin ice form an emergent three dimensional Coulomb gas (Castelnovo et al., 2008). The monopoles arise from the spins that separate into two magnetic charges in a similar fashion that a salt dissociates in a solution. Yet the crucial difference is that the spins are not originally composed of magnetic monopoles because alone they are spin states of rare-earth ions. The monopoles emerge from the collective behaviour of spin ice. This is a prime example of the concept of *fractionalization* that I discuss in detail later.

The Coulomb gas in spin ice can be called a *magnetolyte*. I show on the following pages how the knowledge of electrolytes translates into the study of the magnetolyte. The magnetolyte is a very effective description in comparison with the original spin model with its complex

---

1 The name plasma is sometimes used as synonymous for a Coulomb gas. I consider them different in this work. Many concepts are shared between the two, but describing plasma often requires the whole electromagnetic theory beyond the electrostatic approximation taken here.

2 The emergent magnetic monopoles in spin ice are different from the elementary magnetic monopole particles which remain elusive to this day (Milton, 2006).

interactions. In fact, the emergent nature of monopoles means there is no analogue of solvent which influences the properties of the Coulomb gas. Also any hydrodynamic interactions are absent. Moreover, the positive and negative monopoles have identical properties apart from the sign of the charge. This brings the magnetolyte close to the ideal abstraction of electrolytes called the *restricted primitive model* (McQuarrie, 2000).

Numerical simulations of spin ice are simpler in the magnetolyte picture (Jaubert and Holdsworth, 2011). Monte Carlo simulations serve as a gauge for the theory both in electrolytes and magnetolytes. Along this path, I present the first numerical simulation of the *second Wien effect* — the universal non-linear non-equilibrium increase in charge density of weak electrolytes in external field (Wien, 1931). The simulations confirm the seminal theory of the Wien effect by Onsager (1934) but also help describe several of its extensions and gain insight into the underlying microscopic processes (Kaiser et al., 2013). The final result of this thesis is an illustration of the second Wien effect in the magnetolyte and as a consequence, a prediction for the non-linear susceptibility of spin ice.

There is a longstanding hypothesis that language has a degree of influence on perception. The classic argument states that distinguishing two colours is made easier by having different two words for them (see Regier and Kay (2009) for a recent discussion). Similarly, a chemist and a physicist have a different point of view. For example, physicists tend to use absolute temperature scales and fundamental constants to describe a system. Chemists compare it to a reference state at standard conditions. Terms like fugacity or chemical potential have a related but distinct meaning in the two sciences. This thesis will try to provide translations when necessary.

Having charted the frontiers and boundaries, I devote the rest of this introduction to elaborating the ideas sketched so far. First, I motivate the study of Coulomb gases. I present a brief historic outline and concepts of electrolytes and frustrated magnets. The final section of this chapter describes the division of the thesis.

1.1 Why Coulomb gases?

I have already defined the Coulomb gas, but the question arises why is their study worth while and how they stand out between other non-ideal gases. The Coulomb gases lie "at the edge of statistical mechanics". The long-range Coulomb potential allows for configurations whose electrostatic energy diverges in thermodynamic limit. However, the electroneutrality means that screening can make the Coulomb po-

tential effectively short-range. This guarantees that concepts of statistical mechanics are applicable to Coulomb gases (Lebowitz and Lieb, 1969; Lieb, 1976), even though the methods of computation often need extending to fully describe the underlying long-range interactions.

If the cluster expansion of Montroll and Mayer (1941) is applied to a Coulomb gas, infinite series of divergent integrals need to be resummed to obtain a finite result (Mayer, 1950; McQuarrie, 2000). The critical behaviour of the Coulomb liquid-gas transition was only established in the last two decades. The difficulty lies in disentangling the divergent correlation length due to the criticality from the natural divergences of the Coulomb potential. Ultimately, the critical behaviour falls into the same three dimensional Ising class as short-range interacting gases (Luijten et al., 2002). Thus the equilibrium behaviour seems to resemble other non-ideal gases due to the electrostatic screening.

Out of equilibrium, the long-range nature of Coulomb interactions make phenomena possible that differ strongly from those observed in other non-ideal gases. One of the most astonishing effects is that the conductivity of Coulomb gases increases linearly with applied field if the coupling is strong and the gas dilute (so-called *weak electrolyte limit*). This is the second Wien effect, also called the field dissociation effect. The enhanced conductivity is caused by a number of charge carriers generated by the field driven dissociation.

In equilibrium, equivalence of ensembles guarantees that the same results will be obtained whether we fix the particle density or the chemical potential. Away from equilibrium such equivalence is not at all guaranteed. Yet it is surprising how different the canonical and grandcanonical results are in a weak electrolyte. In a Coulomb gas, the local screening is wiped out by an external field if the charges flow too fast for the ionic atmosphere to establish. As the correlations vanish in the field, the systems starts to resemble a flowing ideal gas more and more. However, the grand canonical case will resemble an ideal gas at much higher density due to the Wien effect than the system with its density fixed.

The classical example of Coulomb gases are electrolytes, I describe next how their theory developed and how these developments closely followed the advances in thermodynamics, statistical physics, and the kinetic theory.

1.2 Electrolytes

It took two centuries from Newton's law of gravity to Coulomb's law although they have the same mathematical form and the electromagnetism is a much stronger force than gravity. The electroneutral-

ity causes the electrostatic forces to be compensated in most observed objects while the positivity of gravitational mass manifests itself on astronomical scales. When Coulomb discovered the law of electrostatic attraction and repulsion in 1785, it helped fuel the concurrent growth of interest in electricity.

The first electric cells by Galvani and Volta provided the first stable currents for electromagnetic experiments and drew a connection between chemical reactions and electricity. Thus electrochemistry lies at the foundations of the practical study of electromagnetism and of the physical chemistry. Faraday established the electrochemical terminology and the relation between the mass and charge of ions transferred during electrolysis. Yet he believed that ions are liberated from chemical compounds only due to an applied voltage.

Meanwhile, thermodynamics and the kinetic theory developed drawing inspiration from the study of heat engines and various states of matter. This allowed quantitative descriptions of solutions. A breakthrough came around when Arrhenius (1887) and van 't Hoff (1887) described electrolytes as composed of separate ions. Moreover, these ions were to follow the same laws that described gases. At the same time, Raoult (1887) established experimentally, by measuring their partial pressure, that mixtures of solutions also follow the ideal gas law. A year later, Ostwald (1888) used the Guldberg–Waage law of mass action to compute the extent of dissociation of electrolytes. This was the first time that the thermodynamic theory of gases was applied beyond the state of matter it was concieved for.

Electrochemistry has always investigated transport phenomena in parallel with equilibrium properties. Kohlraush measured a large number of electrolytes and found out that each type of ions has a well defined specific resistance. The total resistance of the electrolyte was obtained by summing over the constituents. This discovery was named the law of independent migration of ions (Kohlrausch, 1880). Nernst and Planck subsequently developed transport theory of electrolytes in a form of a convection–diffusion equation (Barkan (2011) describes the evolution of this equation); a more specific version of the later equation of Smoluchowski (1916).

As experiments became more precise in the following decades, it became obvious that the ideal gas description is not sufficient. Deviations from the ideal behaviour were observed in two quantities – the freezing point depression and the mobility of ions. Raoult (1882) has shown that a mixture has a lower freezing point than each of the components on its own. But measurements in electrolytes led to a different freezing temperature dependence on concentration than that predicted by the ideal gas theory.

Deviations from ideal gas behaviour were also measured in conductivity. Kohlrausch et al. (1898) made an observation that the molar conductivity of ions decreases with increasing salt concentration. He proposed a dependence on a cube or square root of concentration. Again, this paralleled the development in thermodynamics, where van der Waals proposed his equation of state to account for the finite compressibility and condensation of real gases. The Van der Waals correction to the ideal gas law for gases was different to the correction necessary for electrolytes. Lewis established the terms *fugacity* (Lewis, 1901) and *activity* (Lewis, 1907) to capture the effective pressure and concentration which would need to be assigned to an electrolyte if it followed the ideal gas model. For early accounts of the evolution of the concept of activity see (Bjerrum, 1919; Brønsted, 1927).

Initially it was thought that the decrease of conductivity originates in the increase in association with growing concentration. This effect plays a role in weak electrolytes, including acetic acid and ammonia in water. However, Sutherland (1905) first proposed and afterwards Bjerrum (1909) showed that another class of electrolytes – *strong electrolytes* – have a negligeable degree of association. The elegant experiment of Bjerrum demonstrating this effect is based on dissolving chromium salts in water. Chromium salts and ions in solution have a strong yet different colour. While changing their concentration and observing the colour of the solution, Bjerrum could not observe any change in the tone of their colour which would have happened if the ions associated to chromium salt molecules in the solution. Thus the change in molar conductivity has to be explained by considering interionic forces rather than the dissociation equilibrium.
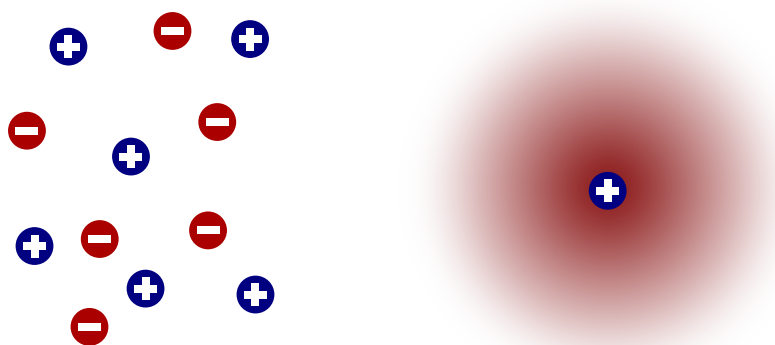
Figure 1.1: **Charge screening.** Coulombic interactions cause each charge to be surrounded by charges of opposite sign (left). The Debye–Hückel theory treats this problem in a mean field fashion and gives a probability distribution for the charges in the screening cloud (right).

Debye and Hückel have formulated the first consistent theory of non-ideality of electrolytes. The basic result was that each ion is surrounded by an atmosphere of equal but opposite charge. The ionic atmosphere screens the central charge so that the effective potential decays exponentially at long distances. This was also the first theory for a Coulomb gas and the basis of many further extensions. While the predictions for the freezing point depression and the activity coefficient (Debye and Hückel, 1923a) were correct, the conductivity theory predicted incorrect prefactors for the correct square root dependence on density (Debye and Hückel, 1923b). The missing piece was that Debye and Hückel considered only the Brownian motion of one of two kinds of ions present in their model. Onsager (1926) amended the theory and obtained the correct limiting law for conductivity of strong electrolytes.

Bjerrum (1926) added the first correction to Debye–Hückel theory in the form of neutral pairs bound via the Coulomb interaction. Further developments of the theory of conductivity followed, for example the theory of Fuoss and Onsager (1957). The thermodynamics followed this suit with almost every method of modern statistical mechanics being applied to electrolytes at some point. For an overview see for example (Falkenhagen, 1971; Levin and Fisher, 1996; McQuarrie, 2000; Levin, 2002; Wright, 2007).

I conclude this overview with two effects discovered by Max Wien and named after him (early review in Eckstrom and Schmelzer (1939)). Both effects result in increased conductivity of the electrolyte. Wien speaks about these effects as the first deviations from Ohm's law observed. The first effect was observed in strong electrolytes (Wien, 1927, 1929). The theory of this effect was found by Wilson in 1936 in his unpublished thesis and simplified and extended by Onsager and Kim (1957). In equilibrium the presence of screening cloud around them slows down ions. The first Wien effect is an increase in conductivity as the screening cloud is first perturbed and then removed by the applied field which allows the ions to move faster.

The second Wien effect[3] (Wien, 1931; Schiele, 1932) was already mentioned in the previous section. The increase in conductivity is observed exclusively in weak electrolytes and it is caused by the field reorienting and subsequent dissociation of the Bjerrum pairs. Onsager (1934) was the first to elucidate this mechanism. He gave a solution that is valid to all orders of field. This can be seen as a precursor to his subsequent mathematical exploits like the solution of the two dimensional Ising model.

The calculation involves solving the drift-diffusion (Smoluchowski / Fokker–Planck) equation for the ions in their mutual Coulomb poten-

---

3 If the type of the Wien effect is not specified, we shall mean the second Wien effect. The first Wien effect is always named in full.

tial and the external linear potential. This task can be compared to finding a complete eigensystem of the Schrödinger equation for such a system. For this exact solution, Onsager developed a new theory of Mathieu functions which was the subject of his doctoral thesis. A famous anectode tells that the thesis was accepted by the department of chemistry only at the insistence of the department of mathematics (Hemmer et al., 1996).

The second Wien effect was also among the first "unmeasurably fast reactions" whose kinetics were measured by Manfred Eigen (Eigen and Schoen, 1955; Eigen and De Maeyer, 1956). The increase in conductivity due to the Wien effect was observable on shorter timescales than other previously measured effects because the electric field can be generated with higher frequencies than for example ultrasound waves (Eigen et al., 1953). The work on very fast kinetics earned Eigen the Nobel Prize in Chemistry in 1967 (Eigen, 1967).

In the following decades the second Wien effect was measured in a myriad of systems that all map to a weak electrolyte (an overview can be found in (Kaiser et al., 2013) and this thesis). I present the first numerical simulations of the second Wien effect in this thesis which among other extensions clarify the interplay between the first and the second Wien effect. The simulation was inspired by spin ice which leads us to the second aspect of the thesis.

1.3 Frustrated magnets

Frustrated magnetism is a field with a great promise for constructing unconventional states of matter. The magnetolyte in spin ice is only one of many examples. *Frustration* refers to the impossibility of minimizing the global energy by simultaneously satisfying all local constraints. This can be caused by disorder as in the case of spin glasses (see for example Young and Young (1998)), by competing interactions, by a purely geometrical frustration, or a combination of these. Here I will deal only with the geometrical frustration. The part of the local constraints that is satisfied to minimize the energy can be chosen in many ways leading to an extensive degeneracy of the groundstate (see figure 1.2 for a simple example). The large degeneracy means that even very large fluctuations are energetically cheap. This supresses ordering and gives rise to unusual quasiparticles related to these fluctuations.

1.3.1 Magnetic behaviour

Non-frustrated magnets tend to order around the Curie–Weiss temperature $T_{CW} = q|J|/k_B$, where q is the coordination number of the lat-
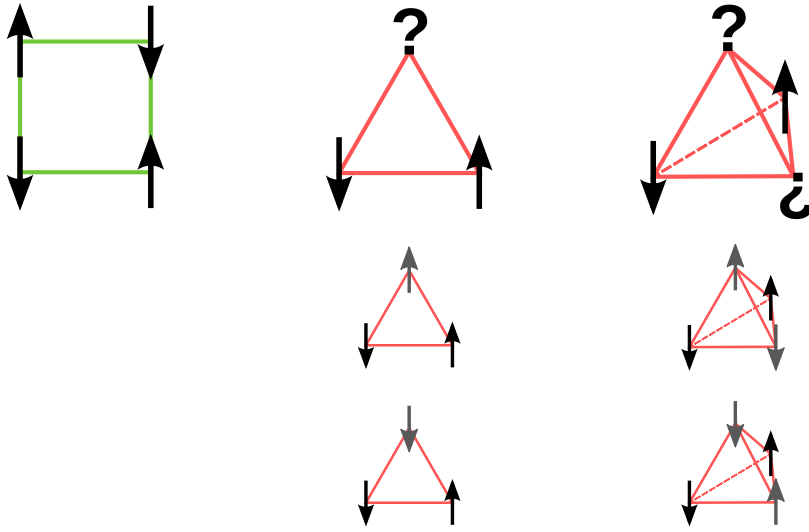
(a) Frustration in clusters.
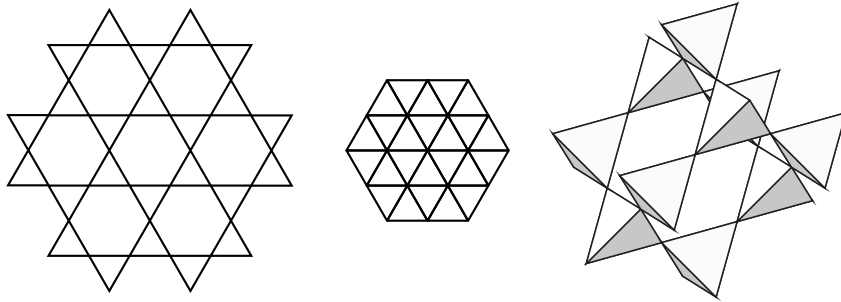
(b) Lattices supporting frustration.

Figure 1.2: **Geometrical frustration.** The energy of a square cluster of Ising spins with antiferromagnetic interactions can be minimized by minimizing the energy on all bonds (upper left). This is impossible in a triangular cluster or in a tetrahedron of Ising spins (upper right). If two of the spins are fixed, the lowest energy state of the square cluster is unique whereas it is degenerate in the triangle and the tetrahedron. Lattices composed of these simplexes are prone to give rise to frustration (lower panel). Examples shown are the kagome lattice (Zeng and Elser, 1990; Huse and Rutenberg, 1992), the triangular lattice (Wannier, 1950), and the pyrochlore lattice (Anderson, 1956).
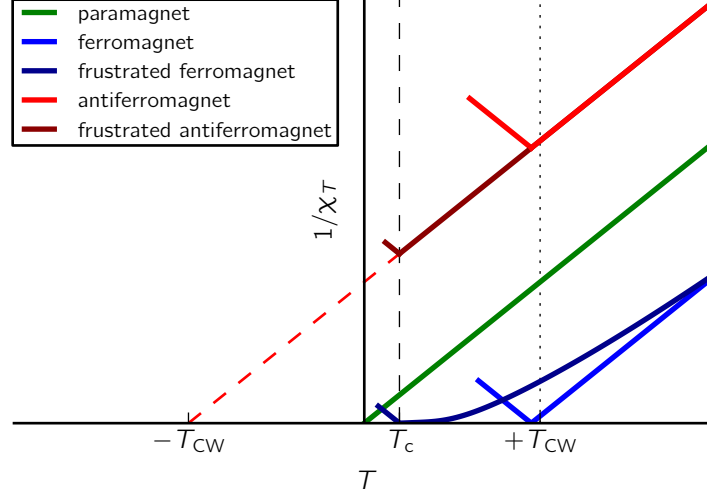
Figure 1.3: **Inverse susceptibility in different types of magnets.** All types of magnets follow the Curie–Weiss law $\chi_T \propto 1/(T \pm T_{\mathrm{CW}})$ in the paramagnetic phase (at high temperatures). Unfrustrated magnets order close to the mean-field prediction. The fluctuations lower the critical temperature only slightly. In frustrated magnets, the ordering is supressed to temperatures T_{c} much below the Curie–Weiss temperature T_{CW} which nevertheless dictates the crossover from high temperature behaviour (Curie–Weiss law). In the range of temperatures $T_{\mathrm{c}} < T < T_{\mathrm{CW}}$ frustrated magnets behave as a cooperative paramagnet (Villain, 1979). Below T_{c} the susceptibility is determined by the type of order.

Antiferromagnets have a maximum of susceptibility at the critical Néel temperature. As the critical temperatures decreases, the maximum shifts. In contrast, ferromagnets exhibit a divergence of susceptibility at the ordering transition. In the diagram we can see that to lower the transition temperature while avoiding this divergence, the ferromagnets cannot keep following the high temperature Curie–Weiss law to low temperatures. A deviation from the Curie–Weiss law has to occur in frustrated ferromagnets to remediate this situation. The most studied frustrated ferromagnet – spin ice – exhibits a Curie law crossover from $\chi_T = C_{\mathrm{C}}/T$ to $\chi_T = 2C_{\mathrm{C}}/T$ at low temperatures (Jaubert et al., 2013). For clarity, we draw a Curie law crossover in the figure that is more pronounced than the one in spin ice.

tice (Mattis, 2006). T_{CW} is a mean field prediction for both ferro- and antiferromagnets (called the Néel temperature T_N in antiferromagnets). Fluctuations in conventional magnets lower the transition temperature only slightly. For example, the square lattice Ising model orders at $k_B T_c = 2J/\log(1 + \sqrt{2}) \simeq 2.27 J$ (Onsager, 1944) which is comparable to the mean field prediction $k_B T_{CW} = 4J$. The ratio is $T_c/T_{CW} = 0.57$ on a square lattice and for the simple cubic lattice Ising model it is close to 0.8.

In frustrated magnets, the fluctuations between the degenerate states prevent the ordering either completely or down to a temperature $T_c \ll T_{CW}$. The degree of frustration expressed as T_{CW}/T_c is typically of the order of a hundred. This is the strongest experimental signature of frustrated magnets, others being broad diffuse features in neutron scattering (see Lacroix et al. (2011) for extensive discussion). Frustrated magnets are paramagnetic at high temperatures and follow the Curie–Weiss law (schematic diagram in figure 1.3) to temperatures below T_{CW} until they order below T_c to a model specific state. The state between the Curie temperature and the actual ordering phase transition is called the *collective paramagnet* (Villain, 1979). Unlike spins in common paramagnets, spins in collective paramagnets are not independent; their low energy fluctuations are correlated.

Frustrated antiferromagnets keep following the Curie–Weiss law $\chi_T \propto 1/(T + T_{CW})$ down to the ordering temperature[4]. On the other hand, frustrated ferromagnets exhibit a more complex paramagnetic behaviour with a crossover to a modified Curie law (Jaubert et al., 2013). This is necessary because following the Curie–Weiss law $\chi_T \propto 1/(T - T_{CW})$ into the cooperative paramagnetic regime would lead to a divergence in susceptibility above the ordering temperature.

The third law of thermodynamics forbids any extensive degeneracy at zero temperature. Eventually the system has to either order or end in a superposition of many equal states that are connected by quantum resonances. The ordering either happens due to a weaker interaction that lifts the degeneracy or via a mechanism called the *order by disorder* (Villain et al., 1980; Shender, 1982). The degenerate manifold contains state of the same energy. However, the surroundings of these states are not equivalent. The larger the number of states accessible with small thermal or quantum fluctuations from one of the degenerate states, the more probable it is to observe the system in that state or in its vicinity (see figure 1.4). This is akin to the entropic force that causes a Gaussian polymer to prefer a certain radius of gyration (Gennes, 1979). A compelling example of the order-by-disorder is the highly

---

4 The positive sign in the Curie–Weiss law for antiferromagnets can be equally described by a negative Curie–Weiss temperature $(-T_{CW})$.
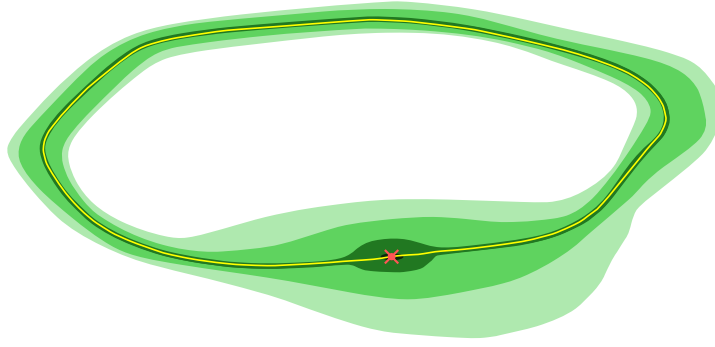
Figure 1.4: **Order by disorder.** A sketch of how fluctuations select one state out of a degenerate manifold. The degenerate manifold (yellow loop) has fluctuations of different strength for different states (shades of green). The ground state (red point) is selected out of the manifold as the dominant state at low temperatures because the large fluctuations cause the system to spend most time in its neighbourhood.

frustrated XY pyrochlore antiferromagnet $Er_2Ti_2O_7$ (Champion et al., 2003; Zhitomirsky et al., 2012; Savary et al., 2012).

If ordering is absent down to absolute zero, frustrated magnets are expected to form a *quantum spin liquid* (Balents, 2010; Gingras and McClarty, 2014). The idea of a quantum spin liquid first appeared as the resonating valence bond phase (Anderson, 1973). The behaviour of quantum spin liquids includes topologically ordered states (Wen, 1990, 2002), fractionalized quasiparticles with Abelian or non-Abelian statistics (Kitaev, 2006; Stern, 2010), and the complex behaviour of entanglement among parts of the system (Vidal et al., 2003; Li and Haldane, 2008). The references given are either reviews or articles illustrating the concepts mentioned and by no means exhaustive. Quantum spin liquids currently form a very active field of study which is beyond the scope of this thesis.

1.3.2 History of frustrated magnetism

I now shortly mention the history of frustrated systems which allows us to outline several concepts relevant for the study of spin ice. The term frustration was coined by (Toulouse, 1977) in relation to spin glasses. However, geometric frustration was first observed in a non-magnetic system – water ice (Giauque and Ashley, 1933; Giauque and Stout, 1936). Bernal and Fowler (1933) postulated the rules of bonding in water ice. Their x-ray scattering studies were able to observe only

the positions of oxygens which form a regular lattice. There are two equivalent positions for a H^+ proton on an O–O bond giving covalent and hydrogen bonds. Pauling (1935) used these *ice rules* to compute the *residual entropy* of water ice, i.e. the entropy $k_B \ln \Omega$ corresponding to the number of microstates Ω accessible to the low energy hydrogen configurations. His prediction falls very close to the measured value. Nagle (1966) later gave a series expansion that furter improves the match with experiment. Water ice and spin ice have a very close connection, illustrated by figure 1.5.
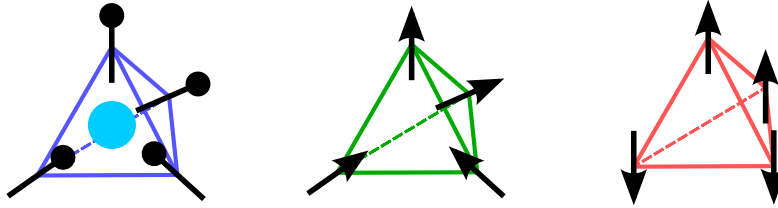
Figure 1.5: **Water ice, spin ice, and pyrochlore antiferromagnet** can be mapped onto each other. On this tetrahedron, hydrogens close to the central oxygen map onto the "in" spins in spin ice and the "up" spins in the pyrochlore antiferromagnet (and vice versa). The oxygens in water ice Ih form a hexagonal lattice (with bonding angles very close to the tetrahedral angle), while the centres of tetrahedra in the pyrochlore lattice form a diamond lattice. The graph of the lattice is identical.

First proposals for frustrated systems were put forward less than ten years after the exact solution of the Ising model on a square lattice. Onsager's solution drove a wave of interest in critical phenomena (Cardy, 1996; Chaikin and Lubensky, 2000) and solvable lattice systems (Baxter, 2008). Wannier (1950) and Houtappel (1950) argued independently concerning the absence of ordering in a triangular lattice antiferromagnet. Wannier gave an estimate of the residual entropy. Anderson (1956) studied the Ising antiferromagnet on the pyrochlore lattice and its degeneracy in the context of spinels and the Verwey transition in magnetite (Verwey and Haayman, 1941). Anderson pointed out that his model can be mapped on water ice as shown in figure 1.5. On its own, Anderson's model is very artificial because selecting an easy axis for the Ising spins is not compatible with the cubic symmetry of the pyrochlore lattice. Villain (1979) studied the symmetry allowed Heisenberg antiferromagnet on the pyrochlore lattice and discussed the absence of order in this system. These arguments were later generalised by Moessner and Chalker (1998).

The first geometrically frustrated antiferromagnet $SrCr_8Ga_4O_{19}$ (magnetoplumbite, SCGO) was discovered by Obradors et al. (1988). SCGO has a three lattice kagome–triangular–kagome sandwich struc-

ture of Cr^{3+} ions with spin 3/2. The structure can be viewed as a slab of a pyrochlore lattice. The exchange interaction between the chromium ions is antiferromagnetic. SCGO was also the first real-world material for which order-by-disorder was proposed to explain scattering signatures (Chalker et al., 1992). Later numerical (Reimers and Berlinsky, 1993) and theoretical (Moessner and Chalker, 1998) work showed that the more probable scenario for SCGO at low temperatures is a crossover to a spin liquid. While historically important, it is difficult to synthetise stoichiometerically clean samples of SCGO (Lacroix et al., 2011, Ch.9.). This disorder results in sites where gallium ions substitute chromium ions and create orphan spins which in turn induce complex spin textures (Sen et al., 2011, 2012). Many vexing features of SCGO already observed in (Broholm et al., 1990; Ramirez et al., 1990) remain unresolved.

A whole range of other frustrated magnets has been discovered in the last twenty five years since SCGO. Many go beyond the basic frustrated spin lattice paradigm and include strong quantum effects, interactions with itinerant electrons, etc. The book (Lacroix et al., 2011) gives an extensive introduction to this field. We will limit ourselves to spin ice and even further only to the "classical" spin ice where the spins are Ising like.

Spin ice was discovered as the first geometrically frustrated ferromagnet (Harris et al., 1997; Bramwell and Harris, 1998). Dysprosium titanate $Dy_2Ti_2O_7$ (DTO) and holmium titanate $Ho_2Ti_2O_7$ (HTO) possess two interpenetrating pyrochlore lattices, one of the magnetic rare-earth ions Dy^{3+} or Ho^{3+} and the other of the non-magnetic Ti^{4+}. The crystal field enviroment causes the lowest energy state of the rare-earth ions to be a large spin doublet with a significant gap to higher states. The easy axis of the Ising-like doublet lies along the line connecting the centres of the pyrochlore lattice tetrahedra (see figure 1.5). Due to the bonding angles, the ferromagnetic interactions are minimized if each tetrahedron has two spins pointing in and two pointing out. There is an exact mapping between the ground states of water ice and spin ice if only the exchange interaction is considered. The ice rules apply to spin ice, leading to an extensive degeneracy of ground states. The residual entropy of spin ice matches Pauling's prediction for water ice very well (Ramirez et al., 1999), although recently signatures of ordering in DTO at very low temperatures have been observed (Pomaranski et al., 2013).

The large dipole moments of the magnetic ions necessitate including dipolar interactions to the spin ice model (Siddharthan et al., 1999; den Hertog and Gingras, 2000). These do not change the nature of the selected ground state because the correlations in the original ferromagnetic Ising model are already dipolar (Youngblood and Axe, 1981; Isakov et al., 2004). This *projective equivalence* guarantees that the degen-

eracy is preserved down to very low temperatures (Isakov et al., 2005) below which the dipolar model orders (Melko et al., 2001). In the next section we discuss how breaking of the ice rules creates the magnetic monopoles.

1.3.3 Fractionalization

The Coulomb gas of magnetic monopoles emerges from spin ice. The elementary degrees of freedom are spins – large rare earth-ion dipoles. The monopoles arise from the dipoles via a processed called the fractionalization. Fractionalization was first observed in polyacetylene (Su et al., 1979) and other conducting polymers (Heeger et al., 1988) where doping allows covalent bonds to break up into mobile defects with the charge of an electron but no spin (see figure 1.6); the magnetic and electric quantum numbers of the electron separate. Defects in polymers with other bond configurations in their ground state can carry fractional charges (Su et al., 1979; Wilczek, 2002). Fractional quasiparticles came into the spotlight with the fractional quantum Hall effect which has led to the occurrence of a plethora of Hall phases with different fractional quasiparticles (Tsui et al., 1982; Laughlin, 1999).

We illustrate the fundamentals of fractionalization in lattice models (see figure 1.6). In all the cases we present, the fractionalization proceeds as follows. First a pair of defects is created locally, e.g. a missing bond in polyacetylene which is a singlet with charge $+2e$ and no spin. Afterwards the defects separate and each carries half the quantum numbers of the original perturbation. This allows for the occurence of novel quasiparticles that carry a charge that is a fraction of the elementary charge.

The degeneracy of the ground state is fundamental for the separation. The space between the separating defects has to be locally in a different ground state again. Otherwise energetic cost of the segment between defects would grow linearly with the defect separation. This would strongly confine the defects. For a one dimensional model, two ground states are sufficient as demonstated by polyacetylene (Su et al., 1979) and the AKLT spin-1 chain (Affleck et al., 1987), which we show in figure 1.6a. For higher dimensions, extensive frustration is required which makes frustrated magnets prime candidates for fractionalized particles.

This does not mean that all the configurations of the defects are equal. Often there is a non-confining entropic force acting to bring the defects together because larger separation of defects constrains the system more. This holds even if the defects form a gas in which it is no longer possible to find their original partner. In the dimer models
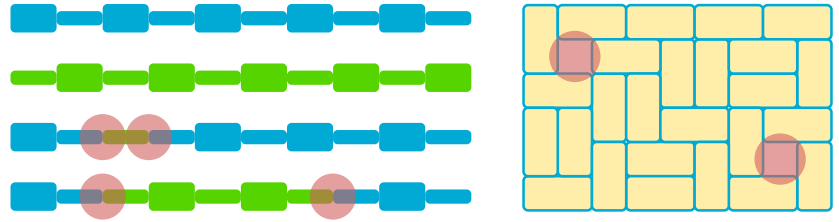
(a) Fractionalization in chains and dimer systems.
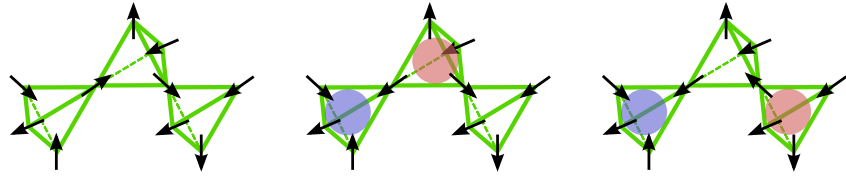
(b) Fractionalization in spin ice.

Figure 1.6: **Fractionalization.** Effective degrees of freedom can be parts of the fundamental constituents. **a)** Left panel shows a one dimensional example which can be seen as polyacetylene (Su et al., 1979) or the resonating valence bond solid of the AKLT model (Affleck et al., 1987). In polyacetylene, the thick and thin rectangles represent double and single carbon bonds respectively. In the AKLT model, the thick rectangles represent a single spin $S = 1$ which can be seen as composed of two $S = 1/2$ spins each of which forms a singlet (thin rectangle) with the neighbouring site. Both systems have two ground states (green and blue). A defect can be added to the system, for example by doping the polyacetylene (green rectangle in the third row). Due to the equivalence of the ground states the defect can fractionalize and propagate (lowest row). Each of the domain walls between the two ground states carries only half the charge of the original defect pair which can be verified by counting the bonds. In higher dimensions, fractionalization can be demonstrated using dimer models. The right panel shows a dimer covering with a removed dimer that has fractionalized into two defects half the size of the original dimer. Note that in one dimension a line of inverted bonds can be identified but there is no unique way in higher dimensions how to assign a string of dimers connecting the two defects. **b)** In spin ice, the ice manifold plays the same role as the dimer covering in the upper panel by providing sufficient number of configurations for the monopoles to propagate through. There are two types of monopoles in spin ice because the degree of freedom being fractionalized is a dipole instead of a dimer. Also note that the manifold of dimers and of ice states is not the same; for the dimer-monomer problem on the diamond lattice see (Pollmann et al., 2006).

and in spin ice this entropic force has a Coulomb form which does not confine the defects (Fisher and Stephenson, 1963; Nagle, 1979; Henley, 2010).

Dimer models demonstrate the mechanism with which dipoles in spin ice fractionalize into monopoles (compare figure 1.6a and 1.6b). The missing dimer corresponds to the spin that violates the ice rules in two neighbouring tetrahedra whereas the monomers correspond to a spin violating the ice rule in a single tetrahedron. The crucial difference is that the dipole splits into two monopoles of unlike charge while a dimer splits into two identical monomers.

In the dipolar model of spin ice, the low energy state manifold conforms to the ice rules as well. In this case the spins interact with dipolar interactions. To obtain the dipolar spin interaction in the monopole picture, the fractionalized charges need interact with a magnetic Coulomb interaction (Castelnovo et al., 2008). This is in full analogy to the entropic force caused by the local interactions. As this force is deconfining, the monopoles form a magnetic Coulomb gas. We give a thorough derivation of this emergent magnetostatics in the chapter about spin ice.

1.4 Outline of the thesis

The remainder of this thesis is structured into four parts as follows. The second chapter introduces necessary concepts of electrolyte theory. The third describes the second Wien effect and presents its first numerical simulation and what one can learn from it. The fourth chapter describes spin ice, its equilibrium properties and characterizes the magnetolyte. In the final fifth chapter, we show the existence of the Wien effect in spin ice and propose several experimental protocols for its detection.

2

Concepts of Electrolyte Theory

The study of electrolytes and Coulomb gases has produced an immense amount of insights over the last century. Covering all the developments would require a monograph far beyond the scope of a thesis. We refer to (McQuarrie, 2000; Levin, 2002; Wright, 2007) for a basic introduction to electrolyte theory, (Moore, 1999) for physical chemistry, and (Levin and Fisher, 1996; Falkenhagen, 1971; Hansen and McDonald, 2006) for more involved discussions. We focus on parts of electrolyte theory relevant to the weak electrolyte limit which is relevant to spin ice physics and which exhibits the second Wien effect. This chapter serves as a staging area for our work on these topics and it aims to establish a common language for readers from different communities.

The fundamental property of Coulomb gases is electrostatic screening. This guarantees the very existence of a thermodynamic limit (Lebowitz and Lieb, 1969). Without screening, the internal energy would diverge. In addition to this long-wavelength singularity, a short-wavelength divergence is caused by an infinitely close approach of charges (Onsager, 1939). This is avoided with presence of a cut-off, e. g. the finite extent of the charged particles. For a review of screening theorems and convergence conditions for Coulomb gases see (Brydges and Martin, 1999).

The character of an electrolyte depends on the properties of the constituent ions and the solvent. In general, ions can have very complex properties – size, shape, density, charge magnitude and distribution. However, in many instances an ion is well described by its diameter a and its charge which is an integer multiple of the elementary charge $Q_e = 3e$. Complimentary to this, the solvent comprises molecules which often have non-trivial charge distributions and orientational dynamics, yet it can often be treated as a continuum with permittivity ϵ. This is conventionally expressed relative to the permittivity of vacuum ϵ_0 (also electric constant). The factor is the relative permittivity $\epsilon_r = \epsilon/\epsilon_0$ also called the dielectric constant (especially in older literature using cgs units). Hydrodynamic properties of the solvent are described by its dynamic viscosity and density. A small ionic diameter results in a very low value of the Reynolds number such that any hydrodynamic effects are well described by an incompressible laminar flow (Onsager, 1926).

To capture the general properties of Coulomb gases, the restricted primitive model (RPM) is introduced. The first use of this name that we find is by Stillinger Jr and Lovett (1968). The primitive model consists of spheres with hard core and Coulombic interactions. The restriction is that the charges of opposite sign have the same absolute value of charge $|Q_e|$ and the same diameter a. For an introduction to this model, see for example the book of Hansen and McDonald (2006). As we will deal with transport properties, we add the condition that the charge mobilities $\varkappa$ are also identical. We further neglect any hydrodynamic effects, for example electrophoresis.

In this work, we focus on the RPM in the grand canonical ensemble and its lattice version which are easily simulated. We formulate the electrolyte theory in terms of variables most suitable for describing a lattice gas. This leads only to minor modifications compared to continuous theories. In the lattice case, we assume that the lattice spacing plays the role of the ion diameter. We denote both by a because they have a common interpretation as the distance of closest approach. An additional factor of the volume per lattice site $\tilde{V}$ often appears in the lattice counterpart of a continuum theory because we tend to work with number densities $n_x = \tilde{V} \rho_x$ where ρ_x is the corresponding volumic density. One of our aims is to describe the Coulomb gas in spin ice. Due to the symmetry between the emergent magnetic monopoles of opposite charge, spin ice is one of the best physical realizations of the restricted primitive model.

In the following, we first discuss the parametrization of electrolytes and Coulomb gases in general. A brief review of equilibrium properties follows with derivations of basic theories for screening (Debye–Hückel) and pairing (Bjerrum). We use the activity coefficient γ to characterize corrections captured by these theories. As we work in a grand canonical ensemble, the activity coefficient γ can be interpreted as a logarithmic measure of the difference between the bare chemical potential ν_0 in the absence of interactions and the actual chemical potential $\nu = \nu_0 - k_B T \ln \gamma$. We then show how equilibrium correlations modify charge mobility in the linear response limit. In the final section we describe simulation methods for Coulomb gases.

2.1 Parametrization of Coulomb gases

Before we embark on deriving electrolyte theory we would like to characterize Coulomb gases using two approaches: reduced variables and length scales. We will also give conversions between the two parametrizations. We tend to use the reduced variables to classify materials according to parameters of the Coulomb gas that models them. The

characteristic lengths are useful for describing processes in a Coulomb gas and comparing their relative strength.

In the canonical ensemble, the independent thermodynamic variables are temperature and number densities of constituent ions (T, n_x)[1]. In the grand canonical ensemble we use temperature and respective chemical potentials (T, ν_x). We define the inverse temperature in the usual form $\beta = 1/(k_\mathrm{B} T)$. The electroneutrality condition has either the form $\sum_\mathrm{x} Q_\mathrm{x} n_\mathrm{x} = 0$ or $\sum_\mathrm{x} Q_\mathrm{x} \nu_\mathrm{x} = 0$. As we limit ourselves to the restricted primitive model of a $1:1$ symmetric electrolyte, we have $n_- = n_+ = n/2$ and $Q_+ = -Q_- = e$.

2.1.1 Reduced variables

The behaviour of the RPM electrolyte in equilibrium is fully characterised by the magnitude of the Coulomb interaction at contact $U_\mathrm{C}(a) = Q_\mathrm{e}^2/4\pi\epsilon a$, the chemical potential ν, and the temperature T. As the absolute energy scale does not play a role in the results, we introduce the reduced chemical potential $\nu^* = \nu/U_\mathrm{C}(a)$ and temperature $T^* = k_\mathrm{B} T/U_\mathrm{C} a$ as free dimensionless grand canonical variables. We also introduce the reduced bare chemical potential $\nu_0^* = \nu_0/U_\mathrm{C}(a)$ and discuss its importance for simulations. A similar set of reduced variables can be introduced for the canonical ensemble as well (Friedman and Larsen, 1979; Weingärtner, 2001; Hansen and McDonald, 2006). The reduced density is then compared to a characteristic volume and is similar to the number density n. Systems can be classified into corresponding states according to their reduced variables.

2.1.1.1 Chemical potential

Chemical potential is a quantity both invaluable and often misinterpreted (see Job and Herrmann (2006); Kaplan (2006) for a thorough discussion). Because of this we find that it requires a brief digression. We give the main result beforehand and then discuss the definitions in detail. Each ion in the Coulomb gas has a chemical potential given by the derivative of the free energy $\nu_\pm = (\partial \mathscr{A}/\partial N_\pm)_{T,V,N_\mp}$ which can be estimated from theory. In simulations, it is however more practical to work in a modified ensemble, where we fix a bare chemical potential ν_0 which is equal to the chemical potential in the limit of infinite dilution $\nu_0 = \lim_{n\to 0} \nu_\pm$ (in an electroneutral 1:1 electrolyte both charges have the same chemical potential). The bare chemical potential can be also seen as the chemical potential of a non-interacting gas under the same conditions as the Coulomb gas that we study. The excess chemical potential $\Delta\nu$ can be expressed in terms of the activity coefficient γ

---

1 The number densities are the same as amount fractions used in chemistry.

as $\Delta \nu = \nu - \nu_0 = -k_B T \ln \gamma$. We now continue with a detailed discussion of the chemical potentials ν and ν_0.

In deriving the grand canonical ensemble, the system is considered to be in contact with a particle reservoir at chemical potential ν (Huang, 1987). The total number of particles in the system and the reservoir is conserved. In physics, this is extended to include the possibility of creating elementary particles and quasiparticles from vacuum while another quantity such as the total charge is held constant. In the canonical ensemble, the chemical potential is defined as $\nu = (\partial \mathscr{A} / \partial N)_{T,V}$. For the same thermodynamical relation to hold in the grandcanonical ensemble, it is necessary to fix the chemical potential at ν and allow the particle number N to fluctuate. The results in the thermodynamic limit are independent of the ensemble.

However, it is often easier to find the energy cost ν_0 of a bare particle or quasiparticle rather than the chemical potential ν which requires knowledge about the interactions in the system. Such knowledge is rarely exact in electrolytes and it is often limited to mean-field like theories. It is also conceptually simpler to implement a Monte Carlo simulation where ν_0 is held fixed, because fixing ν would require a more involved approach similar to simulating the (N, p, T) ensemble (Frenkel and Smit, 2001). Fixing ν_0 means that we no longer work in the conventional grand canonical ensemble, but in an ensemble that might be called the "activity ensemble" in reference to activity $\mathfrak{a} = \exp(\beta \nu_0)$ defined below. We will use the word grand canonical for both ensembles to emphasize that the particle number fluctuates, while specifying which chemical potential is held fixed. The grand canonical ensemble where ν is held fixed minimizes the Landau grand potential $\zeta = u - n \nu$ while the activity grand canonical ensemble minimizes a modified Landau potential $\zeta_0 = u - n \nu_0$. Spin ice is a good example where the chemical potential of a bare magnetic monopole is well defined and fixed by the exchange interaction and the dipolar magnetic interaction of spins (Castelnovo et al., 2008; Jaubert and Holdsworth, 2009); ζ_0 is therefore a suitable thermodynamic potential for spin ice.

If the particles are created by a chemical reaction, the chemical potential for adding a particle is the difference $\nu = \nu_A - \nu_B$ between the species A that is being created (in our case ions) and the species B that serves as its source (undissociated molecules). The bare chemical potential ν_0 is the value that the chemical potential would have if both species were ideal gases, and as such it is related to effective variables that are defined in chemistry in relation to the ideal gas law, notable examples of whose are activity (effective concentration) and fugacity (effective pressure) (Moore, 1999).

In chemistry, the activity $\mathfrak{a}$ is introduced as an effective number density in order to use the ideal gas law for non-ideal gases (with substitution $n \rightarrow \mathfrak{a}$). For example, if we used the ideal gas law in a non-ideal gas to calculate the number density from the pressure we would obtain the activity instead. The activity would be lower than the true number density ($\mathfrak{a} < n$) in the case of attractive interactions which reduce the pressure and higher ($\mathfrak{a} > n$) for repulsive interactions. In the same context, we defined the bare chemical potential ν_0 above. Therefore the activity need fulfil the ideal gas relation $\mathfrak{a} = \exp(\beta \nu_0)$.

In the electrolyte theory presented in this chapter, we obtain an average contribution to the free energy per particle from which we then calculate the chemical potential in the canonical ensemble. This mean-field like approximation yields an identical energy for each particle. Therefore, we can compute the number density in the single-particle approximation as $n = \exp(\beta \nu)$.

The shift in the chemical potential between a Coulomb gas and the corresponding ideal gas is $\Delta\nu = \nu - \nu_0 = -k_B T \ln\gamma$ where we introduce the activity coefficient as $\gamma = \mathfrak{a}/n$ (note that $\nu \leq 0$ and for attractive interactions $\Delta\nu \geq 0$). The activity coefficient γ serves as a renormalization parameter which describes the effect of all interactions in a single number. As such it depends not only on the thermodynamic variables (T, ν) or (T, n) but also on the strength of interactions between the particles themselves and between the particles and their environment.

Because the activity coefficient depends on other species present, only the mean activity coefficient of the whole system is measurable experimentally. In the case of the 1:1 electrolyte the mean activity coefficient is defined as $\gamma = \sqrt{\gamma_+ \gamma_-}$ where γ_+ and γ_- are the activity coefficients of the positive and negative ions, respectively. For a symmetric electrolyte, this distinction is only formal because $\gamma_+ = \gamma_-$.

A related well-known method is the Widom insertion method which samples $\Delta\nu$ of inserting a particle in various places in the system while never executing the insertion and holding the particle number constant; ν_0 can then be interpreted as controlling the frequency of the proposed insertion (Widom, 1963; Svensson and Woodward, 1988; Frenkel and Smit, 2001).

Our simulations model a Coulomb gas with onsite exclusion, i. e. at most one particle can occupy a lattice site. We adopt a hybrid approach for describing its density. We include the excluded volume condition neither in the chemical potential nor in the activity coefficient because it is easily treated in full analytically. For the restricted primitive model on a lattice, we obtain the total charge density as

$$n = n_+ + n_- = \frac{2\exp(\beta \nu)}{1 + 2\exp(\beta \nu)} = \frac{2\exp(\beta \nu_0)/\gamma}{1 + 2\exp(\beta \nu_0)/\gamma}. \tag{2.1}$$

We express the total density in terms of ν_0 because the bare cost of a charge is a parameter that we can control in our simulations with greater ease than the chemical potential ν which includes the effects of inter-particle interactions. The activity coefficient γ is then obtained from the electrolyte theory and the resulting density is compared with our simulation results.

The reduced chemical potentials are defined as $\nu^* = \nu/U_C(a)$ and $\nu_0^* = \nu_0/U_C(a)$. Having completed the digression into the chemical potential, we continue by defining the remaining reduced variable.

2.1.1.2 Electric field

The final reduced variable we use is the reduced field E^*. If an external field is applied, it can be characterised by the potential energy gain over the ion size $U_E = Q_e \mathbf{E} \cdot \mathbf{a}$, leading to a definition of the dimensionless field as $E^* = U_E/U_C$. This definition needs to be complemented with the angle between the field and the direction along which the charge moves. In this thesis, we will encounter only the situation of charges hopping on the diamond lattice with the external field applied in the [001] direction. The energy is than identical for all possible movement directions $U_E = Q_e E a/\sqrt{3}$.

2.1.2 Length scales

It is instructive to derive a set of lengths corresponding to various features of the electrolyte. These can be subsequently made dimensionless using the ion diameter a. The motivation for the definitions will be made clear by the theories presented later.

The Bjerrum length $\ell_T = Q_e^2/8\pi\epsilon k_B T$ expresses the relative strength of the Coulomb potential compared to the kinetic energy $k_B T$. The Bjerrum length is closely related to the reduced temperature $T^* = a/(2\ell_T) = 1/(\beta U_C(a))$.

The Debye length $\ell_D = \sqrt{(\epsilon k_B T \tilde{V})/(Q_e^2 n)} = \sqrt{\tilde{V}/(8\pi\ell_T n)}$ gives the extent of the ionic atmosphere and of the correlations in a Coulomb gas. For the diamond lattice we have $\tilde{V} = 8a^3/(3\sqrt{3})$ and the Debye length is the following function of the reduced temperature and number density $\ell_D/a = \sqrt{2T^*/(3\sqrt{3}\pi n)}$. Its expression in terms of the reduced chemical potential is not as simple and is a result of an iterative procedure. This is due to the fact that the Debye length influences the equilibrium density in the grand canonical ensemble and the density in turn defines the Debye length. Occassionaly it is useful to make comparison with the mean charge separation given by $\ell_n = (\tilde{V}n)^{-1/3}$ which scales with the cubic root of density compared to the square root for the Debye length.

The field length $\ell_E = k_B T/Q_e E$ is the distance over which a charge has to be transported by a field to obtain a potential energy comparable with the thermal energy $k_B T$. Effects of the external field E on the distribution of ions become visible at lengths larger than ℓ_E. From the definition of the reduced temperature and field we can deduce immediately that $\ell_E/a = T^*/(\sqrt{3}E^*)$.

The length scales simplify the expressions encountered in electrolyte theories. Their ratios allow the identification of the expected behaviour of the Coulomb gas. The effects whose strength is expressed a function of such a ratio include: ℓ_T/ℓ_D for the strength of screening, ℓ_D/ℓ_E for its decay with field (the first Wien effect), ℓ_T/a for pairing, ℓ_T/ℓ_E for field enhanced dissociation of pairs (the second Wien effect). We continue by describing theories for the thermodynamics of electrolytes.

2.2 Debye–Hückel theory

The Debye−Hückel (DH) theory is the basic theory of correlations in charged systems. Its main result is that every charge is surrounded by a screening cloud that is oppositely charged. The spherical symmetry of the cloud guarantees that all multipoles decay exponentially at long distances[2]. The screening renders the problem of thermodynamics of Coulomb gases treatable by the same methods as short-range interacting fluids. The attractive interaction between the ion and its ionic atmosphere reduces the internal energy of the system.

The Debye−Hückel theory is not a mean field theory in the strictest sense because the charge is not influenced by a mean field generated by itself (Levin, 2002). The feedback is instead between the oppositely charged species of ions and the result is an expression for their average mutual potential and correlations. We present the derivation of Debye−Hückel theory for the case of the restricted primitive model ($Q_+ = -Q_- = e$). This does not lead to any loss of generality since the screening cloud has an equal but opposite charge to the central ion even in the case of asymmetric electrolytes. Moreover we will show that the theory conforms to the electrostatic superposition principle.

---

2 It is interesting to note that screening correlations in a quantum Coulomb gas do not decay exponentially but rather as a power law (Maggs and Ashcroft, 1987; Alastuey and Martin, 1989).

2.2.1 Poisson–Boltzmann equation

The main task of the theory is to find the average electrostatic potential $\Psi(\mathbf{r})$ due to the central ion and its screening cloud. The potential is obtained from the distribution of the ions using the Poisson equation

$$\frac{\rho_{Q_e}(\mathbf{r})}{\epsilon} = -\Delta\Psi(\mathbf{r}) \tag{2.2}$$

with $\rho_{Q_e}(\mathbf{r}) = e(\rho_+(\mathbf{r}) - \rho_-(\mathbf{r}))$ being the volumic charge density at $\mathbf{r}$ which is the position relative to the central ion. We consider the central ion to be a sphere. We will thus further use the spherical coordinates and the only non-trivial dependence will be on the radial variable r.

The charge distribution $\rho_{Q_e}(r)$ is itself dependent on the potential $\Psi(r)$. On average, it follows the Boltzmann distribution

$$\rho_q(r) = e\left(\rho_+^{(0)}e^{-\beta e\Psi(r)} + \rho_-^{(0)}e^{+\beta e\Psi(r)}\right), \tag{2.3}$$

where we use the superscript (0) to denote the average density. The combined Poisson–Botzmann equation is then

$$\Delta\Psi(r) = -\frac{e}{\epsilon}\left(\rho_+^{(0)}e^{-\beta e\Psi(r)} - \rho_-^{(0)}e^{+\beta e\Psi(r)}\right), \tag{2.4}$$

which expanded to the linear term is

$$\Delta\Psi(r) = -\frac{e}{\epsilon}\left(\rho_+^{(0)}(1 - \beta e\Psi(r)) - \rho_-^{(0)}(1 + \beta e\Psi(r))\right). \tag{2.5}$$

We use the electroneutrality $\rho_+^{(0)} = \rho_-^{(0)}$ and substitute the total average density $\rho^{(0)} = \rho_+^{(0)} + \rho_-^{(0)}$

$$\Delta\Psi(r) - \frac{\beta e^2 \rho^{(0)}}{\epsilon}\Psi(\mathbf{r}) = 0. \tag{2.6}$$

Note that the superposition principle is recovered by the linearisation. This equation is called the linearized Poisson–Botzmann equation and it is a Helmholtz-type equation.

Solving the linearised equation and assuming the decay of the potential to zero at infinity gives a screened Coulomb potential of a selected central ion and its atmosphere at distance r from the ion

$$\Psi(r) = -\frac{\mathscr{C}}{r}\exp\left(-\frac{r}{\ell_D}\right). \tag{2.7}$$

Another solution is $\propto \exp\left(+\frac{r}{\ell_D}\right)$ which diverges at infinity and is thus unphysical. The screening length is the Debye length expressed as

$$\ell_D = \sqrt{\frac{k_B T \epsilon}{e^2 \rho^{(0)}}} \equiv \sqrt{\frac{k_B T \epsilon}{e^2 2\mathscr{I}}}, \tag{2.8}$$

where

$$\mathscr{I} = \frac{1}{2} \sum_{i \in \text{ion types}} \mathfrak{z}_i^2 \rho_i^{(0)} \tag{2.9}$$

is called the ionic strength of the electrolyte and it is quadratic in the charge number (valence) $\mathfrak{z}_i$ of the constituent ions. If the charge of the ion increases, the charge of the screening atmosphere has to increase by the same amount yielding an quadratic increase in the interaction. One can also define the numeric ionic strength $\mathscr{I}_n = \mathscr{I}\tilde{V}$ which will be useful in describing double charged defects in spin ice.

The constant $\mathscr{C}$ in the potential can be fixed by assuming that there is a certain minimal distance a below which the ionic atmosphere does not form. In the simplest case, this distance can be identified with the effective ion diameter a. Inside a sphere of this radius there is only the central charge. The potential at the surface is a constant which we express as a sum of the point charge Coulomb potential and an offset

$$\Psi(a) = \frac{e}{4\pi\epsilon}\frac{1}{a} + \mathscr{B}. \tag{2.10}$$

This holds for any spherically symmetric internal distribution of charge. The Gauss theorem gives the electric field on the surface due to the charge within which is up to a sign equal to the derivative of the potential

$$\frac{\mathrm{d}\Psi}{\mathrm{d}r}(a) = -\frac{e}{4\pi\epsilon}\frac{1}{a^2}. \tag{2.11}$$

The two conditions necessary for determining the constants $\mathscr{C}$ in equation 2.7 and $\mathscr{B}$ in equation 2.10 are the continuity of the potential and its derivative. The solution is

$$\mathscr{B} = -\frac{e}{4\pi\epsilon}\frac{1}{\ell_\mathrm{D} + a}$$
$$\mathscr{C} = \frac{e}{4\pi\epsilon}\frac{\exp(a/\ell_\mathrm{D})}{1 + a/\ell_\mathrm{D}} \tag{2.12}$$

and the Debye–Hückel potential reads

$$\Psi(r \geq a) = \frac{e}{4\pi\epsilon}\frac{\exp(a/\ell_\mathrm{D})}{1 + a/\ell_\mathrm{D}}\frac{\exp(-r/\ell_\mathrm{D})}{r}. \tag{2.13}$$

The potential for $r < a$ does not have a clear physical meaning and is irrelevant for our considerations.

We considered the electrostatic potential around a positive central charge. This choice is made only out of convenience. We express the related potential energy $U_\mathrm{DH}(r) = -e\Psi(r)$ which is independent of the charge of the central ion

$$U_\mathrm{DH}(r \geq a) = -k_\mathrm{B}T\frac{2\ell_T}{r}\frac{\exp(-(r-a)/\ell_\mathrm{D})}{1 + a/\ell_\mathrm{D}}. \tag{2.14}$$
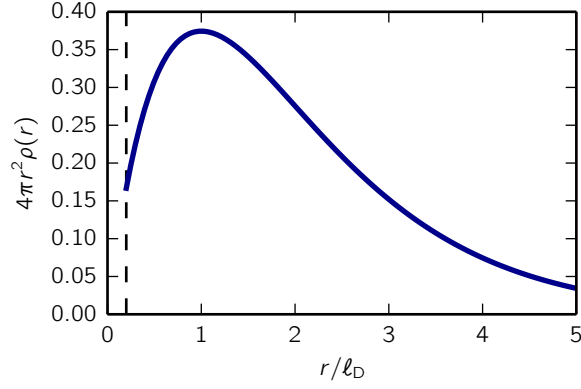
Figure 2.1: **Radial distribution of the ionic atmosphere.** The excess charge density in an infinitesimal spherical shell at distance r from the central ion. The complementary interpretation is the probability of finding a screening ion at distance r. The function has a maximum at ℓ_D. The example is given for $a/\ell_\mathrm{D} = 0.2$ (the dashed line signifies the ion diameter a).

Within the same level of approximation the excess charge in the ionic atmosphere has the following distribution of charge

$$\rho_-(r) - \rho_-^{(0)} = \rho_-^{(0)} \big(\exp\big(-\beta U_\mathrm{DH}(r) \big) - 1 \big)$$
$$\simeq -\rho_-^{(0)} \beta U_\mathrm{DH}(r) = \rho_-^{(0)} \frac{2\ell_T}{r} \frac{\exp(-(r-a)/\ell_\mathrm{D})}{1 + a/\ell_\mathrm{D}} . \qquad (2.15)$$

We show the Debye–Hückel correlations in spin ice in figure 4.11. The total excess charge in the ionic atmosphere is equal to the central charge with opposite sign

$$\int_a^\infty 4\pi r^2 \mathrm{d}r\, \rho_-^{(0)} \frac{2\ell_T}{r} \frac{\exp(-(r-a)/\ell_\mathrm{D})}{1 + a/\ell_\mathrm{D}} = \rho_-^{(0)} = -\rho_+^{(0)}, \qquad (2.16)$$

where the integrand gives the probability of finding an ion at the distance r from the central ion (see figure 2.1). This is an important self-consistency condition which is only obtained due to the appropriate linearization of the Poisson–Boltzmann equation. The full Poisson–Boltzmann equation can still be useful if this symmetry is not central to the problem at hand, e. g. the distribution of ions around a large protein can be important while distribution of proteins around a small ion is less interesting. We are however interested in thermodynamic properties of symmetric electrolytes and therefore we will only consider the results of the linearized Poisson–Boltzmann equation.

2.2.2 Thermodynamic implications

We will now use the Debye potential to derive the free energy due to the electrostatic screening and show how it reduces the cost of adding charges into the Coulomb gas (increases their chemical potential).

2.2.2.1 Free energy due to the ionic atmosphere

The contribution to the free energy due to the electrostatic correlations can be obtained by a charging process. This is a thought experiment where the quantization of charge is lifted and the charge of all ions simultaneously (Debye and Hückel, 1923a) or of the central ion exlusively (Güntelberg, 1926) is increased from zero to the desired value. The two charging procedures are only consistent for solutions of the linearized Poisson−Boltzmann equation. The non-linear equation results in different free energies for the two charging processes. The free energy difference is obtained as the electrostatic work needed to charge a sphere. We express its volumic density as

$$\frac{\Delta \mathscr{A}_{\mathrm{DH}}}{V} = -\frac{k_{\mathrm{B}} T}{4\pi a^3} \left[\frac{1}{2} \left(\frac{a}{\ell_{\mathrm{D}}} \right)^2 - \frac{a}{\ell_{\mathrm{D}}} + \ln\left(1 + \frac{a}{\ell_{\mathrm{D}}} \right) \right]. \tag{2.17}$$

The value per lattice site is obtained by multiplying the previous expression with the volume per site $\tilde{V}$.

2.2.2.2 Activity coefficient

The shift $\Delta \nu_{\mathrm{DH}}$ of the chemical potential due to Debye screening is given as the derivative of the free energy difference with respect to the density (we choose the positive charge density without any loss of generality)

$$\Delta \nu_{\mathrm{DH}} = \left[\frac{\partial \Delta(\mathscr{A}_{\mathrm{DH}}/V)}{\partial \rho_+} \right]_{T,V}. \tag{2.18}$$

A brief calculation yields

$$\Delta \nu_{\mathrm{DH}} = k_{\mathrm{B}} T \frac{\ell_T}{\ell_{\mathrm{D}} + a}. \tag{2.19}$$

Thus the cost of adding a new charge into the system is reduced by the correlations. Recalling the relation $\Delta \nu = -k_{\mathrm{B}} T \ln \gamma$ we obtain the Debye−Hückel activity coefficient

$$\gamma_{\mathrm{DH}} = \exp\left(-\frac{\ell_T}{\ell_{\mathrm{D}} + a} \right). \tag{2.20}$$

Note also that the difference of the screened potential of an ion and its atmosphere and the unscreened Coulomb potential of an isolated ion at the surface of the ion is

$$U_{\mathrm{DH}}(a) - U_{\mathrm{C}}(a) = -2k_{\mathrm{B}}T\frac{\ell_T}{\ell_{\mathrm{D}} + a} = -2\Delta\nu_{\mathrm{DH}}. \tag{2.21}$$

Since the atmosphere is restricted to the exterior of the ion this shift has the same value in the interior as well. Thus the shift in chemical potential can be directly interpreted as being due to the shift of the electrostatic potential. The factor of two comes from the fact that the previous expression counts as a contribution to the chemical potential of both the positive and negative charges.

For low densities $a \ll \ell_{\mathrm{D}}$ and we obtain the Debye–Hückel limiting law

$$-\ln\gamma_{\mathrm{DH}} = \frac{\ell_T}{\ell_{\mathrm{D}}} \propto \rho^{1/2}T^{-3/2}\epsilon^{-3/2}. \tag{2.22}$$

Further corrections are proportional to higher powers of density. The Debye–Hückel theory is a low density, high temperature, and weak coupling expansion.

2.2.2.3 Grand canonical ensemble

The activity coefficient depends on the charge density through the Debye length ℓ_{D}. The charge density in the grand canonical ensemble is in turn influenced by the activity coefficient. If we consider the grand canonical restricted primitive model on a lattice with fixed $\nu_0 = \nu_+ = \nu_-$ we have

$$n = \frac{2\exp(-\beta\nu)}{1 + 2\exp(-\beta\nu)} \tag{2.23}$$

$$\nu = \nu_0 + k_{\mathrm{B}}T\frac{\ell_T}{\ell_{\mathrm{D}} + a}, \tag{2.24}$$

where we combined equations 2.1 and 2.19. This set of equations can be solved iteratively and converges within several iterations. The ion diameter a has a stabilizing role in this process as it gives an upper limit on the chemical potential difference. If the density becomes too large and ℓ_{D} approaches zero, the maximum possible correction is $\beta\Delta\nu = \ell_T/(\ell_{\mathrm{D}} + a) \simeq \ell_T/a$. Nevertheless one has to keep in mind that this approach is based on a low density or high temperature expansion. At fixed ν_0 these two quantities are coupled and the theory is valid at both the lowest and highest temperatures. The width of the window of validity decreases with growing bare chemical potential ν_0.

Debye–Hückel theory on a lattice retains its continuous form if $\ell_{\mathrm{D}} \gg a$. In this work we only require the charges to occupy lattice sites

and allow the fields to be continuous around these sites. However, different models have been put forward in theory (Kobelev et al., 2002) and in simulations (Maggs and Rossetto, 2002) where the fields are themselves restricted to the lattice bonds. In such a case the Laplacian in the Poisson–Boltzmann equation is replaced by a lattice Laplacian and the Debye–Hückel correlations are expressed in terms of lattice Green functions.
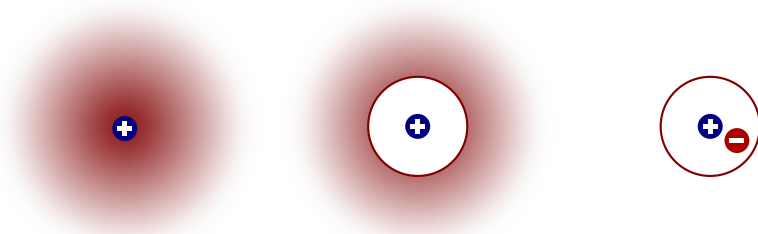
Figure 2.2: **Comparison of Debye–Hückel and Bjerrum theories.** The Debye–Hückel theory (left) treats the average distribution of the ionic atmosphere. The Bjerrum theory divides the charges into free (middle) and bound (right). The red circle denotes the Bjerrum length ℓ_T. The free charges are described in the Debye–Hückel fashion. The bound pairs are considered as non-interacting species. The discontinuity between the two species is non-physical but the Bjerrum theory proves to be a good approximation for weak electrolytes and it can be shown to match cluster expansions for the activity coefficient up to the linear order in density.

2.3 Bjerrum theory of pairing

As ℓ_T/ℓ_D grows, terms beyond Debye–Hückel theory become important. The linearization of the Boltzmann factor leads to largest errors when $-\beta U(r) \gg 1$ which happens for the Coulomb potential if oppositely charged ions approach each other closely. The Boltzmann distribution will thus give a larger population at short distances than the linearized theory predicts. Guggenheim (1959) solved the nonlinear Poisson–Boltzman equation numerically and confirmed that the largest deviations from Debye–Hückel prediction for the charge distribution occur at shortest separations. This further hints at the role of pairing despite the inconsistencies of the full Poisson–Boltzmann equations discussed above.

Bjerrum (1926) interpreted this increase as a formation of Coulombically bound pairs. Bjerrum's theory considers the bound pairs to be a separate neutral chemical species which is in equilibrium with

the remaining charges which are labelled free charges. A charge pair is considered bound if it is separated by less than the Bjerrum length ℓ_T, i. e. if it has a kinetic energy of less than a half of its Coulombic potential energy ($U_C(\ell_T) = -2k_B T$). The association constant K_A controls the equilibrium between bound and free charges

$$K_A \gamma^2 n_+ n_- = K_A \left(\frac{\gamma n_f}{2} \right)^2 = \frac{n_b}{2} = n_p, \tag{2.25}$$

where n_f, n_b, and n_p are the densities of the free charges, bound charges, and the bound pairs respectively. We denote the densities of positively and negatively charged free ions n_+ and n_- in this section ($n_f = n_+ + n_-$). The free charges are considered non-ideal with the activity coefficient given by $\ln \gamma = -\ell_T/(\ell_T + \ell_D/\sqrt{\alpha})$ which is of the Debye–Hückel form with the distance of the closest approach of the free ions being the Bjerrum length ($a \to \ell_T$). Another modification is that only the free charges contribute to the Debye length as expressed by the factor $\sqrt{\alpha}$ where $\alpha = n_f/n$ is the degree of dissociation. The bound pairs are on the other hand treated as ideal particles with activity coefficient $\gamma_p = 1$.
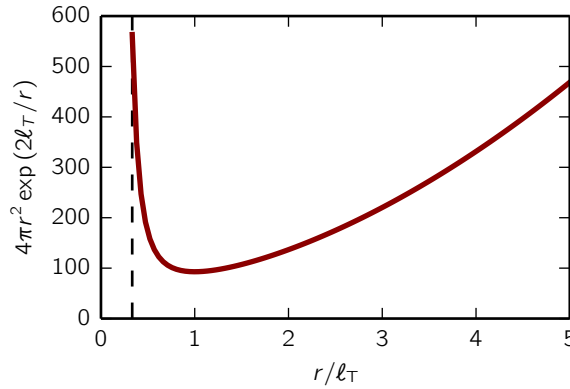
Figure 2.3: **The definition of the Bjerrum length.** The Bjerrum length ℓ_T is the minimum of the probability $4\pi r^2 \exp(2\ell_T/a)$ of finding a charge in vicinity of another that is oppositely charged. The decrease of the function due to the lowered intensity of the Coulombic interaction competes with the increased probability of finding a charge in a spherical shell whose radius grows. This offers the interpretation of ℓ_T as the position of a bottleneck between bound and free charges. The example is given for $a/\ell_T = 1/3$.

The association constant was given by Bjerrum as the total statistical weight of the ion pair configurations

$$K_A = \int_a^{\ell_T} 4\pi r^2 \mathrm{d}r \exp\left(\frac{2\ell_T}{r} \right)/\tilde{V}, \tag{2.26}$$

where we normalized with $\tilde{V}$ to be able to work with number densities. The definition is motivated as follows. The probability of two ions with opposite charge being separated by a vector r is

$$n_{\mathrm{b}}(\mathbf{r}) = n_+ n_- \exp\left(\frac{2\ell_T}{r}\right). \tag{2.27}$$

We are interested in the total density of Bjerrum pairs which we obtain by integrating the previous equation for all $r < \ell_T$. The result has the form of a mass action law with the association constant given by the integral above. This expression neglects further correlations in the system, such as the Debye screening, and it is therefore valid only for $\ell_T < \ell_D$. Furthermore it does not pair the charges uniquely and includes the possibility of another charge being in the vicinity. However we might assume that the identification of the pair is unique if there is on average no more than one charge within the selected distance, i. e. if $\ell_T < \ell_n$. The given inequalities hold in the dilute regime of weak electrolytes which we aim to describe.

The integrand $4\pi r^2 \mathrm{d}r \exp\left(\frac{2\ell_T}{r}\right)$ in 2.26 has a minimum for $r = \ell_T$ (see figure 2.3). This expresses that the probability of two charges having a given separation has its lowest value for the Bjerrum length. The minimum in the charge population can be seen as a phase space bottleneck between two chemical species justifying Bjerrum's choice. If a different length is chosen to separate free and bound charges the association constant and the activity coefficient have to be modified accordingly (see section 2.4.1 for references).

2.3.1 Weak and strong electrolytes

If $\ell_T < a$ the association as defined by Bjerrum does not happen. This is the strong electrolyte regime. All charges can be seen as free and conductivity is mainly influenced by the structure of the ionic atmosphere. The opposite limit of strong binding ($a \ll \ell_T$) is the weak electrolyte regime where the conductivity is dominated by the degree of dissociation of the electrolyte into free charges. If the bound pairs are first created by a chemical process from molecules (double equilibrium), the Coulomb energy difference $U_{\mathrm{C}}(\ell_T) - U_{\mathrm{C}}(a)$ between the molecular state and the free charges can be viewed as a particle gap. The weak and strong electrolyte regimes then roughly correspond to the concepts of a band semiconductor and metal, where the size of the gap determines the conductance. This thesis will mainly deal with weak electrolytes because of their interesting non-equilibrium behaviour.

2.3.2 Bjerrum pairing in the grand canonical ensemble

If the total density of charging is not fixed we have to self-consistently solve a set of equations akin to 2.23 which we again write for the restricted primitive model on a lattice. The total density can be obtained from

$$n = \frac{2 \exp(\beta v_0)/\gamma}{\alpha + 2 \exp(\beta v_0)/\gamma} \tag{2.28}$$

$$\alpha = \frac{2}{1 + \sqrt{1 + 2K_A \gamma^2 n}} \tag{2.29}$$

$$\gamma = \exp\left(-\frac{\ell_T}{\ell_T + \ell_D/\sqrt{\alpha}}\right) \tag{2.30}$$

$$\ell_D = \sqrt{\frac{1}{8\pi\ell_T n}}, \tag{2.31}$$

where we used that $\exp(\beta v) = \exp(\beta v_0)/\gamma$ and the degree of dissociation α is obtained from the mass action law 2.25. In the equation 2.28 we approximated the excluded volume interaction between free and bound charges by inserting the factor α. Without the excluded volume interaction $n = n_f/\alpha = (\exp(\beta v_0)/\gamma)/\alpha$ holds. In this spirit we devide each exponential by α. The resulting role of α in expression 2.28 can be interpreted as a factor renormalising the accessible empty sites for the free charges down from unity due to the bound pairs. Note that this neglects the excluded volume interaction between the bound pairs which is of higher order in density anyway.

The states accessible to bound pairs on a lattice are different from those in a continuum. The value of the association constant is sensitive to this because it has a large contribution from short distances (see figure 2.3). The lattice association constant is given by a sum

$$K_A = \sum_{\{\mathbf{r}: r \leq \ell_T\}} \exp\left(\frac{2\ell_T}{r}\right), \tag{2.32}$$

which approaches the continuum definition if $\ell_T \gg a$. Note that the lattice association constant is discontinuous with changes in ℓ_T (i. e. with temperatures at fixed Coulomb coupling) because of the discrete changes of the number of sites within the Bjerrum volume. We will refer to the self-consistent set of equations equiped with the lattice association constant as the lattice Debye–Hückel—Bjerrum theory. We show the charge density derived from this theory in figure 3.8.

Even though the activity coefficient of free ions in Bjerrum theory is generally closer to unity than it is in the Debye–Hückel theory at identical (T, v_0), the total density in grand canonical ensemble is increased due to the presence of pairing (see figures 3.8 and 3.12). Note that there are theories that consider all charges as a single chemical

species and assign them activity coefficient that includes the pairing effects (Ebeling et al., 2002). Then the equation 2.23 can be used with the modified activity coefficient.

2.4 Other approaches to electrolyte theory

The introduction we have given so far has been mostly phenomenological. However, all the presented theories can be derived as terms of systematic perturbative expansions. This shows that the electrolyte theory is firmly anchored within the statistical thermodynamics. Expansions that we discuss are useful for evaluating the limits of formal validity of Debye–Hückel and Bjerrum theory. We give a brief overview of theoretical approaches to the electrolyte theory and provide the reader with commented references for subjects that are beyond the scope of our current work but might be important for its extensions.

The Debye–Hückel limiting law ($-\ln\gamma = \ell_T/\ell_D$) can be systematically derived using the Mayer cluster expansion (Mayer, 1950; Salpeter, 1958; McQuarrie, 2000). Resummation of classes of divergent integrals eventually results in a finite contribution. The original Debye–Hückel theory makes use of the ion diameter a and it performs better than the limiting law. However this means that it is not a perturbative theory in ℓ_T/ℓ_D. It is of theoretical interest how to reintroduce the influence of the finite diameter into the expansion. Charges with finite diameters were first treated by Meeron (1957, 1958). Justice and Justice (1976) gave a proof that the expansion up to the linear order in density contains terms $\ell_T/\ell_D - (\ell_T/\ell_D)(a/\ell_D)$ which can be interpreted as the first two terms of the geometrical series $(\ell_T/\ell_D)(1/(1+a/\ell_D)) = \ell_T/(\ell_D+a)$.

2.4.1 Different choices for bound pairs

The pairing theory artificially separates the charges into two species. This discontinuity at the pairing length is unphysical (Fisher and Zuckerman, 1998). Onsager characterized the ambiguity of the definition of Bjerrum in his bookkeeping rule (Hemmer et al., 1996): "The distinction between free ions and associated pairs depends on an arbitrary convention. Bjerrum's choice is good, but we could vary it within reason. In a complete theory this would not matter; what we remove from one page of the ledger would be entered elsewhere with the same effect."

While a complete theory of Coulomb gases has not been achieved yet, the situation regarding the consistency of pairing has been largely resolved. A summary of the main theories of pairing can be found in (Ebeling et al., 2002; Marcus and Hefter, 2006). We wish to give several important results.

The perturbative expansions are a useful tool for a critique of Bjerrum's theory. Justice and Justice (1976) have shown that the cluster expansion closely reproduces the Bjerrum theory in the term linear in density. The agreement is exact if the pairing length is shifted to $1.1\ell_T$. The influence of this shift is small because the integrand of the association constant is small compared to the contribution from short distances (see figure 2.3). The theory also includes a term representing how the population of pairs of like charges is reduced at small distances. This effect is small compared to the pairing of charges of opposite sign.

Ebeling and Grigo (1980) gave a theory of pairing that in principle treats only the charge added over and above the original Debye–Hückel theory as bound pairs. This allows one to keep $-\ln \gamma = \ell_T/(\ell_D + a)$ and further has the advantage that the association constant is given as a convergent integral whose upper bound is at infinity thus eliminating the arbitrary pairing length. For further details see (Ebeling and Grigo, 1982). Grigo and Ebeling (1984) analysed the influence of the Ebeling and the Bjerrum theory of pairing on the correlation function between ions. This built on previous analysis of correlations in the Bjerrum theory by Friedman (1980).

Levin and Fisher (1996) show that only the smallest distances contribute the majority of statistical weight to the bound pairs if the Coulomb interaction is strong. This means that reducing the pairing length can sometimes have very little influence. On a lattice it is often useful to consider the nearest neighbour pairs as the only kind of bound pairs (Kobelev et al., 2002). Fuoss (1978) proposed a similar approach where the nearest neighbour pairs are those not separated by any solvent molecules. Fisher and Zuckerman (1998) treat quite generally the consistency of calculations when one arbitrarily divides a fluid of particles into multiple species. They give conditions to be met for such a division to yield physical results and to avoid spurious solutions.

2.4.2 Further corrections

Many theories have explored electrolytes at densities beyond the validity of Bjerrum theory. We mention several approaches and interesting results which should find use if non-equilibrium properties of more strongly correlated Coulomb gases are considered.

The Ornstein–Zernike equation has been used to compute correlations in Coulomb gases; several closure relations have been applied: Percus–Yevick (Allnatt, 1964), the mean spherical approximation (Waisman and Lebowitz, 1970), and hypernetted chain equation (Rasaiah et al., 1972). The results from the mean spherical approximation can be extended to include pairing in the Ebeling theory (Ebeling and Grigo,

1982). While these perform well in the gaseous phase, they do not describe the critical behaviour and do not fulfil some general criteria for the free energy. Despite some attempts to resolve these concerns (Pini et al., 1998; Pini and Stell, 2002), the current state of affairs seems to favour Debye–Hückel based approaches (Zuckerman et al., 1997; Maribo-Mogensen et al., 2012).

Field theoretical calculations have been applied to electrolytes (Netz and Orland, 2000; Moreira and Netz, 2002). The Hubbard–Stratonovich transformation applied in their solution allows simpler calculations for symmetric electrolytes than the diagram resummation. However, Levin (2002) discusses limitations of this approach for asymmetric electrolytes.

For a realistic solvent, solvation of ions plays a role and ions interact differently in presence of solvent molecules in between of them. This issue is mostly solved using the Gurney co-sphere model (Wright, 2007). This motivated Fuoss (1978) to define a complex pairing theory which distinguishes contact pairs from solvent separated pairs and free ions. The lattice model used in this work treats the ion background as a homogeneous medium and avoids the complexity introduced in the Gurney model. Similarly, the Coulomb gas in spin ice has no solvent which simplifies its theoretical treatment.

The restricted primitive model has a liquid and gas phase separated by a critical line ending in a critical point. If it is put on a bipartite lattice ionic crystallization occurs and the critical point is often hidden by the solid phase (Kobelev et al., 2002; Brooks-Bartlett et al., 2014). The critical behaviour of this model has driven many theoretical approaches in the field. Numerical simulations seem to have resolved this problem in favour of standard Ising criticality (see Luijten et al. (2002) and references therein). This liquid–gas phase transition can be interpreted as bound pair condensation. Mutual interactions between the pairs and screening of their dipole moment have to be taken into account to locate the critical curve precisely.

We can see that a large amount of work has been invested into investigating the behaviour of Coloumb gases as they become denser and more correlated. However, this thesis focuses on the weak electrolyte limit and the second Wien effect. The Bjerrum–Debye–Hückel treatment is a sufficient approximation in this limit which we show in figure 3.8 in the chapter 3.

2.5 Transport properties of electrolytes

Coulombic correlations influence the transport properties of electrolytes. In this section we discuss effects that can be described in the

scope of linear response theory and their decay with applied field. The equilibrium transport properties also influence the Wien effect as we discuss in section 3.3.2.

2.5.1 Screening and conductivity

If an external field is applied the response of the ion in the field direction is reduced due to the presence of the ionic atmosphere. There are two processes reducing the mobility – relaxation field effect and electrophoresis. The first theory correctly accounting for these effects was given by Onsager (1926). It took another 30 years before Onsager and Fuoss extended the theory to higher orders in density taking also the cross terms between the two effects into account. We focus on the relaxation field due to the absence of electrophoresis in lattice simulations.
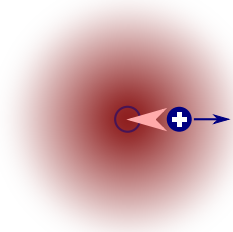
Figure 2.4: **Relaxation field.** The applied field (blue arrow) displaces a charge from the centre of its screening cloud. The resulting charge asymmetry leads to a relaxation field (red arrow) opposing the applied field.

2.5.1.1 Relaxation field

The external field causes the ionic atmosphere to become asymmetric around the ion of reference (see figure 2.4), which leads to an additional field acting on the charge $\Delta \mathbf{E} = \partial \Psi(\mathbf{r})/\partial \hat{\mathbf{E}}$, where Ψ is the potential of the deformed screening cloud and $\hat{\mathbf{E}}$ is the field direction. Within linear response theory, it suffices to shift the equilibrium potential in the field direction to obtain a potential that correctly captures the lowest-order correction to the ion mobility (Onsager, 1926). The result is

$$\Delta \mathbf{E} = -\frac{2-\sqrt{2}}{3}\frac{\ell_T}{\ell_D}\mathbf{E}. \tag{2.33}$$

The relaxation field opposes the applied field and the effective field felt by the ion is reduced as a result. This in turn reduces the mobility

$\varkappa = \sigma/n$ ($\sigma = J/E$ is the bulk conductivity). The reduction of the mobility due to the relaxation field is

$$\frac{\varkappa(0)}{\varkappa_0(0)} = 1 - \frac{2-\sqrt{2}}{3}\frac{\ell_T}{\ell_D}, \tag{2.34}$$

where $\varkappa(0)$ and $\varkappa_0(0)$ are the zero field mobilities of the Coulomb gas and its non-interacting counterpart, respectively.

Electrophoresis is the flow induced in a solvent due to the drift of ions in an electric field. This induced flow then acts back on other ions in the electrolyte. The flow caused by a positive ion will be in the opposite direction to the movement of a negative ion and will slow it down and vice versa. This hydrodynamic coupling is enhanced by the Debye correlations. To the lowest order of approximation, the correction is proportional to the square root of the density, specifically to a/ℓ_D (Onsager, 1926). Thus it is of the same magnitude as the relaxation field effect. The force acting on the ion can be obtained from Stokes equation thanks to the small value of the Reynolds number at the scale of ions. Compared to experiment, this approximation fares suprisingly well if we consider that it treats the solvent as a continuum on scales comparable with the sizes of the solvent molecule. Higher order terms in the conductivity expansion also involve cross-terms that combine the electrophoresis with the relaxation field. We will neglect the electrophoresis and any cross-terms related to it due to the absence of a solvent in lattice models.

2.5.1.2 First Wien effect

An external field reduces both the relaxation field effect and electrophoresis, since the ions pass each other faster than the ionic atmosphere can constitute. A theory for the decay of both effects was given by Wilson (1936) and later extended and simplified by Onsager and Kim (1957). The main result is that the initial increase in conductivity is quadratic with field due to the elimination of the screening charge cloud. The relaxation field effect completely disappears in the strong field limit, while electrophoresis remains present in a reduced but finite form (corresponding to the flow caused by uncharged particles). The decay of the relaxation field effect modifies the conductivity increase caused by the second Wien effect. For this reason, we give a more detailed treatment of the first Wien effect in section 3.3.2.2.

2.5.1.3 Debye–Falkenhagen effect

Due to the finite relaxation rate of the ionic atmosphere, alternating external fields with frequencies above this rate prevent the ionic atmosphere from forming (Debye and Falkenhagen, 1928). The alternating

current measurements allow for the determination of the time necessary to establish the screening.

2.6 Simulation methods

To capture the properties of lattice electrolytes and later the dumb-bell model of spin ice, we use numerical simulations. These simulations are conceptually quite simple because we simulate the restricted primitive model on a lattice. We work on the diamond lattice (see figure 2.5). The diamond lattice sites that can be either empty or occupied by a positive or a negative charge. We evaluate the electrostatic energy of the system via Ewald summation. The system evolves using Monte Carlo dynamics with three types of move: charge creation, displacement, and annihilation. The acceptance probabilities follow the update scheme given by Metropolis et al. (1953). We interpret these updates as moves that model a fundamentally diffusive dynamics of the system. This interpretation underpins extending the Monte Carlo simulations out of equilibrium. We give details of each component of the simulations in the following.
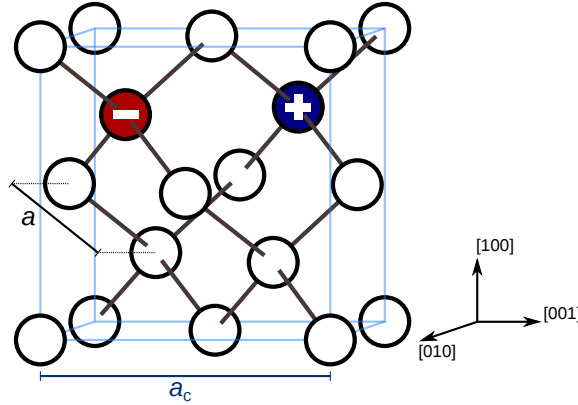
Figure 2.5: **Diamond lattice Coulomb gas.** Our simulations are performed on a diamond lattice. Each site can either be empty or be occupied by a single positive or negative charge. To study the second Wien effect in chapter 3, we apply a field in the [001] direction.

2.6.1 Monte Carlo methods

Monte Carlo (MC) methods were originally proposed for evaluating integrals by Ulam and von Neumann. Their main application lies in evaluating high dimensional integrals which includes averages of physical quantities over a large phase space.

For high-dimensional intergrals, integration schemes based on regular discretization of the integration set have a computational cost that increases exponentially with the dimension of the space (Press et al., 2007). For example the error of the rectangle rule scales as $\mathcal{O}(N^{-1/d})$ with the number of samples N and dimension d. This requires an exponentially increasing number of samples $\propto N^d$ to keep the error constant. The exponential scaling is common for all quadrature rules that evaluate the integral on a regular grid.

On the other hand, the Monte Carlo method has an error that scales as $\mathcal{O}(N^{-1/2})$ and that is independent of dimension. This is achieved by randomly selecting a point and asking if it lies within the set whose volume we seek than to evaluate. The fraction of points that land in the integrated set approximates the fraction of volume that the set occupies in the space that we sample from. The error of the method is then the statistical uncertainty of the result. A detailed introduction to Monte Carlo methods in general is given in (Newman and Barkema, 1999; Krauth, 2006).

Average quantities in many body systems are integrals over high dimensional phase spaces and the Monte Carlo method is suitable for evaluating them. An average of a quantity $\mathcal{Q}$ over states with probability distribution p_i is

$$\langle \mathcal{Q} \rangle = \frac{\sum_i \mathcal{Q}_i p_i}{\sum_i p_i} \tag{2.35}$$

where we have assumed a probability distribution that is discrete which incurs no loss of generality. It is however often costly to sample directly from the probability distribution. Metropolis et al. (1953) put forward a first example of the so-called Markov chain Monte Carlo method which circumvents this problem by generating a point in the integration set (a physical state) based on an update of the previous state. The transitions between states are selected stochastically. The rules for the transitions can be often described in a simple fashion because we can use the insight about the physical meaning of the system.

To obtain the correct sampling of states $\{i\}$ with probabilities p_i we impose the detailed balance condition

$$\mathcal{P}_{ij} p_i = \mathcal{P}_{ji} p_j \tag{2.36}$$

for $\mathcal{P}_{ij}$ which is the transition probability of the Monte Carlo update $i \rightarrow j$. Note that this is a sufficient but not necessary condition for the probability vector $\mathbf{p}$ to be the steady-state eigenvector of the transition matrix $\hat{\mathcal{P}} \mathbf{p} = \mathbf{p}$ (Stirzaker, 2001).

Another important property of any update scheme is ergodicity. If we aim to find the statistical average of a quantity over the whole ensemble it is necessary that the algorithm contains moves that allow access to all

states eventually. This requires the irreducibility of the transition matrix $\hat{\mathscr{P}}$. More commonly a situation occurs when ergodicity is guaranteed theoretically but the path between some states is too improbable to be followed within the computational time available. Such a situation is common in spin glasses (Young and Young, 1998) and frustrated magnets (Lacroix et al., 2011).

For the purposes of developing an algorithm, the transition probability $\mathscr{P}_{ij}$ is conventionally split into the proposal probability $\mathscr{R}_{ij}$ and the acceptance probability $\mathscr{S}_{ij}$

$$\mathscr{P}_{ij} = \mathscr{R}_{ij}\mathscr{S}_{ij}. \tag{2.37}$$

We will focus on the update scheme due to Metropolis et al. (1953) and specify these probabilities for a grand canonical Coulomb gas.

2.6.2 Metropolis algorithm

We consider the canonical Boltzmann distribution $p_i = e^{-\beta E_i}/Z$ where $Z = \sum_i e^{-\beta E_i}$ is the partition sum. Detailed balance condition 2.36 takes on the form

$$\frac{\mathscr{P}_{ij}}{\mathscr{P}_{ji}} = \frac{p_j}{p_i} = e^{-\beta \Delta E}, \tag{2.38}$$

where $\Delta E = E_j - E_i$ is the energy gained by the transition $i \to j$. Detailed balance does not fix the absolute value of the transition probability. The Metropolis algorithm adds the condition that all moves that decrease the energy ($\Delta E \leq 0$) are accepted. The moves that increase the energy are thus accepted with probability $e^{-\beta \Delta E}$. This choice is expressed as $\mathscr{S}_{ij} = \min[1, e^{-\beta \Delta E}]$. The proposal probability is not specified but it is commonly chosen to be equal for all possible updates of the system $\mathscr{R}_{ij} = 1/N_U$. For the total transition probability we have

$$\mathscr{P}_{ij} = \min[1, e^{-\beta \Delta E}]/N_U. \tag{2.39}$$

The probabilities in the grand canonical ensemble can be obtained by substituting by $E_i \to (E - \nu_0 N)_i$. Similarly for the microcanonical ensemble, we have $e^{-\beta E_i} \to 1$. Thus all moves are accepted in a microcanonical Metropolis simulation. A useful example is the worm algorithm that allows the exploration the highly degenerate groundstate manifold of spin ice. We discuss the worm algorithm in section 4.8.1.

2.6.3 Grand canonical lattice gas

In this subsection we present the specific choice of moves and their proposal probabilities that we use in our simulations. We work in
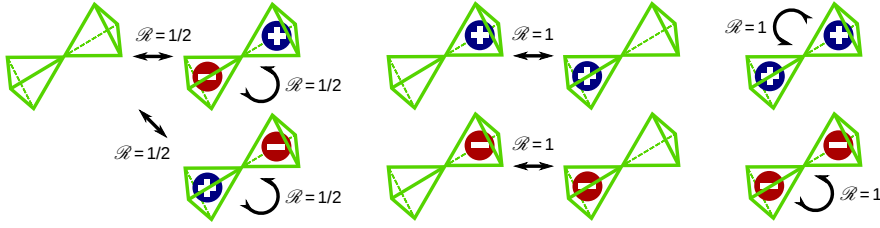
Figure 2.6: **Proposal probabilities.** Possible configuration of two randomly selected neighbouring sites are shown together with the proposal probabilities for various transitions. The round arrow signifies keeping the system in its initial state. See text for details.

the grand canonical ensemble, allowing charges to be created or annihilated. To mimic the dissociation of molecules in a solution or the creation of magnetic monopoles from the vacuum, we create the charges in pairs on neighbouring sites. This also ensures electroneutrality throughout the simulation. An existing charge can propagate through the system by hopping to a neighbouring site.

All these moves can be unified in a single framework. We randomly select a site (with equal probability over all sites). Then we select one of the four neighbouring sites. This is equivalent to selecting a random bond in the diamond lattice. There are the following possible situations (also shown in figure 2.6):

- If both selected sites are empty we propose creating a pair of positive and negative charges. The proposed orientation of the pair is chosen at random.

- If one of the sites is occupied and the other is empty, we propose moving the charge from its original position to the empty site.

- If both sites are occupied and the charges have opposite signs we propose annihilation with a probability of one half. In the other half of situations we propose no move. This is to respect detailed balance with respect to the creation move that allows two different orientations to be proposed.

- If both sites are occupied with equal charges no move is proposed.

The Metropolis algorithm requires efficient evaluation of the energy of the system. This comprises the electrostatic energy and the number of charges $N = N_+ + N_-$ multiplied by the absolute value of the bare chemical potential ν_0 (the choice of chemical potential is discussed in section 2.1.1.1). While the latter is readily found by keeping count of the charges, the electrostatic energy requires more involved methods. We

use the Ewald summation in our simulations. The following subsection introduces it briefly.

2.6.4 Ewald Summation

Evaluating the potential energy of a long-range interacting system requires care. We use the Ewald method which computes the energy of a periodic array of simulation boxes. A general sum of an infinite number of electroneutral boxes is only conditionally convergent and thus not defined unless the order of summation is given as well. Typically, the series is summed by adding up contributions from expanding spherical shells.

We give the result obtained in the rigorous introduction by de Leeuw et al. (1980). The total energy of a cubic simulation box with charges at positions $\mathbf{r}_i$ that is periodically repeated at positions numbered by a vector $\mathbf{n}$

$$U_{\text{Ewald}} = \frac{Q_e^2}{4\pi\epsilon_0\epsilon_r}\left[\sum_{\langle i,j \rangle} \frac{1}{L}\mathfrak{z}_i\mathfrak{z}_j\psi\left(\frac{\mathbf{r}_{ij}}{L}\right) + \frac{\mathfrak{f}}{2L}\sum_{i=1}^N \mathfrak{z}_i^2 \right.$$
$$\left. + \frac{2\pi\epsilon_r}{(2\epsilon_{r0}+\epsilon_r)V}\left|\sum_{i=1}^N \mathfrak{z}_i\mathbf{r}_i\right|^2 \right], \tag{2.40}$$

where

$$\psi(\mathbf{r}) = \sum_{\mathbf{n}} \frac{\text{erfc}(\alpha(\mathbf{r}+\mathbf{n}))}{|\mathbf{r}+\mathbf{n}|}$$
$$+ \frac{1}{\pi}\sum_{\mathbf{n}\neq\mathbf{0}} \frac{\exp\left(2\pi i\mathbf{r}\cdot\mathbf{n} - \pi^2|\mathbf{n}|^2/\alpha^2\right)}{|\mathbf{n}|^2} \quad \text{and} \tag{2.41}$$

$$\mathfrak{f} = \lim_{|\mathbf{r}|\to 0}\left(\psi(\mathbf{r}) - 1/r\right)$$
$$= \sum_{\mathbf{n}\neq\mathbf{0}}\left[\frac{\text{erfc}(\alpha\mathbf{n})}{|\mathbf{n}|} + \frac{\exp\left(-\pi^2|\mathbf{n}|^2/\alpha^2\right)}{\pi|\mathbf{n}|^2} \right] - \frac{2\alpha}{\sqrt{\pi}}, \tag{2.42}$$

where ϵ_{r0} is the permittivity of the material in which the system is embedded, $\mathfrak{z}_i$ the valence of the ith charge, L is the length of the side of the simulation box, and $V = L^3$ is the volume of the simulation box. The Ewald parameter α parametrizes the convergence factor used by de Leeuw et al. (1980) to sum the conditionally convergent series. The full expression is independent of this factor but it determines the accuracy and convergence speed of numerical approximations of the sum.

We interpret the terms in equation 2.40 as follows: the first term in U_{Ewald} is the mutual interaction between charges with the pair potential $\psi(\mathbf{r})$, the second term is the charge self-energy, and the last term is

the depolarization term due to the interaction with the surrounding medium.

The potential $\psi(\mathbf{r})$ has two contributions which also appear in the self energy. The two parts can be seen as sums in real space and in quasi-momentum $\mathbf{n}$ space. This allows one to adopt a truncation scheme for each part. The convergence is controlled by α in a competing fashion for the two sums. Usually, values around unity perform well but the exact value of α also depends on the efficiency of algorithms used for computing the constituents of the sums. We circumvent this problem by pre-computing $\psi(\mathbf{r})$ for all possible separation vectors in our lattice as well as storing $\mathfrak{f}$. Thus our updates use a fast lookup of the values instead of their computation.

The Gaussian convergence factor that renders the Ewald sum convergent is often visualized as an artificial Gaussian screening cloud around the charges (Frenkel and Smit, 2001). The charge distribution in the screening cloud is $\pm Q_e (\alpha/\pi)^{3/2} \exp(-\alpha r^2)$ and the sign is opposite to the sign of the charge at its centre. The real space sum then comes from the screened charges interacting with each other via an effective potential that is short-range. The reciprocal space sum captures the internal electrostatic energy of the artificial screening cloud that needs to be subtracted. The term $2\alpha/\sqrt{\pi}$ in $\mathfrak{f}$ then corrects for the spurious energy coming from the interaction of a charge with its own artificial screening cloud.

Rigorous limits for the error of the sum can be established and used to optimize its evaluation. However, there is also a systematic deviation because we embed the system in a lattice of its copies. An example is the energy of a dipole $-Q_e^2/4\pi\epsilon a$ compared with the energy of a dipole embedded in a one dimensional chain $(\cdots - + - + \cdots)$ of dipoles $-2\ln 2 \times Q_e^2/4\pi\epsilon a \simeq -1.386 \times Q_e^2/4\pi\epsilon a$, where the prefactor is called the Madelung constant. The three dimensional CsCl cubic structure, where each Cs ion is at the centre of a cube of Cl ions and vice versa, yields the maximum Madelung constant 1.763 possible in our simulations (Hoppe, 1966). This deviation can be neglected most of the time since the Coulombic interaction is screened on distances short compared to the size of the simulation box ($L \gg \ell_D$).

Dielectric properties of the surroundings have to be taken into account, even though the system with periodic boundary conditions appears infinite. All partial sums correspond to a finite sphere embedded in an external medium. The infinite Ewald sum results from these partial sums and the influence of the boundary condition does not vanish. This is the source of the third term in equation 2.40. A useful discussion of the experimental implications of this term for electrolytes was given by Roberts and Schnitker (1995).

For the lattice electrolyte, we choose tinfoil boundary conditions at infinity, i.e. a perfect conductor with $\epsilon_{r0} = \infty$. This makes the third term in equation 2.40 vanish. This allows us to focus on the bulk properties of the system. For spin ice, the choice is more involved because the term due to the boundary conditions at infinity is exactly equal to the contribution to the internal energy due to demagnetization (Melko and Gingras, 2004). We discuss demagnetization in section 4.8.

2.6.5 Dynamics in Monte Carlo simulations

The ergodic theorem equates statistical averages with temporal averages (Huang, 1987). Therefore the Markov chain Monte Carlo sampling can be interpreted as a stochastic process in time. However, the dynamics of this process does not necessarily correspond to any physical dynamics. Nevertheless, the Metropolis algorithm for particles that hop locally in an external potential corresponds to a diffusive process which is described by a drift-diffusion equation in the continuum limit (Kikuchi et al., 1991). Such a derivation can be found more generally as a limit of local random walks (Risken, 1996), even in cases when the waiting times diverge (Metzler and Klafter, 2000). The drift-diffusion equation corresponding to the Metropolis algorithm can be as well interpreted as a regular Smoluchowski (Fokker–Planck) equation with a field dependent mobility which we discuss in section 3.3.2. We also show that the second Wien effect can be used as a diagnostic tool for this mobility.

The locality of the updates plays an important role because it allow one to interpret the chosen dynamics in terms of the physical time – the number of Monte Carlo steps taken has to be rescaled by the average acceptance probability (Cheng et al., 2006; Sanz and Marenduzzo, 2010). Thus the field dependent mobility can be mapped to a physical mobility. The stochastic dynamics of the Coulomb gas is fixed by selecting the update scheme. However, the choice is quite simple and the non-equilibrium results can be rescaled to describe a system with a different real-world mobility.

We are at this point equipped with a description of the equilibrium properties of electrolytes, basic notions of their linear response, and numerical algorithms to simulate them. This knowledge will help us treat the non-equilibrium response of weak electrolytes in the next chapter. Later in the thesis, the emergent Coulomb gas in spin ice will be described by simple extensions of these theories.

3

SECOND WIEN EFFECT

The second Wien effect is an increase of conductivity of a weak electrolyte in an external electric field. This increase is driven by an enhanced dissociation of ions into free charges, which in turn results in an increase in the total number of charge carriers in the presence of the double equilibrium. It is a remarkable effect in many respects. The underlying non-equilibrium process lies completely beyond linear response theory. Nevertheless Onsager (1934) found a non-trivial solution in the limit of infinite dilution. We start this chapter by describing the basic features of the second Wien effect and several experimental examples.

The long-range Coulombic interactions render the Wien effect universal to a high degree. One might call this Coulombic censorship since details of the ion size and shape are hidden on length scales below the Bjerrum length $\ell_T = Q_e^2/(8\pi\epsilon k_B T)$. In symmetrical electrolytes, the relative increase depends only on a single parameter $b = \ell_T/\ell_E = Q_e^3 E/(8\pi\epsilon(k_B T)^2)$ as

$$\frac{n_f(E)}{n_f(0)} = \sqrt{\frac{K_D(E)}{K_D(0)}} = \sqrt{F(b)} \simeq 1 + \frac{1}{2}\frac{\ell_T}{\ell_E} = 1 + \frac{Q_e^3}{4\pi\epsilon k_B T}E \qquad (3.1)$$

where ℓ_T measures the strength of Coulomb interaction compared to the temperature and the field length $\ell_E = k_B T/Q_e E$ measures the length along which the field $E = |\mathbf{E}|$ has to act to perform work on the charge equal to $k_B T$ (see section 2.1.2). A typical temperature dependence of these length scales is shown in figure 3.1. The function $F(b)$ was defined by Onsager in terms of the modified Bessel function I_1 as

$$F(b) = \frac{I_1(2\sqrt{2b})}{\sqrt{2b}} \simeq 1 + b. \qquad (3.2)$$

The initial increase in density is linear not only in the applied field but also in the Coulomb coupling strength $1/4\pi\epsilon$. The growth in dissociation with increasing attractive interaction between charges is remarkable because it stands in contrast to the intuition for escape rates to decrease with increasing height of the potential barrier.

The universality of the dependence only on b is not perfect because the formula 3.1 neglects the effects of the ionic atmosphere. $K_D(0)$ has to be interpreted as the ideal dissociation constant in the absence of
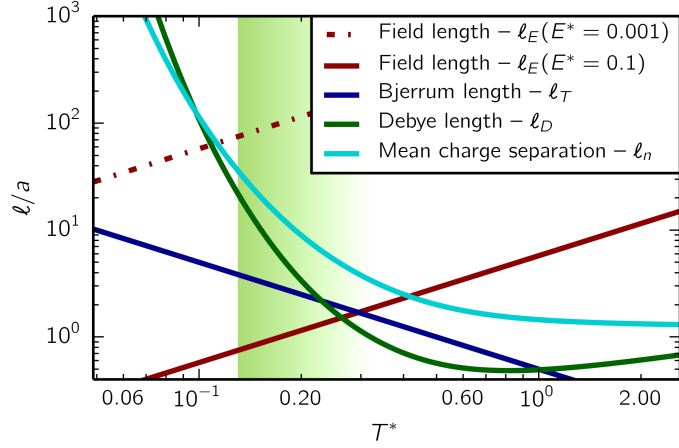
Figure 3.1: **Length scales for the second Wien effect ($v_0^* = -1.45$).** This figure shows the temperature dependence of characteristic lenghts in a lattice electrolyte compared to the minimal ion separation a. As the temperature lowers, the Wien effect becomes prominent as evidenced by the ratio ℓ_T/ℓ_E (at constant field). Lowering the temperature at constant chemical potential reduces the density. This leads to the decreased effect of screening which can be characterized by the ratio ℓ_T/ℓ_D. The values roughly correspond to low temperature behaviour of DTO spin ice ($v_0 = -4.35\,\text{K}$, $T \simeq T^* \times 3\,\text{K}$). The green shaded area represents the temperature range where we carry out the numerical simulations.

the Debye screening. The screening increases the equilibrium density of free charges roughly by a factor $1/\gamma$ (inverse activity coefficient). The concentration quotient, defined as the dissociation constant including all activity coefficients, is $\mathscr{K}_D = K_D(0)/\gamma^2$. The increase due to screening disappears in high fields as the screening atmosphere cannot establish itself in the flowing Coulomb gas and $\mathscr{K}_D(E \to \infty) = K_D(E \to \infty)$.

We now rewrite equation 3.1 in terms of the increase $\Delta n_f(E) = n_f(E) - n_f(0)$ taking the screening into account.

$$\frac{\Delta n_f(E)}{n_f(0)} = \sqrt{\frac{\mathscr{K}_D(E)}{\mathscr{K}_D(0)}} - 1 = \sqrt{\gamma^2 \frac{K_D(E)}{K_D(0)}} - 1 \tag{3.3}$$

$$= \gamma \sqrt{F(b)} \simeq \gamma \left(1 + \frac{1}{2} \frac{\ell_T}{\ell_E} \right) \tag{3.4}$$

The activity coefficient γ reintroduces the dependence on equilibrium density into the theory of the Wien effect. It can be only neglected at very low densities (i.e. high chemical potential). Also note that Onsager's theory gives a prediction for the dissociation constant. The density increase has to be calculated from the mass action law $n_f^2 = 2K_D(1 - n_f)$. At low densities $1 - n_f \simeq 1$ and we can use the approxima-

tion $n_f = \sqrt{2K_D}$. Even with screening, the high field behaviour of weak electrolytes is fully characterised by two parameters: b and γ.
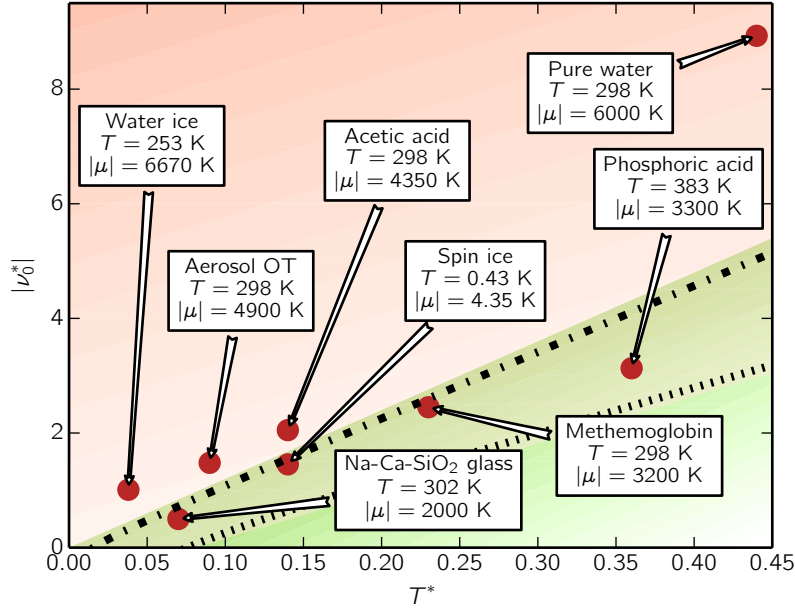
Figure 3.2: **Corresponding states for the second Wien effect.** The materials are classified by their estimated reduced temperature $T^* = k_B T / U_C(a)$ and reduced bare chemical potential $\nu_0^* = \nu_0 / U_C(a)$. The red shading shows the weak electrolyte limit (low temperature / high chemical potential) where the Wien effect should be observable. The green area is accessible to our simulations. The dash-dotted, and the dotted line give the limit of applicability of the original, and the screened, Onsager's theory in the simulations, respectively. Typical field strenghts necessary to double the charge density at room temperature (i.e. $b/2 = \ell_T / 2\ell_E = 1$) are of the order of $E \simeq 200\,\text{MV/m}$ for 1:1 aqueous electrolytes and $E \simeq 5\,\text{MV/m}$ for non-aqueous 1:1 electrolytes. In $Dy_2 Ti_2 O_7$ spin ice, the equivalent magnetic field is $\mu_0 H = 25\,\text{mT}$ at $T = 0.43\,\text{K}$.

The presence of only few quantities is a characteristic of Onsager's theory. This allows a simple classification of materials exhibiting the second Wien effect according to the law of corresponding states (figure 3.2). Regardless of their equilibrium properties, the observed Wien effect should be identical in materials with equal reduced chemical potential ν_0^* and reduced temperature T^* (i.e. the related energies compared to the Coulomb coupling at contact $U_C(a)$, see section 2.1.1). We show the Wien effect in several materials in figure 3.3.

Having given a phenomenological introduction to the second Wien effect, we follow with a detailed overview. We find it necessary to treat the experimental and theoretical description in much greater detail than other topics in this thesis because there has been no review pub-

lished in the last 75 years since (Eckstrom and Schmelzer, 1939) and many aspects were considered separately by independent groups of scientists and scattered over journals with focus ranging from mathematics to chemistry. Apart from collecting these pieces of knowledge in one place, we give a comparative commentary.

Results of our numerical simulations form an important part of our presentation. We have simulated a lattice Coulomb gas in an external field. The lattice gas is a minimal model for the Wien effect (see figure 3.3e). At the same time, the model is very versatile as its parameters can be selected to match various materials exhibiting the Wien effect (compare with figure 3.2). Finally, it is readily extensible; for example annealed disorder can be implemented by fixing charge at certain lattice sites or by preventing moves along certain bonds between the sites; see (Sala et al., 2014) for one of examples of implementing disorder in spin ice. We use the insights from our numeric simulations of the lattice Coulomb gas which allow us to liberate ourselves from material specific behaviour and judge the quality of approximations made in the previous theoretical work. We clearly mark whenever an original idea from a reference and our evaluations and extensions overlap.

The next section is devoted to a short introduction of the broad range of materials exhibiting the Wien effect. The following section treats the theory, first giving an insight into the mechanism of the Wien effect and subsequently reviewing Onsager's exact solution. In the final sections we discuss extensions of the theory due to screening, finite size of charges, and field dependent mobility. We also show how the simulations allow access to the correlations underlying the Wien effect and the direct computation of the association constant which is unaccessible to experimental methods.

If the reader is interested in a fast introduction to the topic we recommend starting with figure 3.3 for experimental evidence of the linear increase of conductivity with field, followed by section 3.2.1 explaining the mechanism behind the linear law and finally continuing to figures in section 3.3 which illustrate the extensions of the Wien effect on the example of simulations of the Wien effect in the lattice Coulomb gas.

3.1 Experimental signatures of the second Wien effect

The effect was first observed in water solutions of acetic acid CH_3COOH, chloracetic acid $CH_2ClCOOH$ and propionic acid CH_3CH_2COOH (Wien, 1931; Schiele, 1932). This was one of the first deviation from Ohm's law ever observed. Other simple aqueous electrolytes like ammonia NH_3 in water (Berg and Patterson Jr, 1953; Eigen and Schoen, 1955) or carbonic acid H_2CO_3 exhibit the effect as well.

(a) Acetic and chloracetic acid in water.

(b) 2,6-dinitrophenol in water.

(c) Aerosol OT in cyclohexane.

(d) Polyelectrolyte example.

(e) Lattice gas simulation.

(f) Water ice.
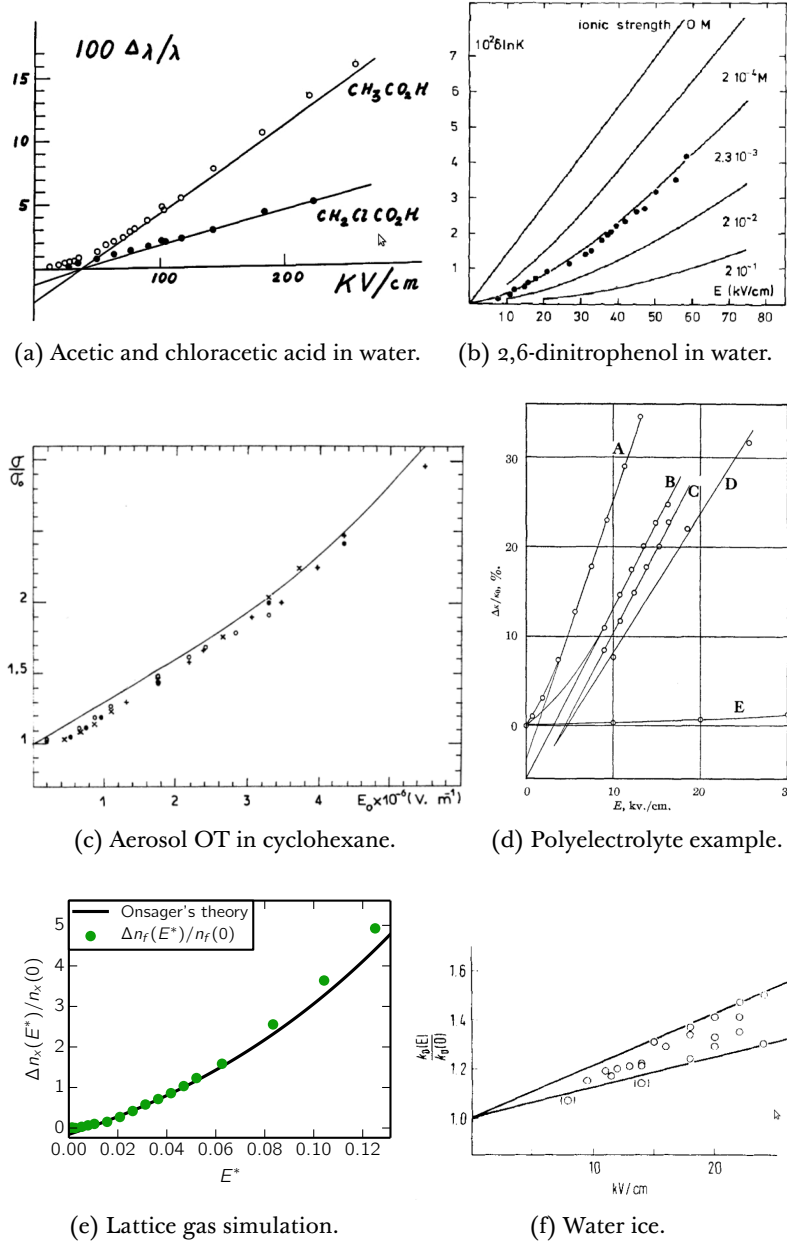
Figure 3.3: **Wien effect – experimental signatures. a)** Acetic acid is a proto-
type of a weak aqueous electrolyte. Chloracetic acid is more disso-
ciated in equilibrium so the increase as computed from the mass
action law is lower (Onsager, 1934). The negative offset is due to
the Debye screening (see equation 3.3). **b)** Dinitrophenol under-
goes protolysis in water. Bräunig et al. (1987) used it to study
the crossover from the screened Wien effect to the unscreened
linear law. **c)** The second Wien effect is much stronger in non-
aqueous solvents. Also note that Aerosol OT is a large surfactant
molecule which can take both positive and negative charge and
is known to form micelles. **d)** Poly-4-vinyl-N-n-butylpyridinium
bromide (B–D) is a complex aqueous polyelectrolyte which ex-
hibits conductivity increase comparable with non-aqueous electro-
lytes (A – (Bz)$_3$NHPi) and larger than those for aqueous electro-
lytes (E – MgSO$_4$) (Bailey et al., 1952). **e)** Lattice Coulomb gas
simulations for $v_0^* = -1.45$ and $T^* = 0.135$. **f)** Wien effect in water
ice as measured by Eigen et al. (1964)

In all of these examples, the proton H^+ dissociates from the corresponding anion (protolysis). Similarly, dissociation of water itself into protons and hydroxide ions can be enhanced by strong fields. The field necessary can be achieved in bipolar membranes (Simons and Khanarian, 1978; Mafé et al., 1990; Tongwen, 2002) or in electrical double layers (Brüesch and Christen, 2004). In water ice, the Wien effect has been measured by Eigen et al. (1964).

The second Wien effect is much more common in non-aqueous electrolytes – water has static relative permittivity $\epsilon_r = 80$ in standard conditions while most non-polar solvents have $\epsilon_r \simeq 2$–4. This leads to the second Wien effect being roughly thirty times stronger in non-aqueous than in aqueous electrolytes. Onsager (1934) cites results by Gemant (1930) on picric acid in benzene. While these results match the theory, there is no conductivity increase observed in the transverse direction which is incompatible with an increased population of free charges. The first conclusive non-aqueous examples were tetrabutylammonium picrate in diphenyl ether (Mead and Fuoss, 1939; Nauwelaers et al., 1976) and tetrabutylammonium bromide in diphenyl ether (Mead and Fuoss, 1940). While many experiments had used alternating current before, the frequency dispersion of the Wien effect was first extensively studied by Eigen and Schoen (1955) in aqueous electrolytes and by Persoons (1974); Persoons and Hellemans (1978); Persoons and Beylen (1979) in non-aqueous electrolytes.

The validity of the theory is not limited to simple electrolytes. It has been confirmed in polyelectrolytes with large charge (Bailey et al., 1952), large organic molecules (Bräunig et al., 1987), surfactant solutions (Randriamalala et al., 1985) and other dielectric liquids (Park et al., 2009; Dukhin and Parlia, 2013). As we will discuss below, the linear law is not influenced by the size of the charge (McIlroy and Mason, 1984).

In solids, electrolyte models have been applied to mobile defects in glasses (Ingram et al., 1980; Feltz and Schirrmeister, 1980) and ion-doped solid PVC (Wingrave, 1980). Most recently spin ice was used to test the Wien effect theory (Bramwell et al., 2009). We devote the second half of this thesis to showing that spin ice is in fact one of the most suitable and versatile materials to observe the second Wien effect.

The strong fields necessary for the second Wien effect can be generated on short distances in biological membranes. This led to several proposals regarding the role of the Wien effect in ion kinetics in membranes (Bass, 1968; Tsong and Astumian, 1987) and neurotransmission (McIlroy and Mason, 1981). These are chiefly theoretical works and to our knowledge have not been reviewed in the light of contemporary knowledge about membrane biochemistry.

The theory of the Wien effect has also been invoked in the problem of photogeneration in organic solids (Hong and Noolandi, 1978; Noolandi and Hong, 1979) and solar cells (Pai, 1975; Yuan et al., 2011). These studies use the theory which Onsager (1938) developed for geminate recombination and escape probabilities for which the solution of the Wien effect drift-diffusion equation is used (Onsager, 1938). This is not the Wien effect per se since the charges are not generated from a chemical equilibrium and only a single charge pair is considered. Moreover, care has to be taken in interpreting the input parameters of the theory (Wojcik and Tachiya, 2009; Hilczer and Tachiya, 2010). The single ion pair nature of the recombination allowed for numerical simulations (Bartczak and Hummel, 1987) which preceded our simulations of the full second Wien effect by 25 years (Kaiser et al., 2013).

3.2 Theory of the second Wien effect

The second Wien effect is caused by the applied field enhancing the dissociation of Coulombically bound charge pairs into free charges. We will start this section by describing this process in a simple approximation to obtain the linear increase in the dissociation constant $K_{\mathrm{D}}(E)/K_{\mathrm{D}}(0) \simeq 1 + \ell_T/\ell_E$. The aim will be to clarify the nature of the dissociation.

Subsequently, we will explore the full solution given by Onsager (1934). We separate his solution to three phases which we label by their character: mathematical, physical, and chemical. The theory is based on treating the diffusive dynamics of charges. The dynamics are described by a drift-diffusion equation for a pair of opposite charges with mutual Coulomb attraction in the external field (mathematical phase). The solutions of this equation need to be interpreted to obtain the modification of the dissociation constant (physical phase). The modified dissociation constant shifts the equilibrium between bound and free charges or alternatively the double equilibrium between neutral species or charge vacuum, bound pairs, and free charges (chemical phase). We discuss each part separately below.

3.2.1 Linear law

In this subsection we give a simple derivation of the linear increase in conductivity. Persoons and Hellemans (1978) gave a simple argument elucidating the nature of the linear law. We will follow their derivation.

In equilibrium, Bjerrum length ℓ_T gives the minimum of the probability to find an ion around an oppositely charged central ion. This population minimum forms a phase space bottle neck that separates
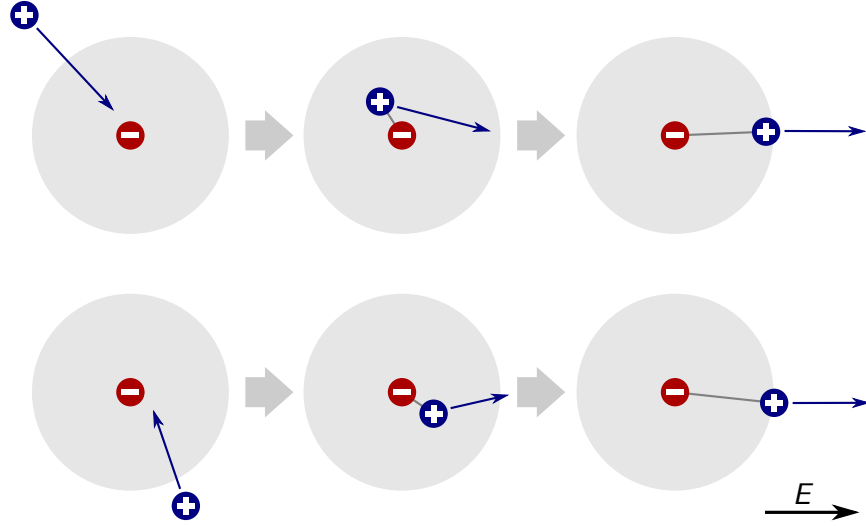
Figure 3.4: **Field induced dissociation**. A sketch of two trajectories of free charges that first associate to create a bound pair and subsequently dissociate again under the influence of the field. The bound pair can be seen as a metastable dipole which stretches under the influence of the field. Once the size of the dipole becomes comparable to ℓ_T (grey circle) it is energetically favourable for it to dissociate due to the action of the field.

the bound and free charges and allows one to treat them as separate species (see section 2.3). Note that the important length scale is not the maximum of the potential barrier. The escape rate is given by the Gibbs energy $\Delta G(0)$ necessary for the charge pair to get separated by the Bjerrum length ℓ_T. We will refer to this state as the Bjerrum dipole.

When the field is switched on, the rate will be limited by the passage through the Bjerrum dipole state parallel to the field. If the size of the dipole becomes comparable with the Bjerrum length the bound pair becomes metastable and can dissociate. We give a sketch of this process in figure 3.4. It is useful to study the shift in the Gibbs potential[1] of the Bjerrum dipole.

$$\Delta G(E) - \Delta G(0) = -\ell_T Q_{\mathrm{e}} E \tag{3.5}$$

This reduction in Gibbs energy exponentially increases the escape rate. Langevin (1903) showed that association stays unmodified by field; we give the proof below. As a result, the dissociation constant increases as

$$\frac{K_{\mathrm{D}}(E)}{K_{\mathrm{D}}(0)} = \exp\left(\frac{\ell_T Q_{\mathrm{e}} E}{k_{\mathrm{B}} T}\right) = \exp\left(\frac{\ell_T}{\ell_E}\right) \simeq 1 + \frac{\ell_T}{\ell_E}. \tag{3.6}$$

The result reproduces Onsager's prediction to linear order. The derivation shows how the Bjerrum dipoles provide leverage to the external

---

1 Note that the Gibbs potential can be only defined locally once we are out of equilibrium. Here we treat a single dipole.

field. This explains the paradoxical enhancement of the density increase as the attractive Coulomb potential becomes stronger.

We only consider the dipoles aligned with the field because the oppositely aligned dipoles are not unstable towards dissociation but towards realignment along the field. In fact the exact solution shows that the dissociation in the direction against the field stays constant as a function of the applied field. This asymmetry and the fact that the association flow is not compensated by the dissociation flow are signs of the system being out of equilibrium. The non-equilibrium character also explains the response of a scalar variable which is linear in the modulus of the vector, which would be forbidden in the linear response theory.

3.2.1.1 Perturbative approaches to the linear law

Liu (1965) and Mason and McIlroy (1976) both developed perturbative approaches to Wien effect which yield the correct linear law. The intent of the two approaches is different. The derivation of Liu (1965) is suitable for calculating the Wien effect in potentials other than the Coulombic one. The solution of the full drift-diffusion equation is expanded in ℓ_T, so in nature it is a weak coupling expansion. It finds its use if the Debye screening influences the Wien effect significantly.

The approach of Mason and McIlroy (1976) is applicable to the Coulomb potential only. Their expansion in b has the weak field / weak coupling character. The expansion is performed only after several transforms which are specific to the Coulomb potential and occur in the nonperturbative solution as well (hence the presence of b). Nevertheless, this expansion is useful because it takes a different path than Onsager did in the final phases of the calculation. Onsager's exact solution allow for the calculation of the Wien effect in principle for any boundary conditions. However, the result is usually a sum of special functions. The perturbative approach simplifies obtaining a theory for the Wien effect with charges that are spheres of a finite diameter.

3.2.1.2 Counterexamples

It is worthwhile to consider how Kramer's escape rate would look like for a process resembling the Wien effect if the dissociation in the direction antiparallel to the field also occured. We provide an artificial one dimensional model. Contact charge pairs are generated with a low energy but are allowed to dissociate after forming dipoles of fixed length ℓ_T which are either aligned with or against the field. These dipoles are the states with the maximal Gibbs energy. The resulting free charges carry current and escape towards an absorbing boundary.

The maxima of the Gibbs potential shift by $\pm\beta\ell_T Q_e E$ if the field is applied. The dipoles would follow Kramer's escape rate, both direc-

tions would contribute and the resulting dissociation constant would increase quadratically with the applied field

$$\frac{K_{\mathrm{D}}(E)}{K_{\mathrm{D}}(0)} = \cosh(\beta \ell_T Q_{\mathrm{e}} E) \simeq 1 + \frac{1}{2}\left(\frac{\ell_T}{\ell_E}\right)^2 . \tag{3.7}$$

Similar quadratic dependence of statistical weights would be borne out by applying magnetic field to the spin-1 Blume–Capel model where the $S = \pm 1$ states represent the charges and $S = 0$ the empty sites. The magnetic field would serve as a shift in chemical potential for the charges with equal magnitude and opposite sign. The Boltzmann factors would again compensate to the linear order and the density of $S = \pm 1$ states would increase quadratically. The connection of the charge model to the Blume–Capel model was proposed and developed in (Brooks-Bartlett et al., 2014).

The quadratic response is to be expected of equilibrium models in general. If a thermodynamical potential would depend on the modulus of a field $|\mathbf{E}|$, the derivative of this potential with respect to $\mathbf{E}$ would not be defined at zero field and would have a direction dependent limit (proportional to $\hat{e} = \mathbf{E}/|\mathbf{E}|$). If the quadratic term vanishes, a quartic term or any other function analytic in the field would also lead to a physical response to the field.

Two other attempts have been made to explain the Wien effect as an escape rate process. Bass and McIlroy (1968) presented an approach which interprets to the Wien effect in very high fields. This interpretation gives a result which is close to the Onsager's solution but gives a worse agreement with experiments. McIlroy and Mason (1976) derived a similar escape rate approach to the screened Wien effect at the very low fields. This approximation does not compare well with our numerical results.

3.2.2 Onsager's theory

Onsager only gave results of his computation in his 1934 paper. The full derivation can be found in Onsager's PhD thesis which is accessible in his collected works (Hemmer et al., 1996). The thesis solves the drift-diffusion equation for general boundary conditions and develops a theory of special functions which had not been studied previously. As his thesis had not been published before the collected works, there have been several other independent derivations published. The one given by Mason and McIlroy (1975); McIlroy (1988) is the only one that is as advanced as Onsager's even though this solution is only for the case of a boundary condition that signifies an immediate equilibration at infinetisimal approach (a local Boltzmann equilibrium). Their solution is

shorter than Onsager's full treatise but nevertheless too long to reproduce here in full. McIllroy and Mason were mathematicians drawn to the problem by their studies of neural transmission; their subsequent work further developed many concepts either omitted by Onsager or implied without comment. We present only an outline of the mathematics underlying the solution. Nevertheless, a reader only interested in the physical implications is invited to continue reading after the following subsection.

3.2.3 The drift-diffusion equation

Onsager starts by deriving the drift-diffusion (Smoluchowski / Fokker–Planck) equation from general considerations about the motion of ions. Because the derivation follows a common procedure (Risken, 1996), we state directly the general form of the drift-diffusion equation in terms of the normalized correlation function[2] $g_{\pm} = \langle n_{+}(0) n_{-}(r)\rangle / \langle n_{+}\rangle \langle n_{-}\rangle$ and the related probability current density $\mathbf{S}$

$$\partial_t g = -\nabla \cdot \mathbf{S} = D\nabla \cdot \left(\nabla g + g\nabla(\beta U)\right), \qquad (3.8)$$

where D is the diffusion constant, U is the potential and $\beta = 1/k_B T$ is the inverse temperature. We used the Einstein relation for the electric mobility $\varkappa_e = Q_e \beta D$. Note that the equation has a character of a continuity equation for the probability current.

The equation is written in a reference frame with a fixed central ion, which means that the diffusion constant has to take into account the motion of both ions $D = D_+ + D_-$. The calculation does not depend on the sign of the central charge since the Coulomb potential is unmodified by changing the sign of the charges simultaneously; the external field has to change its sign under the symmetry $\mathbf{E} \to -\mathbf{E}$ which is equivalent to the inversion $\mathbf{r} \to -\mathbf{r}$. The character of the solutions is not influenced by this transformation. For magnetic monopoles in spin ice, the same symmetry holds $(Q_m, \mathbf{H}) \to (-Q_m, -\mathbf{H})$ despite the magnetic field being a pseudovector. This is because the monopoles are excitations of a vacuum formed by spins which have the same parity as the field.

We are only interested in steady-state solutions[3] so we set $\partial_t g = 0$. The equation for the steady-state correlation function is

$$\nabla \cdot \mathbf{S} = -D\nabla \cdot \left(\nabla g + g\nabla(\beta U)\right) = 0. \qquad (3.9)$$

---

2 We drop the lower index ($g = g_{\pm}$) until it is necessary to discuss other correlation functions

3 Hong and Noolandi (1978) gave an analysis of the time-dependent equation which is based on the solution of the time-independent equation.

This equation can be also written as

$$\nabla\cdot\left[\mathrm{e}^{-\beta U}\nabla\left(g\,\mathrm{e}^{+\beta U}\right)\right]=0.\tag{3.10}$$

It is easily verified that the Boltzmann distribution $g_{\mathrm{eq}}=\mathrm{e}^{-\beta U}$ solves this equation if there are no sinks or sources on the boundary. This solution has the special property that the current vanishes everywhere $\mathbf{S}=0$. The opposite implication does not hold out of equilibrium, where the current can vanish for other solutions as well. The solution g_{ss} in equation 3.46 is an example. However, g_{eq} only has a straightforward physical meaning in equilibrium situations.

3.2.3.1 Coulomb potential

First we study the equilibrium case ($\mathbf{E}=0$). This will allow us to introduce the relation between the solutions of the drift-diffusion equation and the association and dissociation rates. It also serves as a limiting case of the non-equilibrium solution. The solution with finite field approaches the solution without applied field for $r\rightarrow 0$ as the Coulomb potential dominates at small distances.

In the absence of an external field, the potential is spherically symmetric and reads $U(r)=-Q_{\mathrm{e}}^2/(4\pi\epsilon r)$. We write the radial part of equation 3.9 and use the definition of the Bjerrum length $\beta U(r)=-2\ell_T/r$ to obtain

$$\frac{1}{r^2}\partial_r\left(r^2\partial_r g\right)+\frac{1}{r^2}\partial_r\left(2\ell_T g\right)=0.\tag{3.11}$$

This equation is solved by

$$g=\mathscr{C}_1 g_{\mathrm{d}}+\mathscr{C}_2 g_{\mathrm{eq}}=\mathscr{C}_1+\mathscr{C}_2\exp\left(\frac{2\ell_T}{r}\right),\tag{3.12}$$

where $\mathscr{C}$ stands for an arbitrary constant. The first part $g_{\mathrm{d}}(\mathbf{r})=1$ can be identified with a fully dissociated uncorrelated gas while the other part of the solution corresponds to the Boltzmann function.

In the context of Coulombic interactions, it is useful to investigate when a constant is a solution. We substitute g_{d} into the general equation 3.9 to obtain a Laplace equation

$$\Delta(\beta U)=0.\tag{3.13}$$

The Coulomb potential can be obtained as the Green function of the Laplace operator and as such fulfils the equation everywhere apart from the origin. Adding an external field – a potential with constant gradient – will preserve the constant solution of the steady-state drift-diffusion equation.

There is by definition no current associated with the Boltzmann distribution. However, the constant solution has a radial current density associated with it

$$S_r = -D\nabla(\beta U) = -2D\ell_T/r^2. \tag{3.14}$$

The flux to origin due to this current is independent of the integration surface due to the continuity condition $\nabla \cdot \mathbf{S} = 0$. It is convenient to consider a sphere because the current density is constant on its surface. The resulting flux is

$$\Phi_A = \int \mathbf{S} \cdot d\Sigma = -8\pi D\ell_T = -8\pi(D_+ + D_-)\ell_T. \tag{3.15}$$

The negative sign corresponds to the association of the dissociated ions. The association rate constant is $k_A = -\Phi_A/\tilde{V} = 8\pi(D_+ + D_-)\ell_T/\tilde{V}$. The factor of the characteristic volume $\tilde{V}$ appears in our calculations because we have chosen to work with numerical densities instead of volumic densities. On a lattice $\tilde{V}$ is the volume per lattice site. This simplifies the comparison with simulations.

Langevin (1903) was the first to find this result. He considered the solution that is constant everywhere to be the dissociated part of the Coulomb gas and k_A the diffusion controlled association rate. In equilibrium the dissociation has to compensate the association and thus $\Phi_D^{(0)} = -\Phi_A$ and $k_A = k_D(0)$. This can be achieved by setting the constants in equation 3.12 to obtain the solution corresponding to the bound charges $g_a^{(0)}(r) = \exp(2\ell_T/r) - 1$. The important properties of this solution are that it vanishes at infinity $g_a^{(0)}(r \to \infty) = 0$ and that it has a finite dissociation current density through any angle (Onsager, 1934). Finally note that the unique steady state is the equilibrium distribution $g_a^{(0)} + g_d = g_{eq}$. We will use this interpretation as the starting point for the case of a finite applied field where these statements will be reevaluated.

Debye (1942) extended this reasoning to include the effect of the ionic atmosphere and Eigen et al. (1953) treated more general cases when the approach to origin does not lead to a reaction in all cases which is of importance for enzymes and other complex molecules but can be neglected in most electrolytes.

3.2.3.2 Solutions in external field

The following paragraphs cover the solution of the drift-diffusion equation with Coulomb potential superimposed with a linear potential due to the external field. This part forms the centrepiece of Onsager's theory. The approach is similar to the zero-field computation but the mathematical effort is significantly greater. The symmetry of the problem is reduced from spherical to axial. However, Onsager (1934) found

a transform that makes the problem separable in the radial variable r and in the polar variable θ.

Expressed in spherical coordinates, the external field adds $(-Er\cos\theta)$ to the potential yielding the full potential

$$\beta U(r) = -2\ell_T/r - r\cos\theta/\ell_E. \tag{3.16}$$

Because the potential fulfils 3.13 the constant function solves the drift-diffusion equation. The corresponding radial probability current density gains a contribution from the external field

$$S_r = -D\nabla(\beta U) = -2D\left(\frac{\ell_T}{r^2} + \frac{\cos\theta}{\ell_E}\right). \tag{3.17}$$

Integrating over any sphere encompassing the origin yields the same result as we found in equation 3.15. The additional current caused by the external field flows into and out of the integration sphere without influencing the nature of the sink in the origin (see figure 3.6a). This manifests itself during the integration through $\int_0^\pi \cos\theta = 0$. Thus the rate constant corresponding to the association of dissociated ions $g_d(\mathbf{r}) = 1$ remains $k_A = 8\pi(D_+ + D_-)\ell_T/\tilde{V}$.

If the external field is applied the Coulomb gas is driven out of equilibrium. This means that the Boltzman distribution is no longer a physical solution because it diverges at infinity on the right half plane $g_{eq}(r \to \infty, \theta \in [0, \pi/2)) \to \infty$. Thus we cannot use the Boltzmann distribution to construct the solution g_a representing the associated charges. Our task is to find a different solution that fulfils $g_a(r \to \infty) = 0$ and the finite current condition.

After the preliminary analysis, we write the drift-diffusion equation 3.9 and substitute from equation 3.13

$$0 = \nabla\cdot\left(\nabla g + g\nabla(\beta U)\right) \tag{3.18}$$
$$= \Delta g + (\nabla g)\cdot\nabla(\beta U) + \Delta(\beta U) \tag{3.19}$$
$$= \Delta g + (\nabla g)\cdot\nabla(\beta U). \tag{3.20}$$

In spherical coordinates we obtain

$$\left[\frac{1}{r^2}\partial_r(r^2\partial_r g(r,\theta)) + \frac{1}{r^2\sin\theta}\partial_\theta(\sin\theta\,\partial_\theta g(r,\theta))\right] + \tag{3.21}$$
$$\left[\partial_r g(r,\theta)\partial_r(\beta U(r,\theta)) + \partial_\theta g(r,\theta)\partial_\theta(\beta U(r,\theta))\right] = 0. \tag{3.22}$$

The first step in solving the previous equation is to find a transformation which brings it into a Hermitian form. We revisit 3.10 and consider its Hermitian adjoint

$$\left\{\nabla\cdot\left[e^{-\beta U}\nabla\left(ge^{+\beta U}\right)\right]\right\}^\dagger = e^{+\beta U}\nabla\cdot\left[e^{-\beta U}\nabla g\right] = 0. \tag{3.23}$$

It follows that the following operator is Hermitian self-adjoint

$$\mathbb{L}\bullet = e^{+\beta U/2}\nabla\cdot\left[e^{-\beta U}\nabla\left(e^{+\beta U/2}\bullet\right)\right]. \tag{3.24}$$

We now define a new function $f(r,\theta)$

$$g(r,\theta)=f(r,\theta)e^{-\frac{\beta U}{2}}=f(r,\theta)e^{\frac{\ell_T}{r}+\frac{r\cos\theta}{2\ell_E}}, \tag{3.25}$$

which solves $\mathbb{L}f(r,\theta)=0$, i.e.

$$\Delta f-\left[\nabla\left(\frac{\beta U}{2}\right)\right]^2 f+\Delta\left(\frac{\beta U}{2}\right)f=0. \tag{3.26}$$

Using the harmonic property $\Delta(\beta U)=0$ of the potential 3.13 we obtain

$$\Delta f-\left[\nabla\left(\frac{\beta U}{2}\right)\right]^2 f=0. \tag{3.27}$$

The method of transforming the drift-diffusion equation into a Hermitian form is general (Risken, 1996, Ch.6.). It simplifies the analysis of the eigensystem because eigenvalues of a self-adjoint operator are real.

The special property of the Hermitian equation 3.27 in the case of the potential 3.16 is that it is separable in spherical coordinates

$$\frac{1}{r^2}\left[\partial_r(r^2\partial_r)+\frac{\ell_T}{\ell_E}\cos\theta-\frac{r^2}{4\ell_E^2}+\frac{1}{\sin\theta}\partial_\theta(\sin\theta\,\partial_\theta)-\frac{\ell_T^2}{r^2}\right]f(r,\theta)=0, \tag{3.28}$$

which greatly simplifies the analysis. Note that the separability is for instance absent in the case of the screened Debye–Hückel potential or the two dimensional Coulomb potential.

Onsager further introduced the following substitutions

$$\xi=\cos\theta \tag{3.29}$$
$$r=e^w\sqrt{2\ell_T\ell_E} \tag{3.30}$$
$$\zeta(w,\xi)=e^{w/2}f(r,\theta) \tag{3.31}$$
$$b=\ell_T/\ell_E \tag{3.32}$$

to simplify the problem and reformulate it in terms of a single parameter b

$$\left[\partial_{ww}+\partial_\xi\left((1-\xi^2)\partial_\xi\right)+b\xi-b\cosh(2w)-\frac{1}{4}\right]\zeta(w,\xi)=0. \tag{3.33}$$

For the full solution of this equation we refer to Onsager's PhD thesis published in (Hemmer et al., 1996). We give a brief overview of its properties.

The equation 3.33 has four elementary solutions

$$\zeta_1(w,\xi) = \exp\left[\frac{w}{2} - \sqrt{\frac{b}{2}}\left(\xi e^{+w} + e^{-w}\right)\right] \tag{3.34}$$

$$\zeta_2(w,\xi) = \exp\left[\frac{w}{2} + \sqrt{\frac{b}{2}}\left(\xi e^{+w} + e^{-w}\right)\right] \tag{3.35}$$

$$\zeta_3(w,\xi) = \exp\left[-\frac{w}{2} - \sqrt{\frac{b}{2}}\left(\xi e^{-w} + e^{+w}\right)\right] \tag{3.36}$$

$$\zeta_4(w,\xi) = \exp\left[-\frac{w}{2} + \sqrt{\frac{b}{2}}\left(\xi e^{-w} + e^{+w}\right)\right], \tag{3.37}$$

whose form demonstrates the high symmetry of the transformed equation. Transforming the elemetary solutions back yields

$$g_1(r,\theta) = 1 \tag{3.38}$$

$$g_2(r,\theta) = \exp\left(\frac{2\ell_T}{r} - \frac{r\cos\theta}{\ell_E}\right) \tag{3.39}$$

$$g_3(r,\theta) = \frac{\sqrt{2\ell_T\ell_E}}{r}\exp\left[(1-\cos\theta)\left(\frac{\ell_T}{r} - \frac{r}{2\ell_E}\right)\right] \tag{3.40}$$

$$g_4(r,\theta) = \frac{\sqrt{2\ell_T\ell_E}}{r}\exp\left[(1+\cos\theta)\left(\frac{\ell_T}{r} + \frac{r}{2\ell_E}\right)\right]. \tag{3.41}$$

We have already described the first solution as corresponding to fully dissociated charges. The second is the Boltzmann distribution which we have shown to be unphysical out of equilibrium. The two solutions which were not present in the zero field case appear due to the reduction of the symmetry of the problem from spherical to axial. Note that the third solution $g_3(r,\theta)$ is also unphysical as it does not fulfil the finite current condition and the fourth solution $g_4(r,\theta)$ diverges for large r. However, these elementary solutions play a role in constructing the solution that fulfils these conditions.

To complement the elementary solutions, equation 3.33 can be separated into two ordinary differential equations by setting $\zeta(w,\xi) = W(w)\Xi(\xi)$

$$\left[\partial_{ww} - b\cosh(2w) - \frac{1}{4}\right]W_\lambda(w) = \lambda W_\lambda(w) \tag{3.42}$$

$$\left[\partial_\xi\left((1-\xi^2)\partial_\xi\right) + b\xi\right]\Xi_\lambda(\xi) = -\lambda\Xi_\lambda(\xi). \tag{3.43}$$

The separation introduces a parameter λ which has the meaning of an eigenvalue of the differential operators on the left hand side of the equations. The separated equations are also Hermitian self-adjoint; their spectrum is real and bounded from above or below.

We will at this point only give a general description of the procedure that Onsager took to find a general solution of the current problem.

Onsager pointed out that the solutions of the two separated equations are necessarily related by integral transforms with the elementary solutions 3.34 as kernels; he also gave an exhaustive treatise of their properties. Due to the existence of these kernels it is possible to transform W_λ and Ξ_λ into each other. Onsager also found a different transform whose kernel is the Bessel function I_0 which allows the transformation of functions Ξ_λ corresponding to different values of λ to one another, i. e. $\Xi_\lambda \to \Xi_{\lambda'}$. This knowledge can be used to construct a solution in a spherical shell with any quadratically intergrable boundary conditions given on the inner and the outer sphere.

Finding the solution then progresses as follows. The boundary condition is expanded in Ξ_λ which is a function of the transformed angular variable ξ (akin to a multipole expansion in Legendre polynomials). This allows one to find an expansion of $\zeta(w, \xi)$ in Ξ_λ for every value of the transformed radial variable w. The coefficients of the angular expansion which are a function of w can be further expanded as a series of W_λ which can be in turn transformed into Ξ_λ (using $\zeta_3(w, \xi)$ as the kernel). The result is the solution $\zeta(w, \xi)$ expanded as a double series of Ξ_λ. This series is then expressed as an integral using the integral transform within the class of functions Ξ_λ (using the kernel in terms of the Bessel function I_0). For details we refer to the PhD thesis of Onsager as reprinted in (Hemmer et al., 1996).

The final result for the associated ions is

$$g_{\mathrm{a}}^{(E)}(r, \theta) = \mathrm{e}^{-\frac{r}{2\ell_E} + \frac{r\cos\theta}{2\ell_E} + \frac{2\ell_T}{r}} \int_{s=0}^{2\ell_T} I_0\left(\sqrt{\frac{4s}{\ell_E}}\cos\left(\frac{\theta}{2}\right)\right) \frac{\exp\left(-\frac{s}{r}\right)}{r}\mathrm{d}s.$$

(3.44)

Note that for $E = 0$ we recover $g_{\mathrm{a}}(r) = \exp(2l_T/r) - 1$. The function g_{a} yields the probability flux

$$\Phi_{\mathrm{D}}^{(E)} = \int \mathbf{S} \cdot \mathrm{d}\Sigma = 8\pi D\ell_T F(b) = 8\pi(D_+ + D_-)\ell_T \frac{I_1\left(2\sqrt{2\ell_T/\ell_E}\right)}{\sqrt{2\ell_T/\ell_E}}.$$

(3.45)

For the derivation of this specific result we refer to (Mason and McIlroy, 1975) because (Onsager, 1934) only states the result and Onsager's PhD thesis gives a very general method of computing the fluxes. The lower index $_\mathrm{D}$ and the positive sign mean that the flux corresponds to the associated charges dissociating. The dissociation is enhanced by a factor of $F(b)$.

Also note that there is a unique solution for which the fluxes for $g_{\mathrm{a}}^{(E)}$ and g_{d} compensate and the steady state correlation function approaches unity at infinity $g_{\mathrm{ss}}(r \to \infty) = 1$. This solution is given as the linear combination

$$g_{\mathrm{ss}} = g_{\mathrm{d}}/F(b) + g_{\mathrm{a}}.$$

(3.46)

Since we work with correlation functions normalized to unity $g_{\pm} = \langle n_+(0)n_-(r)\rangle / \langle n_+\rangle\langle n_-\rangle$, the prefactor $1/F(b) \leq 1$ for the dissociated part corresponds to an increase in the free charge density by a factor of $\sqrt{F(b)}$. This is only exact as a low density approximation where the two body correlator contains almost all correlations. The true increase in density in more complex situations has to be computed from chemical kinetics.

3.2.3.3 Stream functions

As a final remark we mention an alternative approach. McIlroy and Mason (1987) pointed out that it is not necessary to know g_a to compute Φ_D. Instead they utilise stream functions ψ whose definition is permitted by the continuity equation $\nabla \cdot \mathbf{S} = 0$ (equation 3.9) which can be seen as governing an incompressible flow. The stream function $\psi(r,\theta)$ expresses the flux across a curve spanned by the point (r,θ) and any point $(r > 0, \theta = \pi)$ on the axis going through the origin in the direction antiparallel to the applied field. We consider only curves confined to a single value of azimuthal angle. The flux through the surface of revolution of this curve is $2\pi\psi(r,\theta)$.

It requires less mathematical effort to compute the stream functions than to find the correlation functions. McIlroy and Mason (1987) found

$$\psi_{\mathrm{d}}^{(E)}(r,\theta)/(2\ell_T D) = -(1+\cos\theta)(1+b\,r^2(1-\cos\theta)) \tag{3.47}$$

$$\psi_{\mathrm{a}}^{(E)}(r,\theta)/(2\ell_T D) = \sqrt{\frac{2}{b}}\cos\left(\frac{\theta}{2}\right)I_1\left(2\sqrt{2b}\cos\left(\frac{\theta}{2}\right)\right) \tag{3.48}$$
$$\times \exp(b\,r(\cos\theta - 1))$$

for the dissociated and associated charges, respectively. From the definition of the streamfunction we can directly obtain the total flux

$$\Phi_{\mathrm{A}} = -2\pi\psi_{\mathrm{d}}(r,\theta = 0) = -8\pi\ell_T D \tag{3.49}$$

$$\Phi_{\mathrm{D}}^{(E)} = 2\pi\psi_{\mathrm{a}}(r,\theta = 0) = 8\pi\ell_T D\frac{I_1\left(2\sqrt{2b}\right)}{\sqrt{2b}} \tag{3.50}$$

which is identical to the result obtained previously. Note that the value of r is irrelevant for the result due to the continuity equation but the calculation is the easiest for $r = 0$.

The curves along which the stream functions are constant form the stream lines of the flux. The derivatives of the stream functions give the local flux density which is the probability current density S multiplied by the surface element $r^2\sin\theta$. We can thus also extract the probability current from the stream functions as well. Visualizations of both types of stream lines are obtained more readily than the correlation functions and allow us to discuss several features of the Wien effect later on. The
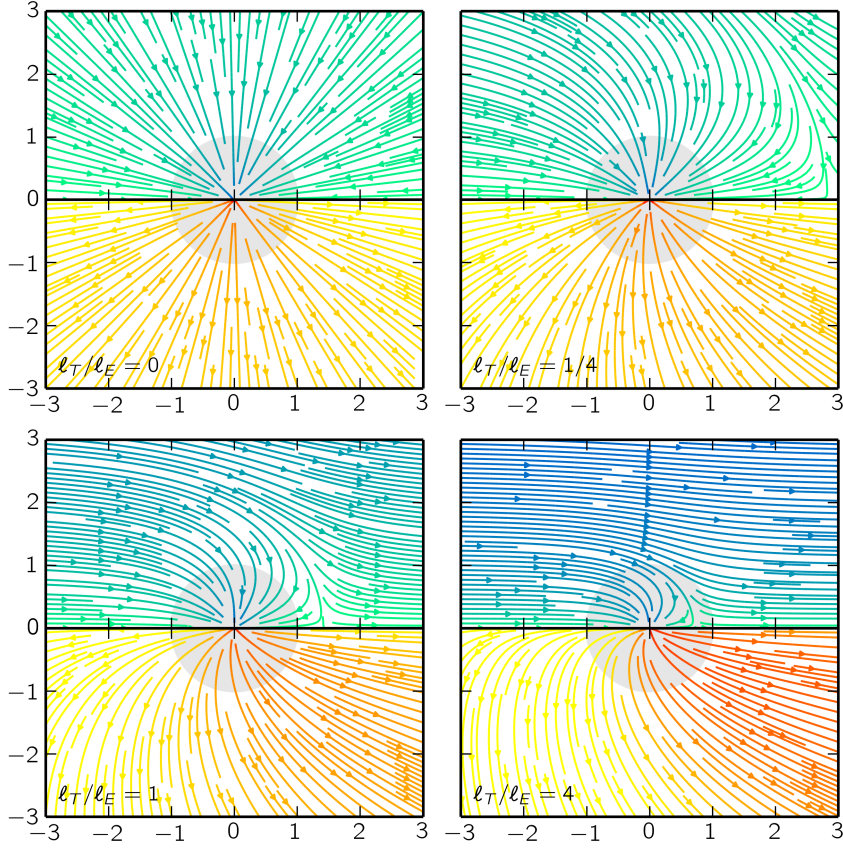
(a) Streamlines of the probability flux.
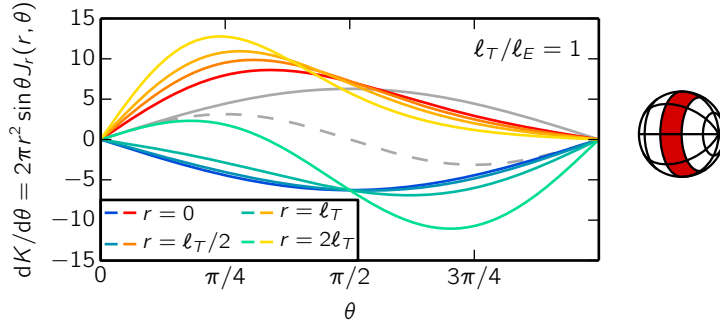
(b) Polar angle resolved probability flux.

Figure 3.5: **Wien effect – probability flux. a)** The stream lines of the probability flux which represent the contribution to the association and the dissociation flux at a given ion separation r and angle θ. The upper panels of each plot show the association flux of the dissociated ions $\psi_d^{(E)}$ and the lower show the dissociation flux of the associated ions $\psi_a^{(E)}$. As the solution is axially symmetric we only show a single half-plane. The lengths are given in units of the Bjerrum length ℓ_T (shown as a grey circle). **b)** The polar angle θ resolved association (cold colors, mostly negative) and dissociation (warm colors, positive) fluxes in units $2\ell_T D$. The largest contribution to the dissociation occurs under a finite angle with the field. We observe that the association flux changes in nature from a radial approach to a flow along the applied field. The full grey line corresponds to the radial dissociation in equilibrium while the dashed grey line corresponds to a constant flow along the field direction.
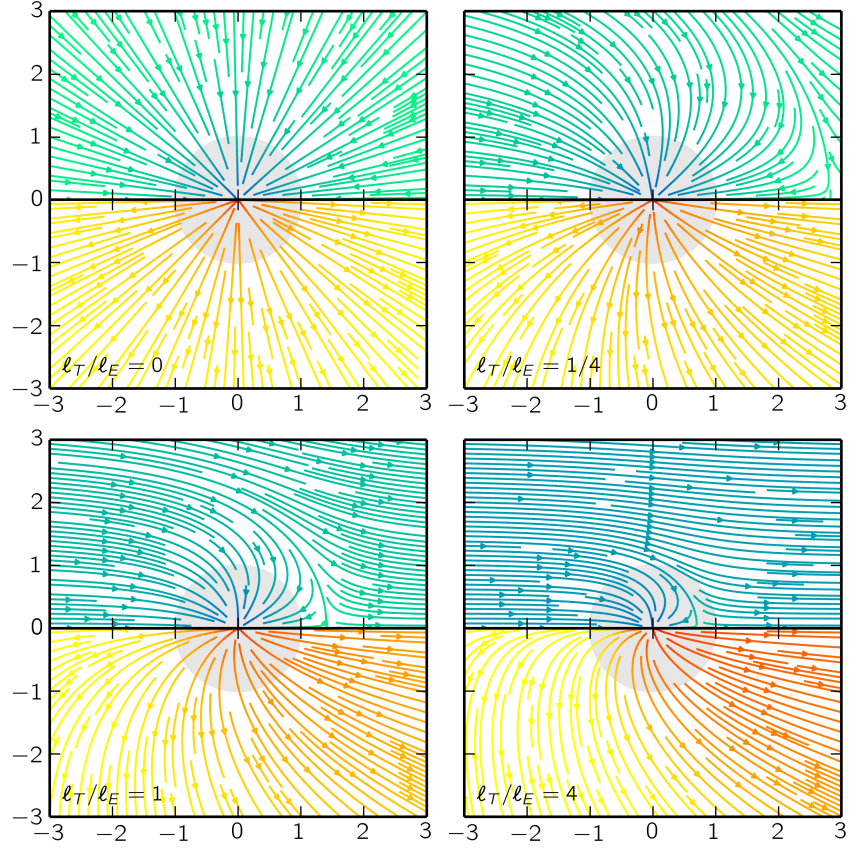
(a) Streamlines of the probability current density.
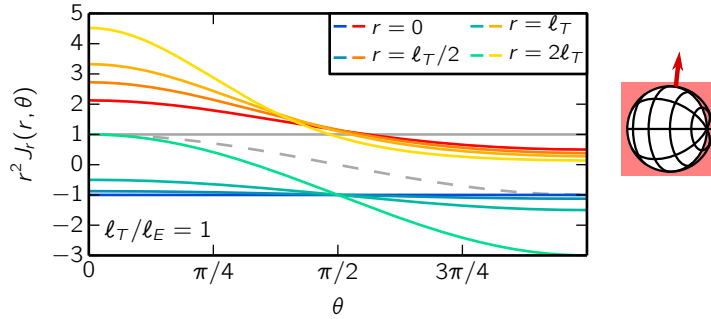
(b) Angular dependence of the radial part S_r of the probability current density.

Figure 3.6: **Wien effect – probability current density. a)** The stream lines of the probability current density **S**. The upper panels of each plot show the current related to the dissociated ion solution g_{d} (which associates) and the current related to the associated ion solution $g_{\mathrm{a}}^{(E)}$ (which dissociates). As the solution is axially symmetric we only show a single half-plane. The lengths are given in units of the Bjerrum length ℓ_T (shown as a grey circle). **b)** The angular dependence of the radial part of the current $S_r(r, \theta)$ corresponding to the dissociated solution g_{d} (cold colors, mostly negative) and the associated solution $g_{\mathrm{a}}^{(E)}$ (warm colors, positive). The current is normalized to unity for the zero field solution (full grey line). The current corresponding to $g_{\mathrm{a}}^{(E)}$ is the strongest parallel to the applied field ($\theta = 0$). The current corresponding to g_{d} behaves exactly as the zero field solution for $r = 0$. At larger diameters it develops a strong contribution from charges which flow without associating (grey dashed line).

stream lines only describe the average motion of ions unlike the more familiar situation in hydrodynamics where the motion is deterministic.

We plot the stream lines of flux in figure 3.5 and of the current in figure 3.6. Because the stream lines of flux include the surface element figure 3.5 answers which directions contribute the most to the total dissociation constant. On the other hand, figure 3.6 shows along which curves the dissociation happens the fastest. The current is the strongest in the direction parallel to the applied field whereas the largest contribution to the dissociation is under a finite angle with the field direction. The dark red and dark blue lines correspond to the highest values.

We also show the flux and the radial part of the current for several values of r on the bottom panels of both figures. The dissociated ions (ψ_d) show two types of behaviour as the radius grows. A part of the initial conditions leads to the association which resembles the solution with no applied field at short distances. For the remaining part of the initial separation vectors the association is impossible and the charges separate to infinity. The minimal distance from the origin that separates the two types of behaviour decreases with increasing field. Eventually it becomes less than the Bjerrum length ℓ_T which shows that the equilibrium definition of free and bound charges loses its validity at high fields. The associated ions (ψ_a) keep escaping in a wedge whose width decreases with increasing distance between the charges.

The streamfunctions ψ_d and $\psi_a^{(E)}$ describe two idealized solutions corresponding to a sink and a source at the origin. The zero total flux solution $g_{ss} = g_d/F(b) + g_a$ has streamlines that go from the left infinity ($\theta \in [\pi, \pi/2)$) to the right infinity $\theta \in [0, \pi/2)$ and get perturbed by the Coulomb potential (see figure 3.7). This shows the out of equilibrium nature of the second Wien effect. The effect of the Coulomb potential on the flow that enhances the dissociation could be described as a Coulombic pump or a diffusive analogue of the gravitational slingshot (Barger, 1994).

3.2.4 Physical interpretation of the solution

In the previous section we have identified the correlation function for a pair of completely dissociated charges $g_d = 1$ which is independent of the applied field. We have also found the correlation function for an associated pair

$$g_a^{(E)}(r,\theta) = e^{-\frac{r}{2\ell_E} + \frac{r\cos\theta}{2\ell_E} + \frac{2\ell_T}{r}} \int_{s=0}^{2\ell_T} I_0\left(\sqrt{\frac{4s}{\ell_E}}\cos\left(\frac{\theta}{2}\right)\right) \frac{\exp\left(-\frac{s}{r}\right)}{r} ds.$$

(3.51)

(a) Streamlines of the probability flux.

(b) Streamlines of the probability current.
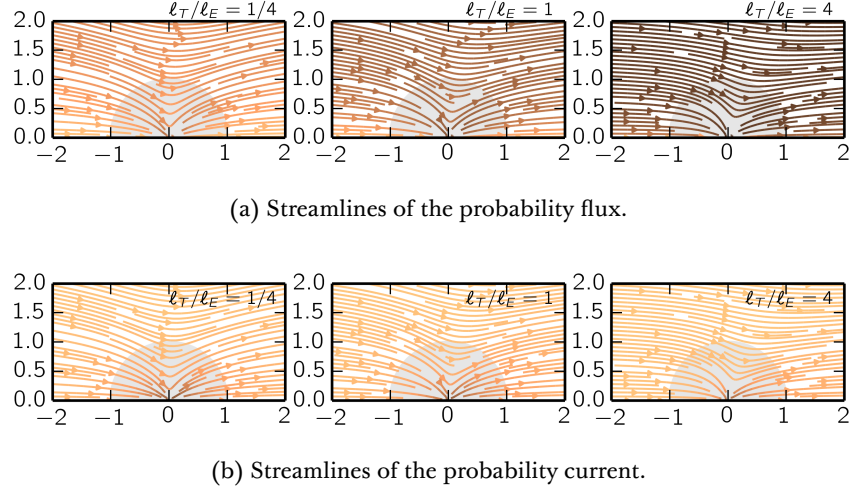
Figure 3.7: **Wien effect – stream lines of the steady state solution.** The solutions of the drift-diffusion equation can be combined to obtain a solution that has zero flux through any closed surface. In the absence of the Coulomb potential the flow would consist of parallel stream lines in the field direction. The Coulomb potential deforms these stream lines. There is no sink at the origin. Instead the stream lines form a bow tie flow pattern. Figure **a)** shows the probability flux and **b)** the probability current density. The length unit is the Bjerrum length ℓ_T. Darker colours correspond to a larger magnitude of vectors tangent to the stream lines.

This solution connects to the zero field solution $g_a^{(0)}(r) = \exp(2l_T/r) - 1$. We have also shown that the corresponding fluxes – the association flux Φ_A of g_d and the dissociation flux Φ_D of g_a – are

$$\Phi_A = -8\pi\ell_T D \tag{3.52}$$

$$\Phi_D^{(E)} = 8\pi\ell_T D \frac{I_1\left(2\sqrt{2\ell_T/\ell_E}\right)}{\sqrt{2\ell_T/\ell_E}} \tag{3.53}$$

In equilibrium the fluxes compensate. In the applied field, the dissociation flux and rate constant are enhanced by the factor

$$\frac{\Phi_D^{(E)}}{\Phi_D^{(0)}} = \frac{k_D(E)}{k_D(0)} = F(\ell_T/\ell_E) = \frac{I_1\left(2\sqrt{2\ell_T/\ell_E}\right)}{\sqrt{2\ell_T/\ell_E}}. \tag{3.54}$$

Note that F is a function of a single parameter $b = \ell_T/\ell_E$. The dissociation equilibrium constant K_D is defined as the ratio between the dissociation rate constant k_D and the association rate constant k_A. The prediction for the increase in the dissociation equilibrium constant is the main result of our analysis

$$\frac{K_D(E)}{K_D(0)} = F(\ell_T/\ell_E) = 1 + \frac{\ell_T}{\ell_E} + \frac{1}{3}\left(\frac{\ell_T}{\ell_E}\right)^2 + \mathcal{O}\left(\left(\frac{\ell_T}{\ell_E}\right)^3\right). \tag{3.55}$$

As $\ell_E \propto E$, the initial increase is linear with the field. It is interesting that this function is neither odd nor even and contains both even and odd powers of the field. At very high fields, the Onsager function F has the following asymptotic behaviour

$$F(\ell_T/\ell_E) = \left(\frac{2}{\pi}\right)^{\frac{1}{2}} \left(\frac{8\ell_T}{\ell_E}\right)^{-\frac{3}{4}} \exp\left(\left(\frac{8\ell_T}{\ell_E}\right)^{\frac{1}{2}}\right) \left(1 - \frac{3}{8\left(\frac{8\ell_T}{\ell_E}\right)^{\frac{1}{2}}} + \mathcal{O}\left(\frac{1}{\left(\frac{\ell_T}{\ell_E}\right)}\right)\right),$$

(3.56)

i. e. the dissociation equilibrium constant grows rapidly as an exponential of the square root of the field.

3.2.5 Shift in the chemical equilibrium

Having obtained the dissociation equilibrium constant $K_D(E) = k_D(E)/k_A$ we now discuss its influence on the densities of bound and free charges. We will consider a general case of the double equilibrium

$$\text{charge source } (n_s) \underset{k_{an}}{\overset{k_{cr}}{\rightleftharpoons}} \text{bound pairs } (n_b) \underset{k_A}{\overset{k_D(E)}{\rightleftharpoons}} \text{free charges } (n_f)$$
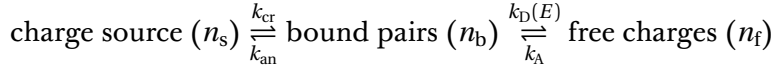
with the normalization condition $n_s + n_b + n_f = 1$ for the number densities. We work in the dilute limit where $n_f \ll n_s$, $n_b \ll n_s$, and $n_s \simeq 1$. The charge source represents the undissociated molecules in case of electrolytes and the more complex charge vacua of solid state systems. We treat the charge creation k_{cr} and annihilation k_{an} rate constants as field independent and consider a process that creates a pair of charges bound at the closest distance. Each pair comprises two bound charges yielding $n_p = n_b/2$ for the bound pair density. The first equilibrium has generally first order kinetics with the creation equilibrium constant K_{cr}

$$n_p = \frac{n_b}{2} = \frac{k_{cr}}{k_{an}} n_s = K_{cr} n_s. \tag{3.57}$$

In most systems the rates of this equilibrium are much faster than those of the subsequent equilibrium $k_{cr}, k_{an} \gg k_A, k_D(E)$. This picture breaks down at very high fields and leads to a saturation of the Wien effect. The second equilibrium is second order in the free charges and first order in the bound charges

$$n_+ n_- = \left(\frac{n_f}{2}\right)^2 = K_D(E) n_p = K_D(E)\frac{n_b}{2} \tag{3.58}$$

$$\text{i. e.} \quad n_f^2 = 2K_D(E)n_b, \tag{3.59}$$

where $n_+ = n_- = n_f/2$ are the positive and negative charge densities. In the following, we present a solution of the equilibrium. We show that

to obtain the increase in free charge density, it is sufficient to consider a single equilibrium. However, solving the double equilibrium reveals an interesting prediction that the bound charge density in almost unaffected by the electric field.

3.2.5.1 Simple equilibrium

We first calculate how the Wien effect influences the chemical equilibrium if the total number of charges $n_f + n_b$ were fixed. This is a simpler calculation than the solution for the double equilibrium, and its result is a relevant limit of the full solution. The double equilibrium can be reduced to a single equilibrium if we are only interested in the free charge density increase. This is the case for conductivity measurements that only measure the contribution of free charges. We can then consider the neutral molecules or the charge background as a special case of bound charges and define $n_b' = n_b + n_s = 1 - n_f$. This is a reasonable approximation if the first equilibrium is much faster than the second. The mass-action law then takes on the form

$$n_f(E)^2 = 2K_D(E)(1 - n_f(E)), \tag{3.60}$$

which is solved by

$$n_f(E) = \sqrt{K_D^2(E) + 2K_D(E)} - K_D. \tag{3.61}$$

We expand in the two extreme cases. First, in the strong association $(n_f \ll 1, K_D \to 0)$ limit we obtain

$$n_f(E) = \sqrt{2K_D(E)} + \mathcal{O}(K_D(E)), \tag{3.62}$$

which yields the relative change

$$\frac{n_f(E)}{n_f(0)} = \sqrt{\frac{K_D(E)}{K_D(0)}} = \sqrt{F(b)} = 1 + \frac{b}{2} + \frac{b^2}{24} + \mathcal{O}(b^3). \tag{3.63}$$

The associated fraction stays close to unity $n_b'(E) \simeq n_b'(0)$.

In the opposite almost completely dissociated limit $(n_f \simeq 1, K_D \to \infty)$ we have

$$n_f(E) = 1 - \frac{1}{2K_D(E)} + \mathcal{O}(K_D(E)^{-2}) \tag{3.64}$$

with the relative change

$$\frac{n_f(E)}{n_f(0)} = 1 - \frac{1 - n_f(0)}{K_D(E)/K_D(0)} = 1 - \frac{1 - n_f(0)}{F(b)}. \tag{3.65}$$

The Wien effect is thus much weaker if most of the charges are already dissociated with its influence being proporional to the remaining associated density $1 - n_f$.

In the following we show that the results obtained for the increase in the free charge density n_f in single equilibrium are relevant for the double equilibrium as well. However, the bound charge density does not decrease but it stays to a good approximation constant as it is replenished from the charge source.

3.2.5.2 Double equilibrium

In our simulations we measure the total charge density $n_\text{tot} = n_\text{f} + n_\text{b}$ which we then separate into the two charge types using correlation functions. Therefore it is necessary to obtain a prediction for both the free and the bound part of the density. We will once more obtain $n_\text{f}(E)/n_\text{f}(0) = \sqrt{K_\text{D}(E)/K_\text{D}(0)}$ in the dissociated limit but we are now also interested in the separate behaviour of the bound charge density n_b as well. The chemical kinetic equations are

$$n_\text{b}(E) = 2K_\text{cr}(1 - n_\text{b}(E) - n_\text{f}(E)) \tag{3.66}$$

$$n_\text{f}^2(E) = 2K_\text{D}(E)n_\text{b}. \tag{3.67}$$

We can solve this system of equations separately in zero field and finite field and compare the results to obtain the relative change in both densities

$$\frac{n_\text{f}(E)}{n_\text{f}(0)} = \frac{\sqrt{[n_\text{f}(0)F(b)]^2 - 4n_\text{f}(0)F(b) + 4F(b)} - n_\text{f}(0)F(b)}{2(1 - n_\text{f}(0))} \tag{3.68}$$

$$\simeq \sqrt{F(b)}\left[1 - \frac{1}{2}\left(\sqrt{F(b)} - 1\right)n_\text{f}(0)\right] + \mathcal{O}\left(n_\text{f}^2(0)\right) \tag{3.69}$$

$$\frac{n_\text{b}(E)}{n_\text{b}(0)} = \frac{2 + n_\text{f}^2(0)F(b) - n_\text{f}(0)\sqrt{[n_\text{f}(0)F(b)]^2 - 4n_\text{f}(0)F(b) + 4F(b)}}{2(1 - n_\text{f}(0))^2} \tag{3.70}$$

$$\simeq 1 - \left(\sqrt{F(b)} - 1\right)n_\text{f}(0) + \mathcal{O}\left(n_\text{f}^2(0)\right) \tag{3.71}$$

where we expanded in the limit $n_\text{b} \ll n_\text{f} \ll 1$ which is relevant for both weak electrolytes and our simulations. The free charge density increases as $n_\text{f}(E)/n_\text{f}(0) = \sqrt{F(b)}$ as in the case of the simple equilibrium. The bound charge density stays constant $n_\text{b}(E)/n_\text{b}(0) = 1$. The corrections are proportional to the zero field free density $n_\text{f}(0)$ and the function $\sqrt{F(b)} - 1 \simeq b$ which is approximately linear in field.

We call the independence of n_b on field the *buffering* of the bound charges. Any decrease in bound charges due to the generation of new free charges is immediately replenished from the charge source (molecules or vacuum). The calculation we have presented uses equilibrium chemical kinetics. The Wien effect is however an intrinsically non-equilibrium process. Thus the actual rate constants whose ratio gives the equilibrium constants matter. The actual rates of transformation

between the charge source and bound pairs have to be faster than the
rates involving exchange between free and bound charges for the buf-
fering hypothesis to hold. We discuss the influence of the length separ-
ating the free and bound charges below.

3.2.5.3 Non-ideal behaviour

The solutions of the equilibria are also valid in the case of some
of the species being non-ideal if their densities are replaced by the
corresponding activities. It is useful to express the activity as a product
of the density n_x and the activity coefficient γ_x. We consider only the
deviations from non-ideality of the free charges which we treat within
the scope of the Bjerrum—Debye–Hückel theory (see section 2.3.2).
We use $\gamma \leq 1$ to describe the free charge activity coefficient and treat
the bound pairs as uninfluenced by interactions ($\gamma_b = 1$). The modified
mass action law reads

$$\gamma^2 n_f^2(E) = 2K_D(E)n_b .\tag{3.72}$$

The Wien effect is influenced by this substitution because the internal
correlations of free charges are swept away by strong fields, i. e. $\gamma(E) = 1$.
The relative increase of density is decreased by a factor $\gamma(0)$ from the
ideal value

$$\frac{n_f(E)}{n_f(0)} = \frac{\gamma(0)}{\gamma(E)}\sqrt{\frac{K_D(E)}{K_D(0)}} = \gamma(0)\sqrt{F(b)}.\tag{3.73}$$

Equally one might keep the mass action law in the form involving
only densities and absorb the activity coefficent into the equilibrium
constant to introduce the concentration quotient (also called the stoi-
chiometric constant) for the dissociation as

$$\mathscr{K}_D = K_D/\gamma^2 = \frac{n_f^2}{2n_b} .\tag{3.74}$$

The concentration quotient has the advantage of being directly access-
ible to our simulations.

3.3 Numerical simulations of the second Wien effect

Lattice Coulomb gas simulations are particularly useful for explor-
ing the physics of the second Wien effect. The lattice Coulomb gas is
very versatile due to the tunability of parameters that allows us to ex-
plore regimes which otherwise correspond to very different materials.
It is also a very clean system avoiding the necessity to treat details of the
solvent dynamics. Despite these benefits, no previous numerical simu-
lations of the Wien effect have been conducted. This seems to be due

to the necessity to simulate large out-of-equilibrium long-range interacting systems at low densities.

We performed numerical simulations for a range of parameters. In this section we show selected results to demonstrate agreement with, limits of, and corrections to Onsager's theory. The grandcanonical ensemble is best suited for simulating the second Wien effect because it allows varying the particle number. We use the Metropolis Monte Carlo algorithm to propagate our system. This algorithm is in a strict sense designed to stochastically integrate partition sums in equilibrium. However if all moves are local, it can be also interpreted as generating stochastic dynamics for the charges. We take care to interpret the role of the time in simulations which can be seen as being scaled by the acceptance probability. The long-range interactions are treated using the Ewald summation. Details of the algorithms are given in section 2.6.

We chose to work on the diamond lattice because it describes the sites available for magnetic monopoles in spin ice and it is equally relevant for water ice. The diamond lattice has cubic symmetry which allows one to treat the diffusion constant tensor as a single scalar which means that Onsager's theory is the correct continous limit. However, the four-fold connectivity of the diamond lattice is the lowest possible in three dimensions and as such it is quite far from the continuous limit. Despite this, we will see that it can be used to successfully simulate the second Wien effect.

The simulation protocol is as follows. The lattice gas is first equilibrated in zero field at the given temperature. Afterwards a constant field is switched along the [100] direction of the diamond lattice. We wait until the system reaches a steady state and measure the relevant quantities. The zero-field quantities are obtained from simulations of equal length with no field applied. The number of zero-field samples is larger than the number of the finite field samples because they serve as a reference point for calculating the relative changes of observables. The lowest achievable densities in our simulations are of the order of 10^{-5}. We will however present results from somewhat higher densities which have a better signal-to-noise ratio.

We measure two macroscopic observables – charge density and conductivity – complemented with the microscopic pair correlation functions. The field dependence of charge mobility can be found by dividing the conductivity by the charge density. The pair correlation functions allow one to compute the association concentration quotient $\mathcal{K}_A$ by integrating over the volume assigned to the bound charges (usually $r < \ell_T$). The concentration quotient is the apparent equilibrium constant which we use for a direct comparison with Onsager's prediction. We also use it to separate the observed charge density into the free and bound charge contributions.

First we will discuss the charge density. We highlight the role of activity coefficients for correct comparison of theory and experiment or simulations. This leads to the question of the screening which dominates the equilibrium correlations of the Coulomb gas and as such it influences the Wien effect as well. The following part of the results shows how the conductivity is influenced by the field-dependent mobility stemming from the Coulomb interactions and the stochastic dynamics we impose in the simulations. In the final part we discuss the pair correlation functions. We show how the dissociation constant can be obtained from the correlation functions although a direct comparison with Onsager's solution for the correlation functions is precluded by the lattice discreteness at smallest distances where the exact solution possesses most features.
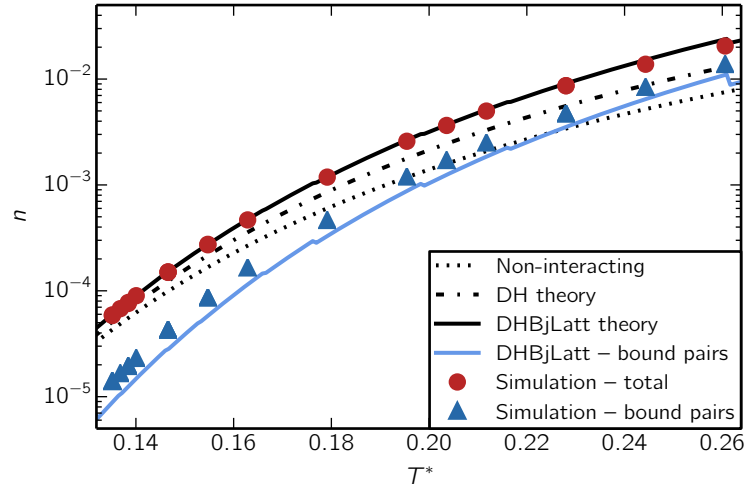
Figure 3.8: **Equilibrium density.** The temperature dependence of the zero field density for $\nu_0^* = -1.45$. In the grand canonical ensemble, the temperature strongly influences the density. The total density has contributions from free and bound charges. We use the Bjerrum—Debye–Hückel theory to treat the pairing and the non-ideality of free charges. Its details are extensively discussed in the previous chapter. In the following figures we show the Wien effect at $T^* = 0.140$ and $T^* = 0.212$ whose density differs by more than one order of magnitude.

3.3.1 Density increase

The charge density is the macroscopic observable which is the most closely connected to the second Wien effect. Unlike the situation in real experimentals, the density of a simulated lattice Coulomb gas is easily computed. Before we deal with the field induced increase in
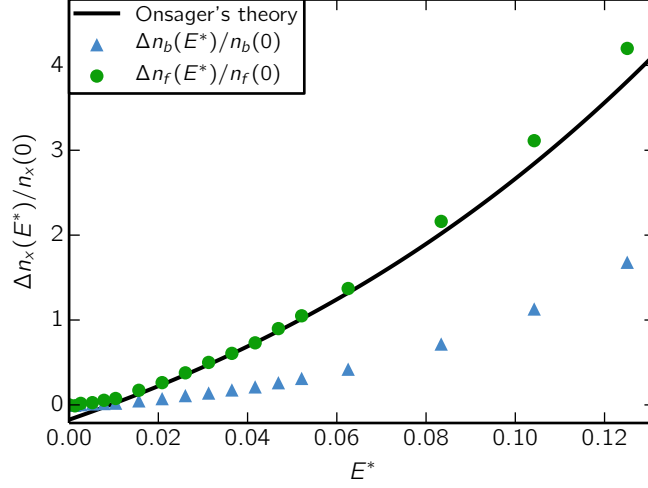
Figure 3.9: **Density increase – low density.** Lattice Coulomb gas simulation at $\nu_0^* = -1.45$ and $T^* = 0.140$. The free charge density (green) increase follows Onsager's theory. The negative offset is due to Debye screening whose destruction lowers the density thus weakly counteracting the Wien effect. Above $E^* \simeq 6 \times 10^{-3}$ the data follows the theoretical curve. The reduced field $E^* = U_E(a)/U_C(a)$ compares the energy gain by a charge hopping to a neighbouring site in field $U_E(a)$ with the nearest neighbour Coulomb interaction $U_C(a)$. Even if the Coulomb interaction dominates tenfold ($E^* = 0.1$) the field quadruples the density. The bound charge density (blue) stays buffered up to $E^* \simeq 0.04$. It increases afterwards because the equilibrium definition separating the free and bound charges is no longer fully longer valid. The total charge density (not shown) increases similarly to the free charge density. The zero field densities are $n_f(0) = 7.8 \times 10^{-5}$ and $n_b(0) = 1.1 \times 10^{-5}$.

the density, we first revisit the equilibrium results for density in figure 3.9. We can see that the simulation is tunable to obtain the zero field density which varies over orders of magnitude. In the region of interest the equilibrium density can be computed from the Bjerrum—Debye–Hückel theory which treats the screening of the free charges and their equilibrium with the bound charges. The tunability of the simulations allows us to compare with the exactly solvable limits but also see what happens as we depart from them. The related temperature evolution of length scales is presented in 3.1. We would also like to refer to figure 3.2 for our estimates of ν_0^* and T^* for various materials.

Throughout this section we use the reduced variables defined in section 2.1.1. We define reduced temperature as $T^* = k_B T / U_C(a)$, reduced chemical potential as $\nu_0^* = \nu / U_C(a)$, and the reduced field as $E^* = Q_e \mathbf{E} \cdot \mathbf{a} / U_C(a)$. We choose the Coulomb energy at contact $U_C(a) = Q_e^2 / 4\pi\epsilon a$ as the reference energy scale because it suitable to describing

the lattice Coulomb gas simulations. Onsager's parameter is conveniently expressed as $b = E^*/[2(T^*)^2]$.

3.3.1.1 Validity of Onsager's theory

The density increase in the low density limit is shown in the figure 3.9. The results confirm Onsager's theory for the second Wien effect and constitute its first numerical verification. The theory derived in a continuum shows no significant deviations due to the discreteness of the lattice. The free charge density increases significantly as the field is increased. We observe the linear law followed by the upturn due to the higher order terms. The bound charge density is buffered in low fields and increases in high fields but significantly less than the free charge density. As the total charge population is mostly composed of free charges, the total number of charges increases significantly.

The Debye screening is significant even at these low densities but is destroyed already in very low fields by the flow of the charges. Thus the effect of screening is almost completely described by the equilibrium activity coefficient $\gamma(0)$ of the free charges. We then make the approximation that the screening disappears in a finite field (formally $\gamma(E) = 1$). From the mass action law prediction 3.73 we obtain

$$\Delta n_{\mathrm{f}}(E)/n_{\mathrm{f}}(0) = \gamma(0)\sqrt{F(b)} - 1 \simeq \frac{\gamma(0)b}{2} \tag{3.75}$$

for comparison with the data. The screening decreases the slope of the linear law and leads to a negative point of intersection with the vertical axis. This is caused because the correlations in equilibrium permit the accomodation of a larger population than an uncorrelated gas would have. Removal of this excess population counteracts the second Wien effect. This correction was already considered in the original article (Onsager, 1934) and manifests itself in most experimental measurements shown in figure 3.3.

There is a small window of essentially Ohmic behaviour before the Wien effect occurs. The field above which the screening vanishes can be estimated by setting $\ell_E \simeq \ell_{\mathrm{D}}$ because the field length can be interpreted as the distance over which the field needs to act to influence the correlations in the system (see figure 3.11).

3.3.1.2 Role of the ionic atmosphere

We have already seen that the screening reduces the Wien effect and that it ensures Ohmic behaviour at the lowest fields. Its role becomes stronger as the density increases. Figure 3.10 shows the typical behaviour at high densities. The Debye length ℓ_{D} is comparable to the Bjerrum length ℓ_T thus the role of screening is strong. The initial increase
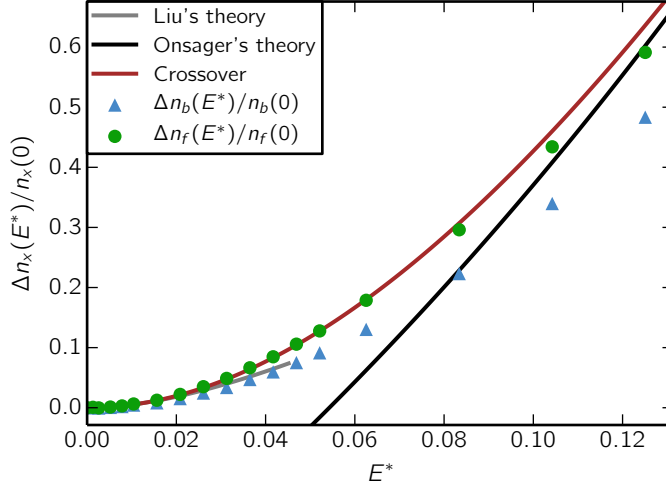
Figure 3.10: **Density increase – crossover to screening at high density.** Lattice Coulomb gas simulation at $v_0^* = -1.45$ and $T^* = 0.212$. As the density increases the screening length ℓ_D decreases. The parameters for this figure yield $\ell_T/\ell_D \simeq 1$ which is the perturbative parameter of Debye–Hückel theory. Therefore the linear regime of the Wien effect is completely screened and the higher order unscreened expression is first approached at high fields.

Liu's theory of diffusion in the Debye potential (grey line) describes the low field behaviour and Onsager's unscreened expression (black line) is approached in high fields (diffusion in the Coulomb potential). The crossover is well characterised by a phenomenological theory (red line) that extends the activity coefficient out of equilibrium to describe the decay of the ionic atmosphere in applied field (equation 3.88).

The computed zero field densities are $n_f(0) = 1.24 \times 10^{-3}$ and $n_b(0) = 1.25 \times 10^{-3}$. The bound charge density is computed from the pair correlation functions which leads to an overestimate at higher densities.

is quadratic at first and then at relatively high fields we obtain a crossover to the unscreened behaviour. The increase in temperature from $T^* = 0.140$ in figure 3.9 to $T^* = 0.212$ in figure 3.10 should lead to a reduction of the effect to roughly a half according to the unscreened theory. However, the observed decrease is approximately eightfold due to the enhanced screening. Moreover, the distinction in behaviour of the bound and free charges starts to disappear as the mean charge separation approaches the Bjerrum length ℓ_T. The charges approach each other more often due to the random motion instead of the Coulomb attraction.

Describing the influence of screening on the Wien effect theoretically is not straightforward. The unscreened Wien effect is well described
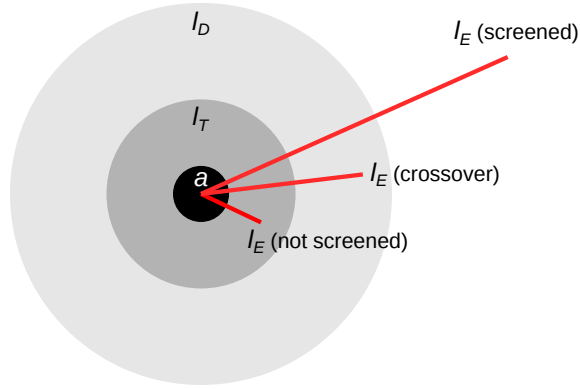
Figure 3.11: **Length scales describing the screening of the second Wien effect.** At low fields ($\ell_E \gg \ell_D$) the charges effectively interact with the screened potential and the screened theory by Liu describes the increase in charge density. At high fields ($\ell_E \ll \ell_D$) the screening is destroyed and Onsager's theory holds. A crossover behaviour occurs if the field requires leverage over a length ℓ_E, similar to the screening length ℓ_D, to modify the charge distribution. As neither of the two previous theories describes it in full, we present a phenomenological treatment of the crossover using the non-equilibrium activity coefficient $\gamma(E)$.

by the stochastic dynamics of two charges. The screening on the other hand is a collective phenomenon which is described by the Debye–Hückel theory only at the mean-field level. A full treatment of the screened Wien effect would require an exact treatment of at least three-body dynamics which we do not find conducive to the admission of exact solutions.

It is however possible to theoretically describe the low and high field limit independently. We have already given the high field limit. At low fields the length ℓ_E over which the field has to gain leverage is much larger than the Debye screening length ℓ_D. This means that we can use the Debye–Hückel potential to describe the interaction between two charges as it is not going to be strongly perturbed from its equilibrium form. The charges will experience an influence of many other charges during the association and dissociation. This further justifies the use of the mean-field Debye–Hückel theory. A perturbative treatment of two charge diffusion in the Debye potential can be found in the PhD thesis of Liu (1965)[4]. The result matches well the screened Wien effect enhancement of protolysis in aqueous 2,6-dinitrophenol and methemoglobin (Bräunig et al., 1987). We present this theory in the next subsection. The crossover between the low field and high field limit is the most

---

4 Liu's PhD thesis under Onsager's supervision was never published. It is interesting to note the 30 year gap after the original Wien effect theory.

challenging. We find a phenomenological description of the crossover below that well matches the simulation results.

3.3.1.3 Liu's theory

Liu's method expresses the correlation function $g_\pm(r)$ as a series of functions with powers of the Bjerrum length as prefactors. This is a weak coupling expansion since the Bjerrum length expresses the strength of the Coulomb potential in comparison with the average thermal energy. Using standard perturbation theory, Liu substituted the functional series in the drift-diffusion equation which converts it into a hierarchy of equations for individual orders of perturbation. Liu gives results for the first order in the Fourier picture. The functions do not have a form suitable for the inverse Fourier transform. Therefore, it is not possible to compute the dissociation constant from the probability flux in the same fashion as in the solution without screening.

However, it is possible to find the limiting value $g_\pm^E(0)$ at the central ion. One can now assume that the correlation function in an infinitesimal neighbourhood of the origin behaves in a similar fashion

$$\frac{g_\pm^E(|r| < \varepsilon)}{g_\pm^0(|r| < \varepsilon)} = \frac{g_\pm^E(r=0)}{g_\pm^0(r=0)} .$$

(3.76)

The association constant can be defined as $K_A = \int g_\pm \, dV_{Bj}$ where the Bjerrum volume V_{Bj} is a sphere with the diameter of the Bjerrum length ℓ_T (or a pairing length in another equilibrium theory). Therefore, we can further approximate and use the behaviour of the correlation function at the origin to describe the change in the association constant, i. e. we take $\varepsilon = \ell_T$ in 3.76. The dissociation constant is the inverse of the association constant yielding the relative increase

$$\frac{K_D(E)}{K_D(0)} = \frac{K_A(0)}{K_A(E)} \simeq \frac{g_\pm^0(r=0)}{g_\pm^E(r=0)} .$$

(3.77)

This approximation is justified by the fact that the largest contribution to the association constant comes from ion pairs with small separations (as discussed in figure 2.3).

For the Debye-Hückel potential, Liu gives the first order result

$$\frac{K_D(E)}{K_D(0)} = 1 + \frac{\ell_T}{\ell_E} + \frac{2\ell_T}{\ell_D} f_L\left(\frac{\ell_D}{\ell_E}\right) + \mathcal{O}\left(\left(\frac{\ell_T}{\ell_E}\right)^2\right),$$

(3.78)

$$\text{where } f_L(x) = \frac{\ln(1+x)}{x} .$$

(3.79)

Note that this formula captures the approach only to the order of the linear term ℓ_T/ℓ_E of the Wien effect. Again it is necessary to take into account the equilibrium activity. In the same order of approximation,

the Bjerrum—Debye–Hückel activity coefficient is $\gamma = \exp(-\ell_T/(\ell_T + \ell_D/\sqrt{\alpha})) \simeq 1 - \ell_T/\ell_D$. The concentration quotient (defined in equation 3.74) can be expressed as

$$\frac{\mathscr{K}_D(E)}{\mathscr{K}_D(0)} = \frac{1}{\gamma^2(0)} \frac{K_D(E)}{K_D(0)} \simeq \frac{1 + \frac{\ell_T}{\ell_E} + \frac{2\ell_T}{\ell_D} f_L\left(\frac{\ell_D}{\ell_E}\right)}{1 + \frac{2\ell_T}{\ell_D}}. \tag{3.80}$$

Using the expansion $\sqrt{1+x} \simeq 1 + x/2$, Liu gives the predicted density increase in the following form

$$\frac{n_f(E)}{n_f(0)} \simeq \sqrt{\frac{\mathscr{K}_D(E)}{\mathscr{K}_D(0)}} = \frac{1}{\gamma(0)}\sqrt{\frac{K_D(E)}{K_D(0)}} = \frac{1 + \frac{\ell_T}{2\ell_E} + \frac{\ell_T}{\ell_D} f_L\left(\frac{\ell_D}{\ell_E}\right)}{1 + \frac{\ell_T}{\ell_D}}. \tag{3.81}$$

As evidenced by the figure 3.10, Liu's theory works well as a low field limit of the screened Wien effect.

The Fourier picture approach also allowed Liu to use the more advanced Onsager–Kim potential (Onsager and Kim, 1957). The result requires replacing f_L with a more complex function. On the scale of our plots the two predictions are indistinguishable.

We would also like to mention the theory of McIlroy and Mason (1976) for the screening which effectively assigns a leverage of ℓ_D to the external field leading to a prediction $\Delta n_f(E)/n_f(0) \propto (\ell_D/\ell_E)^2$. This overestimates the effect for all simulated parameters. We have not found a limit where this theory is valid.

Liu's approach is only valid if the correlations stay close to the equilibrium shape and only their total magnitude changes. This approximation fails in higher fields as the correlations become strongly deformed. Moreover, the use of the Debye-Hückel potential only approximates the many-body effects on the two-body potential between charges. In the following section we describe a phenomenological approach to the screening crossover.

3.3.1.4 Screening crossover

When we studied the results obtained from the chemical equilibrium in equation 3.73, we formally wrote

$$\frac{n_f(E)}{n_f(0)} = \frac{\gamma(0)}{\gamma(E)}\sqrt{\frac{K_D(E)}{K_D(0)}}. \tag{3.82}$$

and we set $\gamma(E) = 1$ and $\gamma(0) = \gamma_0$ immediately afterwards. However such a discontinuity in the activity coefficient is unphysical because it would mean that infinitesimally small fields could destroy the ionic atmosphere. The Debye–Hückel correction does only disappear for a field that is sufficiently strong to modify the correlations on the scale of the screening length or smaller, i.e. if $\ell_D \gg \ell_E$. In this section we

show that it is possible to treat $\gamma(E)$ as a phenomenological parameter to describe the decay of the Debye screening out of equilibrium.

Patterson and Freitag (1961) were the first to discuss that setting the activity coefficient to unity for all applied fields is not correct and proposed the use of $\gamma(E)$ which they called the unscreening coefficient. However they have not given any prediction or analysis of its behaviour.
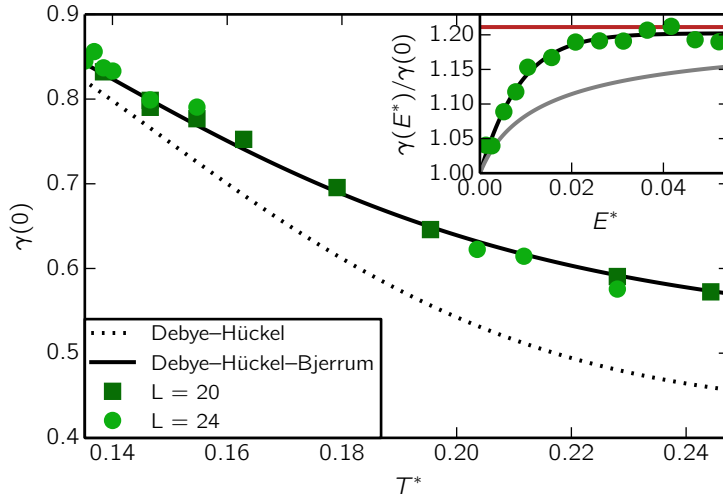
Figure 3.12: **Non-equilibrium activity coefficient.** The main figure shows the equilibrium activity coefficient γ_0 extracted from fitting the free charge density increase with the equation 3.88. The fitted values compare well with the Bjerrum—Debye–Hückel theory while the Debye–Hückel theory without pairing deviates from the obtained values. This shows a consistency in the definition of the Bjerrum length as the pairing length. The reduced chemical potential is $\nu_0^* = -1.45$.
The inset shows the field dependence of the non-equilibrium $\gamma(E)$ at $T^* = 0.140$. Equation 3.87 gives a good phenomenological description of the data. Liu's theory (grey line) recast in the activity coefficient form gives an approach to the infinite field value that is too slow compared to the observed one. The red line is the theoretical Bjerrum—Debye–Hückel value.

We find that the numerical simulations allow us to obtain sufficient amount of data to make assumptions about the functional form of $\gamma(E)$. We will call this quantity the non-equilibrium activity coefficient because it has an inherent connection with γ_0 and we find that the possibilities for confusion with the equilibrium activity coefficient are low. We use γ_0 to denote the equilibrium value in this paragraph to distinguish it formally from the limiting value $\gamma(0)$. We will require them to be equal in the end.

An important criterion is that the screening should lead to the recovery of Ohmic behaviour at low fields because the inherently short range nature of the screened potential requires linear response theory to be valid in the neighbourhood of equilibrium

$$\frac{n_{\mathrm{f}}(E \to 0)}{n_{\mathrm{f}}(0)} = \frac{\gamma(0)}{\gamma(E \to 0)} \sqrt{\frac{K_{\mathrm{D}}(E \to 0)}{K_{\mathrm{D}}(0)}} = 1 + \mathcal{O}\left(E^2\right). \tag{3.83}$$

We already know that $\sqrt{K_{\mathrm{D}}(E)/K_{\mathrm{D}}(0)} = 1 + \ell_T/(2\ell_E) + \mathcal{O}\left(E^2\right)$ which means that

$$\frac{\gamma(0)}{\gamma(E)} = 1 - \frac{\ell_T}{2\ell_E} + \mathcal{O}\left(E^2\right). \tag{3.84}$$

The non-equilibrium activity coefficient has to converge to the equilibrium value at low fields and to unity at high fields

$$\lim_{E \to 0} \gamma(E) = \gamma_0 \quad \Longrightarrow \quad \lim_{E \to 0} \frac{\gamma(0)}{\gamma(E)} = 1 \tag{3.85}$$

$$\lim_{E \to \infty} \gamma(E) = 1 \quad \Longrightarrow \quad \lim_{E \to \infty} \frac{\gamma(0)}{\gamma(E)} = \gamma_0. \tag{3.86}$$

Based on these conditions we have found that the screening crossover observed in simulations is well described by a simple exponential decay of the prefactor

$$\frac{\gamma(0)}{\gamma(E)} = \gamma_0 + (1 - \gamma_0) \exp\left(-\frac{\ell_T}{2\ell_E} \frac{1}{1 - \gamma_0}\right). \tag{3.87}$$

The relative increase in the free charge density increase is then

$$\frac{n_{\mathrm{f}}(E)}{n_{\mathrm{f}}(0)} = \left[\gamma_0 + (1 - \gamma_0) \exp\left(-\frac{\ell_T}{2\ell_E} \frac{1}{1 - \gamma_0}\right)\right] \sqrt{\frac{K_{\mathrm{D}}(E)}{K_{\mathrm{D}}(0)}}. \tag{3.88}$$

which gives a good match with the numerical results in figure 3.10. Finally, isolating the non-equilibrium activity coefficient yields

$$\gamma(E) = \left[1 + (1/\gamma_0 - 1) \exp\left(-\frac{\ell_T}{2\ell_E} \frac{1}{1 - \gamma_0}\right)\right]^{-1}. \tag{3.89}$$

Equation 3.88 can be either considered as a parameter free description of the crossover or as a fitting function to obtain γ_0 from measured or simulated data. We use this as a consistency check whose results are shown in figure 3.12. We can see that for all simulated temperatures we obtain a good agreement with the Bjerrum—Debye–Hückel theory prediction $\gamma_0 = \exp(-\ell_T/(\ell_T + \ell_{\mathrm{D}}/\sqrt{\alpha}))$ while the Debye–Hückel theory without pairing ($\gamma_0 = \exp(-\ell_T/(a + \ell_{\mathrm{D}}))$) fails to describe the fitted values (see sections 2.2 and 2.3 for the derivation of the activity coefficients). This is also consistent with our definition of free charges as

being separated by more that the Bjerrum length ℓ_T. We also show a comparison with Liu's theory. Equations given in (Liu, 1965) can be recast in the non-equilibrium activity form to obtain $\gamma_L(E) = \gamma_0^{f_L(\ell_D/\ell_E)}$. This function only describes the lowest fields as expected from the previous analysis.

In experiment, fitting the Wien effect is not the most efficient or precise way for obtaining the activity coefficient. Nevertheless, Mead and Fuoss (1939) used Onsager's theory to obtained a qualitatively but not quantitatively correct values for γ_0 in this fashion.

We conclude the discussion of screening. We have shown that Onsager's theory describes the high field limit well, while a theory of Liu desribes the lowest fields. The intermediate regime exhibits a crossover for which we have found a phenomenological description. The resulting function 3.88 describes all our data without any free parameters.

There is only a small discrepancy due to finite size effects left which is observable in the highest simulated fields (for example in figure 3.9). In the following two subsections we discuss two such scaling corrections – the finite radius of the ions and the finite scope of our simulations – and conclude that the increase is spurious and caused by the latter.
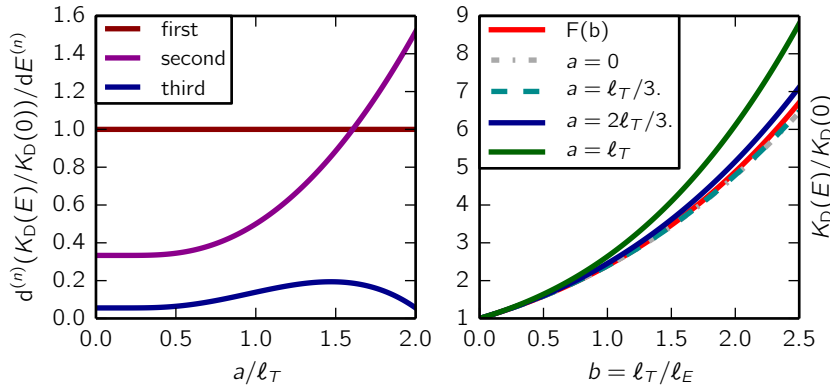
Figure 3.13: **Effect of the finite diameter a on the Wien effect.** Left plot shows the ion diameter dependence of coefficients c_i in the expansion $K_D(E)/K_D(0) = 1 + c_1 b + c_2 b^2 + c_3 b^3 + \mathcal{O}(b^4)$. The right panel shows $K_D(E)/K_D(0)$ as a function of b for selected values of a. The ion diameter a has to become comparable to the Bjerrum length ℓ_T to visibly influence the Wien effect. The curves following curves are almost indistinguishable to the naked eye: the full solution $F(b)$ (red), its expansion up to third order in field (grey), and the expansion corrected for the ion diameter $a = \ell_T/3$ (teal).

3.3.1.5 Finite ion radius

We note that the simulations systematically surpass the theoretical values by a small amount at the very highest fields in figure 3.9. This

trend appears at other temperatures as well. We wish to give two possible hypothesis regarding the cause of this deviation. First we discuss the role of the finite size of the charges on the Wien effect and afterwards the effect of the finite size of our simulations.

McIlroy and Mason (1984) found an expression taking the finite size of ions into account using a perturbative approach. Their method assumed a local Boltzmann equilibrium at contact of the two ions. This assumption describes our simulations well since an annihilated charge pair can occur anywhere in the simulation box with the probabilities of its orientation given by the local potential. The local Boltzmann equilibrium is also a reasonable approximation if the charge pair at contact associates to form a molecule which has a significantly faster orientational or vibrational dynamics than the diffusing charges.

McIlroy and Mason computed the correction stemming from the finite ion radius a up to third order in field:

$$
\begin{aligned}
\frac{K_\mathrm{D}(E)}{K_\mathrm{D}(0)} = 1 &+ \frac{\ell_T}{\ell_E} + \left(\frac{1}{3} + \frac{\exp(-2\ell_T/a)}{3(1-a/\ell_T+(1+a/\ell_T)\exp(-2\ell_T/a))} \right) \left(\frac{\ell_T}{\ell_E} \right)^2 \\
&+ \left(\frac{1}{18} + \frac{(1-a/2\ell_T)\exp(-2\ell_T/a)}{3(1-a/\ell_T+(1+a/\ell_T)\exp(-2\ell_T/a))} \right) \left(\frac{\ell_T}{\ell_E} \right)^3 \\
&+ \mathcal{O}\left(\left(\frac{\ell_T}{\ell_E} \right)^4 \right).
\end{aligned}
\tag{3.90}
$$

The diameter dependence of the expansion prefactors is shown in figure 3.13. The second Wien effect turns out to be very robust against this perturbation. The linear term in field is completely independent of the ion diameter. For higher order terms, significant deviations are first observable for $a > \ell_T/2$.

On a lattice the nearest neighbour distance plays the role of the ion diameter. We thus use the distance between neighbouring sites on the diamond lattice a in equation 3.90 to estimate the correction to the Wien effect even though the expression is derived for spherical ions. It would be very difficult to obtain such an analytic prediction for a lattice gas due to its discrete structure at short distances. We find $\ell_T \simeq 3a$ for the temperature range simulated in our simulations. In figure 3.13 we can see that the $a = \ell_T/3$ curve barely deviates from the $a = 0$ curve. We thus conclude that the high-field deviations of simulation results from theoretical values not due to the finite size of the charges.

3.3.1.6 Finite size corrections

The numerical simulations are limited to sizes much smaller than physical samples. The main condition for neglecting corrections from the finite size of the samples is that the typical scale of correlations does not exceed the size of the simulation box. In equilibrium this

scale is given by the Debye length. We observe no finite size effects in equilibrium as long as $\ell_D \ll L/2$ where L is the linear extension of the simulations. This is due to the fact that in equilibrium the system is deep in a gas phase, away from any critical points, and all correlations decay exponentially with ℓ_D. The temperature can be decreased down to $T^* = 0.135$ for $\nu_0^* = -1.45$ and $L = 24 \times 4a/\sqrt{3}$, i.e. total number of 24^3 unit cells and 110592 diamond lattice sites.

At even lower temperatures, the simulation size L becomes smaller than the Debye length due to the decreasing density of the charges. The charges can no longer be considered as deconfined in the absence of screening and behave as pairs. This is accompanied by a drop in charge density because the effective chemical potential almost doubles. We have confirmed this by exactly evaluating the partition function of two charge system.

We now adress the non-equilibrium corrections. High fields prevent the screening cloud from forming. However in a periodic system, screening can be restored in a stroboscopic fashion. While the screening cloud becomes weaker it is also deformed and winds around the system. This can lead to an unphysical increase in concentration of opposite charge around the central ion. The winding of the screening cloud thus creates a spurious decrease in activity. This effect becomes more prominent with decreasing size of the simulations, increasing field, and decreasing temperature. We consider this the most probable cause of the slight increase of the simulated densities above the theoretical value in figure 3.10. If we observe the pair correlation functions in our system, we can see that at high fields the influence of a charge on charges of opposite signs spreads over a distance that is longer along the field than the size of our simulation box.

In the following section we continue by presenting results for conductivity and conclude that their description requires the inclusion of a field dependent mobility.

3.3.2 Conductivity and field dependent mobility

In our simulations, we measure current and conductivity $\sigma(E)$ independently of the charge density. We observe that the conductivity increase lags behind the free charge density increase. This is due to the field dependence of mobility $\varkappa(E) = \sigma(E)/n_f(E)$. There are two independent effects influencing the mobility – the choice of the Metropolis dynamics and Coulombic interactions manifested in the first Wien effect.
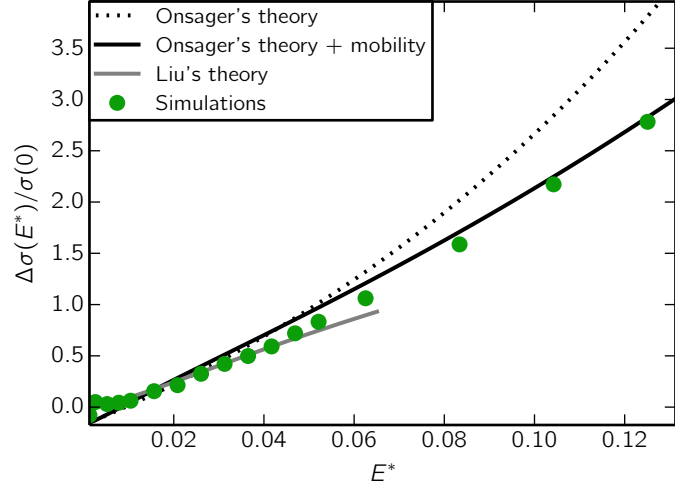
(a) Conductivity.
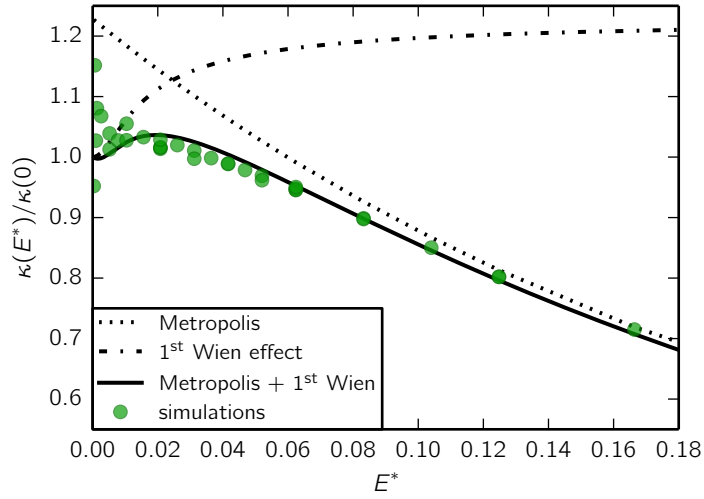
(b) Field dependent mobility.

Figure 3.14: **Wien effect – conductivity and mobility.** The upper figure is the relative increase in conductivity observed in our system. Unlike the situation for the density increase (compare with figure 3.9 with the same parameters $\nu_0^* = -1.45$ and $T^* = 0.140$), the conductivity exhibits deviations from Onsager's prediction (dotted line). We identify the field dependent mobility as the cause (full black line). In the lowest fields the mobility is roughly constant and Liu's theory describes the screened behaviour (grey line).

The mobility (lower figure) has two contributions: the mobility reduction due to the Metropolis simulation protocol (dotted line) used and the first Wien effect (dash-dotted line), i. e. the Coulombic interactions. The combination (full line) of the first Wien effect and the Metropolis reduced mobility explains the total field dependent mobility (green circles). Note that the data at lowest fields is noisy due to the low drift velocity. The noise disappears as the density increases (see 3.15).
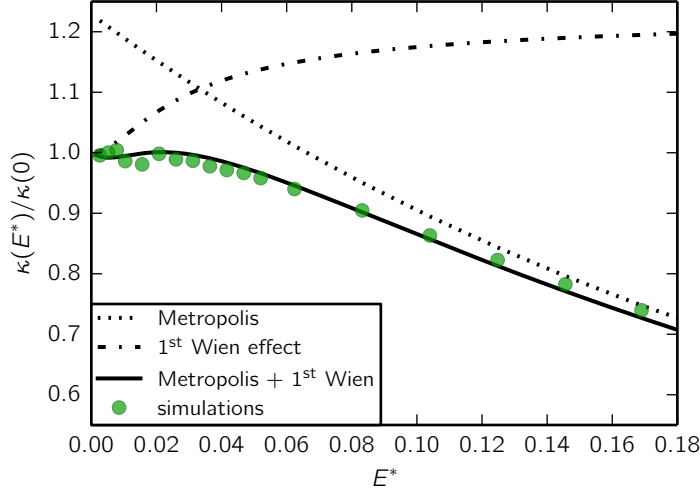
Figure 3.15: **Field dependent mobility – reduced noise.** The noise at low fields is reduced as temperature increases from $T^* = 0.140$ (figure 3.14b) to $T^* = 0.155$ (this figure). The respective zero field total densities are $n_{tot}(0) = 8.9 \times 10^{-5}$ and $n_{tot}(0) = 2.7 \times 10^{-4}$.

3.3.2.1 Stochastic dynamics of the simulations

There is an inherent velocity limit of a single move per Monte Carlo step present in our simulations. We use the algorithm of Metropolis et al. (1953). If only the potential of the external field is considered, a move in the field direction is always accepted while a move against the field has the acceptance probability $\exp(-E^*/T^*)$. The relative decrease in mobility can thus be expressed as

$$\frac{\varkappa_0(E^*)}{\varkappa_0(0)} = \frac{1 - \exp(-E^*/T^*)}{E^*/T^*}, \tag{3.91}$$

where $\varkappa_0$ is the mobility of a particle in an otherwise equivalent non-interacting gas. This decrease dominates the field dependence of mobility in high fields. At low fields it competes with the influence of screening on the mobility and its decay.

In the simulations all proposed steps are local. It is thus possible to rescale the time by the acceptance probability to obtain a close approximation to the physical time (Sanz and Marenduzzo, 2010). The mobility of the real world lattice system would still be field dependent, as predicted for example for monopole hopping in spin ice (Castelnovo et al., 2011). We have discussed the role of time in Monte Carlo dynamics in section 2.6.5.

3.3.2.2 The first Wien effect

In equilibrium, the screening atmosphere reduces the mobility (see section 2.5.1.1). As the charge is displaced away from its screening

cloud, the left-behind opposite charges create a net relaxation field to counteract the displacement. The first Wien effect is the disappearence of the relaxation field which leads to an increase in mobility with applied field as the screening decays.

We split the task into describing the influence of Coulombic interactions in zero field and it the decay of this correction in applied field. We first find that the theory of Fuoss and Onsager (1963) describes well the zero-field decrease of mobility due to the relaxation field effect up to moderate densities. The function for the first Wien effect obtained by Wilson (1936) captures the field dependence of the relaxation field to a good approximation.

The zero-field mobility of the Coulomb gas is reduced from the ideal gas value $\varkappa_0(0)$ to the screened mobility $\varkappa(0)$ because the ionic atmosphere slows down the charges. The zero-field correction is well approximated by Fuoss–Onsager conductivity theory (Fuoss and Onsager, 1957, 1963). Fuoss–Onsager theory for a binary electrolyte takes on the following quite complex form

$$
\begin{aligned}
\frac{\varkappa(0)}{\varkappa_0(0)} &= 1 - f_{\text{FO}}\left(\ell_T, \ell_D, a\right) = \frac{2 - \sqrt{2}}{3}\frac{\ell_T}{\ell_D} \\
&\quad - \frac{1}{3}\left(\frac{\ell_T}{\ell_D}\right)^2 \ln\left(\frac{\ell_T}{\ell_D}\right) - \left(\frac{\ell_T}{\ell_D}\right)^2 N\left(\frac{2\ell_T}{a}\right) \\
&\quad + \left(\frac{\ell_T}{\ell_D}\right)^2 \gamma_0^2 K_c\left(\frac{2\ell_T}{a}\right) \\
N\left(\frac{2\ell_T}{a}\right) &= 1.4985 + \frac{0.2071\, T_1(2\ell_T/a) - 0.03066}{1 - T_1(2\ell_T/a)} \\
T_1\left(\frac{2\ell_T}{a}\right) &= \exp\left(-\frac{2\ell_T}{a}\right)\left(1 + \frac{2\ell_T}{a} + \frac{1}{2}\left(\frac{2\ell_T}{a}\right)^2\right) \\
K_c\left(\frac{2\ell_T}{a}\right) &= \frac{1}{3}\left(\text{Ei}\left(\frac{2\ell_T}{a}\right) - \frac{a}{2\ell_T}\left(1 + \frac{a}{2\ell_T}\right)\exp\left(\frac{2\ell_T}{a}\right)\right),
\end{aligned}
\tag{3.92}
$$

where Ei is the exponential integral. For details of the derivation we refer to the original article. We only note that the very first term

$$
\frac{\varkappa(0)}{\varkappa_0(0)} = 1 - \frac{2 - \sqrt{2}}{3}\frac{\ell_T}{\ell_D}
\tag{3.93}
$$

is the relaxation field term of the original Onsager–Debye–Hückel theory of conductivity (Onsager, 1926) discussed in section 2.5.1.1. We do not include any electrophoretic terms because all solvent effects are absent in the lattice simulations.

To describe the field dependence of this correction, we use Wilson's calculation of the first Wien effect (Wilson (1936), first published in a

review by Eckstrom and Schmelzer (1939)). The resulting evolution of
the term linear in ℓ_T/ℓ_D (equation 3.93) with field is

$$\frac{\varkappa(E)}{\varkappa_0(E)} = 1 - \left(\frac{2-\sqrt{2}}{3}\frac{\ell_T}{\ell_D}\right)f_W\left(\frac{\ell_D}{\ell_E}\right), \quad \text{where}$$

$$f_W(x) = \frac{3}{(4-2\sqrt{2})x^3}\left[x\sqrt{1+x^2} - \arctan\left(\frac{x}{\sqrt{1+x^2}}\right)\right.$$
$$\left. - \sqrt{2}x + \arctan\left(\sqrt{2}x\right)\right], \tag{3.94}$$

and $f_W(x)$ decreases from unity in zero field to zero in infinite field. The
previous formula compares the mobility in the non-interacting lattice
gas $\varkappa_0(E)$ with the mobility of the lattice Coulomb gas at the same field
$\varkappa(E)$. We assume that the other terms in the Fuoss–Onsager theory
3.92 decay in the same or similar fashion. This assumption appears a
posteriori to be a good approximation. We obtain

$$\frac{\varkappa(E)}{\varkappa_0(E)} = 1 - f_{FO}(\ell_T, \ell_D, a)f_W(\ell_D/\ell_E). \tag{3.95}$$

Without the Metropolis dynamics dependent correction 3.91, the mo-
bility would increase with electric field as

$$\frac{\varkappa(E)}{\varkappa(0)} = \frac{1 - f_{FO}(\ell_T, \ell_D, a)f_W(\ell_D/\ell_E)}{1 - f_{FO}(\ell_T, \ell_D, a)}. \tag{3.96}$$

We treat the relaxation field, the first Wien effect, and the second
Wien effect as independent. Our final prediction is effectively a product
of functions describing these phenomena. However, they are all differ-
ent aspects of the same problem of diffusive dynamics of charges. Thus
one expects this decoupled approximation to fail at strong coupling.
Patterson and Freitag (1961) attempted to treat such systems by a set of
coupled differential equations. Up to this day their derivation is prob-
ably the best approach to treat the interplay of the first and the second
Wien effect in the highly correlated regime. Note that the first Wien
effect is often eliminated in electrolyte measurements because a differ-
ence of the high-field conductivity between a weak electrolyte and a
strong one is measured. If the ions in both electrolytes exhibit a similar
first Wien effect, its contribution cancels out.

3.3.2.3 The total field dependent mobility

The relative change of the total mobility is obtained by combining
equations for the Metropolis algorithm mobility of a non-interacting
lattice gas 3.91 and the Coulomb gas correction 3.95

$$\frac{\varkappa(E)}{\varkappa(0)} = \frac{1 - f_{FO}(\ell_T, \ell_D, a)f_W(\ell_D/\ell_E)}{1 - f_{FO}(\ell_T, \ell_D, a)}\frac{1 - \exp(-E^*/T^*)}{E^*/T^*}. \tag{3.97}$$

In figure 3.14b, we compare the previous expression with the simulation data to confirm that both contributions influence the field dependence of the mobility. Verifying the prediction at low fields is complicated by noise. We divide two small numbers – density and conductivity – which leads to a large relative error. This is alleviated if the temperature increases as we show in figure 3.15.

The theoretical prediction for conductivity of the lattice Coulomb gas in external field is of the form

$$\frac{\sigma(E)}{\sigma(0)} = \frac{\varkappa(E)}{\varkappa(0)} \frac{n_{\text{f}}(E)}{n_{\text{f}}(0)}. \tag{3.98}$$

which gives good agreement with the simulation data in figure 3.14a. The expression for the zero field mobility of the Coulomb gas failsaround $T^* = 0.165$ for $v_0^* = -1.45$ as the parameter ℓ_T/ℓ_{D} approaches unity. At higher temperatures the zero field mobility correction has to be extracted from comparing simulations of the Coulomb gas with simulations of a non-interacting gas.

The procedure presented here can be interpreted as a correction to Onsager's prediction but also as a diagnostic method for the field dependent mobility. The Wien effect is highly universal and robust in dilute Coulomb gases. If one can reasonably assume that the increase in density follows Onsager's theory and yet the conductivity deviates from this behaviour, one can extract the field dependence of the mobility. One notable example of an interplay of the Wien effect and mobility is found in oxide glasses (Ingram et al., 1980; Tomozawa et al., 1980). The strong quadratic field dependence of defect mobility completely hides the linear increase in their density due to the Wien effect. However, the hopping distance for defects in oxide glasses is severly overestimated if it is extracted without taking the Wien effect into account.

With the conductivity and mobility, we have concluded the study of macroscopic observables and move on to the microscopic correlations. These allow us to observe the process underlying the second Wien effect. We also gain a direct access to the association constant.

3.3.3 Pair correlations

The simulations allow us to extract the pair correlation functions which are central to Onsager's derivation of the increase in the dissociation constant. The pair correlation functions are difficult to measure experimentally and we are not aware of any such measurement for the
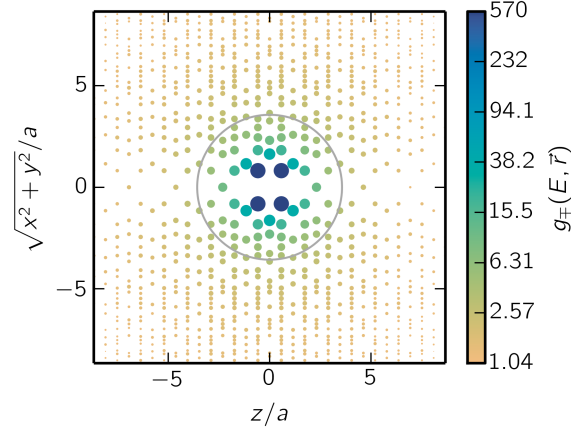
(a) Equilibrium correlations.
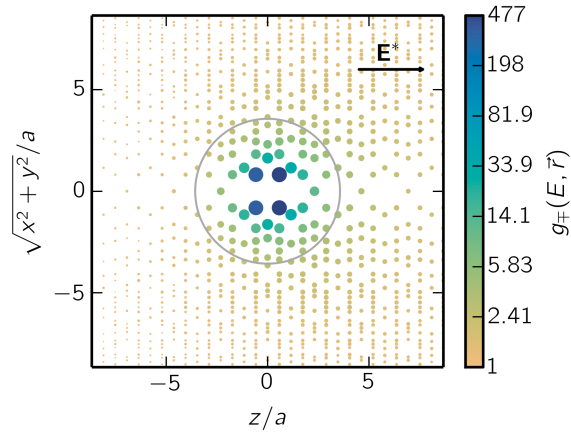
(b) Correlations in field $E^* = 0.021$.
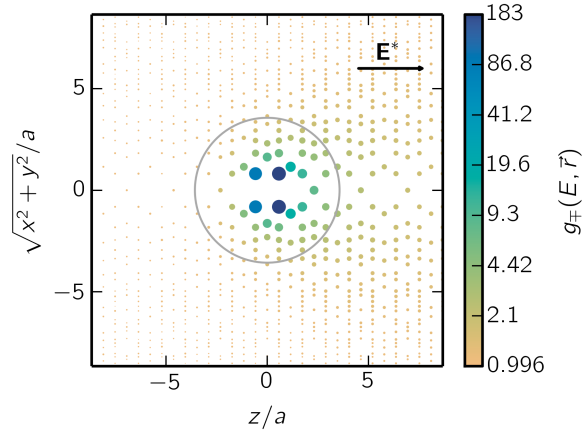
(c) Correlations in field $E^* = 0.062$.

Figure 3.16: **Pair correlation functions.** The figures show a projection of the pair correlation function $g_{\mp}$ averaged over the azimuthal angle and mirrored for clarity. The horizontal axis shows the distance along the field axis and the vertical the distance from this axis. The uncorrelated limit is $g_{\mp}(r \to \infty) = 1$. In equilibrium the negative central ion is symmetrically screened by a cloud of positive charge. The field deforms the screening cloud. The bound pair dipoles align with the field. The Wien effect supresses the correlation function at short distances because the bound pair density contributes less to the total density. Bjerrum length ℓ_T (grey circle) separates the bound and free charges.

Wien effect. We focus on the correlations between charges of opposite signs[5]

$$g_{\mp}(\mathbf{r}) = \frac{\langle n_+(\mathbf{r}) \rangle \langle n_-(0) \rangle}{\langle n_+ \rangle \langle n_- \rangle} = g_{\pm}(-\mathbf{r}).$$ (3.99)

It is sufficient to study $g_{\mp}(\mathbf{r})$ as the inversion $\mathbf{r} \to -\mathbf{r}$ is equivalent to inverting the field direction $\mathbf{E} \to -\mathbf{E}$.

In equilibrium, the correlation function 3.99 is described using the Debye–Hückel correlations 2.15 as

$$g_{\mp}(\mathbf{r}) = \exp\left(-\beta U_{\mathrm{DH}}(r)\right) \simeq 1 - \beta U_{\mathrm{DH}}(r).$$ (3.100)

with an additional contribution at short distances coming from the Bjerrum pairs (illustrated for the magnetolyte in figure 4.11).

If the field is applied, the screening contribution decreases and eventually completely vanishes. The correlations corresponding to the bound charges are also reduced because of the shift in equilibrium towards free charges. The bound charges behave as metastable dipoles and polarize in the field direction. The subsequent escape occurs along a wedge that gets narrower with increasing field. The stream lines in figure 3.6 show the dynamics of the effect.

We illustrate this behaviour in figure 3.16 using the pair correlation functions obtained from numerical simulations. We show a two dimensional projection of the full function which corresponds to folding the azimuthal angle dependence onto a single plane. This visualization is natural given the axisymmetric nature of the Wien effect. We observe the rapid decrease of total correlations with applied field, the increasing asymmetry and the wedge along which the ions escape. Onsager's prediction for the correlation function 3.46 also exhibits this behaviour. We do not plot a direct comparison which is difficult due to the lattice nature of our simulations. Instead we show how the concentration quotient $\mathscr{K}_{\mathrm{A}}$ and the equilibrium constant K_{A} for association can be obtained from the correlation functions.

---

5 We will not discuss the same charge correlation functions g_{--} and g_{++} in detail, because they are much weaker than the correlations between charges of unlike sign. Their behaviour resembles a short-range repulsive gas, i.e. $g_{++} < 1$ for short distances ($r \lesssim \ell_T$). At higher densities, they exhibit weak short distance oscillations due to the ocassional formation of $(-+-)$ or $(+-+)$ clusters. These correlations are also reduced by the applied field.
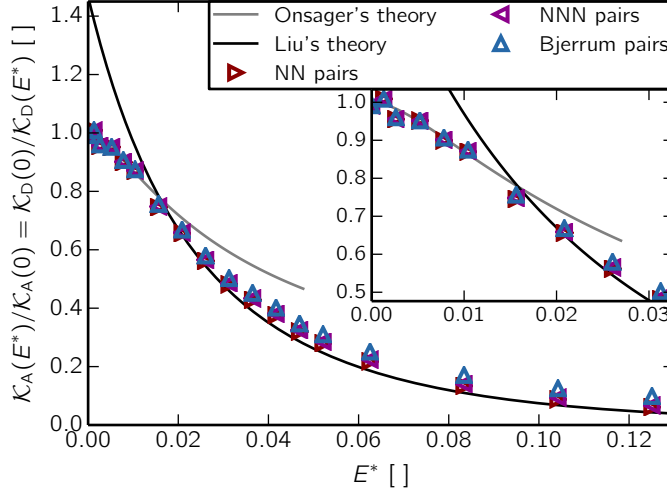
Figure 3.17: **Association constant.** We extract the association concentration quotient $\mathscr{K}_A$ by summing the correlation function $g_\mp$ over the Bjerrum volume. The results match Onsager's theory in the unscreened regime and Liu's theory in the screened regime. The intercept of Onsager's theory with the vertical axis is $1/\gamma^2$.

We repeat the procedure for different choice of the length separating the bound and free charges. The absolute value differs slightly but the relative dependence is identical. This is due to the predicted independence of the unscreened Wien effect on this choice and due to a large contribution from the nearest neighbour pairs. At high fields small deviations develop as the symmetric definition of the bound pair loses its physical meaning.

3.3.4 Association constant

In the scope of the Bjerrum theory of pairing, the association constant $K_A = 1/K_D$ is defined in equation 2.26 as

$$K_A = \int_{V_{Bj}} \exp{-\beta\, U_C(\mathbf{r})} \mathrm{d}r^3 / \tilde{V}\,, \tag{3.101}$$

where $\exp(-\beta\, U_C(\mathbf{r}))$ approximates the correlations of the bound pairs due to the bare Coulomb potential and V_{Bj} is the Bjerrum volume of a sphere with a radius equal to the Bjerrum length ℓ_T. The interpretation is that the association constant corresponds to the volume of phase space occupied by the bound states. We normalized by the volume per lattice site $\tilde{V}$ to obtain an equilibrium constant appropriate for numerical densities.

Similarly we can obtain the concentration quotient $\mathscr{K}_A = \gamma^2 K_A$ by summing the pair correlation function over the Bjerrum volume in the simulations

$$\mathscr{K}_A = \sum_{\{\mathbf{r}:|\mathbf{r}|\leq\ell_T\}} g_{\mp}(\mathbf{r}). \tag{3.102}$$

The sum gives the concentration quotient instead of the association function because the measured pair correlation functions necessarily include a contribution from the screening. From Onsager's theory 3.73 we can write

$$\frac{\mathscr{K}_A(E)}{\mathscr{K}_A(0)} = \frac{1}{\gamma^2}\frac{K_A(E)}{K_A(0)} = \frac{1}{\gamma^2}\frac{K_D(0)}{K_D(E)} = \frac{1}{\gamma^2 F(b)}. \tag{3.103}$$

where we consider the screening cloud to be completely removed by the field. We made the same approximation in the formula 3.75 for the free charge density. Similarly the theory of Liu 3.78 for the screened Wien effect can be rewritten in a form for the association concetration quotient.

The relative change in the association concentration quotient extracted in this fashion closely follows the theoretical predictions. This constitutes a verification of the Wien effect theory directly in the quantities that it is formulated in. Moreover, the relative change is robust with respect to the definition of the bound pairs. This is due to the Gauss law 3.9 for the probability flow $\nabla \cdot \mathbf{S} = 0$ which is also discussed in (Mason and McIlroy, 1978). A complementary reason is that the bound pair correlations on a lattice are dominated by the nearest neighbour contribution.

Whereas the relative change in $\mathscr{K}_A$ is described by the Wien effect theory, its absolute value turns out to be lattice dependent and to deviate significantly from Bjerrum's value. This demonstrates the robustness of the Wien effect as it deals with relative changes only which makes many non-trivial corrections to cancel out.

3.3.5 AC Wien effect

The enhanced charge density can be supported not only by application of a constant field but also by periodic driving. The effect is stable at low frequencies. The effective field is the average modulus of the amplitude as the Wien effect depends linearly on the field.

We expect changes of behaviour around frequencies corresponding to a time scale that limits the effect. This is the lowest of time scales related to the following: establishment of the chemical equilibrium, reorientation of bound pairs, or charge generation from molecules or vacuum. For periodic driving it turns out that the limiting frequency is larger than the inverse time needed to establish equilibrium. This means
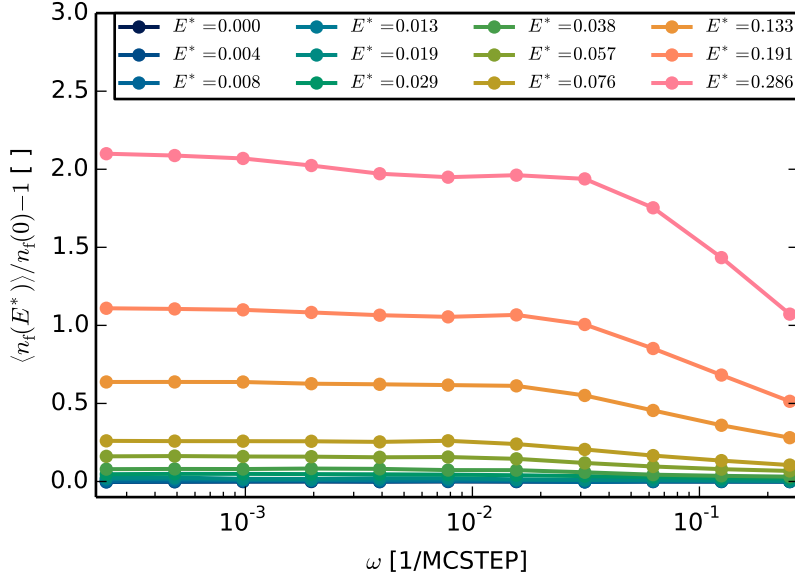
Figure 3.18: **Frequency dependence of the Wien effect.** The Wien effect decays above a characteristic frequency which we conclude to be determined by the orientational dynamics of bound charges and not the chemical kinetics of the dissociation. The amplitude dependence of the Wien effect follows theory presented in section 3.3.1. The parameters used are $T^* = 0.173$ and $\nu_0^* = -1.51$.

that the Wien effect is stablized by its diffusion limited character and shows the limits of its description by chemical kinetics. The limiting frequency is most probably determined by the reorientation of bound dipoles. We give a thorough discussion of these time scales in section 5.1 of the final chapter of this thesis which deals with the Wien effect in spin ice. The DC effect is not stable in spin ice so the AC Wien effect has to be used to probe the Coulomb gas nature of the material (see section 5.5).

3.4 Concluding remarks

We have provided a systematic introduction to the second Wien effect illustrated by results for the first numerical simulations of the Wien effect. Our simulations demonstrate many of the important features of the second Wien effect: non-equilibrium behaviour beyond linear response, high degree of universality, and robustness.

We have verified that the theory of the Wien effect is valid in its limits of applicability. In the case of screening we find a novel phenomenological expression that describes the crossover from the theory of the screened effect to the unscreened effect. We present how the Wien ef-

fect allows analysis of a field dependent mobility and we give expressions valid for a lattice Coulomb gas governed by the Metropolis algorithm. Finally the numerical simulations grant us an access to the microscopic correlations underlying the second Wien effect.

The lattice model we have simulated is tunable to regimes that correspond to many real world materials. These materials often exhibit specific behaviour. The advantage of the lattice model is that it is readily modified to include a wide range of modifications. This thesis deals with the physics of spin ice which is one of them. We present in the following chapters a real material which is successfully modelled as a diamond lattice Coulomb gas with a caveat of having kinetic constraints for the charges. The constraints in spin ice are the underlying spin degrees of freedom which flip as the charges move and in turn restrict the charge motion. We will nevertheless show that the Wien effect in spin ice follows the same expressions as it does in electrolytes. This will allow us to give an expression for the non-linear susceptibility of a frustrated magnet.

4

Spin Ice as a Coulomb Gas

We devoted the first half of this thesis to the study of Coulomb gases and the second Wien effect. In this chapter we introduce the Coulomb gas of magnetic monopoles in spin ice – the magnetolyte. Spin ice encompasses a class of highly frustrated ferromagnets. Chemically, spin ice materials are pyrochlore rare-earth oxides $R_2^{3+}X_2^{4+}O_7$ (Gardner et al., 2010). The crystal field determines the magnetic properties of the rare-earth R^{3+} ions. In the so-called classical spin ices containing Ho^{3+} or Dy^{3+}, the ions behave like Ising spins with a large magnetic moment $\mu \simeq 10\mu_B$ (Harris et al., 1997; Bramwell and Harris, 1998). These Ising spins lie on the pyrochlore lattice and point along its local [111] axes. The tetravalent ions X^{4+} are non-magnetic (Ti^{4+}, Sn^{4+}, or Ge^{4+}) and will not be directly considered in the models of spin ices.

The effective exchange interaction between the Ising spins is ferromagnetic which leads to an extensive degeneracy of the groundstate of the nearest-neighbour model of spin ice (NNSI). This model supports gapped topological defects as lowest lying excitations. These defects are deconfined and possess a weak entropic interaction. Dipolar interactions play an important role in spin ice. Adding them to the nearest-neighbour model results in the dipolar spin ice model (DSI) which preserves the degeneracy to a large extent and lifts it only at very low temperatures (Siddharthan et al., 1999; den Hertog and Gingras, 2000; Isakov et al., 2004). Moreover, the dipolar interactions endow the defects with magnetic charges and therefore we will refer to them as magnetic monopoles (Castelnovo et al., 2008).

The collective behaviour of the gas of the magnetic monopoles is well described by the electrolyte theory (Castelnovo et al., 2008; Bramwell et al., 2009; Castelnovo et al., 2011). The magnetic properties of spin ice fix the chemical potential ν_0 of the monopoles and the strength of their mutual Coulomb interaction U_C. The monopole density increases with temperature and the properties of the magnetolyte range from those of a dilute weak electrolyte at low temperatures to those of a dense Coulombic fluid at high temperatures.

Spin ice has inspired a large amount of diverse research in the recent years, for reference see the spin ice chapter in (Lacroix et al., 2011, Ch. 12), the very instructive thesis of Jaubert (2009), and the review (Castelnovo et al., 2012). General discussion of the Coulomb phase

was given by Henley (2010). In this chapter we describe the general properties of spin ice and its models. Once we will have shown the mapping of spin ice to the magnetolyte, we show how the electrolyte theory applies. We also give an introduction to simulation methods applicable on spin ice.
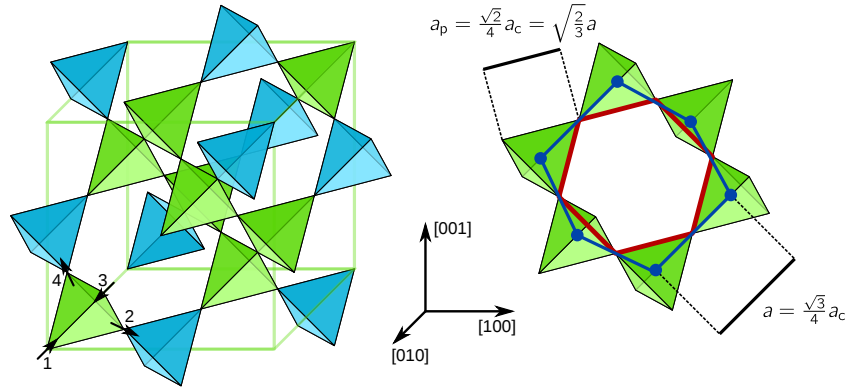
Figure 4.1: **Pyrochlore lattice and its properties.** The pyrochlore lattice (left) is composed of corner-sharing tetrahedra. The spins lie on the local [111] axes connecting the centres of the tetrahedra. Green tetrahedra form a unit cell of the cubic lattice (green cube). In lower left corner, the spins which represent the four spin sublattices are numbered according to the convention used in the main text. On the right we show the smallest loop of spins (red hexagon). The centres of the tetrahedra (blue circles) form a diamond lattice whose smallest loop is shown as well (blue hexagon). The loops play a crucial role in the statistical properties of ground states of spin ice.

4.1 Spin ice materials

First we would like to discuss the chemical composition of spin ice, a representative of magnetic pyrochlore oxides which exhibit a broad range of behaviour (Gardner et al., 2010). Extensive work on pyrochlore materials was driven by theoretical predictions of complex magnetic behaviour in the pyrochlore lattice (Anderson, 1956; Villain, 1979; Reimers, 1992) and by the discovery of frustration in SCGO which can be seen as a pyrochlore slab (Obradors et al., 1988). $Ho_2Ti_2O_7$ (HTO) spin ice was discovered as the first geometrically frustrated ferromagnet (Harris et al., 1997)[1]. Frustration in $Dy_2Ti_2O_7$ (DTO) was described soon after (Ramirez et al., 1999). Currently there are six known clas-

---

1 Signs of residual entropy of DTO were observed already by Blöte et al. (1969) but were left unexplained.

	a_c [Å]	D [K]	D_{NN} [K]	J [K]	J_{NN} [K]	J_{NN}/D_{NN}	$|J_{eff}|$ [K]	$U_C(a)$ [K]	ν_0 [K]
$Ho_2Sn_2O_7$	10.37	1.30	2.17	−1.68	−0.56	−0.26	1.61	−2.83	−5.19
$Ho_2Ti_2O_7$	10.10	1.41	2.35	−1.89	−0.63	−0.27	1.72	−3.07	−5.57
$Ho_2Ge_2O_7$	9.90	1.50	2.50	−2.64	−0.88	−0.35	1.62	−3.27	−5.51
$Dy_2Sn_2O_7$	10.40	1.29	2.15	−2.97	−0.99	−0.46	1.16	−2.81	−4.27
$Dy_2Ti_2O_7$	10.10	1.41	2.35	−3.45	−1.15	−0.49	1.20	−3.07	−4.53
$Dy_2Ge_2O_7$	9.93	1.48	2.47	−5.40	−1.80	−0.73	0.67	−3.23	−3.58

Table 4.1: **Spin ice parameters.** Values as given in (Zhou et al., 2012). Other references give values that vary within 5 % for HTO and DTO. The values for other materials are less precise with varations of 10 % depending on the reference. The two columns at the utmost right show parameters for the Coulomb gas in spin ice. While the nearest-neighbour magnetic Coulomb interaction $U_C(a)$ does not vary much between while the bare chemical potential ν_0 can be tuned using chemical pressure.

sical spin ice materials $(Dy/Ho)_2^{3+}(Sn/Ti/Ge)_2^{4+}O_7$ (Zhou et al., 2012), among which DTO and HTO are available as monocrystals, and many quantum spin ice candidates (Gingras and McClarty, 2014). We now focus on the origin of magnetism in classical spin ice.

The total angular momentum $\mathbf{J} = \mathbf{L} + \mathbf{S}$ is a good quantum number for the rare-earth ions Ho^{3+} ($J = 7$) and Dy^{3+} ($J = 15/2$). In spin ice, the crystal field environment of the magnetic ions selects the Ising doublet of magnetic quantum number $J_z = \pm J$ as the lowest energy level. The easy axis connected with this anisotropy lies along one of four local [111] axes of the pyrochlore lattice (see figure 4.1). The Ising doublet is well separated from higher levels by energy $20.4\,\text{meV} \sim 236\,\text{K}$ in HTO (Rosenkranz et al., 2000), and by $28\,\text{meV} \sim 325\,\text{K}$ (Jana et al., 2002) or $33\,\text{meV} \sim 383\,\text{K}$ (Rosenkranz et al., 2000) in DTO.

This large level splitting means that the Ising like nature is protected over a range of temperatures, for example at $T = 10\,\text{K}$ the single ion anisotropy in DTO is $\chi_z/\chi_\perp \simeq 300$. Below this temperature the anisotropy could be higher even as the susceptibility measurements no longer see a signature of the hard-plane components (Snyder et al., 2003, 2004) and are fully described by models based on Ising spins together with their mapping to magnetic monopoles (Jaubert and Holdsworth, 2009).

Substitutions of the nonmagnetic ions $(Sn/Ti/Ge)^{4+}$ vary the cubic lattice constant a_c – an effect dubbed chemical pressure (Zhou et al., 2012). The first column in table 4.1 shows how the lattice constant changes for different spin ice materials.
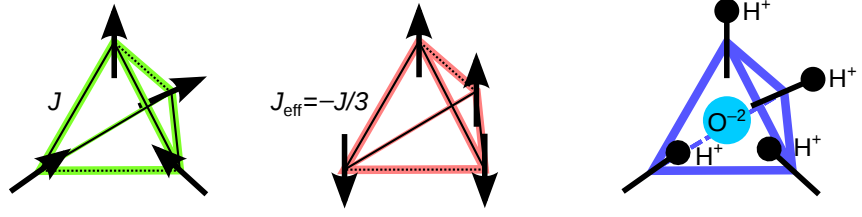
Figure 4.2: **Nearest-neighbour spin ice, pyrochlore Ising antiferromagnet, and water ice.** We show the mapping between the ground states of the three systems. For spin ice and the antiferromagnet the mapping is valid for excited states as well while water ice possesses additional defects due to two protons occupying the same bond. The full black lines show bonds whose energy is minimized while the full dotted lines show frustrated bonds.

4.2 Nearest-neighbour spin ice

The basic model of spin ice considers only the nearest neighbour interaction between the Ising spins with the Hamiltonian

$$\mathcal{H}_{\mathrm{NNSI}} = -J_0 \sum_{\langle i,j \rangle} \hat{\mathbf{s}}_i \cdot \hat{\mathbf{s}}_j \tag{4.1}$$

The spins are divided into four sublattices $\alpha \in \{1,2,3,4\}$ and point along the local axes $\hat{\mathbf{s}}_\alpha$. We give the normalized directions for the inward pointing spins of an "up" tetrahedron (see figure 4.1)

$$\begin{aligned}
\hat{\mathbf{s}}_1 &= (+1,+1,+1)/\sqrt{3} \\
\hat{\mathbf{s}}_2 &= (-1,-1,+1)/\sqrt{3} \\
\hat{\mathbf{s}}_3 &= (-1,+1,-1)/\sqrt{3} \\
\hat{\mathbf{s}}_4 &= (+1,-1,-1)/\sqrt{3}
\end{aligned} \tag{4.2}$$

The outward pointing spins have the opposite sign $(-\hat{\mathbf{s}}_\alpha)$. It is readily verified that $\hat{\mathbf{s}}_\alpha \cdot \hat{\mathbf{s}}_\beta = \pm 1/3$. The positive sign is obtained if both spins point out or if both point in. The negative sign corresponds to one in spin and one out spin which minimizes the energy along the bond.

The global energy cannot be minimized by separately minimizing the energy of all bonds. The energy of a tetrahedron is minimized if two spins point out and two point in. This two-in-two-out state is not unique and the ground state is thus extensively degenerate. The nearest-neighbour spin ice is thus an archetypal highly frustrated magnet. We discuss the entropy of the ground state in the following subsection.

Note that the nearest-neighbour spin ice model is equivalent to the antiferromagnetic pseudospin model given by Anderson (1956) which has the Hamiltonian

$$\mathscr{H}_{\mathrm{AFM}} = -J_{\mathrm{eff}} \sum_{\langle i,j \rangle} s_i' s_j', \tag{4.3}$$

where $J_{\mathrm{eff}} = -J_0/3$. The mapping from spins to pseudospins can be performed by setting $s_i' = \sqrt{3}(\hat{\mathbf{s}}_i)_z \eta_i$ where the $\sqrt{3}$ ensures that the pseudospins take on values ± 1 and η_i is a function that alternates sign in every layer of spins in the z direction, which can be for example expressed as $\eta_i = (-1)^{(4z_i/a_c) \bmod 2}$. The out spins in NNSI map to up spins in the Anderson model in one layer and to down spins in the following, and vice versa for the in spins. See figure 4.2 for an illustration of the mapping.

Due to the cubic symmetry of the pyrochlore lattice there is a mapping for each of the axes x, y, z. The ground state of the pyrochlore antiferromagnet is thus a zero total magnetization state $\left(\sum_{i \in \boxtimes} s_i' = 0 \right)$. The antiferromagnetic model has a global $\mathbb{Z}_2$ Ising symmetry that is lower than the cubic symmetry of the lattice. Because there is no effect that would select the easy Ising axis and leave the total cubic symmetry intact, the pyrochlore Ising antiferromagnet has no direct physical realizations.

Ground state properties of the nearest-neighbour spin ice are also equivalent to the Pauling model for the disordered phase of water ice, where the in or out spin represents a proton which close to or far from an oxygen, respectively. The ice rules governing this model were proposed by Bernal and Fowler (1933) and its residual entropy was found by Pauling (1935) using a single tetrahedron approximation. Pauling's argument for the residual entropy is valid for both the hexagonal lattice of water ice and the diamond lattice formed by the centres of the tetrahedra of pyrochlore lattice. We give its version for spin ice below.

4.2.1 Ground state entropy

In the ground state of each tetrahedron, exactly two of the four spins have to point in while the remaining two point out. There are six ways how to fulfil this condition out of the total sixteen configurations of the tetrahedron (see figure 4.6). Each spin connects two tetrahedra. The total number spins is $N_{\mathrm{S}} = 2N_{\mathrm{T}}$, i. e. double the number of of tetrahedra N_{T} and thus the total number of configurations is

$$\Omega_{N_{\mathrm{S}}} = 2^{N_{\mathrm{S}}} \left(\frac{6}{16} \right)^{\frac{N_{\mathrm{S}}}{2}} = \left(\frac{3}{2} \right)^{\frac{N_{\mathrm{S}}}{2}} \tag{4.4}$$
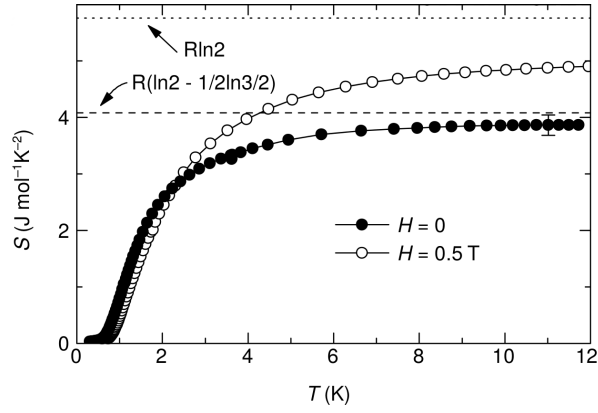
(a) (Ramirez et al., 1999)
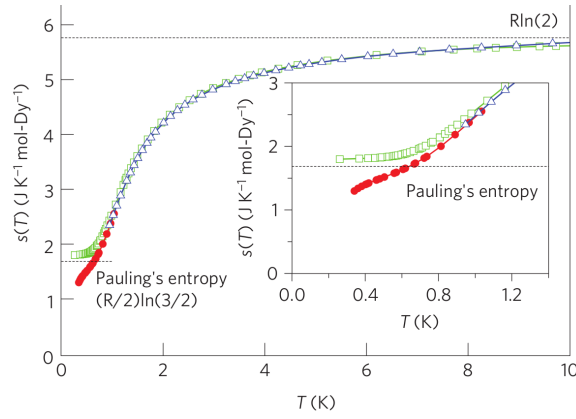
(b) (Pomaranski et al., 2013)

Figure 4.3: **The residual entropy of DTO spin ice. a)** The entropy is obtained by integrating the specific heat. The zero of entropy is set to the value at lowest measured temperature. The high temperature value in zero field (full circles) should then approach the paramagnetic $k_B \ln 2$ per spin. If the measurement is performed only over short times (Ramirez et al., 1999), a missing entropy is observed which matches well with Pauling's prediction $(k_B/2)\ln(3/2)$ per spin. A magnetic field acts to order spin ice and recover the entropy (empty circles). **b)** If DTO is equilibrated for longer periods of time, the Pauling entropy gets recovered (Pomaranski et al., 2013). Possible explanations include ordering (Melko et al., 2001) or a crossover to a quantum spin liquid (Hermele et al., 2004; Shannon et al., 2012; Gingras and McClarty, 2014).

The resulting entropy per spin is

$$\frac{S_{ice}}{N_S} = \frac{k_B \ln \Omega_{N_S}}{N_S} = \frac{1}{2} \ln\left(\frac{3}{2}\right) \tag{4.5}$$

Pauling's result is often interpreted as assigning $\Omega_T = 3/2$ microstates to each tetrahedron. The predicted value agrees well with experimental results for the disordered phase of water ice (Giauque and Stout, 1936) and for relatively short times in spin ice (Ramirez et al., 1999) (see figure 4.3). The third law of thermodynamics prevents the system from keeping the residual entropy down to absolute zero. In water the missing entropy is recovered by a phase transition to the proton ordered XI phase of water (Petrenko and Whitworth, 1999). In DTO spin ice, it is not understood if there is an ordering phase transition or a crossover to a quantum spin liquid but the entropy is slowly recovered by equilibrating the sample for longer periods of time: 10^3 s at $T = 0.45$ K and 10^5 s at $T = 0.34$ K (Pomaranski et al., 2013). If other spin ice materials exhibit the same behaviour is currently unknown. The spin ice models that we give are valid as a good description of the long lived state. Moreover, the non-equilibrium processes that we study are orders of magnitude faster than the observed recovery of the entropy.

Nagle (1966) gave a series expansion for the number of microstates per tetrahedron with the result $\Omega_T = 1.50685 \pm 0.00015$ which showed that the neglected correlations are due to the existence of loops in spin ice. For square ice, the two dimensional version of spin ice, there exists an exact solution (Lieb, 1967). In three dimensions, the loops have not been treated in an exact fashion but there is a numerical analysis of their statistics (Jaubert et al., 2011). The ground state can be seen as a network of closed loops (see figure 4.7). The identification of loops is not unique. There are two out spins in every tetrahedron which means that every loop can be continued in two ways. Therefore the correct loop model of spin ice is the fully packed two colour model discussed in (Jacobsen and Kondev, 1998).

4.3 Topological character of spin ice

Apart from yielding a correction to the entropy, the loops play an important role in dynamical properties of the ice manifold. A single spin cannot be flipped in the ice manifold without creating a defect. The only way to make a transition from one ground state to another is to flip a whole closed loop of spins. This means that spin fluctuations are strongly correlated in the spin ice manifold despite its high entropy and paramagnetic character. This is a prime example of the cooperative paramagnetism (Villain, 1979).

Susceptibility bears an experimental signature of the cooperative paramagnetism in spin ice. Jaubert et al. (2013) show based on simulations of NNSI and Husimi tree calculations, that the isothermal susceptibility should follow a modified Curie law at low temperatures

$$\chi_T = \frac{2C_C}{T}, \tag{4.6}$$

where the Curie constant is

$$C_C = \frac{\mu_0 \mu^2}{3 k_B T} \frac{1}{V_S} = \frac{\mu_0 \mu^2}{3 k_B T} \frac{3\sqrt{3}}{4a^3}. \tag{4.7}$$

The expected low temperature susceptibility of spin ice is thus double the value of a conventional paramagnet. Collective fluctuations of spins in loops enhance the susceptibility above the value obtained by considering fluctuations of independent spins. At high temperatures, Jaubert et al. (2013) predict the standard Curie law $\chi_T = C_C/T$. In between of the low- and high-temperature behaviour a Curie law crossover occurs. Experimental susceptibilities of spin ice materials exhibit such a crossover although it does match the theory in all aspects as discussed in detail in (Jaubert et al., 2013; Bovo et al., 2013b). It remains an interesting theoretical question how exactly the dipolar interaction between spins introduced in 4.5 influences the Curie law crossover.

For a finite system with periodic boundaries the loops can wind around the whole system. The ice manifold can only have a finite magnetization if there are more winding loops with one orientation than another; all closed non-winding loops contribute zero magnetization (Jaubert et al., 2008). The topological sector of a ground state in the ice manifold is given by the winding number which is the difference between the number of loops that wind the system in one direction and the number of loops that wind it in the opposite. There are multiple winding numbers depending on the topology of the system; they can be represented as a winding vector whose number of components is equal to the genus of the mainfold. As the magnetization is proportional to the winding vector, the susceptibility 4.6 of NNSI in its ground state is related to the fluctuations of its topological sector. While no single topological sector is selected in the absence of an external field, spin ice is often called topologically ordered because of its emergent gauge structure (Castelnovo et al., 2012) which is akin to a local order parameter that appears in more conventional ordered phases. Therefore spin ice can be considered as a classical analogue of topologically ordered states (Wen, 1990; Castelnovo and Chamon, 2007; Moessner and Sondhi, 2010).

4.4 Gauge structure

It is instructive to formulate a continuum theory for spin ice by coarse graining the spins. We define a local magnetization

$$\mathbf{M}(\mathbf{r}) = \mu \sum_{\mathbf{r}'_i \in V_e} \hat{\mathbf{s}}(\mathbf{r}'_i)/V_e \qquad (4.8)$$

by averaging the dipolar moments of the spins over a volume $V_e(\mathbf{r})$ around $\mathbf{r}$. We can see that the average magnetization over all 2-in-2-out tetrahedra is zero as there is no preference for any of tetrahedra in the absence of applied field. Any bias in the choice of tetrahedra will reduce the entropy, which has to be even in $\mathbf{M}$ due to the symmetry $\mathbf{M} \rightarrow -\mathbf{M}$ which corresponds to relabeling the tetrahedra. To the lowest order, the entropy is quadratic in the local magnetization

$$S[\mathbf{M}(\mathbf{r})] = S_0 - \frac{\mathfrak{K}}{2V} \int |\mathbf{M}(\mathbf{r})|^2 \, \mathrm{d}V \qquad (4.9)$$

which was first proposed for spin ice by Isakov et al. (2004) and Henley (2005) in order derive the dipolar correlations we give below. The generalized stiffness constant for NNSI $\mathfrak{K} = \mu_0/(2C_C)$ was derived by Ryzhkin (2005) using an analogy to the water ice theory (Jaccard, 1964; Ryzhkin and Whitworth, 1997). This yields

$$\frac{\mathfrak{K}}{2} |\mathbf{M}(\mathbf{r})|^2 = -\frac{1}{2} \frac{8 a \, k_B}{\sqrt{3}} |\mathbf{W}(\mathbf{r})|^2 \, , \qquad (4.10)$$

where $\mathbf{W}(\mathbf{r}) = \mathbf{M}(\mathbf{r}) a/(2\mu)$ is the configurational vector (with the units of length). The magnetic moment cancels out because only the configuration of the spins matters.

The spins can be seen as flux lines of magnetization (or the configurational vector). The 2-in-2-out ice manifold condition is equivalent to a divergence-free condition

$$\nabla \cdot \mathbf{M} = 0. \qquad (4.11)$$

The solenoidal character of the coarse-grained magnetization captures how the spin ice manifold is composed of closed loops.

The entropy 4.9 is a logarithmic measure of the number of accessible microstates. Together with the divergence-less constraint we can thus obtain a functional for the probability distribution of the coarse-grained ground states

$$\mathscr{P}[\mathbf{M}(\mathbf{r})] = \delta(\nabla \cdot \mathbf{M}) \exp\left[-\frac{\mathfrak{K}}{2} \int |\mathbf{M}(\mathbf{r})|^2 \, \mathrm{d}V\right] \qquad (4.12)$$

The energy functional and the divergenceless constraint exactly mirror the behaviour of magnetic field in electrodynamics. Therefore spin ice possesses the $U(1)$ gauge structure with a vector potential **A** yielding

$$\mathbf{M} = \nabla \times \mathbf{A}. \tag{4.13}$$

The distribution of states can be stated in the terms of the gauge-dependent vector potential

$$\mathscr{P}[\mathbf{A}(\mathbf{r})] = \exp\left[-\frac{\mathfrak{K}}{2}\int |\nabla \times \mathbf{A}(\mathbf{r})|^2\, \mathrm{d}V\right]. \tag{4.14}$$

This emergent gauge behaviour even led to proposals that quantum electrodynamics could emerge in spin ice as quantum fluctuations become strong at low temperatures (Hermele et al., 2004). See (Henley, 2010) for a review of models that possess a Coulomb phase with the $U(1)$ gauge structure. Also note that the analogy with electrodynamics is only valid at long wavelengths.
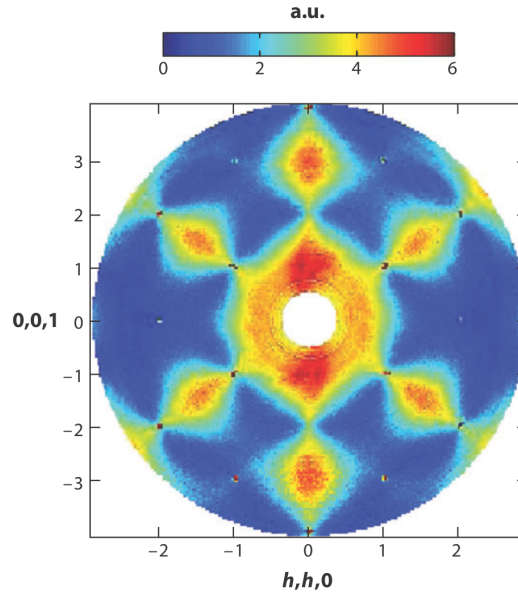
Figure 4.4: **Pinch points in HTO spin ice.** The ice rules lead to dipolar correlations in spin ice. Their reciprocal space signature are the pinch points which are revealed by polarized neutron scattering. Figure from (Fennell et al., 2009).

4.4.1 Pinch points

The continuum theory allows calculating correlations in the spin ice manifold. The distribution 4.12 can be seen as an action of a Gaussian theory which would yield no correlations between different points in

space $\langle \mathbf{M}(\mathbf{r})\mathbf{M}(0)\rangle \propto \mathbb{1}\delta(r)$ where $\mathbb{1}_{ij} = \delta_{ij}$ is the identity tensor. In Fourier space, this means that the scattering function at $\mathbf{k}$ would be diagonal and wave-vector independent

$$\langle \mathbf{M}(\mathbf{k})\mathbf{M}(-\mathbf{k})\rangle = \frac{\mathbb{1}}{\mathfrak{K}}. \tag{4.15}$$

The divergence-free constraint 4.11 changes this radically. In Fourier picture, the constraint reads

$$\mathbf{k}\cdot\mathbf{M} = 0 \tag{4.16}$$

Thus the component of magnetization at $\mathbf{k}$ is transverse to the respective wave vector. If we project out the longitudinal components we obtain

$$\langle \mathbf{M}(\mathbf{k})\mathbf{M}(-\mathbf{k})\rangle = \frac{1}{\mathfrak{K}}\left(\mathbb{1} - \frac{\mathbf{k}\otimes\mathbf{k}}{k^2}\right), \tag{4.17}$$

where $\otimes$ denotes the tensor product. The components of this scattering tensor can be measured by polarized neutron scattering. The tensor is a non-analytic function of the wave vector for $\mathbf{k} \to 0$ because its limit depends on the direction of approach. This non-analyticity manifests itself as a pinch point – a bowtie structure observed in scattering experiments. Pinch points were first proposed in ferroelectrics by (Youngblood and Axe, 1981). The occurrence of pinch points in neutron scattering is one of the strongest confirmations of the ice-like nature of spin ice (Morris et al., 2009; Fennell et al., 2009). We reproduce the experimental result in figure 4.4.

Inverse transforming the equation 4.17 back to the real space yields algebraic dipolar correlations

$$\langle \mathbf{M}(\mathbf{r})\mathbf{M}(0)\rangle \propto \frac{1}{\mathfrak{K}}\left(\frac{\mathbb{1} - 3(\mathbf{r}\otimes\mathbf{r})}{r^3}\right). \tag{4.18}$$

In the following section we show the importance of these correlations as they allow for the introduction of dipolar interactions between spins without fundamentally influencing the spin ice ground state.

4.5 Dipolar spin ice

The nearest-neighbour spin ice gives a relatively good description of fundamental properties of spin ice. However, an analysis of energy scales in spin ice materials shows that for neighbouring spins the exchange interaction is comparable to the dipolar interaction. The exchange interaction is quite weak (order of $1\,\mathrm{K}$ compared to $1000\,\mathrm{K}$ in strong ferromagnets) because it is mediated by electrons buried
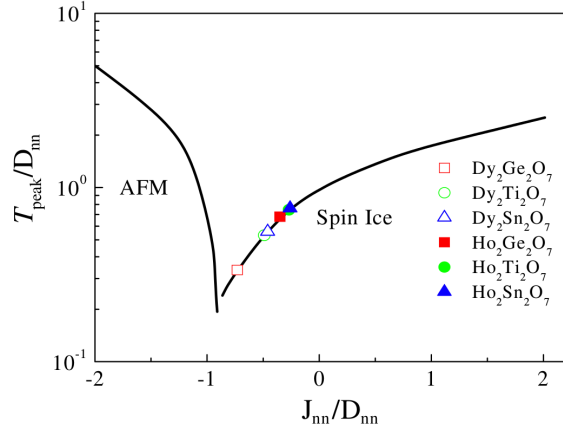
Figure 4.5: **Phase diagram of dipolar spin ice by den Hertog and Gingras (2000).** The ratio of the nearest–neighbour exchange J_{NN} and the dipolar interaction D_{NN} between spins determines the phase of the dipolar spin ice. The spin ice phase is stabilized even for antiferromagnetic exchange interaction ($J_{NN} < 0$) down to $J_{NN}/D_{NN} = -0.91$. At this value, there is a phase transition to the all-in-all-out phase ($Q = 0$ ground state of the antiferromagnetic NNSI model). The lines show the temperature where the magnetic part of the specific heat has its maximum for given J_{NN}/D_{NN}. The prediction obtained by simulating DSI is quantitatively very accurate. The figure is reproduced from (Zhou et al., 2012).

deep in the shells of the rare-earth ions (Harris et al., 1998; Moessner, 1998). At the same time dipolar moment of the rare-earth ions is large ($\sim 10\mu_B$). This necessitated a formulation of the dipolar spin ice model (Siddharthan et al., 1999; den Hertog and Gingras, 2000; Bramwell and Gingras, 2001)

$$\mathscr{H}_{DSI} = -J \sum_{\langle i,j \rangle} \hat{\mathbf{s}}_i \cdot \hat{\mathbf{s}}_j + D a_p^3 \sum_{i<j} \left[\frac{\hat{\mathbf{s}}_i \cdot \hat{\mathbf{s}}_j}{|\mathbf{r}_{ij}|^3} - \frac{3(\hat{\mathbf{s}}_i \cdot \mathbf{r}_{ij})(\hat{\mathbf{s}}_j \cdot \mathbf{r}_{ij})}{|\mathbf{r}_{ij}|^5} \right], \quad (4.19)$$

where both the short-range exchange interaction and the long-range dipolar interaction are included. The coupling constant is defined as $D = \mu_0 \mu^2/(4\pi a_p^3)$ and the nearest neighbour dipolar introduction is $D_{NN} = 5D/3$. Similarly, the strength of the nearest-neighbour exchange interaction is $J_{NN} = J/3$; the factor of 1/3 comes from the spins not being colinear. Note that the NNSI coupling constant J_0 obtained by truncating the DSI to the nearest-neighbour distance has contributions from both the exchange interaction and the dipolar interaction

$$J_0 = -3 J_{eff} = 3(D_{NN} + J_{NN}) \qquad (4.20)$$

From table 4.1 we can see that spin ice is a ferromagnet due to the dipolar interaction and despite the antiferromagnetic exchange interaction.

The DSI is known to describe scattering (Bramwell and Gingras, 2001) and specific heat (den Hertog and Gingras, 2000) of spin ice materials to a high degree of accuracy. As an example we show the comparison of experimental data and the predicted DSI phase diagram which shows the presence of the spin ice phase and of an all-in-all-out phase (see figure 4.5). The DSI supports a spin ice phase down to $J_{NN}/D_{NN} = -0.91$.

4.5.1 Projective equivalence

Interestingly, very few fundamental properties of spin ice are influenced by including the long range part of the dipolar interactions because the NNSI model itself already contains dipolar correlations. Isakov et al. (2005) proved this statement in detail and named it the projective equivalence.

If the exchange and dipolar contributions to the Hamiltonian 4.19 are Fourier transformed, their mean-field dispersion is given by 4×4 matrices whose dimension corresponds to the four sublattices $\hat{\mathbf{s}}_\alpha$ (Canals and Garanin, 2001). If the dispersion matrices are diagonalised, two flat and two dispersive bands are found. The flat bands have lower energy and their flatness represents the degeneracy of the ice manifold. The dipolar part of the DSI Hamiltonian has two almost degenerate low energy bands that are only weakly dispersive (first described by numerical simulations of Gingras and den Hertog (2001)) and two higher energy dispersive bands.

The crucial insight is that the (almost) flat energy bands correspond to the same eigenvectors for both parts of the DSI Hamiltonian. By projection to these lowest energy bands, Isakov et al. (2005) showed that the groundstates of DSI and NNSI are (almost) identical; the long-range dipolar interactions screen themselves due to the dipolar nature of the ice manifold. The correction to projective equivalence decays as r^{-5} in the real space and makes the DSI ground state manifold obtain a small bandwidth which leads to ordering of DSI at very low temperatures into a phase described by Melko et al. (2001). While a signature has been presented recently of spin ice recovering the Pauling entropy at cooling (Pomaranski et al., 2013), it is unclear whether this ordering is due to the dipolar interactions, further neighbour exchange interactions (Yavors'kii et al., 2008) or if it is a signature of a transition to a quantum spin liquid phase (Hermele et al., 2004; Shannon et al., 2012).
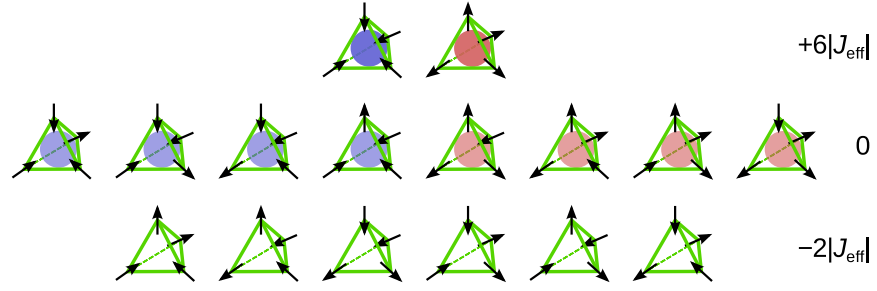
Figure 4.6: **Single tetrahedron configurations in spin ice.** We present an overview of the sixteen configurations of a single tetrahedron. The lowest row are the ground state configurations. In the middle row are the 3-in-1-out and 3-out-1-in carrying a single topological or magnetic charge. The upper row shows the doubly charged 4-in and 4-out tetrahedra. The cost of the defects in NNSI is shown on the right.

4.6 Defects in spin ice

So far we have only described the ground state properties of spin ice and left excitations out because it is useful to study defects in NNSI and DSI at the same time due to their shared properties. We start by describing the defects in the nearest-neighbour spin ice.

At finite temperatures there is a finite population of tetrahedra in NNSI that violate the ice rules. A single spin violating the ice rule leads to a 3-in-1-out or a 3-out-1-in tetrahedron. There are four 3-in-1-out and four 3-out-1-in configurations. In such a case two more bonds in the tetrahedron are frustrated setting the energy cost of the single defect at $2 J_{\text{eff}}$. In the language of grand canonical gas, this equates setting the bare chemical potential at $\nu_0 = -2 J_{\text{eff}}$. Two spins violating the ice rule results either in a four-in or in a four-out tetrahedron requiring all bonds to be in an energetically unfavourable state. The total cost of a double defect is $8 J_{\text{eff}} = -4 \nu_0$ which is the quadruple of the single defect cost. We show all possible configurations of a single tetrahedron in figure 4.6.

The single defects are created in pairs by a single spin flip which creates neighbouring 3-in-1-out and 3-out-1-in tetrahedra. However the defects are free to propagate by flipping another spin which does not change the total number of frustrated bonds in the system (see figure 4.7). It is impossible to identify a unique sequence of spins connecting the two defects. The defects have to be treated as independent particles. In NNSI, it costs energy to create the defect but no energy to move it – the defects become deconfined. The spin underlying the original defect pair fractionalizes. All defect configurations have the same energy but not the same entropy. This entropic interaction is weak and we will

discuss it below in the context of the magnetic interaction between defects in DSI.
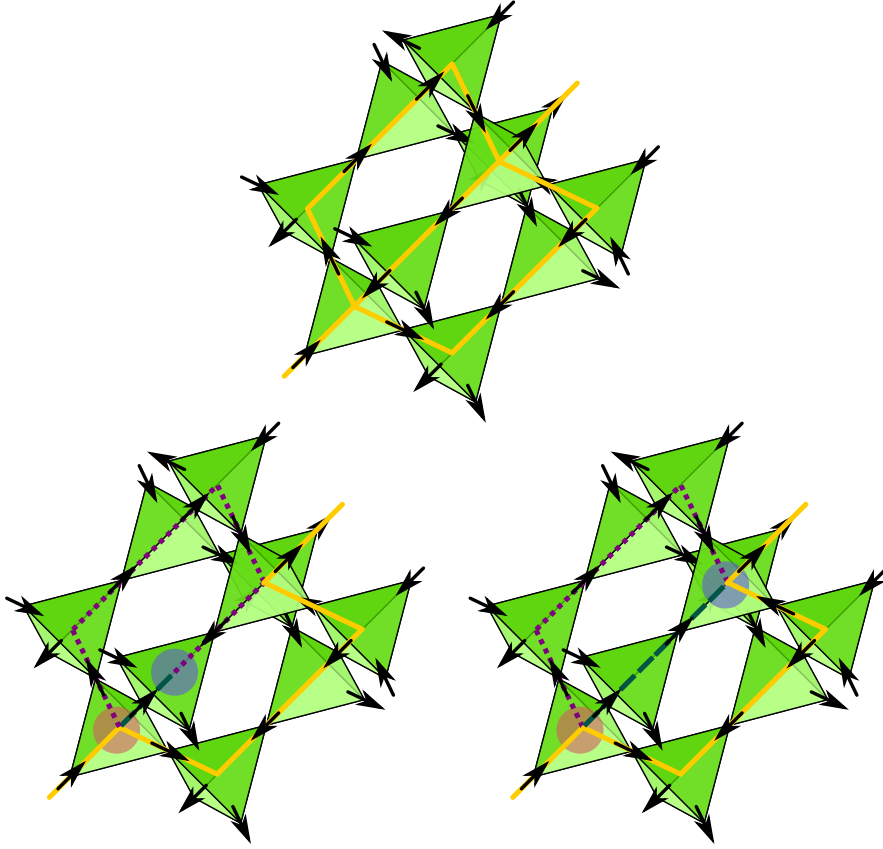
Figure 4.7: **Dirac strings in spin ice.** In the ground state the spins form a network of closed loops (upper panel). If a pair of defects is created a loop is broken which results in a string connecting the two defects (lower panel). For magnetic monopoles, the spin network is a classical equivalent of the unobservable Dirac strings connecting the elementary magnetic monopoles. Note that neither the loops nor the strings are uniquely identifiable. Both the dotted magenta line and the dashed cyan line connect the defects. If one of them is identified as a string, the other forms a part of a closed loop. This freedom underlies the gauge structure of spin ice. It also means that the pair of defects cannot be seen as a stretched dipole but have to be considered as independent quasiparticles.

4.6.1 Magnetic monopoles

In DSI, the projective equivalence guarantees only the screening of dipolar interactions in the ground state. Once the defects are created, the dipolar interaction of spins in the tetrahedra violating the ice rules

starts contributing to the energy once more. The defects form a decon-fined gas as in the NNSI but they possess important additional fea-tures – magnetic charge and Coulomb interaction. Its source is the long-range dipolar interaction between spins. Castelnovo et al. (2008) first described the Coulomb gas of magnetically charged defects in spin ice – magnetic monopoles. They put forward the dumbell model to il-lustrate the equivalence of the dipolar interactions of spins and Cou-lombic interactions of the magnetic monopoles.

Ryzhkin (2005) proposed a similar treatment of spin ice as a gas of charges. However, he described the charges as effectively non-interacting. His method was based inverting a pseudospin mapping used for protons in the theory of water ice which led to a mis-identification of the entropic interaction as stronger than the magneto-static one. However, his formula for the frequency dependence of the susceptibility of spin ice in terms of charge density has proven useful for NNSI.
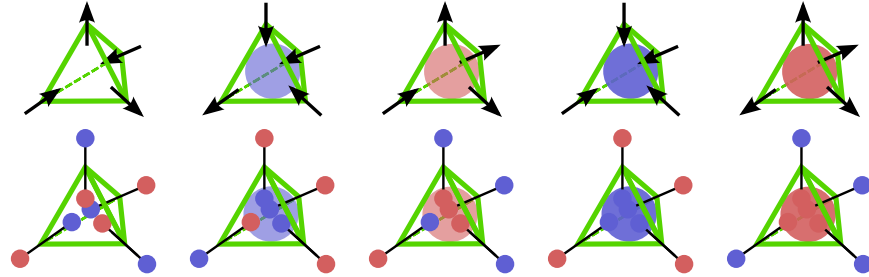
Figure 4.8: **Dumbbell model.** Examples of tetrahedra are shown that have zero, single positive, single negative, double positive, and double negative magnetic charge (ordered from left to right). The up-per and lower rows show their representation in the dipolar spin ice model and the dumbbell model respectively. In the dumbbell model the dipoles are extended to the centres of the tetrahedra, we show them shorter to illustrate the concept and to avoid overlaps. The total charge of the tetrahedron is the sum of contributions from the ends of the dipoles.

The main idea of the dumbbell model is to consider the spins as di-poles of finite extent, namely of the length a that separates the centres of neighbouring tetrahedra (see 4.8) which form a diamond lattice. The elongated dipole is a dumbbell with a magnetic charge $Q_m = \pm \mu/a$ at each end. In the centre of each tetrahedron these charges add. If the ice rules are respected, the tetrahedron is neutral because there are two positive and two negative contributions that compensate. If a single spin in a tetrahedron violates the ice rules, there is an excess charge $Q_m = \pm 2\mu/a$; the sign being positive for a three-in-one-out de-fect and negative for a three-out-one-in defect. Because only multiples

of the charge $Q_m = \pm 2\mu/a$ are realised, we will call these defects singly charged. Similarly the 4-in and 4-out defects have a double positive and negative charge respectively. In the dumbbell model, the degeneracy of the ice manifold is exact because any ground state is a charge vacuum. The error that is made by extending the dipoles decays as r^{-5} as it is exactly the weak violation of the projective equivalence discussed above.

The Hamiltonian of the dumbbell model is stated in terms of the Coulomb interaction between the magnetic monopoles

$$\mathcal{H}_D = \frac{\mu_0}{4\pi} \sum_{i<j} \frac{Q_i Q_j}{r_{ij}} + \frac{1}{2} \sum_i v_0 Q_i^2 \, , \tag{4.21}$$

where the on-site contribution v_0 is fixed by requiring that the energy of two neighbouring dipoles in the dumbbell and the DSI model matches, thus avoiding a divergent term coming from placing the charges at the ends of two extended dipoles on top of each other at the centres of the tetrahedra. The total energies of the dumbbell and the DSI models then differ by a constant for any given system size that scales as the total number of spins N_S. The value obtained by (Castelnovo et al., 2008) for a singly charged defect is

$$\frac{v_0}{2} Q_m^2 = \frac{v_0}{2} \left(\frac{2\mu}{a} \right)^2 = 2 J_{NN} + \frac{8}{3} \left(1 + \sqrt{\frac{2}{3}} \right) D_{NN} \, . \tag{4.22}$$

The double defects have an onsite contribution that is four times larger.

If we consider the dumbbell model as a grand canonical Coulomb gas (Jaubert and Holdsworth, 2009; Brooks-Bartlett et al., 2014) we can express the Hamiltonian as

$$\mathcal{H}_D = \frac{\mu_0}{4\pi} \sum_{i<j} \frac{Q_i Q_j}{r_{ij}} - (N_+ + N_-)\nu_0 - (N_{++} + N_{--})4\nu_0 \tag{4.23}$$

where the bare chemical potential of a single defect is given by the onsite energy $\nu_0 = \nu_\pm = v_0 Q_\pm^2/2$ from equation 4.22. The Coulombic interaction is not confining because it costs only a finite amount of energy to separate a pair of monopoles of unlike charge from the nearest-neighbour distance a to infinity. The Coulombic energy of two neighbouring charges and the bare chemical potential for a monopole are given in table 4.1. We will refer to the Coulomb gas of magnetic monopoles as the magnetolyte.

The dumbbell Hamiltonian 4.23 has clearly a simpler form than the DSI Hamiltonian 4.19. The dumbbell model is essentially a diamond lattice Coulomb gas which we have studied in the previous two chapters. This allows for the use of the whole apparatus of electrolyte

Dipolar spin ice	Dumbbell model
2-in-2-out ground state	Vacuum
3-in-1-out defects (local excitations)	Quasi-particles (monopoles)
Dipolar interactions	Coulomb interactions
between magnetic dipoles	between magnetic monopoles
Pyrochlore lattice	Diamond lattice
Canonical ensemble	Grand canonical ensemble

Table 4.2: **Mapping between the dipolar spin ice and the dumbbell model.** Reproduced from (Jaubert and Holdsworth, 2011).

theory for the study of spin ice and only minor modifications are necessary. We show that analytic expressions can be obtained for thermodynamic quantities in the dumbbell model that can be only found using numerical simulations in the DSI model. If further neighbour exchange interactions are considered, they add a short range interaction between the monopoles and shift the chemical potential. Nevertheless the Coulomb gas picture is preserved.

The validity of the mapping between DSI and the dumbbell model in the many body context was rigorously established by Jaubert and Holdsworth (2011). They have shown by coupled simulations of the two models that the bare chemical potential is a well defined property. We reproduce their translation between the canonical DSI and the grand-canonical dumbbell model in table 4.2. In the following we restrict ourselves to the single charged defects unless stated otherwise. This is a good approximation at low temperatures as the double defects are four times as costly.

4.6.2 Magnetization and Dirac strings

The spins do not appear in the Hamiltonian of the dumbbell model but they still constrain the configurations accessible to it. We would like to mention several effects that this has on the monopoles and their dynamics. We have already seen that even in the absence of any monopoles the spins possess a rich structure of a loop model that is described by the $U(1)$ gauge theory.

If a spin is flipped to create a pair of monopoles, any loop passing through the spin is split into two strings (see figure 4.7). As the division of the ice manifold into loops is not unique, there is also a freedom in chosing the strings. This reflects how the gauge structure is preserved even in the presence of monopoles. The strings are oriented and the 3-in-1-out and 3-out-1-in tetrahedra correspond to their sinks and sources,

respectively. In the continuum theory, the strings correspond to lines of magnetization flux connecting the monopoles. The divergence free condition 4.11 is violated

$$\nabla \cdot \mathbf{M} = -\rho_{Q_{\mathrm{m}}} \tag{4.24}$$

where $\rho_{Q_{\mathrm{m}}}$ is the volumic monopole charge density defined by the same coarse graining procedure as the magnetization.

Note that the monopoles in spin ice differ from magnetic monopoles as elementary particles as proposed by Dirac (1931). The Maxwell equation $\nabla \cdot \mathbf{B} = \mu_0 \nabla \cdot (\mathbf{H} + \mathbf{M}) = 0$ holds in spin ice with no modification. The monopoles are thus sources and sinks of the $\mathbf{H}$-field instead

$$\nabla \cdot \mathbf{H} = \rho_Q . \tag{4.25}$$

This is the equivalent of Gauss law in electrostatic. As the magnetic monopoles react to the $\mathbf{H}$-field, the Coulomb interaction between monopoles can be derived from the continuum theory. Therefore the continuum theory is consistent with the microscopic derivation.

When discussing the emergent gauge theory, we briefly mentioned its equivalent formulation in terms of the configuration vector $\mathbf{W} = \mathbf{M}a/(2\mu) = \mathbf{M}/Q_+$. The monopoles are sources and sinks of this field as well

$$\nabla \cdot \mathbf{W} = -\rho_{Q_{\mathrm{ent}}} . \tag{4.26}$$

The monopoles therefore possess an entropic charge $\rho_{Q_{\mathrm{ent}}} = (a/2\mu)\rho_Q$ in addition to the magnetic one. The singly charged monopoles have a charge with unity magnitude $Q_{\mathrm{ent}} = \pm 1$. By taking the functional derivative of the entropy functional 4.9 we obtain the entropic force

$$\mathbf{F}_{\mathrm{ent}}(\mathbf{r}) = -T \frac{\delta S[\mathbf{M}(\mathbf{r}')]}{\delta \mathbf{M}(\mathbf{r})} = \frac{8a\,k_{\mathrm{B}}T}{\sqrt{3}} \mathbf{W}(\mathbf{r})\delta(\mathbf{r} - \mathbf{r}') . \tag{4.27}$$

Thus the configurational vector mediates an entropic interaction between the charges which can be formally assigned the potential

$$U_{\mathrm{ent}}(r) = -\frac{8a\,k_{\mathrm{B}}T}{\sqrt{3}} \frac{1}{4\pi r} = -\frac{2a\,k_{\mathrm{B}}T}{\sqrt{3}\pi r} , \tag{4.28}$$

where the negative sign corresponds to the case of oppositely charged monopoles. The source of this interaction is the spin network underlying the charges. Even in the absence of dipolar interactions, the spins mediate an entropic Coulombic interaction between defects related to the dipolar correlations that the spins obtain due to the ice rules. If we define a characteristic length for the entropic interaction as an equivalent of the Bjerrum length

$$\ell_{T,\mathrm{ent}} = \frac{2a\,k_{\mathrm{B}}T}{\sqrt{3}\pi r} \frac{1}{2k_{\mathrm{B}}T} = \frac{a}{\sqrt{3}\pi} , \tag{4.29}$$

we can see that it is smaller than the nearest-neighbour distance between the monopoles a and independent of temperature. From this we can infer that the effect of the entropic interactions is quite weak.

As all entropic forces, $\mathbf{F}_{ent}$ expresses the average tendency of the system to move towards states that represent more microscopic configurations. It has a direct interpretation in spin ice. For example, a positive charge represents a 3-in-1-out tetrahedron. If it is surrounded by empty sites, it can only diffuse in the direction by flipping the three in spins. Diffusing in the direction given by the out spin would create a costly double defect. Thus the directions of the three in spins average into a preferrential direction for the monopole to move, which is exactly what the configuration vector $\mathbf{W}(\mathbf{r})$ expresses. Thus the Dirac strings provide kinetic constraints for the monopoles to move.

The charges flip spins as they move. Apart from flipping whole loops of spins which is prohibitively costly, the diffusion of monopoles is the only process for relaxation of the spin network. Thus the monopole current density is equal to the rate of magnetization

$$\frac{d\mathbf{M}}{dt} = \mathbf{j}. \tag{4.30}$$

In chapter 5 we will treat the implications of this equation on the magnetic susceptibility of spin ice focusing on cases when the monopole density is field dependent due to the Wien effect.

Morris et al. (2009) have observed the Dirac strings by first fully polarizing a sample of spin ice in [001] field and then removing the field. The only process that the sample can use to reduce its magnetization is to create a pair of monopoles and let them diffuse which flip the spins away from the direction of the original field. The fully polarized sample is specific because the monopoles always have to hop in the direction of the magnetization while being free to difuse in the remaining two dimensions. Thus they perform a two dimensional random walk with z direction playing the role of time. These random walks introduce correlations that are measurable by neutron scattering which reproduces the predictions.

We now investigate thermodynamic properties of spin ice using the fact that spin ice maps to an emergent magnetolyte. We show that its heat capacity can be described using the Debye–Hückel theory. Our approach is an extension of results obtained by (Morris et al., 2009; Castelnovo et al., 2011). It also serves to illustrate that equilibrium properties of spin ice are described in terms of electrolyte theory which is an important observation before we continue with describing the non-equilibrium properties of spin ice in the same terms.

4.7 Debye–Hückel theory for spin ice

In the grand-canonical Coulomb gas, we have found that the Debye screening leads to an increase in the equilibrium density above the density of the non-interacting gas. We expressed the excess chemical potential of the Coulomb gas above the value of its ideal counterpart by using the Debye–Hückel activity coefficient as $\Delta \nu = -k_B T \ln \gamma = k_B T \ell_T / (\ell_D + a)$ and shown that Debye–Hückel theory takes on the form of coupled equations 2.23. We can restate these equations for spin ice

$$n = \frac{4/3 \exp(-\beta \nu)}{1 + 4/3 \exp(-\beta \nu)} \tag{4.31}$$

$$\nu = \nu_0 + k_B T \frac{\ell_T}{\ell_D + a}. \tag{4.32}$$

The only modification is that the prefactor 4/3 replaces the prefactor 2 in the electrolyte which constitutes a single tetrahedron approximation. This reflects that there are eight singly charged configurations of tetrahedra and six uncharged tetrahedra as opposed to two charged and a single uncharged configurations for diamond lattice sites in the lattice electrolyte. This can be confirmed by measuring the density of defects or the specific heat (figure 4.9a) in the non-interacting limit $Q_m \to 0$. The agreement is not exact but the error of the approximation is small and comparable to the one made by adopting Pauling's approximation for counting the ground states. In figure 4.10a we show the influence of the factor 4/3 on the specific heat of the magnetolyte corresponding to DTO spin ice.

In the equation 4.31, the magnetic Bjerrum length is defined as $\ell_T = \mu_0 Q_m^2 / (8\pi k_B T)$ and the magnetic Debye length as $\ell_D = \sqrt{(k_B T \tilde{V}_T)/(Q_m^2 n)} = \sqrt{\tilde{V}_T/(8\pi \ell_T n)}$ in full analogy to the lattice electrolyte. The number density of monopoles is $n = (N_+ + N_)/N_T$ and N_T is the total number of diamond lattice sites (tetrahedra).

4.7.1 Heat capacity

The Debye–Hückel theory has a direct application to the heat capacity of spin ice as shown by Morris et al. (2009); Castelnovo et al. (2011). We give a short derivation of this result. First we relate the internal energy of the magnetolyte to its activity coefficient. Using the Güntelberg charging procedure, where each added charge responds to the configuration of previously added charges only (see section 2.2.2.1), we obtain the internal energy per site

$$u = \int_0^n k_B T \ln \gamma(T, n') \mathrm{d}n'. \tag{4.33}$$

It is convenient to re-express this procedure as a charging process from the infinitely dilute $(n \rightarrow 0)$ zero temperature state

$$u = \int_0^T k_B T \ln \gamma(T', n(T')) \left(\frac{\partial n}{\partial T'} \right) dT'. \tag{4.34}$$

As we represent spin ice as a grand-canonical gas where the bare chemical potential is fixed by the material properties, we write a Landau-type thermodynamic potential per tetrahedron for the grand canonical ensemble with fixed ν_0 (as define in section 2.1.1.1)

$$\zeta_0 = u - n \nu_0 = -n \nu_0 + \int_0^T k_B T \ln \gamma(T', n(T')) \left(\frac{\partial n}{\partial T'} \right)_{V, \nu_0} dT'. \tag{4.35}$$

Heat capacity at fixed chemical potential can be expressed as the derivative of the Landau potential

$$c_{\nu_0} = \left(\frac{\partial \zeta_0}{\partial T} \right)_{V, \nu_0} = (-\nu_0 + k_B T \ln \gamma) \left(\frac{\partial n}{\partial T} \right)_{V, \nu_0} = -\nu \left(\frac{\partial n}{\partial T} \right)_{V, \nu_0}. \tag{4.36}$$

If double defects are considered, the density n has to be replaced by twice the numerical ionic strength $2\mathscr{I}_n = n_+ + n_- + 4(n_{++} + n_{--})$ which we defined in 2.9 and the number densities of single and double defects are in the single tetrahedron approximation equal to

$$n_+ = n_- = \frac{4 \exp(-\beta \nu)}{6 + 4 \exp(-\beta \nu) + 2 \exp(-4\beta \nu)} \tag{4.37}$$

$$n_{++} = n_{--} = \frac{\exp(-4\beta \nu)}{6 + 4 \exp(-\beta \nu) + 2 \exp(-4\beta \nu)}. \tag{4.38}$$

The chemical potential of the double defects is four times the chemical potential of the single defects. The bare chemical potential is four times which we found while deriving the dumbbell model in section 4.6.1. The activity coefficient also quadruples because a double defect has an ionic atmosphere that is also doubly charged and as a result the Coulombic interaction is four times as strong than the interaction between a single defect an its atmosphere.

In figures 4.9 and 4.10 we compare the heat capacity obtained from the Debye–Hückel theory and from our simulations. We also include experimental results (group of S. T. Bramwell) and DSI simulations (group of M. Gingras). If the Coulombic interactions are switched off $(\ell_T = 0)$, we revert to the NNSI. Figure 4.9a shows that then the specific heat theory is very accurate both if the double defects are allowed or forbidden. In HTO, there is good agreement between the theory and simulations (figure 4.9b). We can see that Debye–Hückel theory
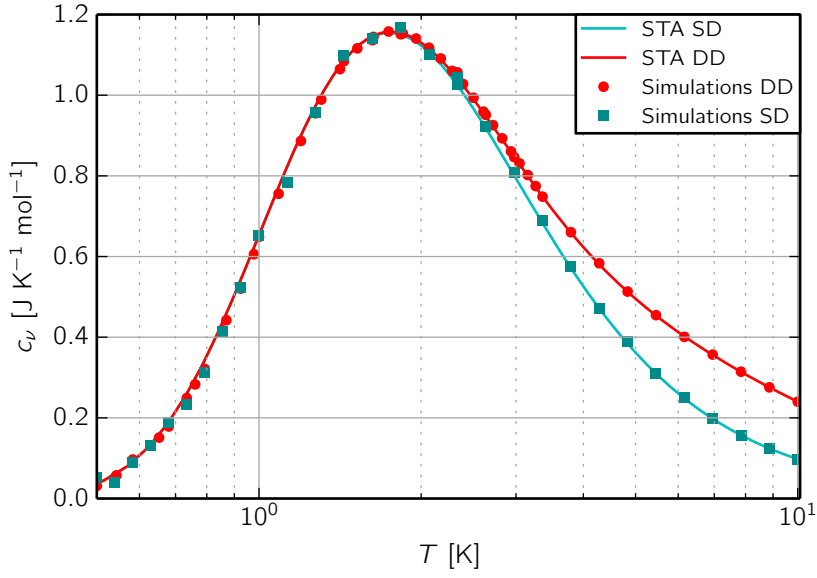
(a) NNSI heat capacity.
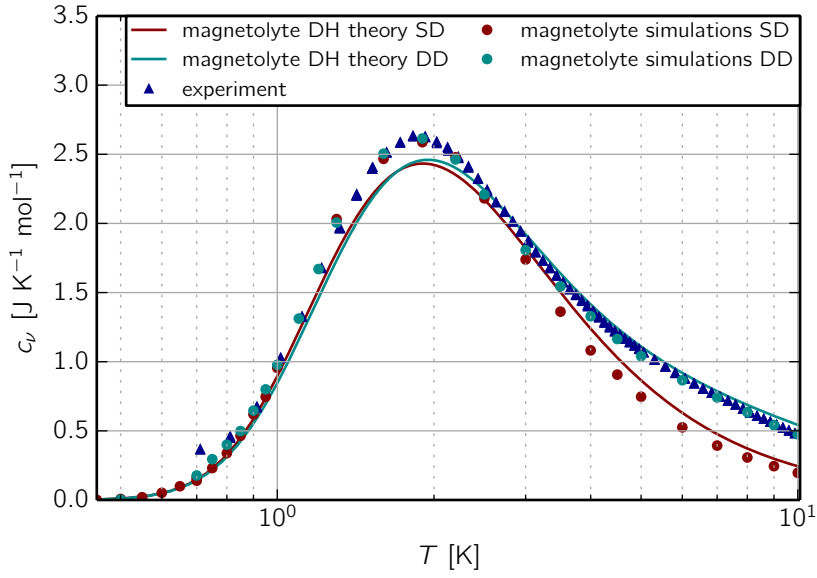
(b) HTO heat capacity.

Figure 4.9: **Heat capacity of spin ice – NNSI and HTO.** The upper panel shows that the single tetrahedron approximation on which we base the Debye–Hückel theory works very accurately in the absence of Coulomb interactions. We make a comparison both for the forbidden and included double defects. The lower panel then shows that the Debye–Hückel theory well describes the heat capacity of HTO. The experimental data are courtesy of S. T. Bramwell, L. Bovo and J. A. Bloxsom.
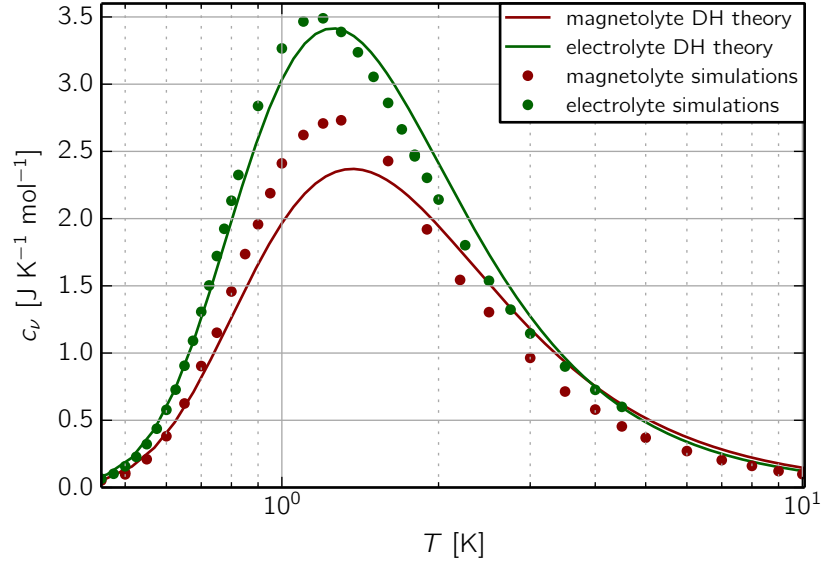
(a) DTO heat capacity – magnetolyte and electrolyte.
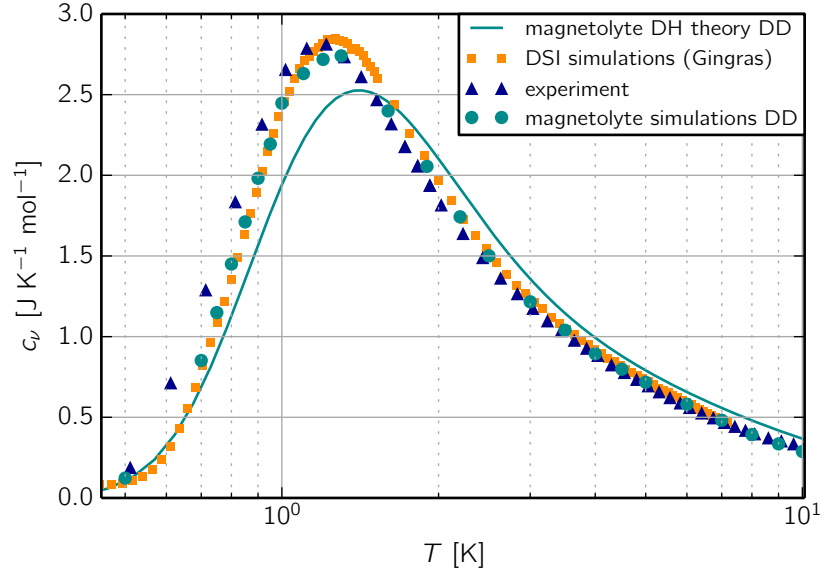
(b) DTO heat capacity – double defects.

Figure 4.10: **Heat capacity of spin ice – DTO.** Upper panel compares the simulations and the Debye–Hückel theory for an electrolyte and a magnetolyte with DTO parameters. The spins constrain the magnetolyte which has a lower specific heat in result. Lower panel shows that Debye–Hückel theory requires corrections around the peak of the specific heat. The discrepancy is due to the neglected pairing of monopoles. The magnetolyte simulations and DSI simulations have slightly different parameters ($U_C(a) = -2.9\,K$ vs. $U_C(a) = -3.07\,K$). The Debye–Hückel theory is plotted using the magnetolyte parameters. Full comparison with the experiment might require tuning the bare chemical potential. The experimental data are courtesy of S. T. Bramwell, L. Bovo and J. A. Bloxsom and the DSI simulations are courtesy of M. J. P. Gingras.

performs the best at low densities and high temperatures which is consistent with its limits of validity.

In figure 4.10 we show the heat capacity of DTO. The upper part 4.10a demonstrates that an electrolyte has a higher heat capacity than a magnetolyte under the same conditions due to the absence of the spin constraints. The residual Pauling entropy corresponds to the integral of the difference of $c_{v_0}(T)/T$ between the electrolyte and the magnetolyte from zero to infinite temperature. The adaptation of the theory by considering the statistical weights of the tetrahedra is necessary for correct a description of a magnetolyte and leads to a lower density of charges in the magnetolyte.

DTO is a more strongly correlated Coulomb gas than HTO. As a consequence, there is a visible discrepancy between Debye−Hückel theory and the simulation results in DTO (figure 4.10b). Pair correlation functions extracted from the simulations show that the discrepancy is due to the Bjerrum pairing; see figure 4.11 where we compare with the Debye−Hückel correlation function 2.15. The pairing is strongly influenced by short distance physics and it will thus differ in an electrolyte and in a magnetolyte[2].

In chapter 5, we study the second Wien effect in spin ice. In the dilute weak electrolyte limit (away from the specific heat peak) we use a modified Debye−Hückel—Bjerrum theory to obtain the zero field density of monopoles

$$n = \frac{4/3 \exp(\beta\, v_0)/\gamma}{\alpha + 4/3 \exp(\beta\, v_0)/\gamma} \tag{4.39}$$

$$\alpha = \frac{2}{1 + \sqrt{1 + 2K_A \gamma^2 n}} \tag{4.40}$$

$$\gamma = \exp\left(-\frac{\ell_T}{\ell_T + \ell_{D,\text{ent}}/\sqrt{\alpha}}\right) \tag{4.41}$$

$$\ell_D = \sqrt{\frac{1}{8\pi(\ell_T + \ell_{T,\text{ent})}n}} \;. \tag{4.42}$$

This is a sufficient approximation for obtaining the activity coefficient γ which is necessary for the description of the interplay between the Debye screening and the second Wien effect. The magnetolyte is a more dilute gas than the unconstrained lattice electrolyte under the same conditions (v^*, T^*). The Debye−Hückel theory thus better approximates the equilibrium density of an magnetolyte than of an electrolyte. As a result the Debye−Hückel—Bjerrum activity coefficient and the Debye−Hückel activity coefficient lie closer together in a magnetolyte than in

---

2 At the time of writing this thesis, it is an ongoing work together with the group of S. T. Bramwell to clarify corrections to the pairing theory due to the spin degrees of freedom, which would provide a better description of the peak of the specific heat.

an electrolyte in the parameter range where we simulate the second Wien effect.
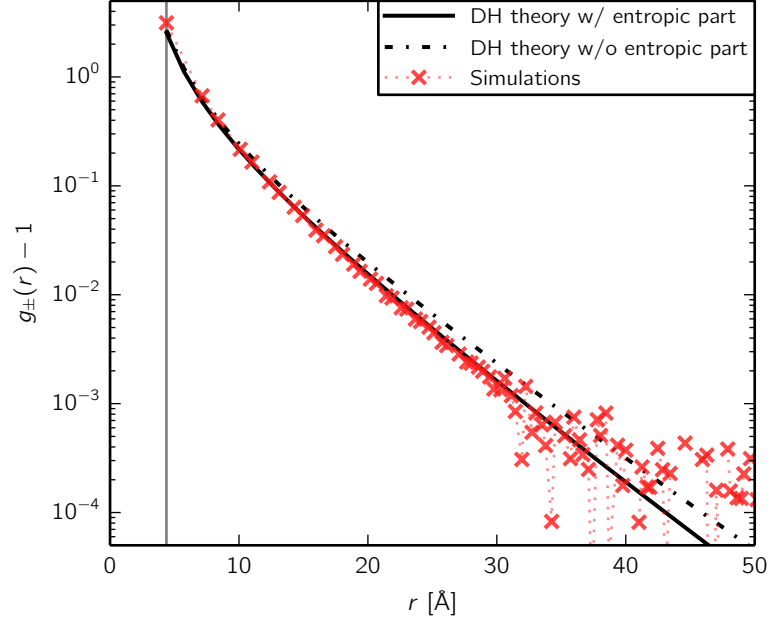
Figure 4.11: **Debye–Hückel correlations in spin ice.** The pair correlation function $g_\pm(r)-1$ in equiblibrium. The long-range decay has contributions from both the entropic and magnetostatic interactions (full black line) and exponential decay $\propto \exp(-r/\ell_{D,tot})$. The simulation results match the theory apart from the values at the shortest distances which is due to the Bjerrum pairing. Omitting the entropic correlations gives an exponential decay $\propto \exp(-r/\ell_D)$ at long distances (dash-dotted line) which deviates from the simulation results.

4.7.2 Magnetic and entropic interactions

Each monopole state is dressed in an extensive number of spin states leading to a effective entropic interaction between the charges. It is an interesting question how the entropic interaction contributes to the Debye–Hückel theory. Clearly, there is no contribution to the internal energy from the entropic interaction, but it contributes to the correlations in the system. One can define the entropic Debye length

$$\ell_{D,ent} = \sqrt{\frac{\tilde{V}_T}{8\pi \ell_{T,ent} n}} = \frac{a}{\sqrt{3n}}, \tag{4.43}$$

where we used the entropic Bjerrum length $\ell_{T,ent} = \frac{a}{\sqrt{3\pi}}$ and $\tilde{V}_T = 8a^3/(3\sqrt{3})$. The entropic Debye length also sometimes called the dif-

fusion length as well because it can be derived by considering the diffusion of defects in NNSI. It is sufficient to require the simultaneous minimization of the ice manifold entropy and the configurational entropy of defects (Bramwell, 2012).

The addition law for the magnetic and entropic Debye lengths follows from superposing the two types of interactions ($\ell_{T,\mathrm{tot}} = \ell_T + \ell_{T,\mathrm{ent}}$) which yields

$$\ell_{\mathrm{D,tot}}^{-2} = \ell_{\mathrm{D}}^{-2} + \ell_{\mathrm{D,ent}}^{-2}. \tag{4.44}$$

This addition law was first put forward in (Sen et al., 2013; Ryzhkin et al., 2013). As only the magnetostatic interaction contributes to the internal energy we have the following relation for the activity coefficient

$$-k_{\mathrm{B}} T \ln \gamma = k_{\mathrm{B}} T \ell_T / (\ell_{\mathrm{D,tot}} + a). \tag{4.45}$$

The entropic contribution can be included in the Debye–Hückel prediction for the specific heat capacity although its influence is hard to discern with the naked eye.

There are several approaches to Debye–Hückel theory in spin ice. Apart from the direct mapping to the Coulomb gas (Castelnovo et al., 2011), it is possible to show that the magnetostatic and entropic Debye–Hückel theory is borne out of the dispersion of bands of DSI and NNSI, respectively (Sen et al., 2013). These bands are obtained in the mean field fashion that was used to prove projective equivalence. An interesting result is the prediction for the scattering factor at pinch points from Debye–Hückel theory. The non-analyticity in the scattering factor at pinch points (see figure 4.4) survives to finite temperatures in DSI while it is smeared out in NNSI for any finite temperatures. The width of the pinch point is given by the total inverse Debye length $\ell_{\mathrm{D,tot}}^{-1}$.

The pinch points are a signature of the long-range behaviour of the magnetolyte which explains the influence of Debye–Hückel theory and the need of including the entropic interaction to confirm the scattering factor observed in simulations. On the other hand, the heat capacity mostly captures the short range behaviour of the system. This clarifies why the slight shift in the activity coefficient due to the entropic interactions has barely any influence on the prediction for the specific heat. We describe the numerical methods used to obtain the previously presented specific heat results in the following part of this chapter.

4.8 Simulating spin ice

Our simulations of spin ice are conceptually very close to our simulations of electrolytes (see 2.6). We simulate the dumbbell model which
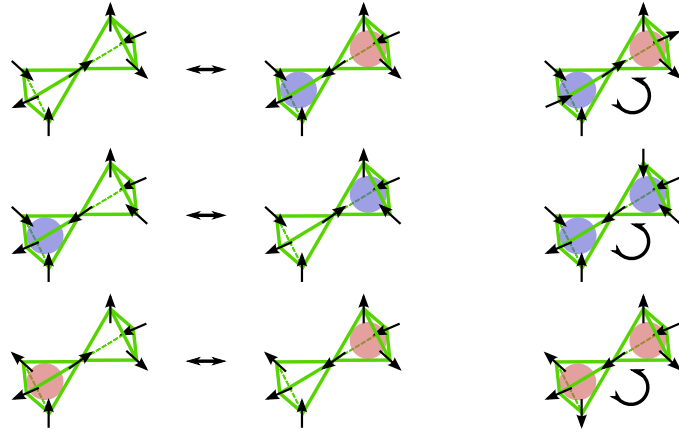
Figure 4.12: **Local moves in spin ice simulations** all correspond to a single spin flip. In the dumbbell model the spins constrain the monopole dynamics but the energy of the system is given by the monopoles. Charge pairs can be created from the ice manifold, moved, and annihilated (left). There are several cases where no spin flip is possible if we wish to avoid creating double defects (right). The upper right configuration is a noncontractible pair which slows down equilibration at low temperatures.

can be seen as a lattice Coulomb gas with spins added. The spins constrain the motion of charges. We use the Metropolis update scheme and we propose flipping a spin which is chosen with equal probability. From the perspective of the emergent Coulomb gas, the spin flip move unifies the creation, annihilation, and movement of charges. We sum up the possible moves in figure 4.12.

The internal energy is evaluated using the Ewald summation as described in the section 2.6.4. The last term in the Ewald expression for the internal energy 2.40 is proportional to the dipolar moment of charges and corresponds to the energy of a system which is embedded in a medium of a finite dielectric constant. A magnetic system surrounded by a medium of finite permeability will similarly have a demagnetization contribution to its energy (Melko and Gingras, 2004). The demagnetization field $-\mathscr{D}\mathbf{M}$ depends on the total magnetic moment of the system and as such it cannot be expressed purely in the terms of the dumbbell model for which all tetrahedra without monopoles are energetically equal. We resort to a hybrid approach, in which the first two terms in equation 2.40 are kept in the charge formalism of monopoles

and the last term is expressed in terms of the total dipolar moment of the system

$$U_{\text{Ewald}} = \frac{\mu_0 Q_{\text{m}}^2}{4\pi} \left[\sum_{\langle i,j \rangle} \frac{1}{L} \mathfrak{z}_i \mathfrak{z}_j \psi \left(\frac{\mathbf{r}_{ij}}{L} \right) + \frac{\mathfrak{f}}{2L} \sum_{i=1}^{N} \mathfrak{z}_i^2 \right.$$
$$\left. + \frac{2\pi}{(2\mu_{\text{r0}} + 1)V} \left| \sum_{i=1}^{N_{\text{S}}} \mu_i \right|^2 \right]. \tag{4.46}$$

This expression corresponds to a spherical sample ($\mathscr{D} = 1/3$) because the Ewald energy is a sum of contributions from concentric spherical shells.

We simulated systems both including and excluding the demagnetization; we note whenever results are shown where it is included. Melko and Gingras (2004) reason that equilibrium results obtained without the demagnetization term are of greater use as the demagnetization can be and has been (Quilliam et al., 2011; Bovo et al., 2013b) accounted for in experiment. This is no longer true out of equilibrium because the demagnetization term becomes time dependent; for example not only the absolute value but also the time dependence of magnetization is influenced. We use this to predict the effect that demagnetization has on the non-linear susceptibility in spin ice; see for example figure 5.15.

An important note regarding the Ewald summation is that evaluating the full long-range interaction is crucial for simulations of spin ice. Any truncation scheme aiming to replace the Ewald sum leads to a spurious behaviour of simulations (Gingras and den Hertog, 2001).

4.8.1 Freezing and worm algorithm

Spin ice is known to freeze at low temperatures. This is evidenced by prohibitively long times needed to equilibrate the samples. There are two reasons for this behaviour – disorder and intrinsic slowing down of monopole dynamics. The role of disorder is currently an active field of study with many open questions. We give two results: substitutions of non-magnetic ions can lead to a topological glassiness (Sen and Moessner, 2014); oxygen vacancies pin monopoles and slow down equilibration (Sala et al., 2014). We focus on the slowing down inherent to spin ice models and show how it can be remedied in simulations by the use of the worm algorithm.

Even the pure DSI and dumbbell models exhibit freezing on their own. Apart from quantum resonances at the very lowest temperatures, the diffusion of monopoles is the only way to equilibrate the spin network. Decreasing temperature leads to an exponential decrease in
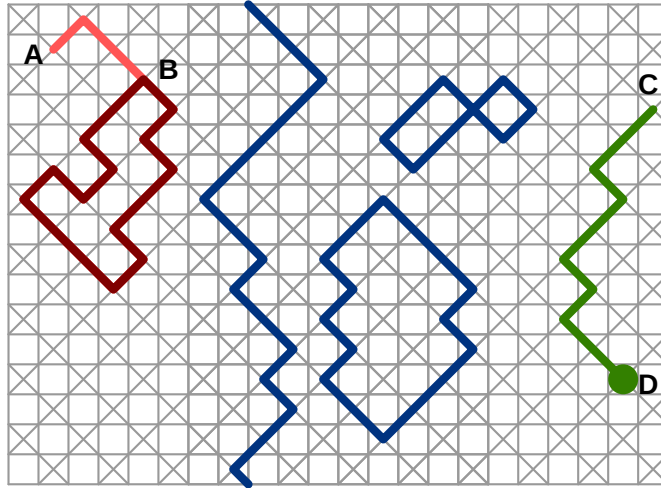
Figure 4.13: **Types of worm algorithm.** The short loop starts from the point A and propagates until it crosses its own path at point B. Only the spins in the closed loop (dark red) are flipped while the tail (light red) is discarded. The long loop (blue) only closes if it reaches its starting tetrahedron. It can thus cross its own path. Both the long and short loops can wind the system, it is however more common for long loops. The charged worm starts at C and propagates until it encounters a charge at D which is then moved back to C while the spins along the worm are flipped. This can be interpreted as creating a pair of defects, one of which is diffuses through the system until it annihilates. The algorithms are shown for two dimensional square ice which can be seen as a projection of the pyrochlore lattice.

monopole density. This leads to an exponential increase in relaxation times (Jaubert and Holdsworth, 2009).

Moreover, a fraction of monopoles ends up in noncontractible pairs (Castelnovo et al., 2010). These Coulombically bound nearest neighbour monopoles have a spin connecting them whose flip would not annihilate the pair but would create two double defects instead. The noncontractible pairs thus need to travel the shortest loop of six spins at minimum to annihilate. This population has a very low mobility yet it contributes to sustaining the total density above the equilibrium value.

The worm algorithm provides a means to equilibrate DSI and dumbell models in numeric simulations (Barkema and Newman, 1998; Melko and Gingras, 2004). The main idea is to propose a move that flips a loop or a string of spins and that can be seen as creation of a pair of virtual charges, their propagation through the system, and their subsequent annihilation. Without any loss of generality we can assume that one virtual charge is kept fixed and the other is mobile. There are three main types of the worm algorithm which we will denote short

loop, long loop, and charged worm (see figure 4.13). In all three cases, the propagation of the virtual defects follows the same rules as the motion of real monopoles with the added posibility of passing through another charge if the type of worm allows this. This results in a temporary creation of a double charge or an empty site. The charge number is recovered once the worm leaves this site.

The difference between the types of the worm algorithm lies in the condition that terminates the propagation. In the short loop algorithm, the mobile monopole propagates through the system until it either meets the fixed monopole or visits a site over which it travelled. The loop of spins which it travelled is flipped. The long loop closes only if the original site (the fixed monopole) is met. Charged worm signifies that the mobile charge propagates until it encounters an oppositely charged real monopole which it annihilates. The fixed virtual monopole is then kept as a real one instead of the annihilated one. As a result the string of spins between the new and the original charge position is flipped and the monopole is effectively transported over a long distance.

4.8.2 Optimal choice of algorithms

The algorithms that we have different efficiency in equilibrating the spin and charge degrees of freedom. We use the spin autocorrelation function $C_s(t) = (1/N_S)\sum_i \hat{\mathbf{s}}_i(0) \cdot \hat{\mathbf{s}}_i(t)$ defined by (Jaubert and Holdsworth, 2009; Brooks-Bartlett et al., 2014) to measure the efficiency of the algorithms in equilibrating the system. Similarly we define the autocorrelation function for the charges $C_Q(t) = (1/N_T)\sum_i \delta(Q_i(t) - Q_i(0))$, which decays from unity down to $1 - 2\langle n \rangle + 3 \langle n \rangle^2/2$ in equilibrium and can be afterwards rescaled to cover the interval $[0, 1]$. The charge autocorrelation function measures how effective the algorithm is in equilibrating the charge degrees of freedom present in the system. Finally, we use the time dependence of the average charge density $\langle n(t) \rangle$ during the equilibration of the system from zero charge density to its thermal value. Note that this last criterion is correlated with the charge decorrelation. All these functions have an exponential time dependence and allow the extraction of a characteristic equilibration time in the units of CPU cycles.

We can in principle choose any combination of the above mentioned algorithms. It is however useful to use a mix that minimizes the computational time needed to decorrelate the system. We have four algorithms at our disposal and we wish to simultaneously minimize three equilibration times. This is a linear optimization problem if we neglect any synergy between the algorithms. As a result we always obtain three

algorithms that are the most efficient ones in equilibrating the whole system. The single spin flips are always included as they are the only means how to change the total charge density. Among the worms, the long loop algorithm is the most efficient in decorrelating the spins. It was indeed shown that the long worm often spans a finite fraction of the spins even in the thermodynamic limit (Jaubert et al., 2011). The short loop algorithm is the least efficient for the parameters we use. The charge worm is particularly useful at low densities but lags behind the single spin flips as the Coulomb gas becomes dense at higher temperatures.

Note that the results of our optimization are in a strict sense only valid for our implementation of the algorithms and the computer system where we run our simulations. We nevertheless expect them to hint at the general applicability of the algorithms discussed.

4.8.3 External magnetic field

When a field is applied we restrict ourselves to local spin dynamics. The energy difference in the Metropolis energy then contains the Zeeman energy $2\mu_0 \mathbf{H} \cdot \mu$ of flipping the spin in magnetic field $\mathbf{H}$. In the monopole picture this is the energy $\mu_0 Q_{\mathrm{m}} \mathbf{H} \cdot \mathbf{a}$ for a charge to hop the nearest neighbour distance in the applied field. It is possible to extend the worm algorithm to situations where an external field or even external pressure is applied to spin ice (Jaubert et al., 2010). But the resulting stochastic process does not correspond to any realistic physical dynamics in time. Such dynamics is our main interest for simulating the out of equilibrium behaviour of the magnetolyte. Therefore we only use local moves as soon as the field is applied.

We have presented an overview of equilibrium properties of spin ice and shown how it maps to a magnetic Coulomb gas, the magnetolyte. We continue in the following chapter by combining the results of this and the previous chapter to show that the non-equilibrium physics of the magnetolyte can be described using the second Wien effect which has interesting implications for the non-linear susceptibility of spin ice.

5

Second Wien Effect in Spin Ice

In the preceding chapters we have established the second Wien effect as a robust and universal non-linear response of a Coulomb gas. We have also given evidence that magnetic monopoles in spin ice form a prime example of such a Coulomb gas. In this chapter we wish to demonstrate that the second Wien effect is largely responsible for the non-linear susceptibility of spin ice at low temperatures. If spin ice is driven periodically, its magnetic response is greatly enhanced as the amplitude of driving grows. The increase in response follows the same theoretical curve as the increase in density of charges in an electrolyte. This is because the monopoles are the dominant degrees of freedom and their density is increased by the Wien effect.

There is no permanent direct current of monopoles in spin ice. As magnetic monopoles flip the spins while moving, the rate of magnetization is equal to the monopole current density $\mathrm{d}\mathbf{M}/\mathrm{d}t = \mathbf{j}_\mathrm{m}$. There is an upper limit to magnetization so that no monopole current can be permanent which precludes the direct field Wien effect (see figure 5.1). The monopole density in spin ice shown in this figure increases only transiently. Afterwards it decreases below the equilibrium value because a state with a finite magnetization supports fewer monopoles in equilibrium than the zero magnetization state.

The Wien effect in spin ice was first proposed by Bramwell et al. (2009). The experiment presented in the same work was based on a muon spin relaxation (μ-SR). The principle of this method is to observe the dynamics of the spin of muons implanted into the sample. The muon spin dynamics is influenced by its environment and can be measured because the direction of the muon spin determines the trajectory of positrons into which the muon decays. The assumption of Bramwell et al. (2009) was that the increased magnetization rate caused by the enhanced monopole density speeds up the muon precession. A second assumption was that the increased monopole density could be observed for a sufficiently long time before the magnetization of the sample suppressed the increase as the applied fields were relatively low.

Interpreting μ-SR is however not straightforward. The described method of measuring the Wien effect was called into question (Dunsiger et al., 2011; Bramwell and Giblin, 2011; Blundell, 2012). The main argument is the presence of large internal fields at perspective muon
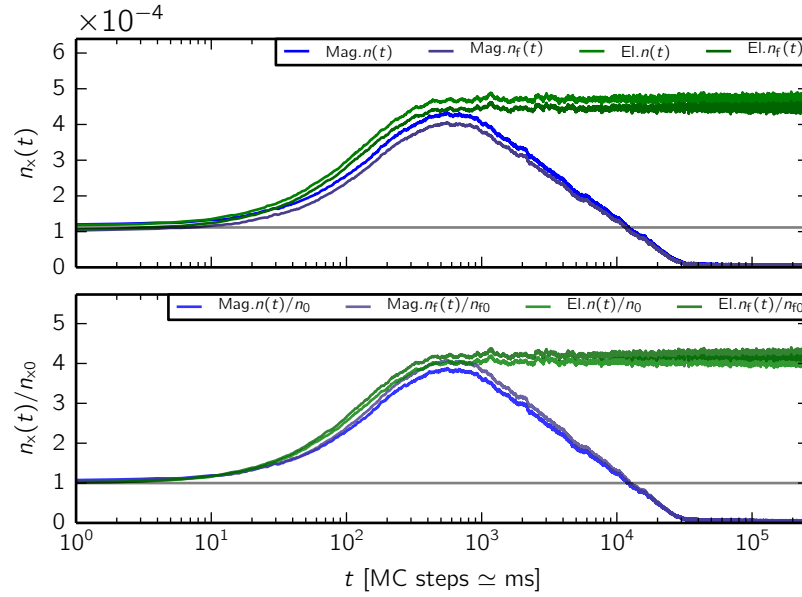
Figure 5.1: **Wien effect in electrolyte and in spin ice.** After a sudden field quench, the charge density in electrolyte relaxes to a steady state value (green line). In spin ice the increase is only transient as the magnetization of the sample prevents permanent currents (blue line). Upper panel shows the absolute change and the lower the relative change in both free and total charge densities. The parameters are chosen so that the zero-field charge density and temperature are equal both in the electrolyte and the magnetolyte. The magnetolyte reacts more slowly due to the presence of kinetic constraints. The figure corresponds to DTO at 0.45 K and 50 mT external field.

sites which are outside the monopole sites (Sala et al., 2012). Such strong fields are supposed to influence the muon precession more than the fields generated by magnetic monopoles. There also another open questions about μ-SR. For example, the signal might describe the diffusive quantum dynamics of the muons and not the spin dynamics (Quémerais et al., 2012). The uncertainty about the exact place where the muons end before they emit the positrons might mean that the Wien effect signal is measured outside of the sample and comes from the long range part of the monopole field (Calder et al., 2009).

Giblin et al. (2011) measured the decay of magnetization in spin ice after the removal of the external field. Observed curves matched a non-linear model involving the Wien effect. Even though it was a step towards a correct description of the orientational dynamics of the Wien effect, their kinetic model exhibited several discrepancies. The final fit of the magnetization curves yielded a bound pair density higher than the free monopole density at temperatures where the opposite is

predicted by the Coulomb gas theory and simulations. We present a kinetic model in this chapter that yields a substantially better fit with our simulation data.

Our proposal concerns a non-linear extension of bulk AC susceptibility which involves fewer assumptions but requires a full treatment of the magnetization dynamics. As we saw in the electrolyte case, the Wien effect can be caused by periodic driving (see section 3.3.5). If the AC Wien effect establishes faster than the system magnetizes, it will remain observable despite the kinetic constrains. Our goal in this chapter to use the second Wien effect to describe the non-linear susceptibility of spin ice. Before we achieve this objective, we provide an analysis of the non-equilibrium dynamics of the magnetolyte in spin ice in the following steps. We use numerical simulations once again to refine our predictions.

We first give an overview of the time scales for the Wien effect and magnetization dynamics. We derive a simple kinetic model motivated by the simulations which describes most of the features of the Wien effect in spin ice. Subsequently, we confirm the presence of the Wien effect in the dumbbell model using simulations.

We put forward three realistic protocols, a sudden field quench, rectangular wave driving, and sine wave driving. In the field quench scenario, we show that the time scales for increase and decrease in the monopole population follow the values predicted from treating these processes as independent. On the other hand, the periodic driving stabilizes the Wien effect over a broader range of frequencies than the characteristic time scale would predict. This is due to its non-linear dependence on the modulus of the applied field. We predict clear experimental signatures of the second Wien effect in the non-linear susceptibility of spin ice at temperatures and fields accessible to current experimental set-ups. Analysis of demagnetization shows that the signature of the Wien effect depends on the shape of the crystal. Nevertheless, it stays visible in both needle shaped and spherical crystals.

The magnetic monopoles in spin ice are sources and sinks of the **H** field and the force applied to them depends on the internal **H** field (see section 4.6.1). In the spin ice literature, we more often found the applied magnetic field **B** in tesla. Therefore we write formulas with **H** field but plot the figures with the applied field $\mathbf{B} = \mu_0 \mathbf{H}$ given in tesla. If there is no index attached, **H** denotes the external magnetic field and H its magnitude. We write the component of vector quantities that is parallel to **H** using the normal font weight (e. g. $\mathbf{j}_m \rightarrow j_m$). The field acting on the monopoles can be expressed as $\mathbf{H}_m = \mathbf{H} - \mathbf{M}/\chi_T$ (see section 4.6.2).

5.1 Time scales

We start by analysing the characteristic time scales in spin ice, considering various effects as independent. Treating the dynamics of each individually allows a deeper analysis which will serve for a later critique of approximations made when we consider coupling between the Wien effect and magnetization dynamics.

5.1.1 Time scales in double equilibrium

Two time scales[1] are relevant for establishing the second Wien effect – the *chemical time lag* τ_c and the *Langevin time lag* τ_L (Onsager, 1934). We consider the double equilibrium

$$\text{charge source} \overset{\tau_c}{\rightleftharpoons} \text{bound pairs} \overset{\tau_{L(H)}}{\rightleftharpoons} \text{free charges} \tag{5.1}$$
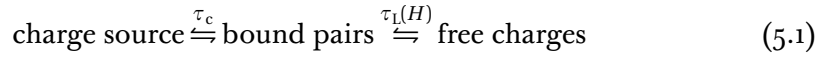
whose steady state properties were treated in section 3.2.5. The first reaction is first order in both molecules (or zero charge sites) and bound pairs, as can be shown by scaling arguments, since doubling the number of zero charge sites doubles the creation rate. The second reaction is first order in bound charges and second order in free charges (i. e. quadratically dependent). The kinetic equations are

$$\frac{\mathrm{d}n_b}{\mathrm{d}t} = k_{cr}(1 - n_b - n_f) - k_{an}n_b \tag{5.2}$$

$$\frac{\mathrm{d}n_f}{\mathrm{d}t} = k_D n_b - \frac{1}{2}k_A n_f^2, \tag{5.3}$$

where k_{cr}, k_{an}, k_A, and $k_D = K_D(H)k_A$ are the creation, annihilation, association, and dissociation rate constants, respectively. The dissociation rate constant is considered field dependent based on the Wien effect theory (see section 3.2.4).

In our simulations, we work in a regime where $1 \gg n_f \gg n_b$ and we assume that the first equilibrium establishes itself faster than the second (buffering of the bound pairs, see equation 3.68). The separation of time scales $\tau_c \ll \tau_L$ is justified because adding or removing charges takes a single MC step whereas τ_L can be estimated as the number of steps to diffuse the Bjerrum length ℓ_T. Hence we investigate the kinetics of the two equations separately.

The definition of a bound pair can be consistently varied as we discussed in section 2.4.1. We do not expect a strong influence of this choice on the dynamics. The rate constants k_A and k_D are independent of the bound pair definition within the scope of Onsager's original

---

1 The names of time scales reflect Onsager's original article. Langevin lag refers to the first kinetic treatment of association in Ref. (Langevin, 1903).

theory as discussed in section 3.2.2 and reference (Mason and McIlroy, 1978). Simulations allow us to investigate different definitions of bound pairs to verify this hypothesis.

5.1.1.1 Charge creation and annihilation

Chemical time lag τ_c describes how fast the first equilibrium reacts to a shift in the number of bound pairs induced by the second equilibrium. For simplicity, reorientation of bound pairs necessary for the subsequent dissociation can be included in the chemical time lag at this point. It cannot be distinguished at this level of treatment what fraction of the pairs reorients by diffusion and what fraction annihiliates and is subsequently re-created in a more favourable orientation.

We treat the free charge density as fixed $n_f(H)$ because it reacts on a slower time scale than the equilibrium between the bound pairs and the charge source. Solving the equation 5.2 yields that, the number of bound charges n_b approaches exponentially the steady-state value

$$n_b(H) = \frac{k_{cr}}{k_{cr} + k_{an}}(1 - n_f(H)) \tag{5.4}$$

with the chemical time lag

$$\tau_c = \frac{1}{k_{cr} + k_{an}}, \tag{5.5}$$

where for our simulations $k_{cr} = \exp(2\beta \nu_0)\exp(-\beta U_C(a))/\tau_0$ is estimated from the Monte Carlo probability of creating a pair on two neighbouring empty sites. The creation is on average proposed every MC step τ_0. The annihilation is always accepted in a dumbbell model simulation for the values of coupling and fields relevant for spin ice. The resulting time lag can be estimated using the bare Coulomb energy to be

$$\frac{\tau_c(0)}{\tau_0} \simeq \frac{1}{1 + \exp(2\beta \nu_0 + 2\ell_T/a)}, \tag{5.6}$$

For our purposes $\exp(2\beta \nu_0 + 2\ell_T/a) \ll 1$ and we can consider $\tau_c(0) \simeq \tau_0$, i.e. the bound pair density relaxes in a single Monte Carlo step.

5.1.1.2 Wien effect time scale

The Wien effect is a diffusive bound pair dissociation which can be cast in terms of chemical kinetics. The rate equation for the bound pair dissociation is

$$\frac{dn_f}{dt} = k_D n_b - \frac{1}{2}k_A n_f^2. \tag{5.7}$$

As we consider the first equilibrium to be much faster, we can substitute for n_b from 5.4

$$\frac{\mathrm{d}n_f}{\mathrm{d}t} = \frac{k_{cr}}{k_{cr} + k_{an}} K_D(H) k_A (1 - n_f) - \frac{1}{2} k_A n_f^2 . \tag{5.8}$$

to obtain a Riccati equation with the solution

$$n_f(t) = \frac{2}{k_A \tau_L} \tanh\left(\frac{t - t_0}{\tau_L}\right) - C_L, \tag{5.9}$$

where τ_L is the Langevin time lag expressed as

$$\tau_L = \frac{2}{k_A \sqrt{C_L(C_L + 2)}}, \tag{5.10}$$

and the constant C_L can hence be expressed in terms of steady state densities

$$C_L = \frac{k_{cr}}{k_{cr} + k_{an}} K(H) = \frac{n_b(H)}{1 - n_f(H)} \frac{(n_f(H))^2}{2 n_b(H)} = \frac{(n_f(H))^2}{2(1 - n_f(H))}. \tag{5.11}$$

Combining the two previous equations, we express the Langevin time lag in the steady state densities as

$$\tau_L(H) = \frac{1 - n_f(H)}{2 - n_f(H)} \frac{4}{n_f(H) k_A} \simeq \frac{2}{n_f(H) k_A}, \tag{5.12}$$

Onsager's theory shows that k_A is field independent (see discussion below equation 3.17). For a 1:1 symmetric electrolyte

$$k_A = \frac{16\pi \ell_T D}{\tilde{V}_T} = \frac{\pi \sqrt{3} \ell_T}{a \tau_0} = \frac{\chi_T}{\tau_0}, \tag{5.13}$$

where D is the diffusion coefficient and $\tilde{V}_T$ is the volume per site (tetrahedron). For a diamond lattice electrolyte, we substitute $D = a^2/(6\tau_0)$, where τ_0 is the hopping time, and $\tilde{V}_T = 8a^3/(3\sqrt{3})$. This yields the Langevin time

$$\tau_L(H) = \frac{1 - n_f(H)}{2 - n_f(H)} \frac{4a\tau_0}{\sqrt{3}\pi \ell_T n_f(H)} \simeq \frac{2a}{\sqrt{3}\pi \ell_T} \frac{\tau_0}{n_f(H)}. \tag{5.14}$$

Taking the variable mobility $\varkappa(H)$ into account gives

$$\frac{\tau_L(H)}{\tau_0} \simeq \frac{2a}{\pi \sqrt{3} \ell_T} \frac{\varkappa(0)}{\varkappa(H)} \frac{1}{n_f(H)} = \frac{2}{\chi_T} \frac{\varkappa(0)}{\varkappa(H)} \frac{1}{n_f(H)}, \tag{5.15}$$

where $n_f(H)$ is the Wien effect enhanced free charge density. The Langevin time lag can hence be expressed in terms of isothermal magnetic susceptibility of spin ice – this is twice the time for relaxation in a hypothetical magnetic RC circuit. Note that the time lag is predicted to decrease with increasing field intensity.

This approach can be generalised to the screened regime or alternatively a different time scale τ_D can be introduced, which can be measured through frequency dependent increase of conductivity (Debye–Falkenhagen effect, Debye and Falkenhagen (1928); Falkenhagen (1971)). This time scale corresponds to the time necessary to traverse a distance equal to the Debye length ℓ_D. If we assume that the atmosphere establishes itself diffusively we obtain

$$\frac{\tau_D}{\tau_0} \simeq \frac{6\ell_D^2}{a^2}. \tag{5.16}$$

This time scale plays a little role in our considerations of the Wien effect but it is important for strong electrolytes, i.e. at higher temperatures in spin ice.

5.1.2 Magnetization rate

We have discussed the Wien effect kinetics which apply both to electrolytes and magnetolytes. In spin ice, we need to consider the dynamics of the underlying spin degrees of freedom and their influence on monopoles. We first treat the magnetization dynamics of spin ice in terms of monopoles while assuming their density is fixed. We discuss later what happens if the Wien effect increases their density.

In spin ice, the magnetization process can be cast in terms of mobile monopoles polarizing the sample under the influence of an external force $F_H = \mu_0 Q_m H$. The magnetized background in turn exerts an entropic force $F_S = \mu_0 Q_m M / \chi_T$ that drags them back (see section 4.6.2). At a fixed number of charges the magnetization dynamics is governed by

$$\frac{dM}{dt} = j_m = \frac{\nu Q_m}{\tilde{V}_S} = \frac{\varkappa_m (F_H - F_S)}{\tilde{V}_S} = \frac{\varkappa_m n_f \mu_0 Q_m}{\tilde{V}_S} \left(H - M/\chi_T \right), \tag{5.17}$$

where the magnetic mobility $\varkappa_m = Q_m D / k_B T$ is calculated from the Einstein relation. This equation yields exponential relaxation towards the equilibrium magnetization $M_0 = \chi_T H$. The relaxation time scale of the Dirac string background is

$$\tau_S = \frac{\chi_T \tilde{V}_S}{n_f \mu_0 Q_m \varkappa_m} = \frac{\tau_0}{n_f}. \tag{5.18}$$

The same time scale appears as the characteristic time in the linear susceptibility which is of the Debye form $\chi(\omega) = \chi_T / (1 - i\tau_S \omega)$ (Ryzhkin, 2005; Ryzhkin et al., 2013). We assume that the magnetization rate will increase as the monopole density increases due to the Wien effect which is beyond the linear response regime.

Demagnetization has to be taken into account if we are to consider a sample surrounded by vacuum (Bovo et al., 2013b). There is then an additional force $F_{\mathscr{D}} = \mu_0 Q_{\mathrm{m}} \mathscr{D} M$ acting on the monopoles. Here we take the assumption that the demagnetization factor $\mathscr{D}$ is constant which is valid for elliptical samples. The effect of the demagnetization force is equivalent to the effect of the entropic force – the magnetization rate slows down as the sample magnetizes. As these forces act together, the time dependence of the magnetization follows from 5.17 with modified susceptibility $\chi_{\mathscr{D}}^{-1} = \chi_T^{-1} + \mathscr{D}$ and has the characteristic time scale

$$\tau_{\mathscr{D}} = \frac{\chi_{\mathscr{D}}}{n_{\mathrm{f}} \mu_0 Q_{\mathrm{m}} \varkappa_{\mathrm{m}}} = \frac{1}{1 + \mathscr{D}\chi_T} \frac{\tau_0}{n_{\mathrm{f}}}. \tag{5.19}$$
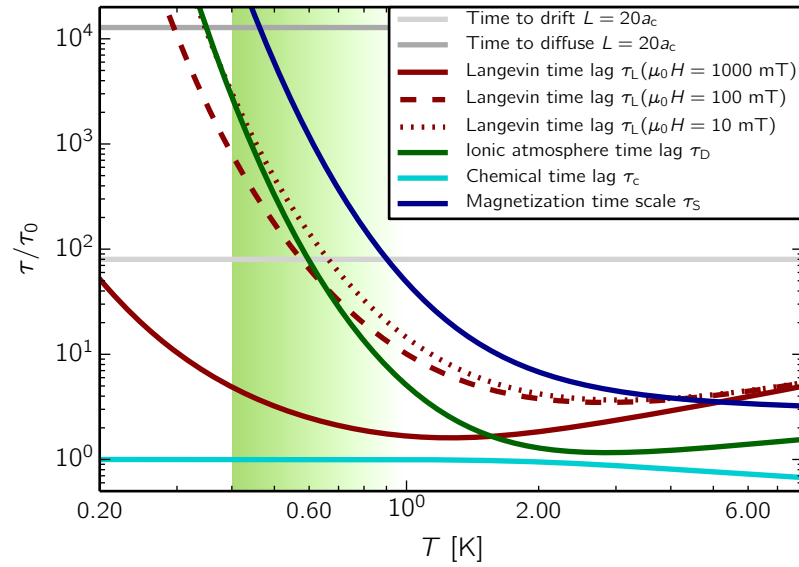
Figure 5.2: **Time scales in spin ice.** The green area marks temperature range where we expect to observe Wien effect in the dumbbell model. At low temperatures, the simulations are restricted by the system size. The period of the driving has to be shorter than the Dirac string relaxation rate τ_{S} (blue) and longer than the inverse Langevin time lag τ_{L} (red) for the Wien effect to appear in spin ice. The Debye–Falkenhagen effect predicts that sufficiently strong driving ($\ell_H < \ell_{\mathrm{D}}$) with periods below the green line would lead to destruction of the Debye screening even in the absence of the Wien effect. Apart from the other finite size effects mentioned during the study of the DC Wien effect, the simulation introduces time scales related to the system size. Times needed to cross a system of 20 unit cells cubed at maximum drift velocity and with an unbiased diffusion are plotted.

Figure 5.2 shows the temperature dependence of the time scales. From the analysis, we find a window $\tau_{\mathrm{S}} \gg \tau \gg \tau_{\mathrm{L}} \gg \tau_{\mathrm{c}}$ of periods and

Bjerrum length	$\ell_T = \mu_0 Q_{\mathrm{m}}^2/(8\pi k_{\mathrm{B}} T)$
Debye length	$\ell_{\mathrm{D}} = \sqrt{k_{\mathrm{B}} T \tilde{V}_{\mathrm{T}}/(\mu_0 Q_{\mathrm{m}}^2 n)}$
magnetic field length	$\ell_H = k_{\mathrm{B}} T/Q_{\mathrm{m}} H$
monopole NN distance	a
chemical time lag	$\tau_{\mathrm{c}}/\tau_0 \simeq 1$
Langevin time lag	$\tau_{\mathrm{L}}/\tau_0 = 2a/(\sqrt{3}\pi\ell_T n_{\mathrm{f}})$
magnetization time scale	$\tau_{\mathrm{S}}/\tau_0 = 1/n_{\mathrm{f}}$

Table 5.1: **Characteristic lengths and time scales in magnetolyte.** For temperature dependence of time scales in DTO see 5.2; length scales for the lattice electrolyte equivalent to DTO are shown in 3.1.

amplitudes, where the AC second Wien effect is plausible in DTO spin ice. The predicted window width $\tau_{\mathrm{S}}/\tau_{\mathrm{L}} = \chi_T/2$ diverges as $1/T$ in theory. In experiment the divergence is cut off be the demagnetization to the maximum width $\chi_{\mathscr{D}}(T=0) = 1/(2\mathscr{D})$.

5.2 Kinetic model

The time scale analysis allows us to identify the dominant processes intervening if spin ice is driven out of equilibrium. In the following we focus on the coupling between the Wien effect and the magnetization of spin ice. We will show that a simple non-linear kinetic model[2] can be constructed to capture the interplay between the Wien effect and the magnetization. We formulate the model first for a general type of driving $H(t) = H_0 h(t)$, where H_0 is the amplitude and $\max(|h(t)|) = 1$. Later we discuss in detail solutions for a sudden quench, rectangle, and sine waves. We show the predictions of the kinetic model together with the simulation results which were its original inspiration.

We assume the buffering hypothesis which states that the number of bound charges stays approximately constant because they are quickly replenished from the quasiparticle vacuum (equation 3.68). and focus on the equilibrium between the free charges and the remainder of the system. Combining equations 5.7 and 5.17 yields

$$\frac{\mathrm{d}n_{\mathrm{f}}}{\mathrm{d}t} = k_{\mathrm{D}}^0 F(b)(1-n_{\mathrm{f}}) - \frac{k_{\mathrm{A}} n_{\mathrm{f}}^2}{2} \tag{5.20}$$

$$\frac{\mathrm{d}M}{\mathrm{d}t} = \frac{\varkappa_{\mathrm{m}} n_{\mathrm{f}} \mu_0 Q_{\mathrm{m}}}{\tilde{V}_{\mathrm{S}}}\left(H(t) - M/\chi_T\right), \tag{5.21}$$

---

2 The linearized model has been first proposed by S.T.Bramwell and further developed in a collaborative effort.

where we assumed the Wien effect in the form $k_D = k_D^0 F(b)$. In the Wien effect formula, we substitute the electric field by a magnetic one $E \to \mu_0 (H(t) - M/\chi_T)$ to take into account that the immediate applied force is a combination of the magnetic and the entropic force and write

$$b = \frac{\mu_0^2 Q_m^3}{8\pi(k_B T)^2} \left(H(t) - M/\chi_T \right) = \frac{\ell_T}{\ell_H} \left(h(t) - m \right), \tag{5.22}$$

where the magnetic length is defined as $\ell_H = k_B T / \left(\mu_0 H Q_m \right)$ and where $m = M/M_0$ is the magnetization relative to the equilibrium value $M_0 = \chi_T H_0$.

The first equation of the kinetic model 5.20 can be linearized in small changes in monopole density $n_f = n_f^0 + \Delta n_f$ and the Wien effect parameter b as

$$\frac{d\Delta n_f}{dt} = k_D^0 b \left(|h(t) - m| \right) - k_A n_f^0 \Delta n_f + \mathcal{O} \left((\Delta n_f)^2 \right). \tag{5.23}$$

This approach was first taken for electrolytes by Pearson (1954). It is convenient to also introduce the density increase relative to the maximum increase possible, $q = \Delta n_f / \Delta n_{f0}$. To linear order of approximation, the highest density increase is the steady-state value in an electrolyte $\Delta n_{f0} = b\, n_f^0 / 2$ yielding

$$\frac{dq}{dt} = k_A n_f^0 \left(|h(t) - m| - q \right), \tag{5.24}$$

where we further use $(n_f^0)^2 = 2 k_D^0 / k_A$. Using the time scales defined above and equation 5.13

$$\frac{dq}{dt} = \frac{1}{\tau_L^0} \left(|h(t) - m| - q \right). \tag{5.25}$$

Note that the linearization removes the field dependence of the Langevin time lag predicted in the full calculation 5.12. The field dependence can be recovered by replacing τ_L^0 with $\tau_L(H)$. This refinement turns out to be necessary to correctly describe the simulation data (see figure 5.4).

The second equation of the model 5.21 can be recast in the same variables as

$$\frac{dm}{dt} = \frac{1}{\tau_S} \left(1 + \frac{bq}{2} \right) (h(t) - m), \tag{5.26}$$

with equation 5.18 defining the time scale. The term $bq/2$ represents the speed up of the magnetization rate due to the increased number of charges present. The parameter τ_S itself is truly field independent. There is however a modification necessary to fit the Metropolis dynamics of the simulations.

Castelnovo et al. (2011) proposed a slightly modified diffusion constant for spin ice $D = 4a^2/(27\tau_0)$ due to the fact that only three out of four directions are available for a monopole if creation of double defects is to be avoided. Their result is based on the assumption that the monopole moves every τ_0 on average. In our simulations, the move creating a double charge is refused and as a result the monopole sits at the same tetrahedron on average 4/3 times longer reducing the diffusion constant to $D = a^2/(9\tau_0)$ which is two thirds of the unconstrained electrolyte value. While comparing with simulations, we therefore modify the mobility in the first equation to read

$$\frac{\mathrm{d}m}{\mathrm{d}t} = \frac{2/3}{\tau_S}\left(1 + \frac{bq}{2}\right)(h(t) - m)\,. \tag{5.27}$$

Despite its simplicity, the kinetic model is successful in capturing the essential non-equilibrium behaviour of spin ice as we show below by comparing with simulation results. Although it cannot be solved exactly in most situations, it is readily solved by numerical integration. We now mention a possible extension of the kinetic model and discuss the choice of initial conditions.

5.2.1 Reorientational dynamics of bound pairs

The kinetic model neglects the internal structure of correlations related to the Wien effect, therefore a sudden change of field direction changes only the phase angle between magnetization and the external field. We will see below that this leads to prediction of a spurious behaviour for the susceptibility at high frequencies.

To incorporate the delay related to reorientation of the bound pairs, a modified form for the equation proposed in (Giblin et al., 2011) would need to be added

$$\frac{\mathrm{d}[n_\mathrm{b}\cos\theta]}{\mathrm{d}t} = -(k_\mathrm{D} + k_\mathrm{Or})[n_\mathrm{b}\cos\theta] - k_\mathrm{an}n_\mathrm{b} + \frac{k_\mathrm{A}n_\mathrm{f}^2}{2} + k_\mathrm{cr}(1 - n_\mathrm{b} - n_\mathrm{f}), \tag{5.28}$$

where θ is of the angle between a bound pair dipole and the external field, $[\ldots]$ is the configurational average over bound pairs, and k_Or the rate constant for bound pair reorientation. There is an ad hoc separation of rate constants here, where k_Or contains all the reorientational dynamics even though parts are related to the bias in creating new monopoles k_cr and their annihilation k_an. Unfortunately, the model of (Giblin et al., 2011) lacked the second equation in our model 5.21 and thus cannot describe the long-term dynamics of spin ice. It would

be an interesting direction of research to combine their approach to re-
orientation with our kinetic model to further the understanding of the
Wien effect in spin ice.
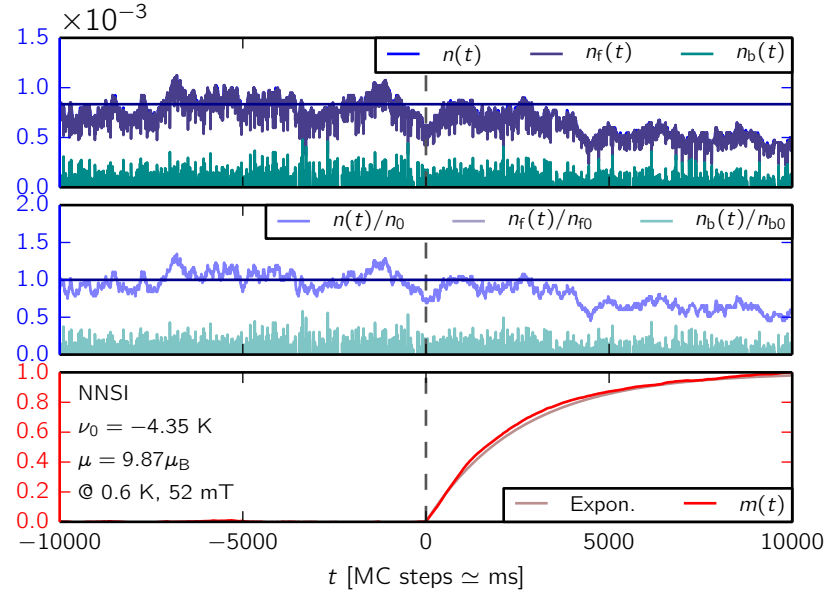
Figure 5.3: **Quench in the nearest-neighbour spin ice – absence of the Wien
effect.** The parameters correspond to the DTO dumbbell model
at $T = 0.6\,\mathrm{K}$ and $\mu_0 H = 52\,\mathrm{mT}$ with the Coulomb interaction re-
moved. The Wien effect is completely absent and the system con-
verges to a reduced charge density in the field. The magnetization
convergence to the equilibrium value resembles a single exponen-
tial. Almost no population of bound monopoles is stabilised. The
concept of charge pairs has no useful physical meaning for a non-
interacting gas because it amounts to an arbitrary separation of the
charge population unlike the well motivated Bjerrum pairs defined
in section 2.3.

5.2.2 Density suppression by field in equilibrium

We have so far discussed no initial conditions for the kinetic model
as these depend on the experimental protocol that we wish to study. A
sample prepared in zero field would correspond to zero initial magnet-
ization $m(0) = 0$ and zero excess charge $q(0) = 0$. However, this is only
true if excess charge is measured in relation to the zero-field equilbrium
monopole density. In spin ice, there is quadratic suppresion of charge
density in the external field **H**.

As spin ice polarizes, the zero charge configurations obtain a larger
Boltzmann weight than the charged configurations due to the Zeeman
energy of spins in field **H**. In the absence of demagnetization, spins

couple only to the applied magnetic field **H**, unlike monopoles which also feel an entropic effect of $\mathbf{M}/\chi_T$ (discussed in section 4.6.2). Therefore, there is an immediate shift in the equilibrium density towards which the system converges

$$n_{\mathrm{f}}^0(H) = n_{\mathrm{f}}^0 \left(1 - \frac{2}{3}(\beta\mu_0\mu\cdot\mathbf{H})^2 \right). \tag{5.29}$$

This result is derived by comparing the statistical weights of tetrahedra with and without a magnetic monopole present in the single tetrahedron approximation discussed below equation 4.31 in the previous chapter. Note that the charge decrease is quadratic in field and does not require a direct modification of the kinetic model which contains only linear terms. However, it is necessary to replace the initial zero-field condition $q(0) = 0$ with

$$q(0) = q_0 = \frac{n_{\mathrm{f}}(0) - n_{\mathrm{f}}^0(H)}{n_{\mathrm{f}}(H) - n_{\mathrm{f}}^0(H)}. \tag{5.30}$$

and reinterpret $q(t)$ as the relative increase in density from the in-field equilibrium base line towards the steady state electrolyte value.

In higher fields, saturation is reached along a curve resembling the Kasteleyn transition (Jaubert et al., 2008) and $n_{\mathrm{f}}^0(H) \simeq 0$ yielding $q_0 = n_{\mathrm{f}}(0)/n_{\mathrm{f}}(H)$. Below $T = 0.4\,\mathrm{K}$ in DTO, a part of the monopoles ends up in non-contractible bound pairs, which take significantly longer to annihilate than contractible bound pairs (Castelnovo et al., 2010). A non-contractible bound pair is pair of monopoles on neighbouring sites connected by a spin whose flipping would not annihilate the pair but create two double defects (see section 4.8.1). The initial condition would have to be amended to take these long-lived monopoles into account.

5.2.3 Demagnetization

The main effect of demagnetization is to modify the equilibrium magnetization to $M_0 = \chi_{\mathscr{D}} H_0$ and the relaxation time τ_{S} to $\tau_{\mathscr{D}}$ from equation 5.19. This leads to a faster relaxation towards a reduced equilibrium value.

If demagnetization is to be taken fully into account, spins react to field $H - \mathscr{D}M$ and the reduction in monopole density becomes dynamic. This additional dynamics can be captured by shifting the dissociation constant to

$$k_{\mathrm{D}}^0(H - \mathscr{D}M) = k_{\mathrm{D}}^0 \left(1 - \frac{1}{3}(\beta\mu_0\mu\cdot(\mathbf{H}(t) - \mathscr{D}\mathbf{M}))^2 \right) \tag{5.31}$$

and taking into account that monopoles respond to $H - M/\chi_T - \mathscr{D}M$ and following the approximation procedure consistently to the second

order in field with the additional parameters. We do not pursue this direction, because the correction is quadratic in field whereas the competing Wien effect is linear.

5.3 Simulations of Wien effect in spin ice

We have introduced the kinetic model for the second Wien effect in spin ice based on the theretical considerations about chemical kinetics of the Wien effect and magnetization dynamics of spin ice. Originally, this model was inspired by a numerical programme searching for a signature of the Wien effect in the dynamics of the dumbbell model. In following parts of this chapter, we present both the simulations results and the corresponding solutions of the kinetic model. A general introduction to the algorithms used is given in sections 2.6.1 and 4.8.

We simulated three protocols whose choice was motivated by their closeness to experiment: a field quench starting from a zero magnetization state, sinusoidal periodic driving, and rectangular wave periodic driving (which can be seen as repeated quenches in opposing field directions). In each of these protocols, the system is first equilibrated using a combination of the worm algorithm and single spin flips. At time $t = 0$, the prescribed time dependent field $H(t)$ is applied and only local single spin flips are performed. The field protocol $H(t)$ is discretized because the minimal time step in the simulations is given by a single Monte Carlo step τ_0 during which a spin flip is proposed N_S times. We now discuss separately the field quenches and the periodic driving together with the simulation results obtained for both of them.

5.4 Quench dynamics

To characterise the response of spin ice to external driving, it is instructive to start with a sudden field quench from a zero-field state. In the kinetic model, this is equivalent to $h(t) = 1$ and initial conditions $m(0) = 0$ and 5.30. Since the field does not change sign during the quench, it is possible to drop the absolute value

$$\frac{\mathrm{d}q}{\mathrm{d}t} = \frac{1}{\tau_L}\left(1 - m - q\right) \tag{5.32}$$

$$\frac{\mathrm{d}m}{\mathrm{d}t} = \frac{1}{\tau_S}\left(1 + \frac{bq}{2}\right)(1 - m) . \tag{5.33}$$

In the absence of the Wien effect, the system would relax to its equilibrium magnetization in a single exponential, in analogy with the charging of a capacitor (see figure 5.3). The presence of the Wien effect leads to a faster magnetization rate.

5.4.1 Approximate solutions

As we are not aware of exact solutions to the model 5.32, we start by considering several approximations to gain insight to its behaviour. First we linearize the kinetic model around its fixed point which corresponds to the long-time behaviour. A second approximate solution consists of assuming that the Wien effect dynamics is infinitely faster than the magnetization. We give a critique of these approximations based on the simulation results.

5.4.1.1 Expansion around a fixed point

The kinetic model has a single fixed point $q^* = 0$, $m^* = 1$ which is the only physical solution of

$$\left.\frac{\mathrm{d}q}{\mathrm{d}t}\right|_{(q^*,m^*)} = 0 = \tau_\mathrm{L}^{-1}\left(1 - m^* - q^*\right) \tag{5.34}$$

$$\left.\frac{\mathrm{d}m}{\mathrm{d}t}\right|_{(q^*,m^*)} = 0 = \tau_\mathrm{S}^{-1}\left(1 + \frac{bq^*}{2}\right)(1 - m^*) \tag{5.35}$$

To analyse the behaviour in the vicinity of the fixed point, we linearize the dynamics by computing the Jacobian matrix at the fixed point

$$\begin{pmatrix} \partial(\mathrm{d}q/\mathrm{d}t)/\partial q & \partial(\mathrm{d}q/\mathrm{d}t)/\partial m \\ \partial(\mathrm{d}m/\mathrm{d}t)/\partial q & \partial(\mathrm{d}m/\mathrm{d}t)/\partial m \end{pmatrix}_{q=q^*,m=m^*} \tag{5.36}$$

$$= \begin{pmatrix} -\tau_\mathrm{L}^{-1} & -\tau_\mathrm{L}^{-1} \\ \tau_\mathrm{S}^{-1}(b/2)(1-m) & -\tau_\mathrm{S}^{-1}(1+bq/2) \end{pmatrix}_{q=q^*,m=m^*} \tag{5.37}$$

$$= \begin{pmatrix} -\tau_\mathrm{L}^{-1} & -\tau_\mathrm{L}^{-1} \\ 0 & -\tau_\mathrm{S}^{-1} \end{pmatrix}. \tag{5.38}$$

The eigenvalues are $\lambda_\mathrm{L} = -\tau_\mathrm{L}^{-1}$ and $\lambda_\mathrm{S} = -\tau_\mathrm{S}^{-1}$ and the fixed point is stable as both eigenvalues are negative. The ratio of the Wien effect response and magnetization rate stays the same as in the previous section $\lambda_\mathrm{L}/\lambda_\mathrm{S} = \tau_\mathrm{S}/\tau_\mathrm{L} = \left(\chi_T/2\right)(n_\mathrm{f}(0)/n_\mathrm{f}(H))$. By using the eigensystem of the Jacobian to construct the time evolution towards the fixed point we obtain

$$q(t) = \frac{\chi_T}{\chi_T - 1}\exp\left(-\frac{t}{\tau_\mathrm{S}}\right) + \frac{\chi_T(q_0 - 1) - q_0}{\chi_T - 1}\exp\left(-\frac{t}{\tau_\mathrm{L}}\right) \tag{5.39}$$

$$m(t) = 1 - \exp\left(-\frac{t}{\tau_\mathrm{S}}\right). \tag{5.40}$$

This approach correctly determines both the initial increase in monopole density and its duration τ_L. It also describes the subsequent decrease in density over the characteristic time τ_S. However, the expansion around the fixed point effectively neglects the $bqm/2$ term, removing the non-linearity from the magnetization curve. We observe

that the density initially behaves in the same way as in unconstrained electrolyte and subsequently follows the magnetization at roughly the same rate (see 5.4).

5.4.1.2 Instantaneous Wien effect

If we are only interested in the magnetization curve and not in the exact form of the density increase, it is instructive to consider the Wien effect dynamics as infinitely fast. In the limit $\tau_L \to 0$, equation 5.32 reduces to $(1 - m(t) - q(t)) = 0$ which allows us to write the magnetization dynamics using the instantaneous Wien effect

$$\frac{\mathrm{d}m}{\mathrm{d}t} = \frac{1}{\tau_S}\left(1 + \frac{b(1-m)}{2}\right)(1-m) . \tag{5.41}$$

The solution is

$$m(t) = 1 + \frac{2}{b - (2+b)\exp(t/\tau_S)} . \tag{5.42}$$

This type of formula has been used to fit recent quench measurements similar to the ones presented in (Paulsen et al., 2014) by the same group. The measured type of non-linearity is consistent with the instaneous Wien effect and its temperature dependence, however the fits tend to overestimate the Wien effect parameter, probably due to the presence of excess thermal monopoles after the quench (S.T. Bramwell, J. Bloxsom, private communication).

5.4.2 Simulation results

Comparing the model with simulations, we find that it captures the character of the dynamics correctly. It is however useful to scale it by substituting the linear approximant b by the full Onsager function $\sqrt{F(b)} - 1$ (see equation 3.2). We show its result after this rescaling in figure 5.4; we also rescale this way the results in all following figures. The simulated increase in density follows the model very closely. There are only small differences between the predicted magnetization and the simulated values. The instaneous Wien effect approximation also performs reasonably well, due to the separation of time scales between the Wien effect and magnetization. There are no fitting parameters, as the predicted modification of mobility 5.27 is confirmed by independent simulations. We observe minor corrections due to the field dependent mobility, however these are not as large as in the lattice electrolyte at equivalent temperatures and can be accounted for if more precise comparison is necessary (see discussion in section 3.3.2).
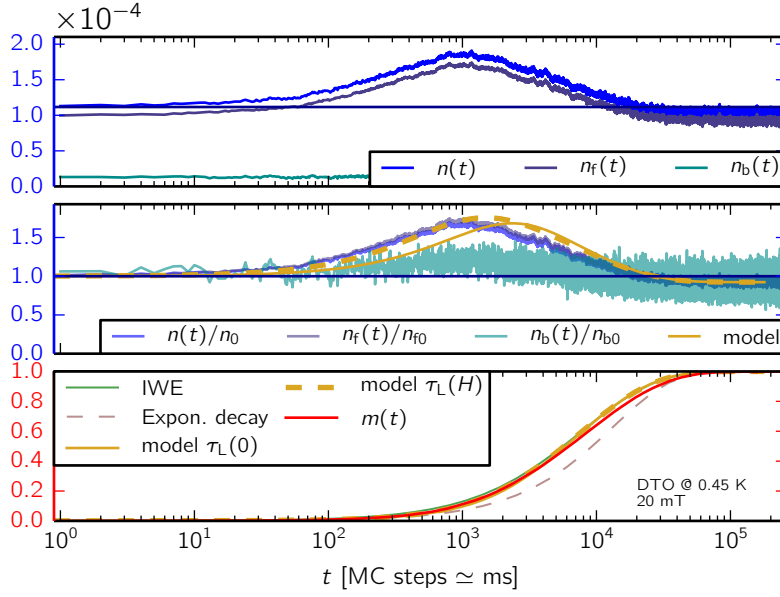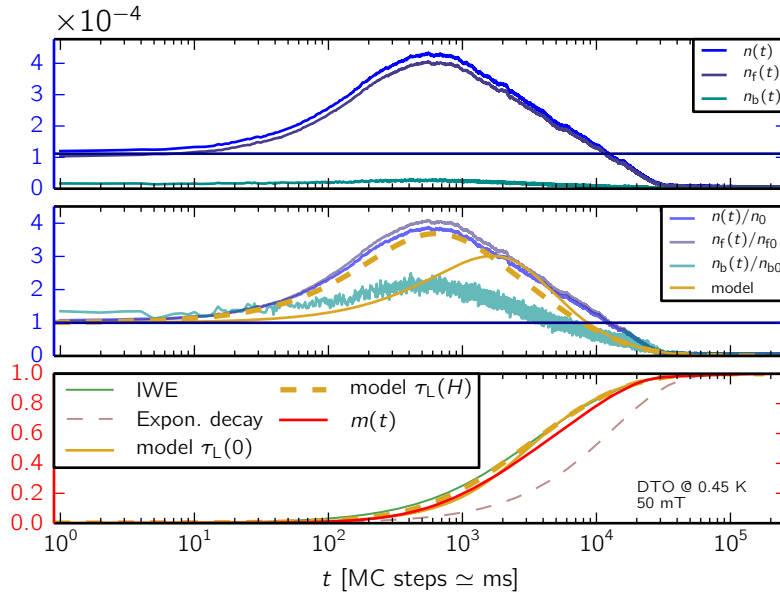
(a) $\mu_0 H = 20\,\text{mT}$

(b) $\mu_0 H = 50\,\text{mT}$

Figure 5.4: **Quench dynamics in DTO spin ice at** $0.45\,\text{K}$**.** The monopole density shows a transient increase whose length is characterised by τ_L and τ_S. The increase in monopole density is driven by the free charges, while the bound charges stay buffered at $\mu_0 H = 20\,\text{mT}$. At $\mu_0 H = 50\,\text{mT}$, the bound charge density also shows a small increase. The density increase manifests itself in a faster magnetization rate. The yellow lines are the kinetic model results, where the dashed line incorporates the field dependence of τ_L. The full line is the unmodified kinetic model with τ_L^0. The field dependence of the Langevin time lag is essential for the correct description of the density curve. The green line is the instantaneous Wien effect (IWE) approximation which well approximates the full solution of the kinetic model and the simulation results. The brown line shows a single exponential decay at rate τ_S^{-1} which fails to describe the simulation data.
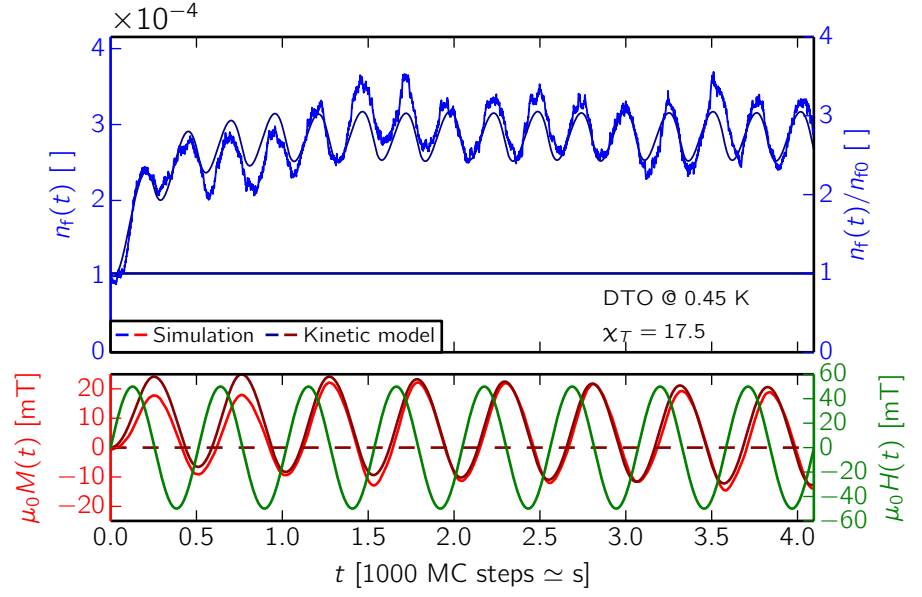
(a) $\mu_0 H_0 = 50\,\text{mT}$, $\mathscr{T} = 512\,\text{MCsteps}$
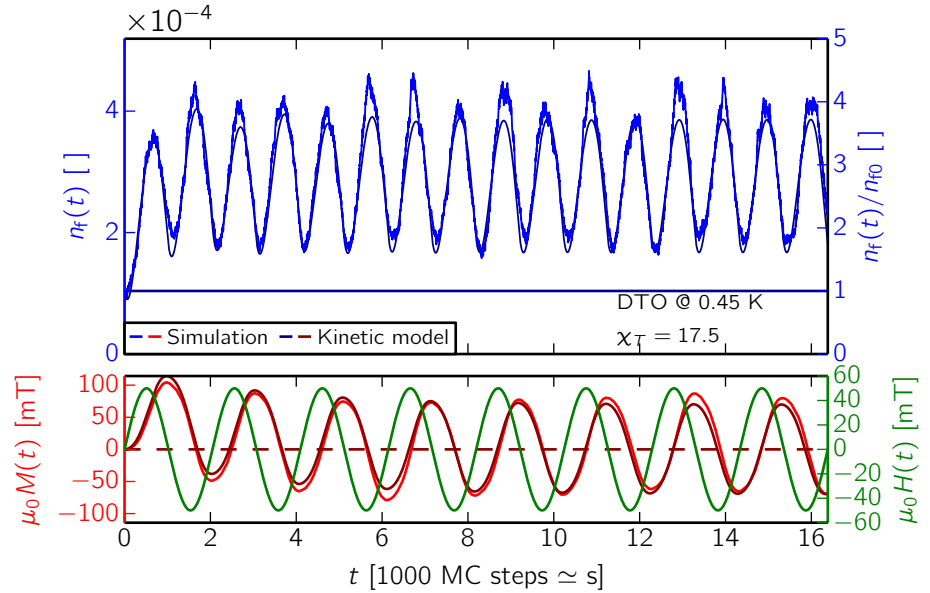
(b) $\mu_0 H_0 = 50\,\text{mT}$, $\mathscr{T} = 2048\,\text{MCsteps}$

Figure 5.5: $50\,\text{mT}$ **sine wave driving in DTO spin ice at** $0.45\,\text{K}$. Periodic driv-
ing stabilises the Wien effect in spin ice. Note that there is a
roughly $\pi/2$ phase shift between the applied field and magnetiz-
ation – a signature of driving above τ_S. Initially, there is a trans-
ition to the steady-state which is comparable to τ_L. During the
transition the density grows and the magnetization still retains
memory of the direction of the first impulse. The kinetic model
well describes the features of the time dependence of density mag-
netization. In the second panel, we see that the kinetic model un-
derestimates the maxima of the density and overestimates the min-
ima. The Onsager's function is convex which is not captured in the
linearization performed to obtain the model.
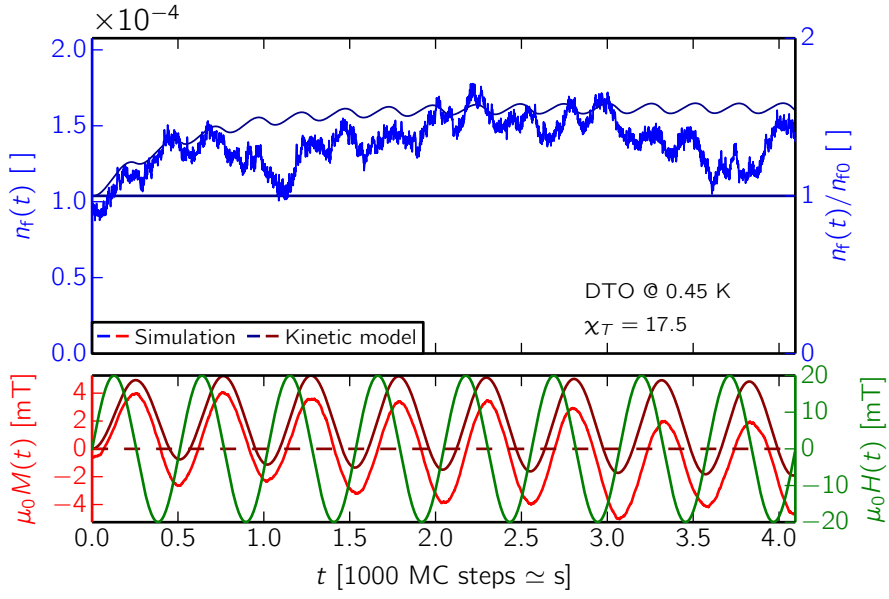
(a) $\mu_0 H_0 = 20\,\mathrm{mT}$, $\mathscr{T} = 512\,\mathrm{MCsteps}$
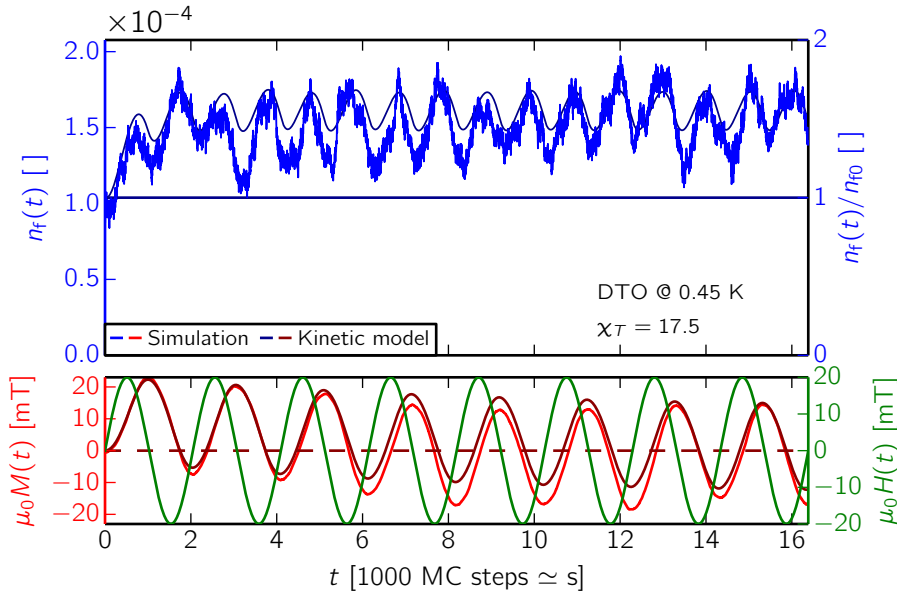
(b) $\mu_0 H_0 = 20\,\mathrm{mT}$, $\mathscr{T} = 2048\,\mathrm{MCsteps}$

Figure 5.6: 20 mT **sine wave driving in DTO spin ice at** 0.45 K. The amplitude in this figure is 2.5 times lower than in figure 5.5. Note in the upper panel that a 60 % increase in density is stabilised while the magnetization stays small (5 mT) compared to the equilibrium magnetization of $\mu_0 M_0 = \chi_T B_0 = 350\,\mathrm{mT}$. Establishing the steady state takes longer which is consistent with the predicted field dependence of τ_L. The noise-to-signal ratio of simulations becomes worse as the field decreases.
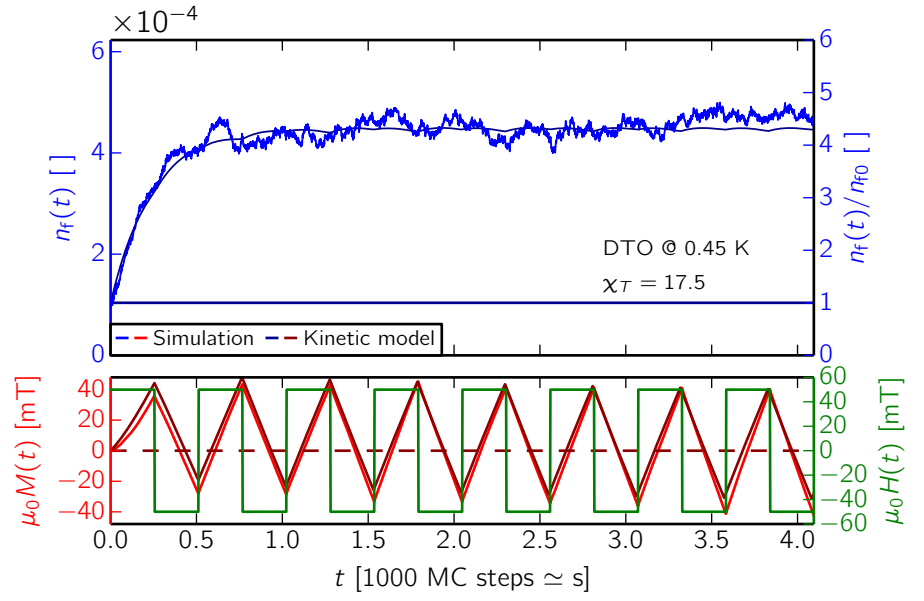
(a) $\mu_0 H_0 = 50\,\mathrm{mT}$, $\mathscr{T} = 512\,\mathrm{MCsteps}$
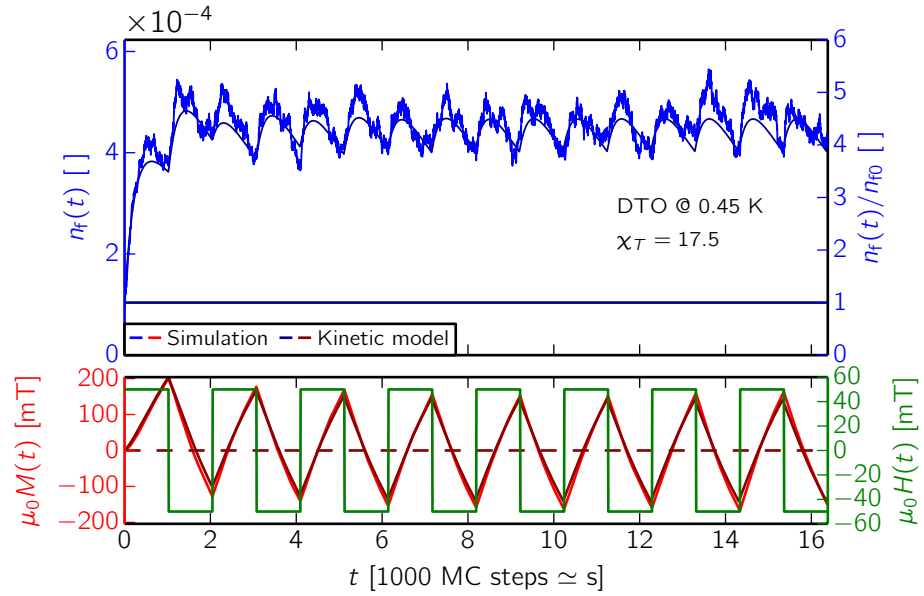
(b) $\mu_0 H_0 = 50\,\mathrm{mT}$, $\mathscr{T} = 2048\,\mathrm{MCsteps}$

Figure 5.7: 50 mT **rectangular wave driving in DTO spin ice at** 0.45 K. Rectangular wave driving has the average amplitude equal to the DC Wien effect in an electrolyte. At short periods, the oscillations above the average value of density stay low and the transition time dependence strongly resembles the DC effect in an electrolyte.

5.5 AC Wien effect

From the quench dynamics we can see that a temporary increase in monopole density can be achieved. The Wien effect is insensitive to the direction of the field as it reacts to the modulus only. If we change the field direction before the additional monopole population decays, we should therefore be able stabilise the increase. Moreover, the entropic force $Q_\mathrm{m} M / \chi_T$ stemming from the magnetization of the sample will help establish the Wien effect in the opposite direction. We analyse two realistic protocols in this section – rectangular wave and sine wave. The rectangular wave has the advantage of reproducing the DC function very closely, while sine driving allows analysing the non-linear susceptibility of spin ice.

We show examples of the AC Wien effect in spin ice in figures 5.5, 5.6, and 5.7. We plot the time dependence of the monopole density and magnetization on time starting from $t = 0$ when the periodic driving starts. A time-periodic steady state is established after some time. The kinetic model describes both the steady state and the transition to it. We comment on the detailed features of the time traces of density and magnetization in captions of figures 5.5, 5.6, and 5.7. Here we would like to emphasize that a significant increase in monopole density can be stabilized by driving that magnetizes only a small fraction of spins in the system. After this demonstration of the presence of the AC Wien effect in magnetolyte, we move on to a quantitative analysis of the results in dependence on the amplitude and the frequency of the applied field.

5.5.1 Density increase

The main signature of the Wien effect is the increase in the free monopole carrier density. We observe that this increase is stabilised over a broad frequency plateau (see figure 5.8). The increase in the total monopole density closely follows the free monopole density increase. The field dependence resembles the case of a constant field in electrolyte[3] (compare figures 5.10 and 3.9). We observe a good agreement with Onsager's prediction $\gamma \sqrt{F(b)} - 1$ where the effective field H_eff is taken to be $\langle |H| \rangle_{\mathscr{T}} = H_0$ in the rectangular wave case and $\langle |H| \rangle_{\mathscr{T}} = 2H_0/\pi$ in the sine wave case (corresponding to the $2E_0/\pi$ field dependence in electrolytes observed by Mead and Fuoss (1939); Persoons (1974)). We first

---

3 Useful conversion for comparing with E^*:
Zeeman energy of
$\mu_0 \mu \cdot \mathbf{H} / k_\mathrm{B} = 1\,\mathrm{K}$ corresponds to $\mu_0 H = 0.262\,\mathrm{T}$
in DTO & HTO.
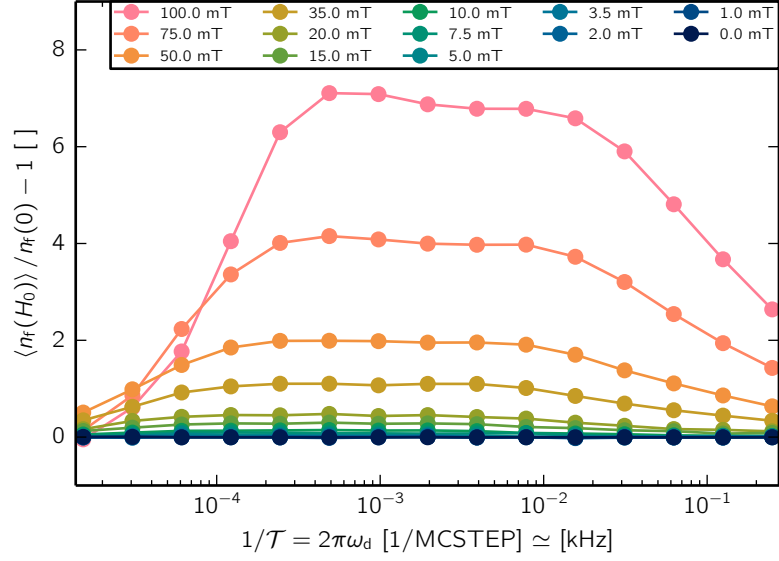
Figure 5.8: **Frequency plateau.** The relative free monopole density increase as a function of frequency for different fields. The Wien effect is stabilised over a broad range of frequencies up to the highest simulated fields. At low frequencies the magnetization of the system supresses the Wien effect. The low cutoff frequency shows a field dependence consistent with the $bq/2$ term in the kinetic model. At high frequencies the magnetolyte is driven faster than the time necessary for Wien effect to establish. The high cutoff frequency is either field independent or only weakly field dependent which we cannot discern conclusively. The present figure is for sine driving. The density increase in response to the rectangular wave driving is even higher and shows the same features. We plot the ordinary frequency at the x-axis and use an approximate conversion $1\,\mathrm{MC\,step} \simeq 1\,\mathrm{ms}$.

discuss the frequency dependence of the AC Wien effect followed by the amplitude dependence for frequencies where the effect manifests itself.

5.5.1.1 Frequency plateau

The frequency plateau has a width surpassing the prediction of $\chi_T/2$ that we obtained in section 5.1.2 from the independent treatment of time scales needed to establish the Wien effect and to magnetize the system. The Wien effect persists to higher frequencies than the computed Langevin time lag predicts. The observed time scale is roughly an order of magnitude faster than predicted. Given that the quenches obeyed the predicted separation of time scales, the transition time scale must be inherently connected to the periodic driving.

In addition, the broadening of the plateau is captured by the following kinetic model ($\mathscr{T}$ is the period of driving)

$$\frac{\mathrm{d}q}{\mathrm{d}t} = \frac{1}{\tau_{\mathrm{L}}}\left(\left|\sin\left(\frac{2\pi t}{\mathscr{T}}\right) - m\right| - q\right) \tag{5.43}$$

$$\frac{\mathrm{d}m}{\mathrm{d}t} = \frac{2/3}{\tau_{\mathrm{S}}}\left(1 + \frac{bq}{2}\right)\left(\sin\left(\frac{2\pi t}{\mathscr{T}}\right) - m\right). \tag{5.44}$$

For the square wave, we replace the sine function with the sign of sine function. The initial conditions are as above, but we focus on the steady state situation. Note that the main difference to the model used to fit the quench is the presence of additional non-linearity in the form of the absolute value. A simpler version of this problem without kinetic constraints was solved by Pearson (1954) in terms of infinite Fourier series. If we compute the frequency dependendence from Pearson's result, the AC Wien effect is stabilised beyond the Langevin time lag in agreement with the numerical solution of the kinetic model[4].

While the kinetic model predicts the broadening qualitatively, the predicted transition frequency is higher than the observed one. Therefore the decay of the density plateau at high frequencies has to be assigned to processes beyond the kinetic model description. This is a signature of the simple chemical kinetics not capturing the whole of the Wien effect diffusional dynamics of pair reorientation and merits further investigation. In the analysis of the susceptibility below we observe that there is an inner structure to the plateau that reveals the true position of the Langevin time lag.

The observed field dependence of the crossover frequency is either absent or much weaker than the one of the Langevin time lag. Due to the breadth of the plateau we rely in principle only on four points to fit the transition. Therefore fitting of the curves results in values of the transition frequency with large uncertainty. However, the frequency where the effect first drops below the plateau is constant in field (see figure 5.8). This absence of the field dependence for the transition time was previously observed in an experiment on tetrabutylammonium picrate in diphenyl ether (Persoons, 1974). Experiments on acetic acid and ammonia in water cover a very limited range of amplitudes but also show no discernible trend (Eigen and Schoen, 1955).

5.5.1.2 Bound and free charges

The bound charge density also increases, because the dividing line between free and bound charges is not as strictly defined as it would

---

4 We observe a similar broadening if we replace the absolute value in the kinetic model with a different function that only depends on the modulus of the field, e.g. with a series of even polynomials.
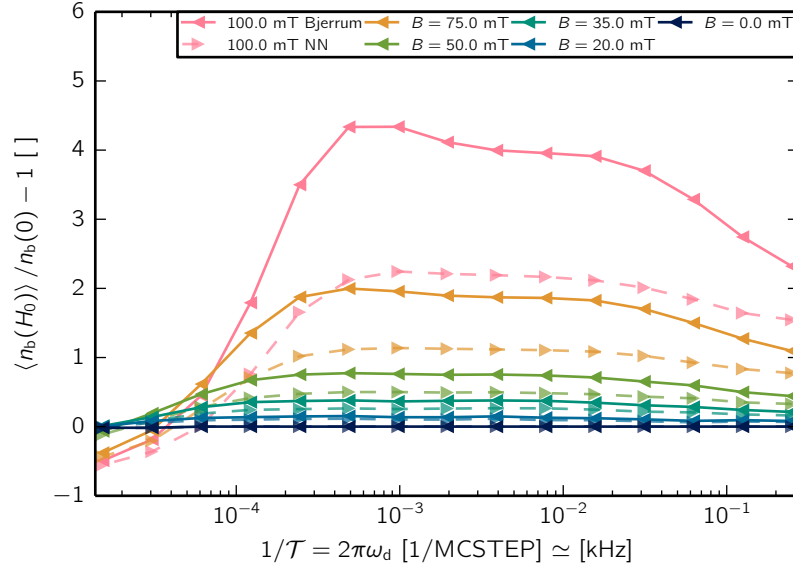
Figure 5.9: **Bound charge density increase** is lower than the free charge density increase. The cause of this is the buffering predicted from chemical kinetics. We compare the nearest-neighbour pairs with Bjerrum pairs. Theopulation of smaller bound pairs increases less than the density of larger pairs. The frequency behaviour is similar to the free charge behaviour. Only in the highest frequencies shown do we see that the bound pair density responds faster to the applied field than the free monopoles.

be between two chemical species, where the phase space bottleneck is much narrower. The increase in free charge density dominates the total charge density increase and its relative value is largely independent of the definition of a bound pair. The relative change in the bound monopole density is however sensitive to the definition. Independently of the definition, the bound charge density increases less than the free charge density (compare figures 5.8 and 5.9). The larger the length separating bound and free monopoles, the more the bound monopole response resembles the response of the total charge density.

The bound charge density relaxes faster than the free charge part. The relaxation of bound charges should be thus close to the predicted chemical time lag. We observe this if we consider nearest neighbour pairs only. If we move from the nearest neighbour pairs to Bjerrum pairs the transition frequency becomes comparable with the transition frequency of the free charges and the total density.

5.5.1.3 Field dependence

In figure 5.10, we show the field dependence of the relative density increase, akin to the DC field figure in the electrolyte case. The strength
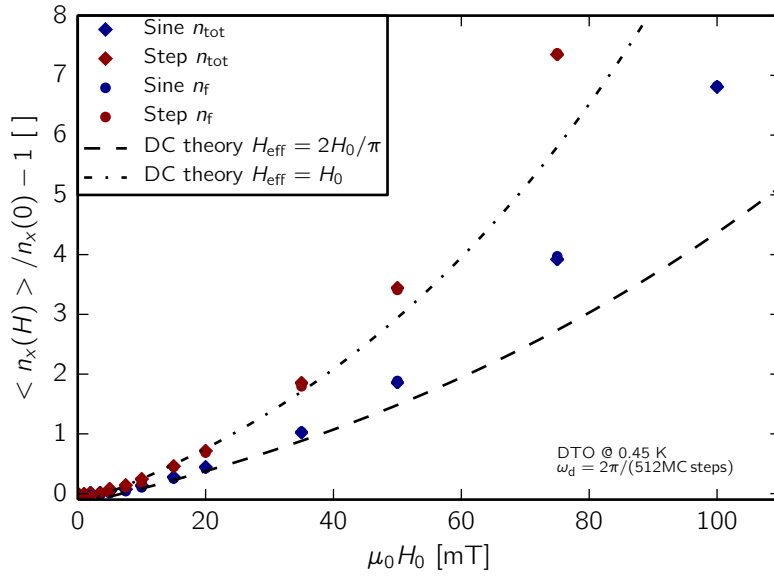
(a) $\mathcal{T} = 512\,\text{MCsteps}$
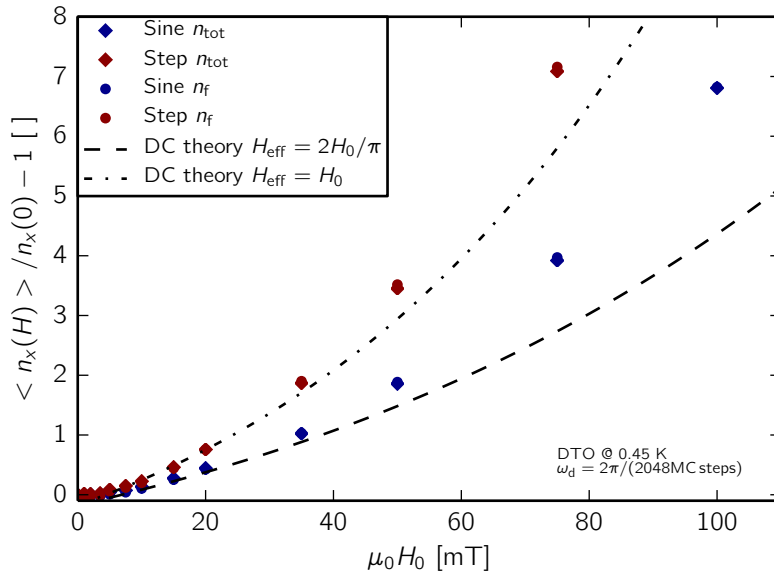
(b) $\mathcal{T} = 2048\,\text{MCsteps}$

Figure 5.10: **Field dependence of the Wien effect in spin ice.** The relative increase in density closely follows the Onsager's function for the DC Wien effect for two selected frequencies from the plateau. Red and blue symbols represent rectangular and sine wave driving respectively. The field dependence of the increase in total charge density (diamonds) closely follows the increase in the free charge density (circles). The effective field H_{eff} is the average modulus of the applied field. In higher fields the simulated value surpasses the prediction. We discuss possible causes in the main text.

of the Wien effect in spin ice is remarkable. For a sine wave with amplitude 100 mT, the magnetic monopole density increases eight times. There is a good parameter free match between the simulations and the Onsager's prediction $\gamma\sqrt{F(b)} - 1$ up to the fields of $\mu_0 H \simeq 50$ mT. The effective field that we use in the Onsager parameter b (defined in equation 5.22) is $H_{\text{eff}} = \langle|H|\rangle_{\mathscr{T}} = H_0$ in the rectangular wave case and $H_{\text{eff}} = \langle|H|\rangle_{\mathscr{T}} = 2H_0/\pi$ for the sine wave. This is an approximation that is valid within the linear regime of the Wien effect.

At higher fields we can see that the density increase in simulations surpasses our theoretical prediction. We do not have a conclusive explanation of this deviation, but we discuss two effects that give corrections in the correct direction: the off-phase magnetization enhancement of the effect and the convexity of Onsager's function $F(b)$.

While the immediate field causing the Wien effect is $H(t) - M(t)/\chi_T$, a substitution $H_0 \rightarrow \langle|H_0|\rangle_{\mathscr{T}} - \langle|M/\chi_T|\rangle_{\mathscr{T}}$ in the Onsager formula would be correct, because the external field and the magnetization are not in phase. The correct addition formula is $H_0 \rightarrow \sqrt{\langle|H_0|\rangle_{\mathscr{T}}^2 + \langle|M/\chi_T|\rangle_{\mathscr{T}}^2 + 2\langle|H_0|\rangle_{\mathscr{T}}\langle|M|/\chi_T\rangle_{\mathscr{T}}\sin\phi(H_0,\omega)}$, where $\phi(H_0,\omega)$ is the field and frequency dependent phase shift between the driving field and magnetization. While this effect yields a positive deviation of simulations above the theoretical line similar to the one in figure 5.10, a fast calculation using the values from figure 5.5 ($\mu_0|H| \simeq 32$ mT, $\mu_0|M|/\chi_T \simeq 4$ mT, $\phi \simeq \pi/2$) shows that this effect is less than 1 % for DTO at $T = 0.45$ K and $\mu_0 H_0 \simeq 50$ mT which is not sufficient to explain the observed discrepancy.

Another reason for the positive deviation would be that the Onsager's function $\sqrt{F(b)}$ is convex and as the monopole population oscilates around the average field value, the average stays above the predicted value (i.e. $F(\langle b\rangle_{\mathscr{T}}) \leq \langle F(b)\rangle_{\mathscr{T}}$). An estimate based on the magnitude of oscillations observed in our simulations also falls short of the density increase in figure 5.10. Not even the off-phase magnetization combined with the increase due to the convexity of $\sqrt{F(b)}$ yields a theory that fully describes the values observed in high fields. Note that unlike the explanation of a similar deviation in the lattice electrolyte, there should be no stroboscopic self-screening effect due to the absence of permanent DC currents in spin ice. Despite the uncertainty about the prediction in the highest fields applied, the electrolyte theory applies well to the amplitude dependence of monopole density in the magnetolyte AC Wien effect.

5.6 Implications for susceptibility of spin ice

The motion of monopoles is the dominant relaxation mechanism of spin ice at low temperatures (Castelnovo et al., 2008; Jaubert and Holdsworth, 2009; Ryzhkin, 2005). This is evidenced by magnetic (Morris et al., 2009; Giblin et al., 2011; Bovo et al., 2013a) and thermal measurements (Klemke et al., 2011; Kolland et al., 2012; Strehlow et al., 2012). The increase in monopole density necessarily leaves a trace in measurements of response functions. AC susceptibility is well suited for this task thanks to the proportionality between the magnetization rate and monopole current.

We focus on driving in the [001] field direction. In this case all spins have equal projection along the field. This direction also avoids any phase transitions apart from residual effects of the Kasteleyn transition at high fields (Jaubert et al., 2008). However our results should equally apply for fields in other directions due to cubic symmetry of spin ice as long as the magnetization stays below critical values for phase transitions, e.g. the [111] magnetization plateau (Moessner and Sondhi, 2003).

We start by defining a suitable non-linear susceptibility, we then show how the second Wien effect in spin ice influences it, and finish this section by discussing possible experimental realizations of our prediction.

5.6.1 Definition of the non-linear susceptibility

For a non-equilibrium system beyond linear response regime, a susceptibility can be defined in many ways which all reduce to the same linear susceptibility in the linear response limit. We introduce a non-linear susceptibility $\chi_{H_0}(\omega_{\mathrm{d}})$ in the following paragraphs based on comparing the amplitude of the magnetization response to the amplitude of external magnetic field driving. While the amplitudes are complex numbers in general, we focus on the modulus of the susceptibility.

We start from completely general assumptions. Due to the non-linearity of the problem, the response to external driving depends on the amplitude of driving. In addition the driving and response need not be on the same frequency. In the most general case

$$M(\omega) = \int \mathrm{d}\omega' H(\omega') \mathscr{X}_{H_0}(\omega, \omega'), \tag{5.45}$$

where $\mathscr{X}_{H_0}(\omega, \omega')$ is the field-dependent non-linear susceptibility. For a time invariant system, only the frequency difference matters $\mathscr{X}_{H_0}(\omega, \omega') = \mathscr{X}_{H_0}(\omega' - \omega)$. If furthermore the driving is periodic, the

steady state response is restricted to the harmonics of the driving fre-
quency ω_d

$$\mathcal{X}_{H_0}(\omega' - \omega_d) = \sum_{n=1}^{\infty} W_n(H_0, \omega_d) \delta((n-1)\omega_d) , \tag{5.46}$$

where n numbers the harmonics and $W_n(H_0, \omega_d)$ is their weight. The
weight can be expressed in terms of amplitudes of the driving H_0 and
response $\tilde{M}$

$$W_n(H_0, \omega_d) = \frac{\tilde{M}_{H_0, \omega_d}(n\omega_d)}{H_0} . \tag{5.47}$$

In the linear response regime (limit of small fields) this definition re-
duces to the standard AC susceptibility for the first harmonic $W_1(H_0 \to 0, \omega_d) = \chi_0(\omega_d)$ while the higher harmonics vanish $W_{n>1}(H_0 \to 0, \omega_d) = 0$.
This allows us to define the non-linear susceptibility studied in this
work as $\chi_{H_0}(\omega_d) = W_1(H_0, \omega_d)$. Non-linear susceptibilities related to
higher harmonics will be referred to as $\chi_{H_0}^{(n)}(\omega_d) = W_n(H_0, \omega_d)$.

Note that $\chi_{H_0}(\omega_d)$ differs from the in-field AC susceptibility meas-
ured by adding a a small AC driving to a time-independent DC com-
ponent of the magnetic field. Such a protocol will not lead to the
Wien effect. Moreover, it will observe rapidly decaying susceptibility
for fields higher than the critical field for Kasteleyn transition in spin
ice (Jaubert et al., 2008). The Kasteleyn transition can be seen as a
transition to the fully saturated state[5] with increasing field. While it
concerns the ground state manifold of spin ice, its features are still vis-
ible at finite temperatures, especially if the zero-field defect density is
low. In our case, the response will stay high as long as the saturation
of magnetization is avoided. This allows for a response at fields higher
than the Kasteleyn critical field.

To extract the harmonics we compute the discrete Fourier transform
of the magnetization time series (Press et al., 2007; Harris, 1978). We
show an example spectrum in figure 5.11. The normalized weight of the
peak equals $\left|\tilde{M}(H_0, n\omega_d)\right|_{\mathbb{C}}$ after integrating over the width of the peak.
The analysis is simplified by the fact that the peaks are very sharp, so the
weight obtained using a Fourier transform with windows[6] and padding
yields almost identical weights to a straightforward implementation.
The main source of uncertainty comes from the limited number of time
traces for each data point since we need to sweep over temperatures,
amplitudes and frequencies independently.

---

5 Magnetization of a fully magnetized sample in the [001] direction is $M = \mu/(\sqrt{3}\tilde{V}_S) = 816.8\,\text{kA/m}$, i.e. $\mu_0 M = \mu/(\sqrt{3}\tilde{V}_S) = 1.026\,\text{T}$

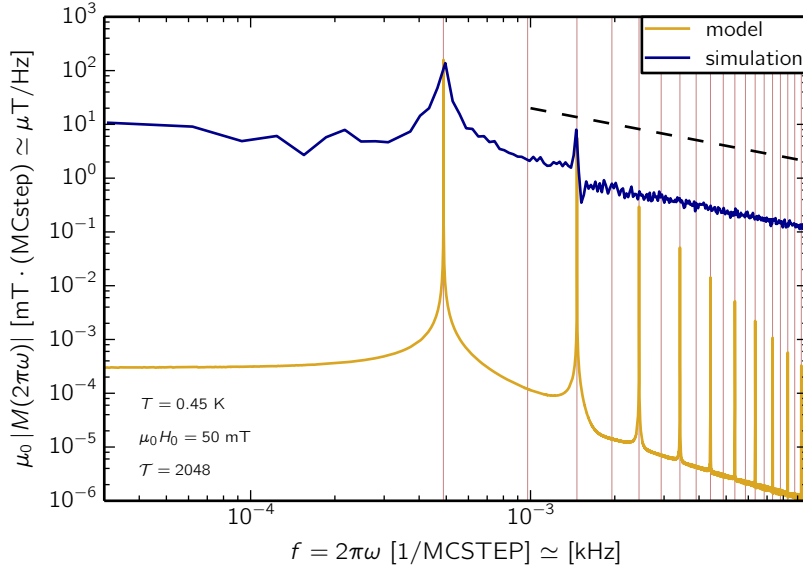6 For different window functions, different coherent gain has to be considered.

Figure 5.11: **Spectral density of magnetization.** DTO at 0.45 K driven by a sine wave with $\mu_0 H_0 = 50\,\text{mT}$ and $\mathcal{T} = 2048\tau_0$. We observe response at the first and third harmonic on a background of thermal fluctuations. The background has the Debye form and is therefore consistent with the Debye-type susceptibility via the fluctuation-dissipation theorem (the dashed black line is $\propto 1/\omega$). The kinetic model (yellow line) gives the correct peak weight. The model is however athermal. Higher harmonics (frequencies denoted by thin red lines) predicted by the kinetic model are below the thermal background in the simulation.

5.6.2 Non-linear susceptibility of spin ice

The linear susceptibility of spin ice has the dispersion $\chi(\omega) = \chi_T/(1 - i\tau_S\omega)$ and $\tau_S = \tau_0/n_f$ (Ryzhkin, 2005). The isothermal susceptibility χ_T is double the Curie law value at low temperatures in the NNSI model (Jaubert et al., 2013). The simplest approximation of the Wien effect signature in the susceptibility involves replacing τ_S with $\tau_S(H_{\text{eff}}) = \tau_0/n_f(H_{\text{eff}})$. The increase in non-linear susceptibility is then

$$\frac{\left|\chi_{H_0}(\omega_d)\right|}{\left|\chi_0(\omega_d)\right|} = \frac{n_f(H_{\text{eff}})}{n_f(0)}\sqrt{\frac{n_f^2(0) + (\omega_d\tau_0)^2}{n_f^2(H_{\text{eff}}) + (\omega_d\tau_0)^2}} \tag{5.48}$$

$$\xrightarrow{\omega_d \gg (n_f(H_{\text{eff}})/\tau_0 > n_f(0)/\tau_0)} \frac{\left|\chi_{H_0}(\omega_d)\right|}{\left|\chi_0(\omega_d)\right|} = \frac{n_f(H_{\text{eff}})}{n_f(0)} = \gamma\sqrt{F(b)}. \tag{5.49}$$

The approximation taken in the previous equation is valid for driving frequencies in the frequency plateau of the monopole density increase. The susceptibility should thus be strongly enhanced at frequen-
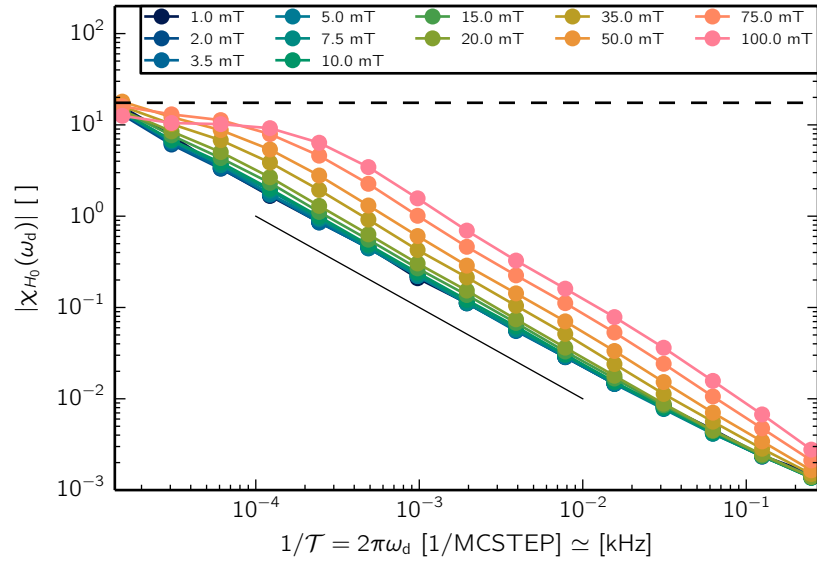
(a) Absolute susceptibility.
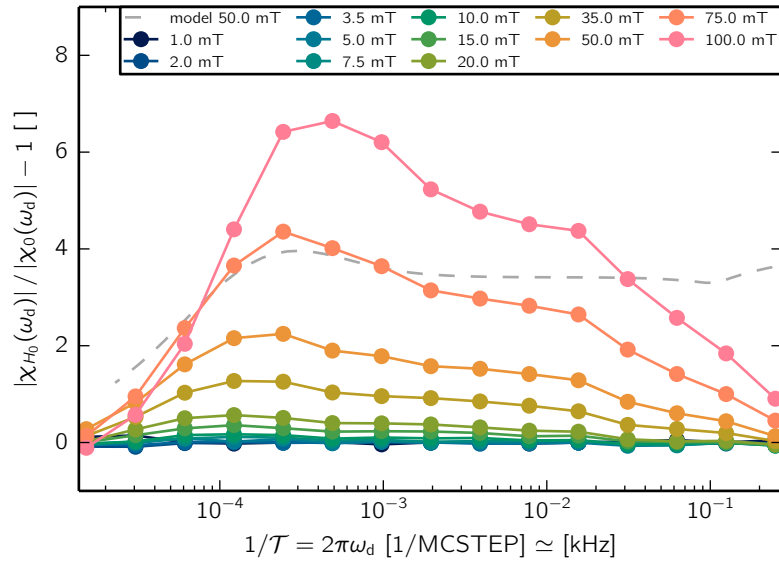
(b) Relative change in susceptibility.

Figure 5.12: **Frequency dependence of non-linear susceptibility in DTO spin ice** for various amplitudes. The absolute value of the susceptibility has the Debye form $\chi_T/\sqrt{1+\omega\tau_S}$ at low fields (dashed black line is χ_T from (Ryzhkin, 2005), the full black line $\propto 1/\omega$). The increased density in applied field shifts the curves to higher values while the general shape stays the same. Note that the high field curves do not reach the isothermal value due to the saturation of magnetization.

The relative increase resembles the increase in free monopole density (see figure 5.8) but the plateau has an additional maximum at the low frequency edge. The edges of the additional feature lie close to the predicted values of τ_S and τ_L. Thus the Langevin time lag which was hidden in the density increase reappears in the susceptibility. The kinetic model (grey dashed line) predicts the existence of this maximum but overestimates the plateau width at high frequencies and eventually fails at the highest frequencies.

cies which correspond to the frequency plateau in density increase. The simulation results support this picture (see figures 5.12 and 5.13).

However, the frequency plateau in susceptibility has an additional feature – a maximum appearing at the lowest frequencies. The local increase becomes more pronounced with increasing field. Interestingly, the position and width of this bump matches the prediction for the plateau if there was no non-linearity involved in the Wien effect and the increase would decay in a Debye fashion at $\tau_S(H_{eff})$ and $\tau_L(H_{eff})$. While we are lacking a simple picture for this heterogenity of the susceptibility plateau, we can confirm that it is reproduced at the correct position by the kinetic model. Therefore the chemical kinetics of monopoles and magnetization response of spin ice alone are responsible for this feature.
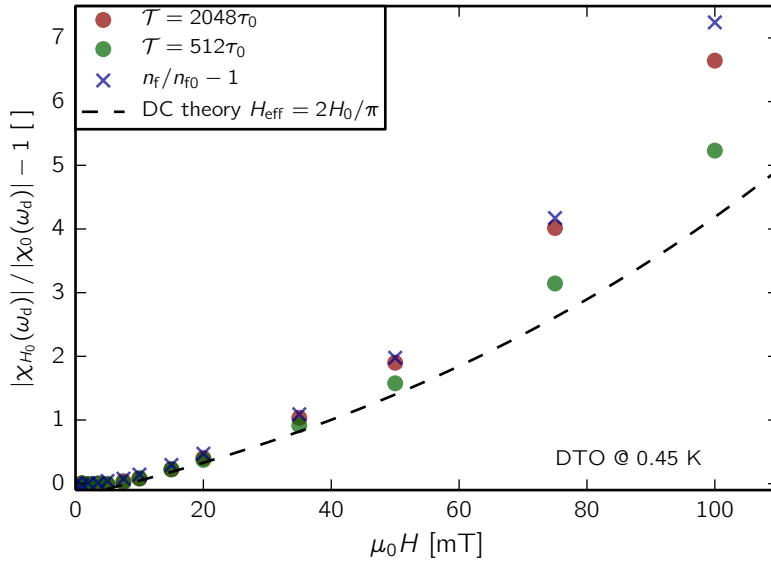
Figure 5.13: **Field dependence of the non-linear susceptibility.** The increase in the susceptibility follows the Onsager prediction in low fields but there is a difference in high fields between the maximal increase ($\mathcal{T} = 2048\tau_0$) and the increase elsewhere in the plateau ($\mathcal{T} = 512\tau_0$). The maximum increase matches the density increase.

5.6.3 Higher harmonics

The higher harmonics provide further insight into the character of the Wien effect. Firstly, only odd harmonics are observed in magnetization in the simulations and the kinetic model alike. Thus only odd susceptibilities $\chi_{H_0}^{(2n+1)}(\omega_d)$ are observed.

In a manner that is quite specific to the second Wien effect, the density responds to the absolute value of the field $\left| H(t) - M(t)/\chi_T \right|$.

Fourier series of absolute value of the first harmonic contains only even harmonics

$$|\sin(\omega_\mathrm{d} t)| = \frac{2}{\pi}\left(1 - 2\sum_{n=1}^{\infty}\frac{\cos(2n\omega_\mathrm{d} t)}{4n^2 - 1}\right).$$ (5.50)

Thanks to this response to the absolute value of field, the density subsequently contains only even harmonics which is confirmed by simulations. The periodicity of the density response is thus doubled due to the absolute value. The magnetization rate is proportional among others to the term $b\,h(t)q(t)/2$ which provides the coupling that generates odd harmonics in magnetization response because multiplying a series of even harmonics by the first harmonic results in a driving term with odd harmonics exclusively.

The observed weights of higher harmonic decrease approximately as a geometric series which makes it difficult to distinguish them reliably above the thermal noise in simulations. With Hamming window, ninth is the highest harmonic seen and observable only at the strongest field 0.1 T at the lowest temperature 0.4 K. The field dependence of $\chi_{H_0}^{(n)}(\omega_\mathrm{d})$ follows the first harmonic $\chi_{H_0}(\omega_\mathrm{d})$ with increasing field although precise quantitative statements are impossible with the given resolution.

It is interesting to note that the thermal background in the spectral density of magnetization (figure 5.11) has the same Debye form as the observed susceptibility. The time scale of the Debye relaxation matches as well. This hints at the validity of a non-equilibrium fluctuation-dissipation theorem in a form first proposed in connection with spin glasses (Cugliandolo et al., 1997a,b; Corberi et al., 2007) and would merit further investigation. Predictions concerning the observability of higher harmonics could be derived from these considerations.

5.6.4 Critique of the experimental proposal

The theory and our simulations predict the Wien effect to modify the non-linear susceptibility in DTO spin ice up to 0.75 K. The intensity of the Wien effect is predicted to scale approximately with H_0/T^2, leading to a tradeoff between the stronger effect at lower temperatures and the difficulties involved in experiments at these temperatures. Below 0.5 K the effect is stabilised over a broad range of frequencies and follows Onsager's formula very closely. Above 0.6 K, the crossover to the screened Wien effect has to be considered in the same fashion as in electrolytes. The only free parameter in our analysis is the absolute time scale τ_0 which we approximate as 1 ms in our plots. Jaubert and Holdsworth (2011) obtain $\tau_0 = 2.5$ ms from the data of (Snyder et al., 2004), whereas (Bovo et al., 2013a) find $\tau_0 = 0.4$ ms.

The proposed temperatures, fields and frequencies are accessible to the existing experimental setups. However, care has to be taken while performing a field quench or driving the system periodically. We mention several relevant issues.

5.6.4.1 Equilibration of the sample

Firstly, the system has to be equilibrated at the given temperature. This requires increasing amounts of time as temperature decreases. Notably, there is a zero-field cooled versus in-field cooled splitting crossover around 0.5 K–0.6 K (Snyder et al., 2004; Slobinsky et al., 2010) and further signatures of slowing down in equilibration (Orendáč et al., 2007; Quilliam et al., 2011; Matsuhira et al., 2011; Bramwell and Giblin, 2011; Yaraskavitch et al., 2012; Pomaranski et al., 2013). The Wien effect manifests itself in full at the highest temperature of 0.5 K. However the screened version of the Wien effect exists even at 0.7 K where there are no reported problems with equilibration (see figure 5.14). A promising piece of information was put forward that annealing the DTO samples in oxygen removes oxygen vacancies pinning the monopoles and promotes equilibration (Sala et al., 2014).

5.6.4.2 Heating of the sample

Similarly, the quench should not heat the sample, otherwise there would be a competing thermal generation of monopoles. If the heating produces fewer monopoles than the Wien effect on a much faster or slower time scale than the Langevin time lag, it is possible to separate these effects in the magnetization curve. If thermal generation is very fast, we can modify the initial condition q_0 in the kinetic model to accomodate the enhanced density. If it is very slow, we can use a modified kinetic model, where the first equation would be the chemical kinetics of the thermal generation and the second would be the instantaneous Wien effect equation. This however introduces fitting parameters into our model.

An alternative approach would be to achieve steady heat fluxes into and out of the sample to obtain a stable monopole temperature. The Wien effect would then not only modify the susceptibility but also the dissipated power due to the phase shift between driving and response. A similar approach was proposed by Pearson (1954) for electrolytes, but lacks experimental verification up to this day.

5.6.4.3 Demagnetization

Demagnetization is another concern because it reduces the effective width of the plateau by accelerating the magnetization processes in the
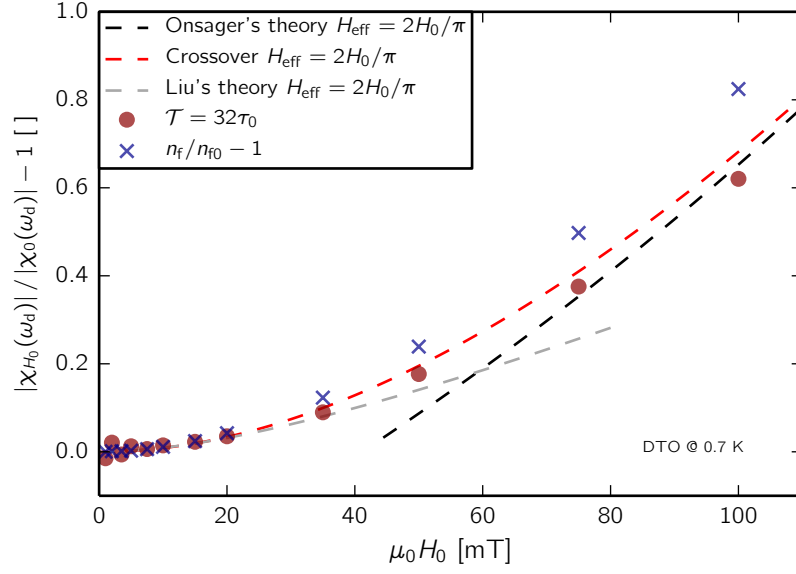
Figure 5.14: **Screened Wien effect in spin ice.** Measurements at higher temperatures facilitate equilibration of the system. The figure represents the maximum increase of the non-linear susceptibility for DTO at $0.7\,$K in the presence of demagnetization ($\mathscr{D} = 1/3$). The maximal response is achieved at $\mathscr{T} = 32\tau_0$ and decays if we tune out of the corresponding frequency. There is a good agreement with the electrolyte theory for the crossover between Liu's theory of the screened Wien effect and Onsager's theory which takes over at high fields once the atmosphere is destroyed. The Debye length in DTO spin ice is five times smaller at $0.7\,$K than at $0.45\,$K (temperature for the unscreened results).

sample (Quilliam et al., 2011; Bovo et al., 2013b). The simulations allow us to study this process[7] (see section 4.8). If vacuum boundary conditions are taken in the Ewald summation (see section 2.6.4), an additional term appears in energy that is exactly equal to the demagnetization contribution with $\mathscr{D} = 1/3$. We are constrained to this value because the Ewald summation has the nature of summing a conditionally convergent series by adding spherical shells. This is also the worst-case scenario, because $\sum_{i\in\{x,y,z\}} \mathscr{D}_i = 1$, so there is always a direction along which $\mathscr{D} \leq 1/3$. The simulations show that even with $\mathscr{D} = 1/3$ the Wien effect is observable at $0.7\,$K, albeit in a screened form (see figures 5.14 and 5.15). The details of the screened Wien effect theory were given in section 3.3.1.2.

---

7 The demagnetization results in spin ice are also relevant for depolarization in electrolytes which is however often removed experimentally (Wright, 2007).

5.6.4.4 Adiabatic susceptibility

There is a small but measurable infinite frequency (adiabatic) susceptibility which is not captured by any spin model of spin ice (Bovo et al., 2013a). For a successful measurement of the Wien effect the experiment has to be performed at frequencies low enough for this contribution not to dominate the susceptibility. Alternatively, it needs to be subtracted. However, the adiabatic susceptibility is predicted to scale with the monopole density so if this condition is fulfiled at one temperature, it should be valid at the other temperatures.

5.6.4.5 Comparison with simulations

A question may arise how reliably the simulation time reproduces physical time as the parameters are varied. In section 2.6.5 about algorithms, that in a Monte Carlo algorithm with local moves the time step can be scaled to physical time using the average acceptance probability per particle. In spin ice, this idea was successfully tested by (Jaubert and Holdsworth, 2009).

We observe in simulations that the acceptance probability is dominated by the motion of existing charges rather than by the creation and annihilation of new charges. We assume that the free charge contribution can be included in the field dependent mobility $\varkappa(\mathbf{H}_{\mathrm{int}})/\varkappa(0) = (1 - \exp \beta \mu_0 \mu \cdot \mathbf{H}_{\mathrm{int}})$, which resembles the functional dependence of the field dependent mobility given for spin ice $\varkappa(\mathbf{H}_{\mathrm{int}})/\varkappa(0) = \tanh(\beta \mu_0 \mu \cdot \mathbf{H}_{\mathrm{int}}/2)/(\beta \mu_0 \mu \cdot \mathbf{H}_{\mathrm{int}}/2)$ (Castelnovo et al., 2011). The reduced mobility will lead to a decrease in susceptibility and an increase in τ_S. However, this effect is small for the parameters considered.

In this chapter we have found a prediction for the non-linear susceptibility of a highly frustrated magnet. This is a result of a series of steps that we have followed throughout this thesis. The following chapter concludes this thesis by discussing the significance of this result in the context of electrolyte theory, frustrated magnetism, and non-equilibrium physics.
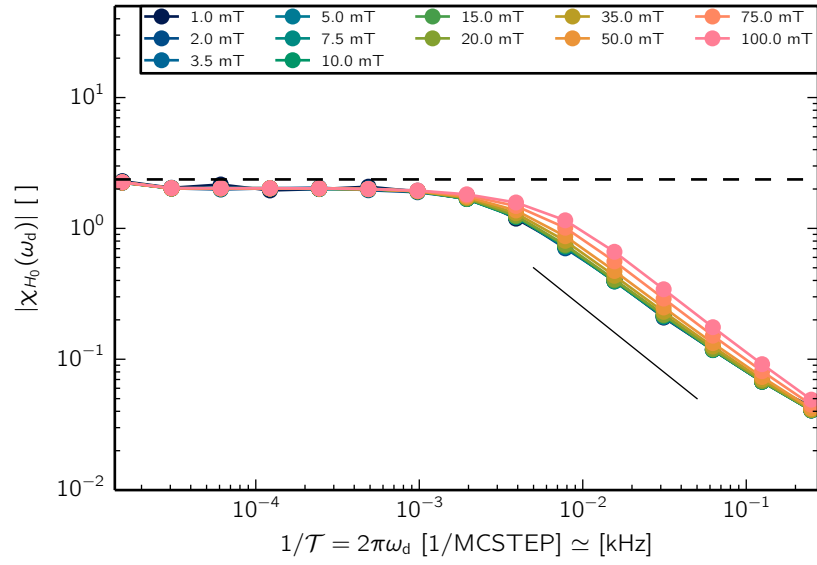
(a) Absolute susceptibility.
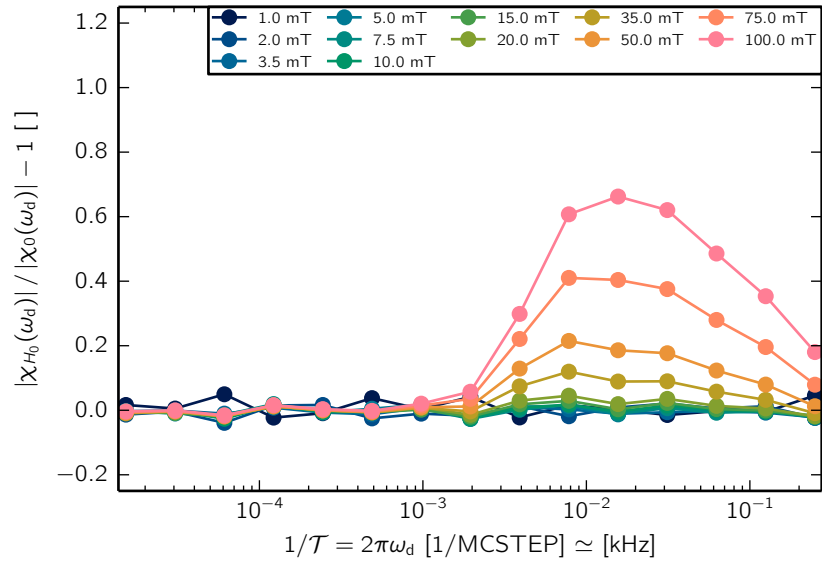
(b) Relative change in susceptibility.

Figure 5.15: **Frequency dependence of the Wien effect in spin ice at higher temperature ($0.7\,$K) and in presence of the demagnetization ($\mathscr{D} = 1/3$).** Although these conditions represent the "worst-case scenario" for observing the second Wien effect in spin ice, it still leaves traces in the non-linear susceptibility. The absolute value of susceptibility keeps the Debye form with $1/\omega$ tail (full black line) but τ_S shifts to higher frequencies as the equilibrium monopole density grows with temperature. The apparent isothermal susceptibility is $\chi_{\mathscr{D}} = 1/(1/\chi_T + \mathscr{D})$ (dashed black line from NNSI approximation). Compared to lower temperatures, the relative increase of the susceptibility is much narrower. The maximum has the field dependence of the screened Wien effect in electrolytes (see figure 5.14).

Conclusions

We have presented two main topics in this thesis: the non-equilibrium behaviour of a Coulomb gas and the non-linear susceptibility of spin ice. These are closely related because spin ice supports a Coulomb gas of magnetic monopoles. In both cases we have presented a theory that predicts behaviour observed in simulations without any free parameters. Here we would like to briefly revisit the main results of this investigation in a broader context.

Since the seminal theory of Onsager (1934) the second Wien effect has been observed in a plethora of materials (see chapter 3). In all of them, an increase in conductivity is seen which follows from an increase in charge carrier density. From the perspective of non-equilibrium physics, this effect has many fascinating properties. It is a stochastic process beyond linear response in a system with long range interactions and yet there is an exact solution to it. This exact solution is for the two-body dynamics of the charges. Strictly considered, it only applies to the many-body dynamics of the Coulomb gas at high fields or strong coupling, but in reality it is robust well beyond and describes many real world materials. The solution captures the paradoxical property that an increase in the attractive Coulombic interaction leads to an enhancement of the field driven dissociation of pairs bound by this interaction into free charges.

We have presented the first numerical simulations of the second Wien effect in the third chapter of this thesis. To this end we introduced a minimal model for the effect, a grand canonical version of the restricted primitive model on a lattice. Our simulations confirmed Onsager's theory in its limits of validity – the dilute weak electrolyte limit – but they also made new aspects of the Wien effect accessible.

The confirmation is itself an interesting result because we apply a continuum theory to a lattice problem. The most important length for characterising the second Wien effect – the Bjerrum length – is typically only two or three times larger than the nearest-neighbour distance in the range of parameters accessible to the simulations. Notably, the dissociation equilibrium constant whose change Onsager calculated has different equilibrium values on the lattice and in continuum. The relative increase is nevertheless robust and universal. This is also the first time the increase in the dissociation constant was seen directly, as

our simulations allow direct access to the correlations underlying the second Wien effect.

As the equilibrium density increases above the dilute limit, screening starts to modify the Wien effect strongly. Liu (1965) presented a theory of the screened Wien effect which fares well if the screening strongly dominates. However, there is a crossover regime between the screened and unscreened Wien effects whose full treatment of the crossover regime would require a solution for the many-body stochastic dynamics of a long-range interacting gas. Instead, we found a phenomenological description of the crossover by extending the activity coefficient out of equilibrium. We provided a plausible functional form for the non-equilibrium activity coefficient together with constraints on its behaviour in low and high field limits. The resulting function gives a parameterless description of all data obtained in our simulations. Materials can as a result be characterised with respect to their Wien effect behaviour using only two reduced variables: temperature and chemical potential.

While the increase in density and the dissociation constant with the external field are robust, the measured conductivity was shown to depend on a model/material specific mobility and its field dependence. We found a full description for the mobility observed in our simulations. There is a contribution from the Coulombic interactions – the first Wien effect – and from the choice of the stochastic dynamics in our simulations – the Metropolis algorithm. While the Coulombic contribution is inherent to any Coulomb gas, the dynamics can be chosen to match a specific material. In ionic glasses (Ingram et al., 1980) or dielectric liquids (Dukhin and Parlia, 2013) the change in conductivity can overshadow the second Wien effect which nevertheless contributes to the field depedence. Neglecting the Wien effect can then lead to significant modelling errors. Our simulations provide a model that can be readily extended for analysis of such situations.

Frustrated magnets act as a 'substrate' for many unusual quasi-particles. One of the notable examples is the Coulomb gas of magnetic monopoles in spin ice (Castelnovo et al., 2008). The grandcanonical Coulomb gas in spin ice is highly tunable through changes in temperature (Jaubert and Holdsworth, 2009). The magnetic monopoles control the equilibrium properties of spin ice at low temperatures (Castelnovo et al., 2011) and also its response properties (Bovo et al., 2013a).

At low temperatures, spin ice finds itself in the dilute weak electrolyte limit which led to the proposal to use the second Wien effect for diagnostics of magnetic charge of the monopoles using μ-SR (Bramwell et al., 2009). As the monopoles constitute the main contribution to the response of spin ice at these temperatures, the increase in monopole

density has to be necessarily observable in a change in the response of spin ice as well. This motivated us to follow up on this proposal by using the second Wien effect to describe the non-linear magnetic susceptibility of spin ice over a broad range of parameters. The prediction was developed using a systematic programme of numerical simulations of the dumbbell model of spin ice.

The proposed protocol resembles AC susceptibility measurements but requires higher amplitudes of driving. We show that the magnetic response is then not only a function of frequency but also of amplitude. We also observe that higher harmonics are generated as behooves a non-linear effect. Interestingly, a simple kinetic model captures the majority of the dynamics found in simulations. This model combines the chemical kinetics of the second Wien effect with Debye-like relaxation of the magnetization. A complementary approach consists of performing a field quench (Giblin et al., 2011; Paulsen et al., 2014). Such a process is more involved than in the equivalent electrolyte because there are no permanent direct monopole currents permitted in spin ice. We found predictions for the time evolution of magnetization and monopole density after a field quench.

We assumed throughout this work that equilibrating the magnetolyte is possible. It is however a well-known experimental fact that equilibrating $Dy_2Ti_2O_7$ spin ice requires prohibitively long times at temperatures below ~ 0.5–$0.6\,\mathrm{K}$. We showed that signatures of the Wien effect should be observable above this temperature and also in the presence of demagnetization fields. The situation in other spin ice materials should be similar with reports of a faster hopping rate of monopoles in $Ho_2Ti_2O_7$ (Quilliam et al., 2011). We therefore conclude that our proposal is realistic within the current experimental state of the art.

The predictions that we make are devoid of any free parameters once the spin ice material is specified by its exchange and dipolar couplings. In the regime of interest, the equilibrium susceptibility is well characterized by the monopole density (Ryzhkin, 2005; Bovo et al., 2013a) which can be found from the Bjerrum—Debye–Hückel theory. The relative increase is then captured by the second Wien effect theory which our work on lattice Coulomb gases extended to include various degrees of screening.

In the context of non-equilibrium physics such a prediction is unusual in many respects. Spin ice is a frustrated magnetic system with long-range interactions, yet its non-linear susceptibility can be described non-perturbatively over a large range of parameters. We have confirmed and refined this prediction in numerical simulations. This is a remarkable confirmation of the strength of modern condensed matter theory with concepts such as fractionalization but also of classic electrolyte theory.

A non-linear susceptibility has been introduced in various contexts. Generation of higher harmonics finds many practical applications in optics (Boyd, 2003). Susceptibility at higher harmonics also allows for the characterization of critical behaviour as evidenced in quantum magnets (Wu et al., 1993), frustrated magnets (Gingras et al., 1997), and other magnetic materials (Banerjee et al., 2005). Glassy systems in particular often require study of various non-linear susceptibilities either related to higher harmonics (Fujiki and Katsura, 1981; Ogielski, 1985) or the time evolution of correlations (Mézard and Parisi, 1991; Cugliandolo et al., 1997b). Glassiness comes into play for a broad range of materials ranging from liquids (Berthier and Biroli, 2011) to superconductors (Rosenstein and Li, 2010).

Our theory contrasts with these results in several aspects. It is neither perturbative nor based on a mean field approach (apart from the electrostatic screening at low fields). We obtain quantitative predictions away from critical points. In principle infinitely many higher susceptibilities can be found from our kinetic model. However, the focus lies on the same frequency response (first susceptibility) whose amplitude dependence is fully characterized beyond linear response.

The present work is based on a simple lattice model whose extensions are limited only by our imagination. Possible future extensions of our work include asymmetric electrolytes where pairing is a multi-stage process; the second Wien effect in the case where one of the species is fixed; effects of disorder; and the interplay between the Wien effect and confinement which promotes pairing.

The electrolytes and their transport theory were one of Onsager's motivations for studying non-equilibrium thermodynamics. It is no exagerration to claim that his reciprocity relations are the foundation of this field (Onsager, 1931). It would be interesting and worthwhile to restate the second Wien effect in this context. The establishment of the second Wien effect connects well described equilibrium and steady states (or two equilibrium states for a quench in spin ice). Modern fluctuation theorems constrain behaviour of thermodynamic quantities along such transitions (Jarzynski, 1997; Crooks, 1999; Seifert, 2005). The second Wien effect could thus provide a non-trivial long-range interacting model for testing the predictions of these fluctuation theorems. These might even be accessible to experiments given the recent progress in nano-fluidics. One might similarly explore the validity of non-equilibrium Green–Kubo relations to see whether the increase in conductivity can be borne out by the non-equilibrium current fluctuations. We would thus like to present this amazing non-equilibrium effect for a reevaluation in the light of the progress of the eighty years since its theory was first put forward.

Bibliography

I. Affleck, T. Kennedy, E. H. Lieb, and H. Tasaki. Rigorous results on valence-bond ground states in antiferromagnets. *Physical Review Letters*, **59**, no. 7, 799–802 (1987).

A. Alastuey and P. A. Martin. Absence of exponential clustering in quantum Coulomb fluids. *Physical Review A*, **40**, no. 11, 6485–6520 (1989).

A. Allnatt. Integral equations in ionic solution theory. *Molecular Physics*, **8**, no. 6, 533–539 (1964).

P. W. Anderson. Ordering and Antiferromagnetism in Ferrites. *Physical Review*, **102**, no. 4, 1008–1013 (1956).

P. W. Anderson. Resonating valence bonds: A new kind of insulator? *Materials Research Bulletin*, **8**, no. 2, 153–160 (1973).

S. Arrhenius. Versuch, die Dissoziation (Aktivitätskoeffizient) bei in Wasser gelösten Körpern zu berechnen. *Zeitschrift für physikalische Chemie*, **1**, 631 (1887).

N. W. Ashcroft and N. D. Mermin. *Solid State Physics* (Cengage Learning Emea, New York, 1976).

F. E. Bailey, A. Patterson Jr, and R. M. Fuoss. Wien Effect in Polyelectrolytes. *Journal of the American Chemical Society*, **74**, no. 7, 1845–1846 (1952).

L. Balents. Spin liquids in frustrated magnets. *Nature*, **464**, no. 7286, 199–208 (2010).

A. Banerjee, A. Bajpai, and S. Nair. Probing Magnetic Phases in Different Systems using Linear and Non Linear Susceptibility. In *Frontiers in Magnetic Materials*, edited by P. D. A. V. Narlikar, pp. 43–69 (Springer Berlin Heidelberg, 2005).

V. Barger. *Classical Mechanics: A Modern Perspective* (McGraw-Hill Companies, New York, 1994), 2nd edition edn..

P. Barham, L. H. Skibsted, W. L. P. Bredie, M. Bom Fr?st, P. M?ller, J. Risbo, P. Snitkjær, and L. M. Mortensen. Molecular Gastronomy: A New Emerging Scientific Discipline. *Chemical Reviews*, **110**, no. 4, 2313–2365 (2010).

D. K. Barkan. *Walther Nernst and the Transition to Modern Physical Science* (Cambridge University Press, Cambridge, 2011), auflage: reissue edn..

G. T. Barkema and M. E. J. Newman. Monte Carlo simulation of ice models. *Physical Review E*, **57**, no. 1, 1155 (1998).

W. M. Bartczak and A. Hummel. Computer simulation of ion recombination in irradiated nonpolar liquids. *The Journal of Chemical Physics*, **87**, no. 9, 5222–5228 (1987).

L. Bass. Wien dissociation as a rate process. *Transactions of the Faraday Society*, **64**, no. 0, 2153–2159 (1968).

L. Bass and D. K. McIlroy. Enzyme Activities in Polarized Cell Membranes. *Biophysical Journal*, **8**, no. 1, 99–108 (1968). PMID: 5641405.

R. J. Baxter. *Exactly Solved Models in Statistical Mechanics* (Dover Publications, Mineola, N.Y, 2008).

D. Berg and A. Patterson Jr. The High Field Conductance of Aqueous Solutions of Carbon Dioxide at 25°. The True Ionization Constant of Carbonic Acid1. *Journal of the American Chemical Society*, **75**, no. 21, 5197–5200 (1953).

J. D. Bernal and R. H. Fowler. A Theory of Water and Ionic Solution, with Particular Reference to Hydrogen and Hydroxyl Ions. *The Journal of Chemical Physics*, **1**, no. 8, 515–548 (1933).

L. Berthier and G. Biroli. Theoretical perspective on the glass transition and amorphous materials. *Reviews of Modern Physics*, **83**, no. 2, 587–645 (2011).

N. Bjerrum. A New Form for the Electrolytic Dissociation Theory. *Proceedings of the Seventh International Congress of Applied Chemistry*, pp. 55—60 (1909).

N. Bjerrum. Der Aktivitätskoeffizient der Ionen. *Zeitschrift für anorganische und allgemeine Chemie*, **109**, no. 1, 275–292 (1919).

N. J. Bjerrum. Untersuchungen über Ionenassoziation. *Det Kgl. Danske Videnskabernes Selskab., Mathematisk-fysiske Meddelelser.*, **7**, no. 9, 1—48 (1926).

H. W. J. Blöte, R. F. Wielinga, and W. J. Huiskamp. Heat-capacity measurements on rare-earth double oxides R2M2O7. *Physica*, **43**, no. 4, 549–568 (1969).

S. J. Blundell. Monopoles, Magnetricity, and the Stray Field from Spin Ice. *Physical Review Letters*, **108**, no. 14, 147601 (2012).

L. Bovo, J. Bloxsom, D. Prabhakaran, G. Aeppli, and S. Bramwell. Brownian motion and quantum dynamics of magnetic monopoles in spin ice. *Nature Communications*, **4**, 1535 (2013a).

L. Bovo, L. D. C. Jaubert, P. C. W. Holdsworth, and S. T. Bramwell. Crystal shape-dependent magnetic susceptibility and Curie law crossover in the spin ices Dy2Ti2O7 and Dy2Ti2O7. *Journal of Physics: Condensed Matter*, **25**, no. 38, 386002 (2013b).

R. W. Boyd. *Nonlinear Optics* (Academic Press, 2003).

S. T. Bramwell. Generalized longitudinal susceptibility for magnetic monopoles in spin ice. *Philosophical Transactions of the Royal Society A: Mathematical, Physical and Engineering Sciences*, **370**, no. 1981, 5738–5766 (2012).

S. T. Bramwell and S. R. Giblin.   Comment on 'Spin Ice: Magnetic Excitations without Monopole Signature Using muSR'.   *arXiv preprint arXiv:1111.4168* (2011).

S. T. Bramwell, S. R. Giblin, S. Calder, R. Aldus, D. Prabhakaran, and T. Fennell. Measurement of the charge and current of magnetic monopoles in spin ice. *Nature*, **461**, no. 7266, 956–959 (2009).

S. T. Bramwell and M. J. P. Gingras. Spin Ice State in Frustrated Magnetic Pyrochlore Materials. *Science*, **294**, no. 5546, 1495–1501 (2001). PMID: 11711667.

S. T. Bramwell and M. J. Harris. Frustration in Ising-type spin models on the pyrochlore lattice. *Journal of Physics: Condensed Matter*, **10**, no. 14, L215 (1998).

R. Bräunig, Y. Gushimana, and G. Ilgenfritz. Ionic strength dependence of the electric dissociation field effect Investigation of 2, 6-dinitrophenol and application to the acid-alkaline transition of metmyoglobin and methemoglobin. *Biophysical chemistry*, **26**, no. 2, 181–191 (1987).

C. Broholm, G. Aeppli, G. P. Espinosa, and A. S. Cooper. Antiferromagnetic fluctuations and short-range order in a Kagomé lattice. *Physical Review Letters*, **65**, no. 25, 3173–3176 (1990).

J. N. Brønsted. Introductory paper.—Part II.: activity. On the activity of electrolytes. *Transactions of the Faraday Society*, **23**, 416–432 (1927).

M. E. Brooks-Bartlett, S. T. Banks, L. D. C. Jaubert, A. Harman-Clarke, and P. C. W. Holdsworth. Magnetic-Moment Fragmentation and Monopole Crystallization. *Physical Review X*, **4**, no. 1, 011007 (2014).

P. Brüesch and T. Christen. The electric double layer at a metal electrode in pure water. *Journal of Applied Physics*, **95**, no. 5, 2846–2856 (2004).

D. C. Brydges and P. A. Martin. Coulomb Systems at Low Density: A Review. *Journal of Statistical Physics*, **96**, no. 5-6, 1163–1330 (1999).

S. Calder, S. R. Giblin, and S. T. Bramwell.   Using as a magnetometer. *Physica B: Condensed Matter*, **404**, no. 5-7, 1017–1019 (2009).

B. Canals and D. A. Garanin.   Spin-liquid phase in the pyrochlore antiferromagnet. *Canadian journal of physics*, **79**, no. 11-12, 1323–1331 (2001).

J. Cardy. *Scaling and Renormalization in Statistical Physics* (Cambridge University Press, Cmabridge ; New York, 1996).

C. Castelnovo and C. Chamon. Topological order and topological entropy in classical systems. *Physical Review B*, **76**, no. 17, 174416 (2007).

C. Castelnovo, R. Moessner, and S. Sondhi. Spin Ice, Fractionalization, and Topological Order. *Annual Review of Condensed Matter Physics*, **3**, no. 1, 35–55 (2012).

C. Castelnovo, R. Moessner, and S. L. Sondhi. Magnetic monopoles in spin ice. *Nature*, **451**, no. 7174, 42–45 (2008).

C. Castelnovo, R. Moessner, and S. L. Sondhi. Thermal Quenches in Spin Ice. *Physical Review Letters*, **104**, no. 10 (2010).

C. Castelnovo, R. Moessner, and S. L. Sondhi. Debye-Hückel theory for spin ice at low temperature. *Physical Review B*, **84**, no. 14 (2011).

P. M. Chaikin and T. C. Lubensky. *Principles of Condensed Matter Physics* (Cambridge University Press, Cambridge; New York, NY, USA, 2000), reprint edition edn..

J. T. Chalker, P. C. W. Holdsworth, and E. F. Shender. Hidden order in a frustrated system: Properties of the Heisenberg Kagomé antiferromagnet. *Physical Review Letters*, **68**, no. 6, 855–858 (1992).

J. D. M. Champion, M. J. Harris, P. C. W. Holdsworth, A. S. Wills, G. Balakrishnan, S. T. Bramwell, E. Čižmár, T. Fennell, J. S. Gardner, J. Lago, D. F. McMorrow, M. Orendáč, A. Orendáčová, D. M. Paul, R. I. Smith, M. T. F. Telling, and A. Wildes. Er2Ti2O7: Evidence of quantum order by disorder in a frustrated antiferromagnet. *Physical Review B*, **68**, no. 2, 020401 (2003).

X. Z. Cheng, M. B. A. Jalil, H. K. Lee, and Y. Okabe. Mapping the Monte Carlo Scheme to Langevin Dynamics: A Fokker-Planck Approach. *Physical Review Letters*, **96**, no. 6, 067208 (2006).

F. Corberi, E. Lippiello, and M. Zannetti. Fluctuation dissipation relations far from equilibrium. *Journal of Statistical Mechanics: Theory and Experiment*, **2007**, no. 07, P07002 (2007).

G. E. Crooks. Entropy production fluctuation theorem and the nonequilibrium work relation for free energy differences. *Physical Review E*, **60**, no. 3, 2721–2726 (1999).

L. F. Cugliandolo, D. S. Dean, and J. Kurchan. Fluctuation-Dissipation Theorems and Entropy Production in Relaxational Systems. *Physical Review Letters*, **79**, no. 12, 2168–2171 (1997a).

L. F. Cugliandolo, J. Kurchan, and L. Peliti. Energy flow, partial equilibration, and effective temperatures in systems with slow dynamics. *Physical Review E*, **55**, no. 4, 3898–3914 (1997b).

P. Debye. Reaction Rates in Ionic Solutions. *Transactions of The Electrochemical Society*, **82**, no. 1, 265–272 (1942).

P. Debye and H. Falkenhagen. Dispersion der Leitfähigkeit starker Elektrolyte. *Zeitschrift für Elektrochemie und angewandte physikalische Chemie*, **34**, no. 9, 562–565 (1928).

P. Debye and E. Hückel. Zur Theorie der Elektrolyte. I. Gefrierpunktserniedrigung und verwandte Erscheinungen. *Physikalische Zeitschrift*, **24**, no. 9, 185—206 (1923a).

P. Debye and E. Hückel. Zur Theorie der Elektrolyte. II. Das Grenzgesetz für die elektrische Leitfähigkeit. *Physikalische Zeitschrift*, **24**, 305 (1923b).

P. A. M. Dirac. Quantised Singularities in the Electromagnetic Field. *Proceedings of the Royal Society A: Mathematical, Physical and Engineering Sciences*, **133**, no. 821, 60–72 (1931).

A. Dukhin and S. Parlia. Ions, ion pairs and inverse micelles in non-polar media. *Current Opinion in Colloid & Interface Science*, **18**, no. 2, 93–115 (2013).

S. R. Dunsiger, A. A. Aczel, C. Arguello, H. Dabkowska, A. Dabkowski, M. Du, T. Goko, B. Javanparast, T. Lin, F. L. Ning, et al.. Spin ice: magnetic excitations without monopole signatures using muon spin rotation. *Physical review letters*, **107**, no. 20, 207207 (2011).

W. Ebeling and M. Grigo. An analytical calculation of the equation of state and the critical point in a dense classical fluid of charged hard spheres. *Annalen der Physik*, **492**, no. 1, 21–30 (1980).

W. Ebeling and M. Grigo. Mean spherical approximation-mass action law theory of equilibrium and conductance in ionic solutions. *Journal of Solution Chemistry*, **11**, no. 3, 151–167 (1982).

W. Ebeling, S. Hilbert, and H. Krienke. On Bjerrum's mass action law for electrolytes and Onsager's bookkeeping rule. *Journal of Molecular Liquids*, **96–97**, 409–423 (2002).

H. C. Eckstrom and C. Schmelzer. The Wien Effect: Deviations of Electrolytic Solutions from Ohm's Law under High Field Strengths. *Chemical Reviews*, **24**, no. 3, 367–414 (1939).

M. Eigen. Immeasurably fast reactions. *Nobel Lecture*, **11**, 1963–1979 (1967).

M. Eigen and L. De Maeyer. Ein stationäres Feldverfahren zur Untersuchung von Dissoziationsprozessen in Flüssigkeiten und Festkörpern. *Zeitschrift für Elektrochemie, Berichte der Bunsengesellschaft für physikalische Chemie*, **60**, no. 9-10, 1037–1048 (1956).

M. Eigen, L. De Maeyer, and H. Spatz. Über das kinetische verhalten von protonen und deuteronen in eiskristallen. *Berichte der Bunsengesellschaft für physikalische Chemie*, **68**, no. 1, 19–29 (1964).

M. Eigen, G. Kurtze, and K. Tamm. Zum Reaktionsmechanismus der Ultraschallabsorption in wässrigen Elektrolytlösungen. *Zeitschrift für Elektrochemie, Berichte der Bunsengesellschaft für physikalische Chemie*, **57**, no. 2, 103–118 (1953).

M. Eigen and J. Schoen. Stoßspannungsverfahren zur Untersuchung sehr schnell verlaufender Ionenreaktionen in wässeriger Lösung. *Zeitschrift für Elektrochemie, Berichte der Bunsengesellschaft für physikalische Chemie*, **59**, no. 6, 483–494 (1955).

H. Falkenhagen. *Theorie der Elektrolyte* (S. Hirzel Verlag Leipzig, 1971).

A. Feltz and F. Schirrmeister. Charge Carrier Transport Mechanism in Amorphous Layers of the Composition Ge4Se5Te. *physica status solidi (a)*, **57**, no. 2, 591–599 (1980).

T. Fennell, P. P. Deen, A. R. Wildes, K. Schmalzl, D. Prabhakaran, A. T. Boothroyd, R. J. Aldus, D. F. McMorrow, and S. T. Bramwell. Magnetic Coulomb phase in the spin ice Ho2Ti2O7. *Science*, **326**, no. 5951, 415–417 (2009).

M. E. Fisher and J. Stephenson. Statistical Mechanics of Dimers on a Plane Lattice. II. Dimer Correlations and Monomers. *Physical Review*, **132**, no. 4, 1411–1431 (1963).

M. E. Fisher and D. M. Zuckerman. Exact thermodynamic formulation of chemical association. *The Journal of Chemical Physics*, **109**, no. 18, 7961 (1998).

D. Frenkel and B. Smit. *Understanding Molecular Simulation, Second Edition: From Algorithms to Applications* (Academic Press, San Diego, 2001), 2 edition edn..

H. L. Friedman. The pair correlation functiong+-(r) implied by Bjerrum's theory of ion pairing. *Journal of Solution Chemistry*, **9**, no. 6, 371–379 (1980).

H. L. Friedman and B. Larsen. Corresponding states for ionic fluids. *The Journal of Chemical Physics*, **70**, no. 1, 92 (1979).

S. Fujiki and S. Katsura. Nonlinear Susceptibility in the Spin Glass. *Progress of Theoretical Physics*, **65**, no. 4, 1130–1144 (1981).

R. M. Fuoss. Conductance-concentration function for the paired ion model. *The Journal of Physical Chemistry*, **82**, no. 22, 2427–2440 (1978).

R. M. Fuoss and L. Onsager. Conductance of Unassociated Electrolytes. *The Journal of Physical Chemistry*, **61**, no. 5, 668–682 (1957).

R. M. Fuoss and L. Onsager. The Conductance Of Symmetrical Electrolytes. II. The Relaxation Field. *The Journal of Physical Chemistry*, **67**, no. 3, 621–628 (1963).

J. S. Gardner, M. J. P. Gingras, and J. E. Greedan. Magnetic pyrochlore oxides. *Reviews of Modern Physics*, **82**, no. 1, 53–107 (2010).

A. Gemant. *Elektrophysik der Isolierstoffe* (Springer, Berlin, 1930).

P. d. Gennes. *Scaling Concepts in Polymer Physics* (Cornell University Press, 1979).

W. F. Giauque and M. F. Ashley. Molecular Rotation in Ice at 10°K. Free Energy of Formation and Entropy of Water. *Physical Review*, **43**, no. 1, 81–82 (1933).

W. F. Giauque and J. W. Stout. The Entropy of Water and the Third Law of Thermodynamics. The Heat Capacity of Ice from 15 to 273°K. *Journal of the American Chemical Society*, **58**, no. 7, 1144–1150 (1936).

S. R. Giblin, S. T. Bramwell, P. C. W. Holdsworth, D. Prabhakaran, and I. Terry. Creation and measurement of long-lived magnetic monopole currents in spin ice. *Nature Physics*, **7**, no. 3, 252–258 (2011).

M. J. Gingras and B. C. den Hertog. Origin of spin-ice behavior in Ising pyrochlore magnets with long-range dipole interactions: an insight from mean-field theory. *Canadian journal of physics*, **79**, no. 11-12, 1339–1351 (2001).

M. J. P. Gingras and P. A. McClarty. Quantum spin ice: a search for gapless quantum spin liquids in pyrochlore magnets. *Reports on Progress in Physics*, **77**, no. 5, 056501 (2014).

M. J. P. Gingras, C. V. Stager, N. P. Raju, B. D. Gaulin, and J. E. Greedan. Static Critical Behavior of the Spin-Freezing Transition in the Geometrically Frustrated Pyrochlore Antiferromagnet Y2Mo2O7. *Physical Review Letters*, **78**, no. 5, 947–950 (1997).

M. Grigo and W. Ebeling. Remarks on the correlation function implied by the Bjerrum theory of ion pairing. *Journal of Solution Chemistry*, **13**, no. 5, 321–333 (1984).

E. A. Guggenheim. The accurate numerical solution of the Poisson-Boltzmann equation. *Transactions of the Faraday Society*, **55**, 1714 (1959).

E. Güntelberg. Untersuchungen über Ioneninteraktion. *Z. Phys. Chem.*, **123**, 199–247 (1926).

J. Hansen and I. R. McDonald. *Theory of Simple Liquids* (Academic Press, Amsterdam ; Boston, 2006), 3 edition edn..

F. Harris. On the use of windows for harmonic analysis with the discrete Fourier transform. *Proceedings of the IEEE*, **66**, no. 1, 51–83 (1978).

M. J. Harris, S. T. Bramwell, P. C. W. Holdsworth, and J. D. M. Champion. Liquid-Gas Critical Behavior in a Frustrated Pyrochlore Ferromagnet. *Physical Review Letters*, **81**, no. 20, 4496–4499 (1998).

M. J. Harris, S. T. Bramwell, D. F. McMorrow, T. Zeiske, and K. W. Godfrey. Geometrical Frustration in the Ferromagnetic Pyrochlore Ho2Ti2O7. *Physical Review Letters*, **79**, no. 13, 2554–2557 (1997).

A. J. Heeger, S. Kivelson, J. R. Schrieffer, and W. P. Su. Solitons in conducting polymers. *Reviews of Modern Physics*, **60**, no. 3, 781–850 (1988).

P. C. Hemmer, H. Holden, and S. K. Ratkje. *Collected Works of Lars Onsager, the* (World Scientific Publishing Company, Singapore ; River Edge, N.J, 1996).

C. Henley. Power-law spin correlations in pyrochlore antiferromagnets. *Physical Review B*, **71**, no. 1 (2005).

C. L. Henley. The "Coulomb Phase" in Frustrated Systems. *Annual Review of Condensed Matter Physics*, **1**, no. 1, 179–210 (2010).

M. Hermele, M. P. A. Fisher, and L. Balents. Pyrochlore photons: The U(1) spin liquid in a S=1/2 three-dimensional frustrated magnet. *Physical Review B*, **69**, no. 6, 064404 (2004).

B. C. den Hertog and M. J. Gingras. Dipolar interactions and origin of spin ice in Ising pyrochlore magnets. *Physical review letters*, **84**, no. 15, 3430 (2000).

M. Hilczer and M. Tachiya. Unified Theory of Geminate and Bulk Electron-Hole Recombination in Organic Solar Cells. *The Journal of Physical Chemistry C*, **114**, no. 14, 6808–6813 (2010).

J. H. van 't Hoff. Die Rolle osmotischen Drucks in der Analogie zwischen Lösungen und Gasen. *Zeitschrift fur physikalische Chemie*, **1**, 481–508 (1887).

K. M. Hong and J. Noolandi. Solution of the Smoluchowski equation with a Coulomb potential. I. General results. *The Journal of Chemical Physics*, **68**, no. 11, 5163 (1978).

R. Hoppe. Madelung constants. *Angewandte Chemie International Edition in English*, **5**, no. 1, 95–106 (1966).

R. M. F. Houtappel. Order-disorder in hexagonal lattices. *Physica*, **16**, no. 5, 425–455 (1950).

K. Huang. *Statistical Mechanics* (Wiley, New York, 1987), 2 edition edn..

D. A. Huse and A. D. Rutenberg. Classical antiferromagnets on the Kagomé lattice. *Physical Review B*, **45**, no. 13, 7536–7539 (1992).

M. D. Ingram, C. T. Moynihan, and A. V. Lesikar. Ionic conductivity and the weak electrolyte theory of glass. *Journal of Non-Crystalline Solids*, **38–39, Part 1**, 371–376 (1980).

S. Isakov, R. Moessner, and S. Sondhi. Why Spin Ice Obeys the Ice Rules. *Physical Review Letters*, **95**, no. 21 (2005).

S. V. Isakov, K. S. Raman, R. Moessner, and S. L. Sondhi. Magnetization curve of spin ice in a [111] magnetic field. *Physical Review B*, **70**, no. 10, 104418 (2004).

C. Jaccard. Thermodynamics of irreversible processes applied to ice. *Physik der kondensierten Materie*, **3**, no. 2, 99–118 (1964).

J. L. Jacobsen and J. Kondev. Field theory of compact polymers on the square lattice. *Nuclear Physics B*, **532**, no. 3, 635–688 (1998).

Y. M. Jana, A. Sengupta, and D. Ghosh. Estimation of single ion anisotropy in pyrochlore Dy2Ti2O7, a geometrically frustrated system, using crystal field theory. *Journal of Magnetism and Magnetic Materials*, **248**, no. 1, 7–18 (2002).

C. Jarzynski. Nonequilibrium Equality for Free Energy Differences. *Physical Review Letters*, **78**, no. 14, 2690–2693 (1997).

L. Jaubert, J. Chalker, P. Holdsworth, and R. Moessner. Three-Dimensional Kasteleyn Transition: Spin Ice in a [100] Field. *Physical Review Letters*, **100**, no. 6 (2008).

L. Jaubert, M. Harris, T. Fennell, R. Melko, S. Bramwell, and P. Holdsworth. Topological-Sector Fluctuations and Curie-Law Crossover in Spin Ice. *Physical Review X*, **3**, no. 1 (2013).

L. D. C. Jaubert. *Topological Constraints and Defects in Spin Ice*. PhD thesis, ENS Lyon (2009).

L. D. C. Jaubert, J. T. Chalker, P. C. W. Holdsworth, and R. Moessner. Spin Ice under Pressure: Symmetry Enhancement and Infinite Order Multicriticality. *Physical Review Letters*, **105**, no. 8, 087201 (2010).

L. D. C. Jaubert, M. Haque, and R. Moessner. Analysis of a fully packed loop model arising in a magnetic Coulomb phase. *Physical review letters*, **107**, no. 17, 177202 (2011).

L. D. C. Jaubert and P. C. W. Holdsworth. Signature of magnetic monopole and Dirac string dynamics in spin ice. *Nature Physics*, **5**, no. 4, 258–261 (2009).

L. D. C. Jaubert and P. C. W. Holdsworth. Magnetic monopole dynamics in spin ice. *Journal of Physics: Condensed Matter*, **23**, no. 16, 164222 (2011).

G. Job and F. Herrmann. Chemical potential—a quantity in search of recognition. *European Journal of Physics*, **27**, no. 2, 353 (2006).

J. V. José, L. P. Kadanoff, S. Kirkpatrick, and D. R. Nelson. Renormalization, vortices, and symmetry-breaking perturbations in the two-dimensional planar model. *Physical Review B*, **16**, no. 3, 1217–1241 (1977).

M. Justice and J. Justice. Ionic interactions in solutions. I. The association concepts and the McMillan-Mayer theory. *Journal of Solution Chemistry*, **5**, no. 8, 543–561 (1976).

V. Kaiser, S. T. Bramwell, P. C. W. Holdsworth, and R. Moessner. Onsager's Wien effect on a lattice. *Nature Materials*, **12**, no. 11, 1033–1037 (2013).

T. A. Kaplan. The Chemical Potential. *Journal of Statistical Physics*, **122**, no. 6, 1237–1260 (2006).

K. Kikuchi, M. Yoshida, T. Maekawa, and H. Watanabe. Metropolis Monte Carlo method as a numerical technique to solve the Fokker—Planck equation. *Chemical Physics Letters*, **185**, no. 3–4, 335–338 (1991).

A. Kitaev. Anyons in an exactly solved model and beyond. *Annals of Physics*, **321**, no. 1, 2–111 (2006).

B. Klemke, M. Meissner, P. Strehlow, K. Kiefer, S. A. Grigera, and D. A. Tennant. Thermal Relaxation and Heat Transport in the Spin Ice Material Dy2Ti2O7. *Journal of Low Temperature Physics*, **163**, no. 5-6, 345–369 (2011).

V. KOBELEV, A. B. KOLOMEISKY, and M. E. FISHER. Lattice models of ionic systems. *The Journal of Chemical Physics*, **116**, no. 17, 7589 (2002).

F. W. G. KOHLRAUSCH. Einfache Methoden und Instrumente zur Widerstandbestimmung inbesondere in Electrolyten. *Ann. der Physik und Chemie*, **9**, 653 (1880).

F. W. G. KOHLRAUSCH, L. F. C. HOLBORN, and UNKNOWN LIBRARY. *Das leitvermo?gen der elektrolyte, insbesondere der lo?sungen. Methoden, resultate und chemische anwendungen* (Leipzig, B. G. Teubner, 1898).

G. KOLLAND, O. BREUNIG, M. VALLDOR, M. HIERTZ, J. FRIELINGSDORF, and T. LORENZ. Thermal conductivity and specific heat of the spin-ice compound Dy2Ti2O7: Experimental evidence for monopole heat transport. *Physical Review B*, **86**, no. 6, 060402 (2012).

J. M. KOSTERLITZ and D. J. THOULESS. Ordering, metastability and phase transitions in two-dimensional systems. *Journal of Physics C: Solid State Physics*, **6**, no. 7, 1181 (1973).

W. KRAUTH. *Statistical Mechanics: Algorithms and Computations* (Oxford University Press, Oxford, 2006).

C. LACROIX, P. MENDELS, and F. MILA (eds.). *Introduction to Frustrated Magnetism: Materials, Experiments, Theory*, vol. 164 of *Springer Series in Solid-State Sciences* (Springer Berlin Heidelberg, Berlin, Heidelberg, 2011).

P. LANGEVIN. L'ionisation dez gaz. *Annales de chimie et de physique*, **28**, 433 (1903).

R. B. LAUGHLIN. Nobel Lecture: Fractional quantization. *Reviews of Modern Physics*, **71**, no. 4, 863–874 (1999).

J. L. LEBOWITZ and E. H. LIEB. Existence of Thermodynamics for Real Matter with Coulomb Forces. *Physical Review Letters*, **22**, no. 13, 631–634 (1969).

S. W. DE LEEUW, J. W. PERRAM, and E. R. SMITH. Simulation of electrostatic systems in periodic boundary conditions. I. Lattice sums and dielectric constants. *Proceedings of the Royal Society of London. A. Mathematical and Physical Sciences*, **373**, no. 1752, 27–56 (1980).

Y. LEVIN. Electrostatic correlations: from plasma to biology. *Reports on progress in physics*, **65**, no. 11, 1577 (2002).

Y. LEVIN and M. E. FISHER. Criticality in the hard-sphere ionic fluid. *Physica A: Statistical Mechanics and its Applications*, **225**, no. 2, 164–220 (1996).

G. N. LEWIS. The Law of Physico-Chemical Change. *Proceedings of the American Academy of Arts and Sciences*, **37**, no. 3, 49–69 (1901).

G. N. LEWIS. Outlines of a New System of Thermodynamic Chemistry. *Proceedings of the American Academy of Arts and Sciences*, **43**, no. 7, 259–293 (1907).

H. Li and F. D. M. Haldane. Entanglement Spectrum as a Generalization of Entanglement Entropy: Identification of Topological Order in Non-Abelian Fractional Quantum Hall Effect States. *Physical Review Letters*, **101**, no. 1, 010504 (2008).

E. H. Lieb. Residual entropy of square ice. *Physical Review*, **162**, no. 1, 162 (1967).

E. H. Lieb. The stability of matter. *Reviews of Modern Physics*, **48**, no. 4, 553–569 (1976).

C.-t. Liu. *The effect of screening of the ionic atmosphere on the theory of the Wien effect in weak electrolytes*. Ph.D., Yale (1965).

E. Luijten, M. E. Fisher, and A. Z. Panagiotopoulos. Universality Class of Criticality in the Restricted Primitive Model Electrolyte. *Physical Review Letters*, **88**, no. 18, 185701 (2002).

S. Mafé, J. A. Manzanares, and P. Ramrez. Model for ion transport in bipolar membranes. *Physical Review A*, **42**, no. 10, 6245–6248 (1990).

A. C. Maggs and N. W. Ashcroft. Electronic fluctuation and cohesion in metals. *Physical Review Letters*, **59**, no. 1, 113–116 (1987).

A. C. Maggs and V. Rossetto. Local Simulation Algorithms for Coulomb Interactions. *Physical Review Letters*, **88**, no. 19, 196402 (2002).

Y. Marcus and G. Hefter. Ion Pairing. *Chemical Reviews*, **106**, no. 11, 4585–4621 (2006).

B. Maribo-Mogensen, G. M. Kontogeorgis, and K. Thomsen. Comparison of the Debye–Hückel and the Mean Spherical Approximation Theories for Electrolyte Solutions. *Industrial & Engineering Chemistry Research*, **51**, no. 14, 5353–5363 (2012).

D. P. Mason and D. K. McIlroy. On the theory of Wien dissociation for weak electrolytes. *Physica A: Statistical Mechanics and its Applications*, **82**, no. 3, 463–476 (1975).

D. P. Mason and D. K. McIlroy. Perturbation expansion for Onsager's linear law for wien dissociation of a weak electrolyte. *Journal of the Chemical Society, Faraday Transactions 2*, **72**, 2195 (1976).

D. P. Mason and D. K. McIlroy. Gauss's divergence theorem in the theory of Wien dissociation of weak electrolytes. *Journal of the Chemical Society, Faraday Transactions 2*, **74**, 2019 (1978).

K. Matsuhira, C. Paulsen, E. Lhotel, C. Sekine, Z. Hiroi, and S. Takagi. Spin Dynamics at Very Low Temperature in Spin Ice Dy2Ti2O7. *Journal of the Physical Society of Japan*, **80**, no. 12, 123711 (2011).

D. c. Mattis. *The Theory of Magnetism Made Simple:An Introduction To Physical Concepts And To Some Useful Mathematical Methods* (World Scientific Publishing Company, Hackensack, NJ, 2006).

J. E. Mayer. The Theory of Ionic Solutions. *The Journal of Chemical Physics*, **18**, no. 11, 1426–1436 (1950).

D. K. McIlroy. Solution of Onsager's equation in closed form. *Physica A: Statistical Mechanics and its Applications*, **152**, no. 3, 459–468 (1988).

D. K. McIlroy and D. P. Mason. Wien dissociation in very low intensity electric fields. *Journal of the Chemical Society, Faraday Transactions 2*, **72**, 590 (1976).

D. K. McIlroy and D. P. Mason. Electric Field Dissociation of Charged Macromolecular Sites in Polarized Biomembranes III. Numerical Results and Application to Nervous Conduction. *SIAM Journal on Applied Mathematics*, **41**, no. 3, 580–591 (1981).

D. K. McIlroy and D. P. Mason. Effect of the boundary condition at distance of closest approach on Wien dissociation of a weak electrolyte: A singular perturbation solution. *Journal of mathematical physics*, **25**, no. 9, 2791–2799 (1984).

D. K. McIlroy and D. P. Mason. The concept of streamfunctions in the Wien effect on a weak electrolyte. *Journal of mathematical physics*, **28**, no. 12, 2999–3005 (1987).

D. A. McQuarrie. *Statistical Mechanics* (University Science Books, Sausalito, Calif, 2000), 1st edition edn..

D. J. Mead and R. M. Fuoss. Dependence of conductance on field strength. I. Tetrabutylammonium picrate in diphenyl ether at 50°. *Journal of the American Chemical Society*, **61**, no. 8, 2047–2053 (1939).

D. J. Mead and R. M. Fuoss. Dependence of conductance on field strength. II. Tetrabutylammonium bromide in diphenyl ether at 50. *Journal of the American Chemical Society*, **62**, no. 7, 1720–1723 (1940).

E. Meeron. Mayer's Treatment of Ionic Solutions. *The Journal of Chemical Physics*, **26**, no. 4, 804 (1957).

E. Meeron. Theory of Potentials of Average Force and Radial Distribution Functions in Ionic Solutions. *The Journal of Chemical Physics*, **28**, no. 4, 630 (1958).

R. Melko, B. den Hertog, and M. Gingras. Long-Range Order at Low Temperatures in Dipolar Spin Ice. *Physical Review Letters*, **87**, no. 6 (2001).

R. G. Melko and M. J. P. Gingras. Monte Carlo studies of the dipolar spin ice model. *Journal of Physics: Condensed Matter*, **16**, no. 43, R1277–R1319 (2004).

N. Metropolis, A. W. Rosenbluth, M. N. Rosenbluth, A. H. Teller, and E. Teller. Equation of State Calculations by Fast Computing Machines. *The Journal of Chemical Physics*, **21**, no. 6, 1087 (1953).

R. Metzler and J. Klafter. The random walk's guide to anomalous diffusion: a fractional dynamics approach. *Physics Reports*, **339**, no. 1, 1–77 (2000).

M. Mézard and G. Parisi. Replica field theory for random manifolds. *Journal de Physique I*, **1**, no. 6, 809–836 (1991).

K. A. Milton. Theoretical and experimental status of magnetic monopoles. *Reports on Progress in Physics*, **69**, no. 6, 1637 (2006).

P. Minnhagen. The two-dimensional Coulomb gas, vortex unbinding, and superfluid-superconducting films. *Reviews of Modern Physics*, **59**, no. 4, 1001–1066 (1987).

R. Moessner. Relief and generation of frustration in pyrochlore magnets by single-ion anisotropy. *Physical Review B*, **57**, no. 10, R5587–R5589 (1998).

R. Moessner and J. T. Chalker. Low-temperature properties of classical geometrically frustrated antiferromagnets. *Physical Review B*, **58**, no. 18, 12049–12062 (1998).

R. Moessner and S. L. Sondhi. Theory of the [111] magnetization plateau in spin ice. *Physical Review B*, **68**, no. 6, 064411 (2003).

R. Moessner and S. L. Sondhi. Irrational Charge from Topological Order. *Physical Review Letters*, **105**, no. 16, 166401 (2010).

E. W. Montroll and J. E. Mayer. Statistical Mechanics of Imperfect Gases. *The Journal of Chemical Physics*, **9**, no. 8, 626–637 (1941).

W. J. Moore. *Physical Chemistry* (Prentice-Hall, 1999), 5 edn..

A. G. Moreira and R. R. Netz. Virial expansion for charged colloids and electrolytes. *The European Physical Journal D - Atomic, Molecular, Optical and Plasma Physics*, **21**, no. 1, 83–96 (2002).

D. J. P. Morris, D. A. Tennant, S. A. Grigera, B. Klemke, C. Castelnovo, R. Moessner, C. Czternasty, M. Meissner, K. C. Rule, J. Hoffmann, K. Kiefer, S. Gerischer, D. Slobinsky, and R. S. Perry. Dirac Strings and Magnetic Monopoles in the Spin Ice Dy2Ti2O7. *Science*, **326**, no. 5951, 411–414 (2009).

J. F. Nagle. New series-expansion method for the dimer problem. *Physical Review*, **152**, no. 1, 190 (1966).

J. F. Nagle. Theory of the dielectric constant of ice. *Chemical Physics*, **43**, no. 3, 317–328 (1979).

F. Nauwelaers, L. Hellemans, and A. Persoons. Field dissociation effect, chemical relaxation, and conductance of tetrabutylammonium picrate ion pairs in diphenyl ether. *The Journal of Physical Chemistry*, **80**, no. 7, 767–775 (1976).

R. R. Netz and H. Orland. One and two-component hard-core plasmas. *The European Physical Journal E*, **1**, no. 1, 67–73 (2000).

M. E. J. Newman and G. T. Barkema. *Monte Carlo Methods in Statistical Physics* (Oxford University Press, Oxford : New York, 1999).

J. NOOLANDI and K. M. HONG. Theory of photogeneration and fluorescence quenching. *The Journal of Chemical Physics*, **70**, no. 7, 3230 (1979).

X. OBRADORS, A. LABARTA, A. ISALGUÉ, J. TEJADA, J. RODRIGUEZ, and M. PERNET. Magnetic frustration and lattice dimensionality in $SrCr8Ga4O19$. *Solid State Communications*, **65**, no. 3, 189–192 (1988).

A. T. OGIELSKI. Dynamics of three-dimensional Ising spin glasses in thermal equilibrium. *Physical Review B*, **32**, no. 11, 7384–7398 (1985).

L. ONSAGER. Zur Theorie der Elektrolyte. I. *Physikalische Zeitschrift*, **27**, 388–392 (1926).

L. ONSAGER. Reciprocal Relations in Irreversible Processes. II. *Physical Review*, **38**, no. 12, 2265–2279 (1931).

L. ONSAGER. Deviations from Ohm's Law in Weak Electrolytes. *The Journal of Chemical Physics*, **2**, no. 9, 599–615 (1934).

L. ONSAGER. Initial recombination of ions. *Physical Review*, **54**, no. 8, 554 (1938).

L. ONSAGER. Electrostatic Interaction of Molecules. *The Journal of Physical Chemistry*, **43**, no. 2, 189–196 (1939).

L. ONSAGER. Crystal Statistics. I. A Two-Dimensional Model with an Order-Disorder Transition. *Physical Review*, **65**, no. 3-4, 117–149 (1944).

L. ONSAGER and S. K. KIM. Wien Effect in Simple Strong Electrolytes. *The Journal of Physical Chemistry*, **61**, no. 2, 198–215 (1957).

M. ORENDÁČ, J. HANKO, E. ČIŽMÁR, A. ORENDÁČOVÁ, M. SHIRAI, and S. T. BRAMWELL. Magnetocaloric study of spin relaxation in dipolar spin ice $Dy2Ti2O7$. *Physical Review B*, **75**, no. 10, 104425 (2007).

W. OSTWALD. Formulierung des Massenwirkungsgesetzes für die Dissoziation schwacher Elektrolyte mit Hilfe der Leitfähigkeit bei endlicher und unendlicher Verdünnung. *Zeitschrift für physikalische Chemie*, **2**, 36–37 (1888).

D. M. PAI. Electric-field-enhanced conductivity in solids. *Journal of Applied Physics*, **46**, no. 12, 5122–5126 (1975).

J. K. PARK, J. C. RYU, W. K. KIM, and K. H. KANG. Effect of Electric Field on Electrical Conductivity of Dielectric Liquids Mixed with Polar Additives: DC Conductivity. *The Journal of Physical Chemistry B*, **113**, no. 36, 12271–12276 (2009).

A. PATTERSON and H. FREITAG. The Wien Effect and Ionic Association. *Journal of The Electrochemical Society*, **108**, no. 6, 529 (1961).

L. PAULING. The structure and entropy of ice and of other crystals with some randomness of atomic arrangement. *Journal of the American Chemical Society*, **57**, no. 12, 2680–2684 (1935).

C. Paulsen, M. J. Jackson, E. Lhotel, B. Canals, D. Prabhakaran, K. Matsuhira, S. R. Giblin, and S. T. Bramwell. Far-from-equilibrium monopole dynamics in spin ice. *Nature Physics*, **10**, no. 2, 135–139 (2014).

R. G. Pearson. Rates of ion recombination in solution by a radio-frequency dispersion method. *Discussions of the Faraday Society*, **17**, 187 (1954).

A. Persoons and M. V. Beylen. The dynamics of electric field effects in ion pairing processes. *Pure and Applied Chemistry*, **51**, no. 4, 887–900 (1979).

A. Persoons and L. Hellemans. New electric field methods in chemical relaxation spectrometry. *Biophysical Journal*, **24**, no. 1, 119–134 (1978). PMID: 708817 PMCID: PMC1473926.

A. P. Persoons. Field dissociation effect and chemical relaxation in electrolyte solutions of low polarity. *The Journal of Physical Chemistry*, **78**, no. 12, 1210–1217 (1974).

V. F. Petrenko and R. W. Whitworth. *Physics of Ice* (Oxford University Press, 1999).

D. Pini and G. Stell. Globally accurate theory of structure and thermodynamics for soft-matter liquids. *Physica A: Statistical Mechanics and its Applications*, **306**, 270–278 (2002).

D. Pini, G. Stell, and N. B. Wilding. A liquid-state theory that remains successful in the critical region. *Molecular Physics*, **95**, no. 3, 483–494 (1998).

F. Pollmann, J. J. Betouras, and E. Runge. Classical correlations of defects in lattices with geometrical frustration in the motion of a particle. *Physical Review B*, **73**, no. 17, 174417 (2006).

D. Pomaranski, L. R. Yaraskavitch, S. Meng, K. A. Ross, H. M. L. Noad, H. A. Dabkowska, B. D. Gaulin, and J. B. Kycia. Absence of Pauling's residual entropy in thermally equilibrated Dy2Ti2O7. *Nature Physics*, **9**, no. 6, 353–356 (2013).

W. H. Press, S. A. Teukolsky, and W. T. Vetterling. *Numerical Recipes 3rd Edition: The Art of Scientific Computing* (Cambridge University Press, Cambridge, UK ; New York, 2007), 3 edition edn..

P. Quémerais, P. McClarty, and R. Moessner. Possible Quantum Diffusion of Polaronic Muons in Dy2Ti2O7 Spin Ice. *Physical Review Letters*, **109**, no. 12, 127601 (2012).

J. A. Quilliam, L. R. Yaraskavitch, H. A. Dabkowska, B. D. Gaulin, and J. B. Kycia. Dynamics of the magnetic susceptibility deep in the Coulomb phase of the dipolar spin ice material Ho2Ti2O7. *Physical Review B*, **83**, no. 9, 094424 (2011).

A. P. Ramirez, G. P. Espinosa, and A. S. Cooper. Strong frustration and dilution-enhanced order in a quasi-2D spin glass. *Physical Review Letters*, **64**, no. 17, 2070–2073 (1990).

A. P. Ramirez, A. Hayashi, R. J. Cava, R. Siddharthan, and B. S. Shastry. Zero-point entropy in 'spin ice'. *Nature*, **399**, no. 6734, 333–335 (1999).

Z. Randriamalala, A. Denat, J. P. Gosse, and B. Gosse. Field-enhanced dissociation, the validity of Onsager's theory in surfactant solutions. *Electrical Insulation, IEEE Transactions on*, **20**, no. 2, 167–176 (1985).

F. Raoult. Loi générale de congélation des dissolvants. *Comptes rendus de l'Académie des Sciences*, **95**, 1030–1033 (1882).

F. Raoult. Loi générale des tensions de vapeur des dissolvants. *Comptes rendus de l'Académie des Sciences*, **104**, 1430—1433 (1887).

J. C. Rasaiah, D. N. Card, and J. P. Valleau. Calculations on the "Restricted Primitive Model" for 1–1 Electrolyte Solutions. *The Journal of Chemical Physics*, **56**, no. 1, 248–255 (1972).

T. Regier and P. Kay. Language, thought, and color: Whorf was half right. *Trends in Cognitive Sciences*, **13**, no. 10, 439–446 (2009). PMID: 19716754.

J. N. Reimers. Absence of long-range order in a three-dimensional geometrically frustrated antiferromagnet. *Physical Review B*, **45**, no. 13, 7287–7294 (1992).

J. N. Reimers and A. J. Berlinsky. Order by disorder in the classical Heisenberg kagomé antiferromagnet. *Physical Review B*, **48**, no. 13, 9539–9554 (1993).

H. Risken. *The Fokker-Planck Equation: Methods of Solution and Applications* (Springer, New York, 1996), 2nd ed. 1989. 3rd printing 1996 edition edn..

J. E. Roberts and J. Schnitker. Boundary conditions in simulations of aqueous ionic solutions: a systematic study. *The Journal of Physical Chemistry*, **99**, no. 4, 1322–1331 (1995).

S. Rosenkranz, A. P. Ramirez, A. Hayashi, R. J. Cava, R. Siddharthan, and B. S. Shastry. Crystal-field interaction in the pyrochlore magnet Ho2Ti2O7. *Journal of Applied Physics*, **87**, no. 9, 5914–5916 (2000).

B. Rosenstein and D. Li. Ginzburg-Landau theory of type II superconductors in magnetic field. *Reviews of Modern Physics*, **82**, no. 1, 109–168 (2010).

I. A. Ryzhkin. Magnetic relaxation in rare-earth oxide pyrochlores. *Journal of Experimental and Theoretical Physics*, **101**, no. 3, 481–486 (2005).

I. A. Ryzhkin and R. W. Whitworth. The configurational entropy in the Jaccard theory of the electrical properties of ice. *Journal of Physics: Condensed Matter*, **9**, no. 2, 395 (1997).

M. I. Ryzhkin, I. A. Ryzhkin, and S. T. Bramwell. Dynamic susceptibility and dynamic correlations in spin ice. *EPL (Europhysics Letters)*, **104**, no. 3, 37005 (2013).

G. Sala, C. Castelnovo, R. Moessner, S. L. Sondhi, K. Kitagawa, M. Takigawa, R. Higashinaka, and Y. Maeno. Magnetic Coulomb Fields of Monopoles in Spin Ice and Their Signatures in the Internal Field Distribution. *Physical Review Letters*, **108**, no. 21, 217203 (2012).

G. Sala, M. J. Gutmann, D. Prabhakaran, D. Pomaranski, C. Mitchelitis, J. B. Kycia, D. G. Porter, C. Castelnovo, and J. P. Goff. Vacancy defects and monopole dynamics in oxygen-deficient pyrochlores. *Nature Materials*, **13**, no. 5, 488–493 (2014).

E. E. Salpeter. On Mayer's theory of cluster expansions. *Annals of Physics*, **5**, no. 3, 183–223 (1958).

E. Sanz and D. Marenduzzo. Dynamic Monte Carlo versus Brownian dynamics: A comparison for self-diffusion and crystallization in colloidal fluids. *The Journal of Chemical Physics*, **132**, no. 19, 194102 (2010).

L. Savary, K. A. Ross, B. D. Gaulin, J. P. C. Ruff, and L. Balents. Order by Quantum Disorder in Er2Ti2O7. *Physical Review Letters*, **109**, no. 16, 167201 (2012).

J. Schiele. Über den Spannungseffekt der Leitfähigkeit bei starken und schwachen Säuren. *Annalen der Physik*, **405**, no. 7, 811–830 (1932).

U. Seifert. Entropy Production along a Stochastic Trajectory and an Integral Fluctuation Theorem. *Physical Review Letters*, **95**, no. 4, 040602 (2005).

A. Sen, K. Damle, and R. Moessner. Fractional Spin Textures in the Frustrated Magnet SrCr9pGa12-9pO19. *Physical Review Letters*, **106**, no. 12, 127203 (2011).

A. Sen, K. Damle, and R. Moessner. Vacancy-induced spin textures and their interactions in a classical spin liquid. *Physical Review B*, **86**, no. 20, 205134 (2012).

A. Sen and R. Moessner. A topological spin glass in diluted spin ice. *arXiv:1405.0668 [cond-mat]* (2014). arXiv: 1405.0668.

A. Sen, R. Moessner, and S. Sondhi. Coulomb Phase Diagnostics as a Function of Temperature, Interaction Range, and Disorder. *Physical Review Letters*, **110**, no. 10 (2013).

N. Shannon, O. Sikora, F. Pollmann, K. Penc, and P. Fulde. Quantum ice: a quantum Monte Carlo study. *Physical review letters*, **108**, no. 6, 067204 (2012).

E. F. Shender. Antiferromagnetic garnets with fluctuationally interacting sublattices. *Sov. Phys. JETP*, **56**, 178–184 (1982).

R. Siddharthan, B. S. Shastry, A. P. Ramirez, A. Hayashi, R. J. Cava, and S. Rosenkranz. Ising Pyrochlore Magnets: Low-Temperature Properties, "Ice Rules," and Beyond. *Physical Review Letters*, **83**, no. 9, 1854–1857 (1999).

R. SIMONS and G. KHANARIAN. Water dissociation in bipolar membranes: Experiments and theory. *The Journal of Membrane Biology*, **38**, no. 1-2, 11–30 (1978).

D. SLOBINSKY, C. CASTELNOVO, R. A. BORZI, A. S. GIBBS, A. P. MACKENZIE, R. MOESSNER, and S. A. GRIGERA. Unconventional Magnetization Processes and Thermal Runaway in Spin-Ice $Dy_2Ti_2O_7$. *Physical Review Letters*, **105**, no. 26 (2010).

M. V. SMOLUCHOWSKI. Über Brownsche Molekularbewegung unter Einwirkung äußerer Kräfte und deren Zusammenhang mit der verallgemeinerten Diffusionsgleichung. *Annalen der Physik*, **353**, no. 24, 1103–1112 (1916).

J. SNYDER, B. UELAND, J. SLUSKY, H. KARUNADASA, R. CAVA, and P. SCHIFFER. Low-temperature spin freezing in the Dy2Ti2O7 spin ice. *Physical Review B*, **69**, no. 6 (2004).

J. SNYDER, B. G. UELAND, J. S. SLUSKY, H. KARUNADASA, R. J. CAVA, A. MIZEL, and P. SCHIFFER. Quantum-Classical Reentrant Relaxation Crossover in Dy2Ti2O7 Spin Ice. *Physical Review Letters*, **91**, no. 10, 107201 (2003).

A. STERN. Non-Abelian states of matter. *Nature*, **464**, no. 7286, 187–193 (2010).

F. H. STILLINGER JR and R. LOVETT. Ion-Pair Theory of Concentrated Electrolytes. I. Basic Concepts. *The Journal of Chemical Physics*, **48**, no. 9, 3858–3868 (1968).

D. R. STIRZAKER. *Probability and Random Processes* (Oxford University Press, Oxford ; New York, 2001), 3 edition edn..

P. STREHLOW, S. NEUBERT, B. KLEMKE, and M. MEISSNER. Thermal transport in spin ice. *Continuum Mechanics and Thermodynamics*, **24**, no. 4-6, 347–359 (2012).

W. P. SU, J. R. SCHRIEFFER, and A. J. HEEGER. Solitons in Polyacetylene. *Physical Review Letters*, **42**, no. 25, 1698–1701 (1979).

W. SUTHERLAND. LXXV. A dynamical theory of diffusion for non-electrolytes and the molecular mass of albumin. *Philosophical Magazine Series 6*, **9**, no. 54, 781–785 (1905).

B. R. SVENSSON and C. E. WOODWARD. Widom's method for uniform and non-uniform electrolyte solutions. *Molecular Physics*, **64**, no. 2, 247–259 (1988).

H. THIS. Molecular Gastronomy. *Angewandte Chemie International Edition*, **41**, no. 1, 83–88 (2002).

M. TOMOZAWA, J. F. CORDARO, and M. SINGH. Applicability of weak electrolyte theory to glasses. *Journal of Non-Crystalline Solids*, **40**, no. 1, 189–196 (1980).

X. TONGWEN. Effect of asymmetry in a bipolar membrane on water dissociation — a mathematical analysis. *Desalination*, **150**, no. 1, 65–74 (2002).

G. Toulouse. Theory of the frustration effect in spin glasses. I. *Communications on Physics*, **2**, no. 4, 115–119 (1977).

T. Y. Tsong and R. D. Astumian. Electroconformational coupling and membrane protein function. *Progress in Biophysics and Molecular Biology*, **50**, no. 1, 1–45 (1987).

D. C. Tsui, H. L. Stormer, and A. C. Gossard. Two-Dimensional Magneto-transport in the Extreme Quantum Limit. *Physical Review Letters*, **48**, no. 22, 1559–1562 (1982).

E. J. W. Verwey and P. W. Haayman. Electronic conductivity and transition point of magnetite ("Fe3O4"). *Physica*, **8**, no. 9, 979–987 (1941).

G. Vidal, J. I. Latorre, E. Rico, and A. Kitaev. Entanglement in Quantum Critical Phenomena. *Physical Review Letters*, **90**, no. 22, 227902 (2003).

J. Villain. Theory of one- and two-dimensional magnets with an easy magnetization plane. II. The planar, classical, two-dimensional magnet. *Journal de Physique*, **36**, no. 6, 581–590 (1975).

J. Villain. Insulating spin glasses. *Zeitschrift für Physik B Condensed Matter*, **33**, no. 1, 31–42 (1979).

J. Villain, R. Bidaux, J. Carton, and R. Conte. Order as an effect of disorder. *Journal de Physique*, **41**, no. 11, 1263–1272 (1980).

E. Waisman and J. L. Lebowitz. Exact Solution of an Integral Equation for the Structure of a Primitive Model of Electrolytes. *The Journal of Chemical Physics*, **52**, no. 8, 4307–4309 (1970).

G. H. Wannier. Antiferromagnetism. The Triangular Ising Net. *Physical Review*, **79**, no. 2, 357–364 (1950).

H. Weingärtner. Corresponding states for electrolyte solutions. *Pure and Applied Chemistry*, **73**, no. 11, 1733–1748 (2001).

X. Wen. Quantum orders and symmetric spin liquids. *Physical Review B*, **65**, no. 16, 165113 (2002).

X. G. Wen. Topological Orders in Rigid States. *International Journal of Modern Physics B*, **04**, no. 02, 239–271 (1990).

B. Widom. Some Topics in the Theory of Fluids. *The Journal of Chemical Physics*, **39**, no. 11, 2808–2812 (1963).

M. Wien. Über eine Abweichung vom Ohmschen Gesetze bei Elektrolyten. *Annalen der Physik*, **388**, no. 11, 327–361 (1927).

M. Wien. Über den Spannungseffekt der elektrolytischen Leitfähigkeit in sehr starken Feldern. *Annalen der Physik*, **393**, no. 3, 400–416 (1929).

M. Wien. *Physikalische Zeitschrift*, **32**, 545–547 (1931).

F. Wilczek. Some Basic Aspects of Fractional Quantum Numbers. *arXiv:cond-mat/0206122* (2002). arXiv: cond-mat/0206122.

W. S. Wilson. *The Theory of the Wien Effect for a Binary Electrolyte*. Ph.D., Yale (1936).

J. A. Wingrave. Electrical behavior of poly (vinyl chloride): Wien-Onsager effect deviations from Ohm's law. *Journal of Vinyl Technology*, **2**, no. 2, 100–105 (1980).

M. Wojcik and M. Tachiya. Accuracies of the empirical theories of the escape probability based on Eigen model and Braun model compared with the exact extension of Onsager theory. *The Journal of Chemical Physics*, **130**, no. 10, 104107 (2009).

M. R. Wright. *An Introduction to Aqueous Electrolyte Solutions* (Wiley, Chichester, England ; Hoboken, NJ, 2007), 1 edition edn..

W. Wu, D. Bitko, T. F. Rosenbaum, and G. Aeppli. Quenching of the nonlinear susceptibility at a T=0 spin glass transition. *Physical Review Letters*, **71**, no. 12, 1919–1922 (1993).

L. R. Yaraskavitch, H. M. Revell, S. Meng, K. A. Ross, H. M. L. Noad, H. A. Dabkowska, B. D. Gaulin, and J. B. Kycia. Spin dynamics in the frozen state of the dipolar spin ice material Dy2Ti2O7. *Physical Review B*, **85**, no. 2, 020410 (2012).

T. Yavors'kii, T. Fennell, M. J. Gingras, and S. T. Bramwell. Dy2Ti2O7 spin ice: a test case for emergent clusters in a frustrated magnet. *Physical review letters*, **101**, no. 3, 037204 (2008).

P. Young and A. P. Young. *Spin Glasses & Random Fields* (World Scientific Pub Co Inc, Singapore : River Edge, N.J, 1998), 1st edition edn..

R. W. Youngblood and J. D. Axe. Polarization fluctuations in ferroelectric models. *Physical Review B*, **23**, no. 1, 232–238 (1981).

Y. Yuan, T. J. Reece, P. Sharma, S. Poddar, S. Ducharme, A. Gruverman, Y. Yang, and J. Huang. Efficiency enhancement in organic solar cells with ferroelectric polymers. *Nature Materials*, **10**, no. 4, 296–302 (2011).

C. Zeng and V. Elser. Numerical studies of antiferromagnetism on a Kagomé net. *Physical Review B*, **42**, no. 13, 8436–8444 (1990).

M. E. Zhitomirsky, M. V. Gvozdikova, P. C. W. Holdsworth, and R. Moessner. Quantum Order by Disorder and Accidental Soft Mode in Er2Ti2O7. *Physical Review Letters*, **109**, no. 7, 077204 (2012).

H. D. Zhou, J. G. Cheng, A. M. Hallas, C. R. Wiebe, G. Li, L. Balicas, J. S. Zhou, J. B. Goodenough, J. S. Gardner, and E. S. Choi. Chemical Pressure Effects on Pyrochlore Spin Ice. *Physical Review Letters*, **108**, no. 20, 207206 (2012).

D. M. Zuckerman, M. E. Fisher, and B. P. Lee. Critique of primitive model electrolyte theories. *Physical Review E*, **56**, no. 6, 6569 (1997).

Versicherung

Hiermit versichere ich, dass ich die vorliegende Arbeit ohne unzulässige Hilfe Dritter und ohne Benutzung anderer als der angegebenen Hilfsmittel angefertigt habe; die aus fremden Quellen direkt oder indirekt übernommenen Gedanken sind als solche kenntlich gemacht. Die Arbeit wurde bisher weder im Inland noch im Ausland in gleicher oder ähnlicher Form einer anderen Prüfungsbehörde vorgelegt.

5. September 2014, Vojtěch Kaiser